Open Clusters as Laboratories for Stellar Spin Down and Magnetic Activity Decay

Stephanie Teresa Douglas

Submitted in partial fulfillment of the
requirements for the degree
of Doctor of Philosophy
in the Graduate School of Arts and Sciences

COLUMBIA UNIVERSITY

2017

ABSTRACT

Open Clusters as Laboratories for Stellar Spin Down and Magnetic Activity Decay

Stephanie T. Douglas

The oldest open clusters within 250 pc of the Sun, the Hyades and Praesepe, are important benchmarks for calibrating stellar properties such as rotation and magnetic activity. As they have the same age and roughly solar metallicity, these clusters serve as an ideal laboratory for testing the agreement between theoretical and empirical rotation-activity relations at 650 Myr. The re-purposed *Kepler* mission, *K2*, has allowed me to measure rotation periods for dozens of Hyads and hundreds of Praesepe members, including the first periods measured for fully convective Hyads. These data have enabled new tests of models describing the evolution of stellar rotation; discrepancies with these models imply that we still do not fully understand how magnetic fields affect stellar spin-down. I show how we can compare the dependence of H-alpha and X-ray emission on rotation in order to test theories of magnetic field topology and stellar dynamos. These tests inform models of stellar wind-driven angular momentum loss and the age-rotation-activity relation. I also present rotation periods measured for 48 Hyads and 677 Praesepe members with *K2*, and discuss the impact of unresolved binaries on the study of rotational evolution.

Contents

List of Figures **iv**

List of Tables **viii**

Acknowledgments **x**

1 Introduction **1**

1.1 The impact of stellar rotation and magnetism on planetary habitability . . . 1

1.2 Stellar Rotation . . . 5

1.2.1 Measuring Stellar Rotation . . . 5

1.2.2 The Evolution of Stellar Rotation . . . 11

1.3 Stellar Magnetism . . . 17

1.3.1 Magnetic dynamos in the Sun and other stars . . . 17

1.3.2 Observations of Stellar Magnetism and its Evolution . . . 20

1.4 The (Age-)Rotation-Activity Relation . . . 25

1.4.1 Magnetic braking on the main sequence . . . 25

1.4.2 Saturation and the Rossby Number . . . 32

1.4.3 Testing theories of saturation . . . 35

1.5 Benchmarking Stellar Evolution with Open Clusters . . . 38

1.6 The Hyades and Praesepe Open Clusters . . . 40

1.7 Structure of Dissertation . . . 42

2 Activity and Rotation in Praesepe and the Hyades **46**

2.1 Introduction . . . 46

2.2 Data . . . 49

2.2.1 Membership Catalogs . . . 49

2.2.2 Photometry . . . 50

2.2.3 Spectroscopy . . . 53

2.2.4 Rotation Periods . . . 59

2.3 Measurements and Derived Quantities . . . 60

2.3.1 $H\alpha$ Measurements and $L_{H\alpha}/L_{bol}$ . . . 60

2.3.2 Stellar Masses . . . 68

2.3.3 Binary Identification . . . 69

2.3.4 Rossby Numbers . . . 70

2.4 Results and Discussion . . . 71

2.4.1 Comparing Chromospheric Activity in the Two Clusters . . . 71

2.4.2 Activity and Measurements of Periodic Variability . . . 74

2.4.3 The Relationship Between $H\alpha$ Emission and Rotation . . . 77

2.4.4 Chromospheric and Coronal Activity-Rotation Relations at 600 Myr 80

2.5 Conclusion . . . 84

3 *K2* Rotation Periods for low-mass Hyads and the Implications for Gyrochronology **87**

3.1 Introduction . . . 87

3.2 Archival Data . . . 89

3.2.1 Membership . . . 89

3.2.2 Photometry . . . 91

3.2.3 Archival Rotation Periods . . . 94

3.2.4 Companions . . . 96

3.3 Stellar masses . . . 101

3.4 *K2* data . . . 102

3.4.1 Light Curve Extraction . . . 104
3.4.2 Accounting for Nearby Stars . . . 106
3.4.3 Detrending Light Curves and Measuring P_{rot} . . . 109
3.4.4 Light Curves With Multiple Periodic Signals . . . 118
3.5 Results . . . 119
3.5.1 Consistency With Prior P_{rot} Measurements . . . 122
3.5.2 Stellar Rotation and Multiplicity at 625 Myr . . . 124
3.6 Discussion . . . 127
3.6.1 Implications for Gyrochronology . . . 127
3.6.2 Implications for Magnetic Braking Models . . . 129
3.7 Conclusions . . . 133

4 Poking the Beehive from Space: *K2* Rotation Periods for Praesepe 135
4.1 Introduction . . . 135
4.2 Existing Data . . . 137
4.2.1 Cluster Catalog . . . 137
4.2.2 Archival Rotation Periods . . . 138
4.3 Measuring Rotation Periods with K2 . . . 143
4.3.1 K2 Light Curves . . . 143
4.3.2 Measuring Rotation Periods . . . 145
4.3.3 Validating the Measured Rotation Periods . . . 147
4.3.4 Photometric Amplitudes . . . 151
4.4 Binary Identification . . . 152
4.4.1 Visual Identification . . . 153
4.4.2 Photometric Identification . . . 153
4.4.3 Literature Identifications . . . 155
4.4.4 Binaries Identified from K2 Data . . . 156
4.5 Results and Discussion . . . 159
4.5.1 Consistency of P_{rot} Measured from Different Surveys . . . 161

4.5.2 Binaries in the Mass-Period Plane 164
4.5.3 Comparison with Models of Rotation Evolution 166
4.6 Conclusions 174

5 Conclusions **177**
5.1 Distribution of rotation periods at 600 Myr 177
5.2 Consistent Activity Distributions in the Hyades and Praesepe 179
5.3 The activity-rotation relation at 650 Myr 180
5.4 Investigating the rotational evolution of binary stars 181

Bibliography **183**

Appendix A Recalculating the χ Factor **212**

Appendix B Candidate Transiting and Eclipsing Systems in Praesepe **219**

Appendix C Acknowledgement of assistance, funding, software, facilities, and data **222**

List of Figures

1.1 Calcium emission, rotation, and lithium abundance versus stellar age, from Skumanich (1972), and an updated version for rotation from Mamajek (2014) 4

1.2 Schematic of stellar light curves produced by solar-type stars at three different ages by Søren Meibom. 7

1.3 Mass-period diagrams for open clusters and the field, showing the evolution of stellar rotation. 10

1.4 Evolution of the fast and slow rotator sequences from Barnes et al. (2003). . 15

1.5 The Solar dynamo model of Babcock (1961) 19

1.6 The approximate temperature profile for the quiet Sun, with the source locations of various emission and absorption features overlaid, from Vernazza et al. (1981) 21

1.7 SOHO image of the Sun, with magnetic field loops and solar wind streams overlaid. 28

1.8 Cartoon of the saturation phenomenon, and demonstration of the Rossby Number. 44

1.9 Distribution of Galactic Open Clusters in distance, age, and Galactic height (Z). 45

2.1 Color-magnitude diagrams indicating the sources of *r'* photometry for Praesepe and the Hyades. 51

2.2 Example spectra from our new observations of Praesepe and Hyades stars with ModSpec on MDM, Hydra on WIYN, and MagE on Magellan. 55

2.3 Color-magnitude diagrams for Praesepe and the Hyades showing the completeness of our spectroscopic samples. 58
2.4 Comparison of EqW measurements from this work with those of Kafka & Honeycutt (2006) and Stauffer et al. (1997). 62
2.5 $H\alpha$ EqW vs. $(r' - K)$ for stars in Praesepe and the Hyades. 63
2.6 $L_{H\alpha}/L_{bol}$ vs. $(r' - K)$ for stars in Praesepe and the Hyades. 64
2.7 Mass-period diagram for Praesepe and the Hyades. 69
2.8 Average $H\alpha$ EqW vs. logarithmically binned color for stars in Praesepe and the Hyades, and for 2800 SDSS M dwarfs. 73
2.9 $H\alpha$ EqWs for stars with and without measured P_{rot} 75
2.10 Mass-period diagram for Praesepe and Hyades stars with measured P_{rot} and $H\alpha$ EqW and $P_{mem} \geq 70\%$ (known and candidate binaries are not included) . 78
2.11 $L_{H\alpha}/L_{bol}$ and L_X/L_{bol} vs. R_o for Praesepe and Hyades stars with various power-laws for the unsaturated regime overlaid. 82
2.12 Marginalized posterior probability distributions for the saturation model fit to Praesepe and Hyades $H\alpha$ data. 83

3.1 Color-magnitude diagram for Hyads showing the source of r' photometry. . 92
3.2 Mass-period distribution for Hyads with period measurements in the literature. 97
3.3 Color-magnitude diagram of the Hyades, demonstrating our method for identifying photometric candidate binaries and the distribution of confirmed multiple systems. 98
3.4 The *K2* Campaign 4 field of view showing our Hyades targets. 103
3.5 Diagnostic plots used to inspect the *K2* data and check for neighboring stars. 105
3.6 *K2* image of EPIC 210736105 and its nearby neighbor, and the extracted light curves of each. 108
3.7 *K2* image of EPIC 210963067 and its nearby neighbor, and the extracted light curves of each. 109
3.8 Demonstration of our *K2* detrending method and period search. 113
3.9 Comparison of P_{rot} measured at different stages of our analysis. 116

3.10 Four light curves for which the P_{rot} measured from the secondary light curve is more likely the true value. . . . 117
3.11 Mass-period distribution for all Hyads with measured periods, highlighting our new *K2* detections. . . . 120
3.12 P_{rot} and $H\alpha$ EqWs vs color for Hyads, with binaries highlighted. . . . 126
3.13 Mass-period distribution for nominally single Hyads compared to Reiners & Mohanty (2012) models at 650 Myr and 10 Gyr. . . . 130
3.14 Mass-period distribution for nominally single Hyads compared to the Matt et al. (2015) model at 650 Myr . . . 131

4.1 Praesepe mass-period plane showing all literature P_{rot} before the addition of the new *K2* data. . . . 139
4.2 K2 field-of-view with Praesepe members and K2 targets . . . 144
4.3 Examples of the light curve shapes where two periods are present or the detected period is spurious. . . . 147
4.4 Histogram of periodogram powers from our sample. . . . 148
4.5 Diagnostic plot used to inspect period detections and check for neighboring stars. . . . 150
4.6 Color-magnitude diagram of Praesepe, showing photometric candidate binaries and the distribution of confirmed multiple systems. . . . 154
4.7 Praesepe mass-period plane showing literature and previously unpublished high-quality *K2* P_{rot} for stars with $P_{mem} > 70\%$. . . . 158
4.8 P_{rot} from *K2* compared to literature P_{rot} for the same stars. . . . 162
4.9 Amplitude of the *K2* light curve as a function of K_p; colors indicate stars with literature P_{rot}. . . . 163
4.10 Mass-period plane with the region that defines $M_* > 0.3\ M_\odot$ rapid rotators outlined. . . . 166
4.11 Comparison of P_{rot} in Praesepe with the P_{rot} distribution predicted by Matt et al. (2015) at 653 Myr. . . . 168
4.12 A box-and-whiskers plot of the Praesepe mass-period plane compared to predictions by Brown (2014) and Matt et al. (2015). . . . 169

4.13 Praesepe P_{rot} distribution compared to that predicted by Matt et al. (2015) for different mass bins. 170

4.14 Comparison of P_{rot} in Praesepe with the P_{rot} distribution predicted by Brown (2014) at 649 Myr. 172

4.15 Praesepe P_{rot} distribution compared to that predicted by Brown (2014) for different mass bins. 173

A.1 χ calculated for SDSS and PMSU data and for PHOENIX model spectra. . . 213

A.2 A comparison of our χ values for SDSS M dwarfs and those listed in West & Hawley (2008). 214

A.3 χ calculated for SDSS M dwarfs and for PHOENIX model spectra, along with parametric functions from our fits and given by West & Hawley (2008) and Schmidt et al. (2014). 215

B.1 Light curves for six candidate eclipsing systems identified by eye from Campaign 5 data. 220

List of Tables

2.1 ModSpec Observations of Praesepe and Hyades Stars 54
2.2 Hydra Observations of Praesepe Fields 54
2.3 MagE Observations of Praesepe Stars 54
2.4 Final Spectroscopic Sample 56
2.5 Praesepe Stars 66
2.6 Hyades Stars 67

3.1 Hyads with multiple P_{rot} measurements 95
3.1 Hyads with multiple P_{rot} measurements 96
3.2 Confirmed and candidate binary and planetary systems among the *K2* targets and Hyads with measured P_{rot} 99
3.3 Rotation periods measured from *K2* data 121
3.4 *K2* targets for which P_{rot} could not be measured 123

4.1 Praesepe members with discrepant P_{rot} measurements 140
4.1 Praesepe members with discrepant P_{rot} measurements 141
4.1 Praesepe members with discrepant P_{rot} measurements 142
4.2 Companions to Praesepe members with measured P_{rot} 157
4.3 P_{rot} measurements for Praesepe stars targeted in K2 160

A.1 χ values for M stars, calculated from SDSS data 216
A.2 Colors and χ values from PHOENIX model spectra 217

A.2 Colors and χ values from PHOENIX model spectra 218

ACKNOWLEDGMENTS

First and foremost, I wish to thank my thesis advisor, Marcel Agüeros. I'm grateful for how he has pushed me to pursue opportunities and to be a more independent researcher. Yet he has also been constantly available whenever I've needed him, from collaborating on proposals (especially at the last minute) to taking the time to talk me through a myriad of research crises that have sent me into his office in a panic. I can't thank him enough for his unwavering support and mentorship over the last five years.

I have also benefited greatly from an incredible network of collaborators and co-authors on my thesis research. I especially thank my co-advisor, Kevin Covey, for being an invaluable source of research and career advice during my time as a graduate student. I am also particularly indebted to Phill Cargile, Ann Marie Cody, Steve Howell, and Adam Kraus for helping me learn statistical and data analysis techniques, and for providing crucial commentary on the papers that form this thesis.

I would not be where I am today (in academia or New York City) without the BDNYC research group. Kelle Cruz, Emily Rice, and Jackie Faherty have helped guide me from a painfully nervous REU student to an NSF Fellow. I especially thank Kelle for being an invaluable mentor to me on many fronts, and for being willing to serve on my committee.

I thank the many members of the Columbia Astronomy Dept who have supported and encouraged me over the last five years. Kathryn Johnston and David Schiminovich, as members of my committee, have provided crucial suggestions and guidance as I have navigated my thesis work. Jeno Sokoloski and Summer Ash have also been sources for

wise advice and excellent discussions on many occasions. I thank many of the graduate students and postdocs at Columbia for their support and friendship, especially Jennifer Weston, Steven Mohammed, Alejandro Núñez, Ruth Angus, Kirsten Blancato, Maria Charisi, Susan Clark, Jason Curtis, Andrea Derdzinski, Ximena Fernandez, Rose Gibson, Aleksey Generozov, Keith Hawkins, Jia Liu, Adrian Lucy, Adrian Price-Whelan, and Yong Zheng. Finally, I have to thank Mildred Kramer-Garcia and Ayoune Payne for their tireless support of all of the graduate students in the department, without which I doubt I could have navigated the last five years.

In the course of my thesis work, I have spent more than 40 nights at the MDM Observatory on Kitt Peak, AZ. Though much of the data that I personally gathered has not made it into this dissertation, MDM data enabled the analysis in Chapter 2. I therefore wish to thank Eric Galayda and Jules Halpern for their support—in particular for their willingness to answer my phone calls in the middle of the night.

Finally, I owe a deep debt of gratitude to my family and friends who have supported me throughout this journey. My parents James and Tracey Douglas have encouraged my interest in science from the beginning, and my sister Taylor has been an incredible source of support while taking on her own challenges in medical school. I also can't thank my friends in NYC enough, especially Charity Kittler, Katrina Wheeler, Krystle Farman, Kathryn Fore, Maggie Duckworth, Jordan Wesley, Amanda Craft, and Sloane Taylor, for putting up with my weird schedules and anxious episodes. I wouldn't have gotten through this without our meals, movies, craft nights, and too many drinks to count.

2017, New York City

Chapter 1

Introduction

1.1 The impact of stellar rotation and magnetism on planetary habitability

The future of exoplanet studies lies around the lowest-mass stars: M dwarfs, the most numerous stars in our Galaxy. Though their faint magnitudes make them a challenge to observe, it also enhances the signal of an exoplanet orbiting in the habitable zone. The relative area blocked by a transiting exoplanet is larger for an M dwarf host than a higher-mass host, producing a more easily detectable transit signal for a fixed planet radius. The Doppler wobble induced in the host's radial velocity signal is also easier to detect, since a planet will cause a larger shift in the motion of a lower-mass host. Furthermore, the liquid water habitable zone of an M dwarf is much closer to the star than for a hotter star, so the total observing baseline needed to detect multiple transits is shorter for M dwarfs. Therefore, most habitable exoplanets are likely to be discovered around nearby M dwarfs.

However, M dwarfs emit high rates of ultraviolet (UV) and X-ray photons for much longer than more massive stars. This high energy emission has the potential to dissociate molecules and prevent or mutate life (e.g., Kasting et al. 1993; Lichtenegger et al. 2010; Segura et al. 2010). The high-energy radiation environment around a planet therefore significantly impacts the probability of life developing (and surviving) on the planet's surface.

The incidence of UV and X-ray photons on a planet depends on its host's magnetic activity, which, in turn, is related to its mass, rotation period, and age (e.g, Shkolnik & Barman 2014; Stelzer et al. 2016). UV and X-ray photons are produced when magnetic fields heat the stellar atmosphere, and this excess energy is then radiated away via line emission. Non-thermal magnetic heating also produces Hydrogen emission in the optical Balmer lines, as well as radio emission (Reid & Hawley 2005; Villadsen et al. 2014). Magnetic heating occurs where magnetic flux tubes emerge through the surface in active regions, so stars with more complex fields and more active regions will produce stronger line emission. Thus, excess emission above the photosphere at key wavelengths is an indicator of the stellar magnetic field strength and topology.

Given that life takes time to develop, measuring the evolution of high energy emission from exoplanet host stars is necessary for understanding the evolution of habitability. Age is difficult to measure for isolated field FGKM stars, however. The luminosity and radius of early-type stars (OBA and early F) evolve significantly over 10s–100s of Myr, so their age can be determined fairly easily if those quantities are known (e.g., Soderblom 2010, and references therein). Solar-type stars ($\approx$0.8–1.3 $M_{\odot}$), in contrast, remain at approximately

the same color and brightness for 5–10 Gyr, and lower-mass stars remain constant for 10s of Gyr. Successful isochronal ages can be determined for stars that have passed through at least one-third of their main sequence lifetime, and even then the resulting age uncertainties are 20–50% (without accounting for systematic effects Soderblom 2010). Thus, it's only possible to pinpoint these stars' ages if they are associated with other, older stars, such as in star clusters where an isochrone can be fit to the entire cluster sequence. Isochronal dating methods are effectively useless for isolated solar-type and low-mass main sequence stars, and some other method is necessary to determine their ages.

The age-rotation-activity relation (ARAR) offers an alternate method for determining ages for main sequence solar-type and low-mass stars. Based on work by Wilson (1963, 1968, 1970) and Kraft (1967), Skumanich (1972) first quantified the decline of rotation and activity (as traced by Ca II H & K emission) with stellar age, and showed that both quantities decrease at approximately the same rate for solar-type stars: $\propto t^{-0.5}$ (Figure 1.1(a)). This is often referred to as the "Skumanich law". Although Skumanich's analysis only included stars in the Pleiades and Hyades open clusters and the Ursa Major association, along with the Sun, his result nonetheless led to hope that rotation and activity could be used as clocks to determine the age of isolated field stars—Boesgaard & Hagen (1974) first used Skumanich's result to measure the ages of the three stars in α Centauri.

For solar-type stars on the main sequence, at least, the Skumanich law has held up well (Figure 1.1(b); Mamajek 2014). Subsequent observations have shown that the magnetic and rotational evolution of pre-main sequence (PMS) and lower-mass main sequence stars is much more complex, though, and the Skumanich (1972) law does not

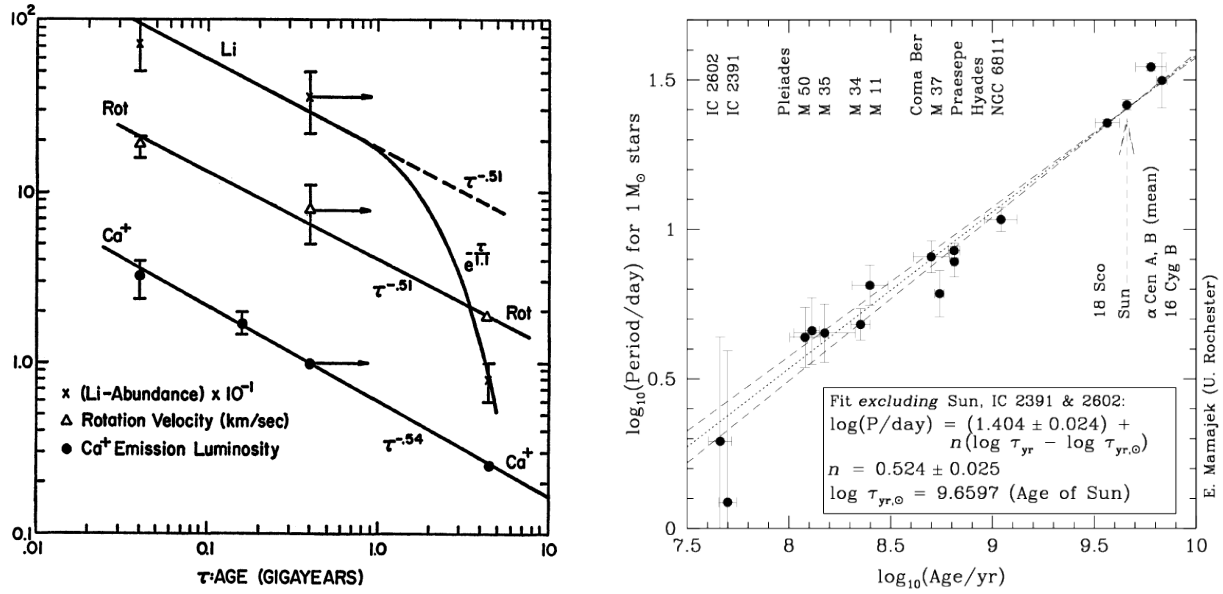

(a) (b)

Figure 1.1 Left—Calcium emission, rotation (measured as $v \sin(i)$), and lithium abundance versus stellar age. The data points come from the Pleiades, Ursa Major, and Hyades clusters, along with the Sun. Image Credit: Skumanich (1972). Right—Rotation (measured as P_{rot}) for solar-type stars in open clusters, the Sun, and field stars. The slope of the relation between P_{rot} and age is consistent with a the Skumanich spin-down law. Image Credit: Mamajek (2014).

capture the full phenomenology of angular momentum evolution on the approach to the ZAMS, and on the main sequence itself for lower-mass stars. Constraining the evolution of rotation and activity for lower-mass stars would expand the possibility of determining ages for all stars with masses 0.1–1.3 $M_{\odot}$.

1.2 Stellar Rotation

1.2.1 Measuring Stellar Rotation

The first star to have its rotation period (P_{rot}) measured was the Sun, where sunspots and active regions can be traced precisely. For example, Carrington (1859) measured the sidereal period[1] to be $P_{rot,\odot} = 25.652$ days. This period corresponds to the typical latitudes for starspots, which appear within $\approx 30^\circ$of the equator.[2] Differential rotation means that the Sun's equator rotates faster than its higher latitudes; after accounting for latitudinal differential rotation, Snodgrass & Ulrich (1990) use full-disk solar magnetograms to derive a sidereal $P_{rot,\odot} = 24.47$ days at the Solar equator. Measuring the rotation rates for other stars is more challenging, however, as their surfaces are not resolved.

Initial measurements of stellar rotation were largely restricted to measurements of rotational broadening in spectral lines; these measurements date back to Abney (1877) (as cited in Bouvier et al. 2014). The blue- and redshifts induced by the approaching and receding limbs of the star cause individual spectral lines to be broadened. This broadening is maximized when the observer's sightline passes directly through a star's equator, and nonexistent for perfectly pole-on sightlines. Therefore, the relevant observable quantity is $v \sin(i)$: the rotational velocity v modulated by the sine of the inclination angle i (defined as the angle between the observed line of sight and the star's rotational axis, such that $i = 0^\circ$ for pole-on views, and $i = 90^\circ$ for equatorial views). It is only possible to convert $v \sin(i)$ to a P_{rot} value if i and the stellar radius R are known; without i, $v \sin(i)$ only yields

[1]The Sun's sidereal P_{rot} is its true P_{rot} as measured relative to the background stars, rather than the observed period from Earth, which is slightly longer due to Earth's orbital motion.

[2]`https://solarscience.msfc.nasa.gov/SunspotCycle.shtml`

an upper limit on P_{rot}.

Time-series Ca II data were also used to infer P_{rot} for much of the mid-20th century, especially in older field stars with longer periods. The Mount Wilson Survey (e.g., Wilson 1978; Vaughan et al. 1981; Baliunas et al. 1996) provided most of this data. As discussed in Section 1.3.2, however, moderate-resolution, high signal-to-noise spectra are needed for these measurements, limiting the applicability of this method for a large sample of stars.

The cumulative effect of starspot groups rotating in and out of view can be seen in time-series photometry, allowing P_{rot} to be measured directly. This interpretation of photometric variability in main sequence stars goes back to explanations of RS CVn and BY Dra variability (Hall 1972; Vogt 1975; Strassmeier 2009). Starspots are darker than the surrounding photosphere, reducing the cumulative brightness of the stellar surface. As viewed from Earth, the brightness of a spotted star will therefore change slightly as active regions rotate into and out of view (Figure 1.2). A photometric P_{rot} can be measured from the frequency of these photometric variations so long as the starspots are distributed asymmetrically around the star and are reasonably static throughout at least one rotation (Aigrain et al. 2016), and as long as the star's pole does not directly face Earth. Initial evidence for rotational variability in low-mass open cluster stars dates to Robinson & Kraft (1974, in the Pleiades) and Radick et al. (1982, in the Pleiades and Hyades). Lockwood and Radick carried out the first P_{rot} survey in a cluster, using individual targeted observations of Hyades members to measure photometric P_{rot} (Lockwood et al. 1984; Radick et al. 1987, 1995).

The amplitude of photometric variability depends on the spot contrast and filing

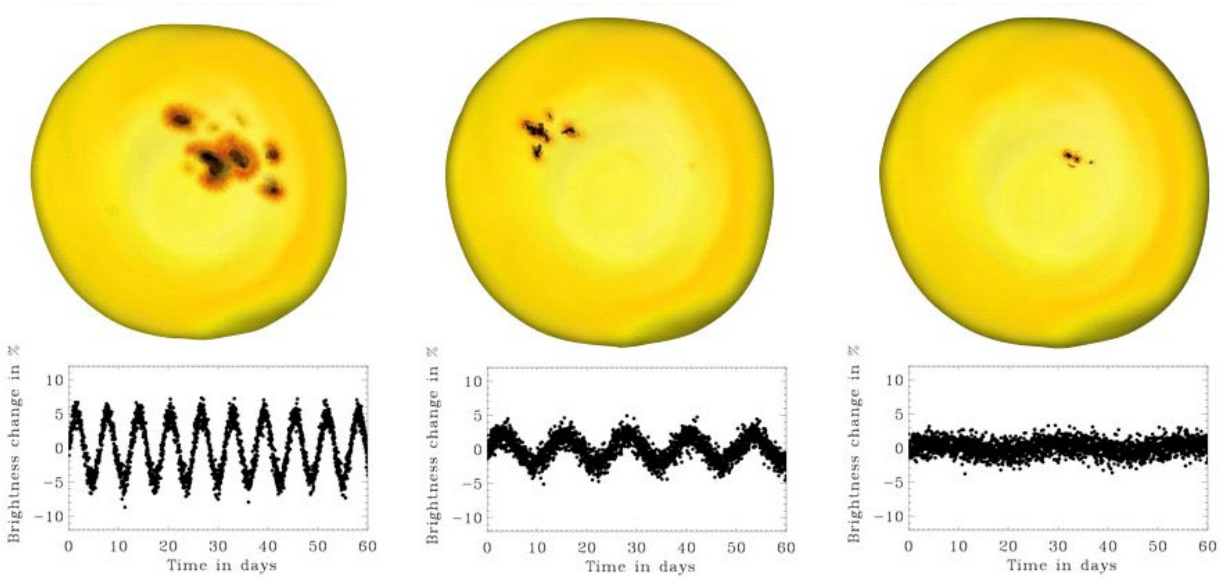

Figure 1.2 Schematic of stellar light curves produced by solar-type stars at three different ages: ZAMS/Pleiades age, Hyades age, and Solar age. Older stars rotate more slowly and have smaller active regions, leading to lower-amplitude rotational signals. Image Credit: Søren Meibom

factor, along with i. Spots typically only cover 0.1-0.5% of the Sun's surface[3], but younger and lower-mass stars may have 40–50% of their surface covered in spots (Fang et al. 2016). Starspots as large as 15% of the stellar surface were detected on a K3 dwarf (Barnes 2005; Wolter et al. 2005), and giant polar spots are often observed on rapidly rotating stars (Strassmeier 2002; Yadav et al. 2015b). Thus, young stars are expected to demonstrate the highest levels of photometric variability (Figure 1.2), although the prevalence of polar spots may complicate or prevent P_{rot} detections for young rapid rotators.

Measuring P_{rot} requires carrying out time series photometric surveys. Unfortunately, these observations are often expensive to obtain, as surveys must trade off between cadence, photometric precision, sky coverage (both for individual fields and the survey as

[3] `https://solarscience.msfc.nasa.gov/SunspotCycle.shtml`

a whole), and baseline of observations. This in turn limits the range of periods that can be detected and the brightness of stars for which periods can be measured: for example, shorter periods require a faster cadence, but this typically limits the exposure times that can be used and the amount of the sky that can be imaged at that cadence.

Nonetheless, photometric P_{rot} surveys have become increasingly common since Radick and Lockwood's survey of the Hyades in the 1980s–1990s, and the field has exploded in the last 5–10 years with the advent of large-scale ground- and space-based planet transit surveys (e.g., SuperWASP and NASA's *Kepler* and *K2* missions; Smith & WASP Consortium 2014; Borucki et al. 2010; Howell et al. 2014). As in the Radick and Lockwood survey, most initial efforts focus on measuring P_{rot} in star-forming regions and young open clusters using existing instrumentation, for example surveys of the Orion Nebula Cluster (ONC; Stassun et al. 1999; Herbst et al. 2001, 2002) and the Monitor Project survey of 5–150 Myr-old open clusters (Irwin et al. 2006, 2007, 2008a,b; Moraux et al. 2013). The state of the field around this time can be seen in Figure 1 of Irwin & Bouvier (2009)—the only clusters older than 200 Myr are M37, the Hyades, and Praesepe, with P_{rot} measurements for ≈60, 23, and 5 members, respectively. Shortly after that review, however, wide-field surveys begin to provide dozens of new P_{rot} for teenaged clusters (≈400–800 Myr), including Coma Ber (Collier Cameron et al. 2009, with SuperWASP), M37 (Hartman et al. 2009), and the Hyades and Praesepe (Delorme et al. 2011; Agüeros et al. 2011, with SuperWASP and PTF, respectively).

Older stars also suddenly become accessible with the advent of the *Kepler* space telescope. *Kepler*'s primary mission was to observe a patch of sky in Cygnus to search for

transiting exoplanets; the telescope therefore carried an extremely precise detector, and stared at the same patch of sky for four years. *Kepler* produced light curves for ≈150,000 stars; in addition to thousands of exoplanets, this data was also ideal for studying stellar astrophysics. In May 2013, the second of *Kepler*'s four reaction wheels, which function like gyroscopes to keep the telescope pointed precisely, failed. The spacecraft engineers then placed the spacecraft flat in the plane of the Solar System, so that the Solar wind torque on the spacecraft could be minimized. Beginning in 2014, the *K2* mission pointed to fields in the Ecliptic for a series of ≈75-day campaigns; *K2* is expected to continue through 2018, when the spacecraft will run out of fuel. *K2* has already observed a wide variety of Galactic environments, from open clusters and star forming regions in the plane to halo stars.

The *Kepler* prime mission observed four old open clusters, and joined new ground-based surveys in producing light curves for older field stars. *Kepler* yielded P_{rot} for ≈60 FGK members of the 1 Gyr-old cluster NGC 6811 (Meibom et al. 2011a), as well as a handful of 2.5 Gyr-old Solar-type stars in NGC 6819 (Meibom et al. 2015). Both *Kepler* and the MEarth survey generated remarkable samples of P_{rot} measurements for field stars (McQuillan et al. 2013, 2014; Newton et al. 2016), but without individual stellar ages these samples are of limited use in constraining P_{rot} evolution. The state of P_{rot} observations for clusters and the field prior to this dissertation (with a focus on ZAMS and teenage clusters) is shown in Figure 1.3.

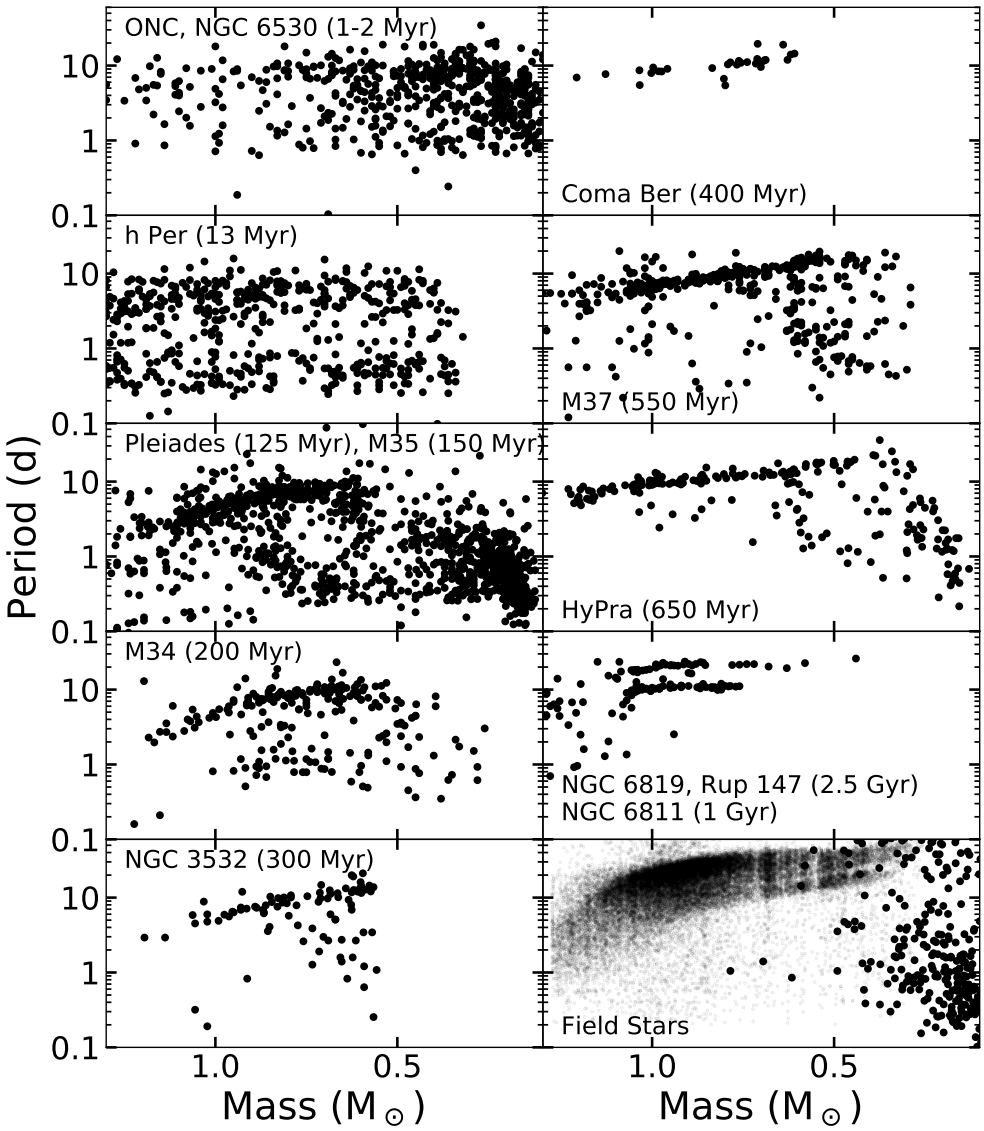

Figure 1.3 The evolution of the P_{rot} distribution from newly formed stars in the ONC to old field stars. Periods shown for the ONC (Herbst et al. 2002), NGC6530 (Henderson & Stassun 2012), the Pleiades (Covey et al. 2016; Rebull et al. 2016b), M35 (Meibom et al. 2009), M34 (Irwin et al. 2006; Meibom et al. 2011b), NGC 3532 (Barnes 2003), Coma Ber (Collier Cameron et al. 2009), M37 (Hartman et al. 2009; Messina et al. 2010), the Hyades and Praesepe (Pre-*K2*; see Chapters 2–4), NGC 6811 and NGC 6819 (Meibom et al. 2011a, 2015), and the field (McQuillan et al. 2014; Newton et al. 2016). Based on plots from Irwin & Bouvier (2009) and Bouvier et al. (2014).

1.2.2 The Evolution of Stellar Rotation

1.2.2.1 Disks and the initial angular momentum distribution

FGKM stars emerge from their protostellar phase with P_{rot} between 1–10 days. A given star-forming region will contain stars with this full range of P_{rot} at all masses $0.08M_{\odot} < M_{*} < 1.3M_{\odot}$. However, within ≈5 Myr, a substantial fraction of stars are observed to have $P_{rot} < 1$ day, while the other stars remain at their slower P_{rot}. The simultaneous presence of both rapid and slowly rotating stars is puzzling, as contraction along the Hayashi track is expected to cause these stars to spin up, leaving no slow rotators (Moraux et al. 2013).

Observations of young clusters indicate the presence of a bimodal P_{rot} distribution with both fast and slow rotators separated by a gap, although this claim was contentious for at least a decade. Attridge & Herbst (1992), Choi & Herbst (1996),Bailer-Jones & Mundt (2001), and Herbst et al. (2001) find that stars in the ONC (~1 Myr) follow a bimodal distribution, and Lamm et al. (2004) find weaker evidence for bimodality in NGC 2264 (~2 Myr). Stassun et al. (1999), Rebull (2001), and Rebull et al. (2004), in contrast, find no evidence for bimodality in the ONC, although Rebull et al. (2004) suggest that there could be a spatial difference, with reduced bimodality in the outer regions of the cluster. A bimodal P_{rot} distribution is much more obvious in the 13 Myr-old h Per cluster (Figure 1.3; Moraux et al. 2013).

Beginning with Edwards et al. (1993), the observed spread in P_{rot} at these young ages is usually attributed to a spread in disk lifetimes. These authors find that, out of 34 T Tauri stars, those with NIR excesses suggestive of a disk are confined to slow rotation periods. *Spitzer*/IRAC mid-IR observations of a far larger sample of ≈900 ONC members confirm

this result (Rebull et al. 2006; Cieza et al. 2007). In both cases, the presence of both fast and slow rotators without disks must still be explained. Nonetheless, Rebull et al. (2004) show that a bimodal P_{rot} distribution could be produced by 2 Myr if 30%–40% of stars are released from their disks within <<1 Myr.

The protoplanetary disk, while still present and close to the star, acts as an angular momentum sink to prevent P_{rot} from increasing while the star contracts. As the star contracts under its own gravity, it should spin up to conserve angular momentum. Instead, if its disk is intact, the star will transfer angular momentum to the disk, allowing the star to contract while keeping a constant P_{rot}. The possible mechanisms advanced as a means of maintaining this spread in p_{rot} include direct transfer of angular momentum from the star to the disk (Koenigl 1991; Konigl & Pudritz 2000) or winds launched from the disk itself (Shu et al. 1994; Matt & Pudritz 2005a,b). In both these models, once accretion ends and the disk dissipates or is destroyed, the star will begin to spin up as it contracts towards the main sequence without a viable means to shed angular momentum (Moraux et al. 2013).

Most computational models of angular momentum evolution assume that stars stay at the same P_{rot} for the first 10 or so Myr of their lives (e.g., Reiners & Mohanty 2012). Once disks are dispersed, the primary drivers of angular momentum evolution are continued contraction (which causes spin-up) and magnetized stellar winds (which cause spin-down). Until stars reach their main-sequence radii, contraction-driven spin-up is the dominant mechanism for rotational evolution.

1.2.2.2 Empirical studies of rotational evolution on the main sequence

At the zero-age main sequence (ZAMS), stars between 0.1–1.3 $M_\odot$ (spectral types FGKM) show a wide spread in rotation rates (e.g., the Pleiades in Figure 1.3; van Leeuwen & Alphenaar 1982; Terndrup et al. 2000; Hartman et al. 2010; Covey et al. 2016; Rebull et al. 2016b). These stars are largely concentrated along a slow-rotator sequence, with a significant tail of faster rotators comprising ≈20–25% of the stars. Stars with $P_{rot} \lesssim 0.5$ days have been referred to as ultra-fast rotators (UFRs, Barnes & Sofia 1996; Barnes & Kim 2010). The slow-rotator sequence extends to ≈0.5 $M_\odot$, where it turns over and the maximum P_{rot} at a given mass declines rapidly with decreasing stellar mass.

There are few constraints on rotational evolution between ≈150 Myr and the Solar age. The existing P_{rot} measurements in this age range are largely concentrated at ≈200 Myr, and rarely cover the full range of masses at a given age (see Figure 1.3). It could be argued that ≈1 $M_\odot$ stars converge to a slow-rotator sequence by ≈200 Myr, and data for NGC 3532 suggests that 0.8–0.9 $M_\odot$ stars spin down by 300 Myr. The sparse data for Coma Ber seems to indicate that all stars with $M_* > 0.6\ M_\odot$ have spun down by 400 Myr, although rapid rotators still exist at these masses in the 550 Myr-old cluster M37.

Radick et al. (1987) and Kawaler (1989) first observed that the FGK stars in the Hyades form a single-valued sequence in color-period space. This slow-rotator sequence has also shifted to slightly longer P_{rot} compared to the ZAMS (see Figure 1.3). More recent observations (e.g., Hartman et al. 2009; Delorme et al. 2011; Agüeros et al. 2011) suggest that, as in Coma Ber, the majority of stars in M37, the Hyades, and Praesepe with $M_* > 0.6\ M_\odot$ have converged to slow periods. A handful of rapid rotators with masses

$\gtrsim$0.6 $M_\odot$ do remain, however, and must also be accounted for. Nonetheless, a comparison between ZAMS and teenage clusters sets the time required for spin-down: most FGK stars converge onto a slow-rotator sequence within 400-650 Myr.

Field FGK stars also primarily reside on a slow-rotator sequence, although this sequence is much wider than in clusters due to the range of field star ages. This slow field sequence was initially noted for the Mount Wilson sample (Baliunas et al. 1996; Barnes et al. 2001; Barnes 2003) and recently updated by McQuillan et al. (2014) using *Kepler* data. Older stars in these samples show longer P_{rot}. Thus, after converging to a slow-rotator sequence within within 400-650 Myr, FGK stars continue to slow their rotation for at least 4–5 Gyr.[4]

Similar to the P_{rot} bimodality on the PMS, some authors find evidence for bimodality or two sequences of P_{rot} for ZAMS and teenaged FGK stars as well (Soderblom et al. 1993; Barnes 2003). Barnes (2003) claim that, beginning within 50 Myr and continuing to at least the Hyades age, the mass period plane consists of two connected branches: the slowly rotating I sequence and the rapidly rotating C sequence. These are so named for the magnetic dynamos that Barnes (2003) predicts are active in the stars on each sequence: an interface (I) dynamo or a convective (C) dynamo. On the PMS, the I and C sequences bifurcate at the F stars, and are fully populated by FGK stars. Moving to older ages, the bifurcation point representing the beginning of the C sequence shifts to lower masses (right panel, Figure 1.4), leaving only the single-valued I sequence at the higher masses.

[4]A detailed discussion of rotation for stars older than a few Gyr is beyond the scope of this dissertation. However, it is worth noting that a Skumanich-like spin-down may not continue past the Sun's age; see Metcalfe et al. (2016) and van Saders et al. (2016) for recent results and discussion on the late-time evolution of stellar rotation on the main sequence.

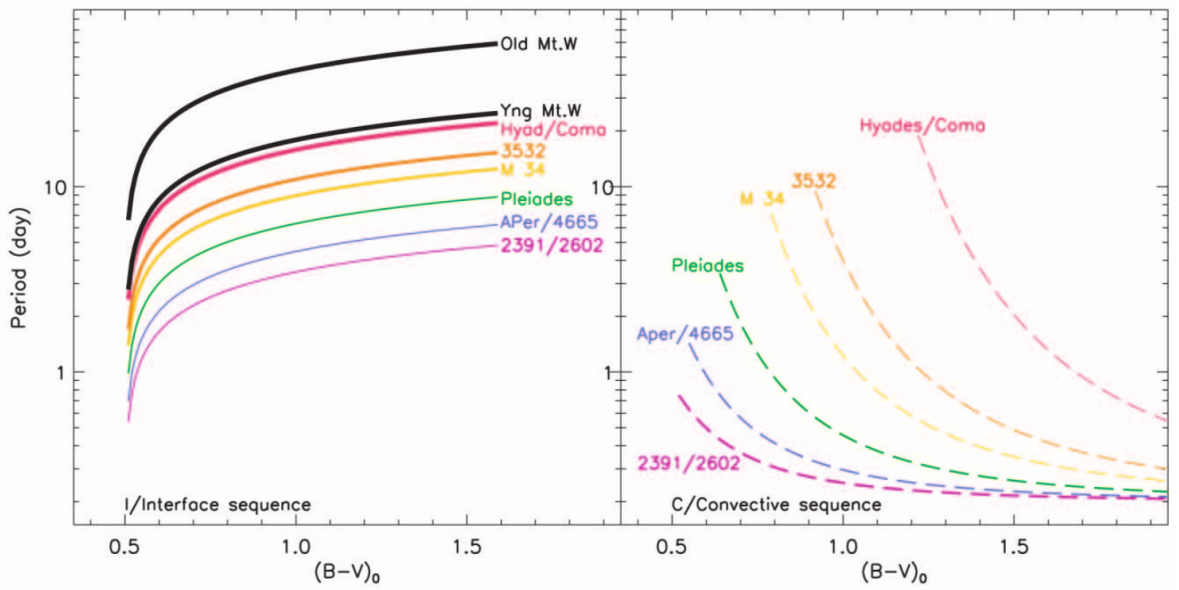

Figure 1.4 The evolution of the empirical fast and slow (I and C) sequences defined by Barnes (2003). Image Credit: Barnes (2003).

By a few Gyr, the C sequence has disappeared and all stars down to the fully convective boundary reside on the I sequence.

The I sequence also slowly evolves to longer periods over time (left panel of Figure 1.4), starting on the PMS and continuing to field ages. Once all the stars have converged to the I sequence, there is a singular relationship between P_{rot} and age for stars at a given mass. This is the same spin-down that Skumanich (1972) found, expanded to all masses 0.3–1.3 $M_{\odot}$, although the timescale for spin-down does vary by mass (e.g., Reiners & Mohanty 2012). The quantification of the mass-dependent I sequence spin down again raised the possibility of determining stellar ages via rotation for all stars between 0.3–1.3 $M_{\odot}$, which Barnes (2003) terms gyrochronology.

The evidence for the Barnes (2003) I and C sequences depends on the mass, age, and number of P_{rot} measurements of the stars in a cluster (Figures 2–3 in Barnes 2003). The I

and C sequences can be clearly seen for stars with ages 50–300 Myr, but the evidence for their continued existence beyond this age is sparse in Barnes (2003). It is also far easier to see the sequences with a linear P_{rot} axis, compared to a logarithmic axis. It must be noted, however, that despite the fact that the Barnes models do not extend to the fully convective M dwarf regime (Barnes 2003, 2010), as noted below, there is strong evidence for a gap between fast and slow P_{rot} for fully convective M dwarfs (Irwin et al. 2011; Newton et al. 2016). If the bimodality is real, then this implies that each star rapidly transitions from fast to slow rotation.

Both partly and fully convective M dwarfs appear to follow a different evolutionary path than FGK stars. As mentioned above, they appear to experience solely contraction-driven spin-up on the PMS, leading to a turnover in the slow-rotator sequence by 40–100 Myr (Irwin et al. 2008a, and references therein). The handful of M dwarf periods in clusters and the field available 5–10 years ago (see, e.g., Irwin et al. 2011, and references therein) suggested that some M dwarfs begin to spin down by 1–2 Gyr, with all early M dwarfs converging to the slow-rotator sequence within 8 Gyr. More recent results, primarily from *Kepler* and MEarth survey data, suggest that slowly rotating M dwarfs are at least 2–5 Gyr old, while rapidly rotating M dwarfs are a mix of old and young stars (Kiraga & Stepien 2007; McQuillan et al. 2013; Newton et al. 2016). This suggests that, while some M dwarfs spin down within 1–2 Gyr, others can retain their rapid rotation for at least 5–10 Gyr. The time when this spin down begins, however, cannot be constrained by field stars alone, and the cluster M dwarf data available 5–10 years ago was insufficient to constrain spin-down times.

1.3 Stellar Magnetism

1.3.1 Magnetic dynamos in the Sun and other stars

The Sun's magnetic field (and, presumably, those of other stars) is produced by a dynamo process. Two primary theories exist for the solar dynamo, both predicated on the latitudinal and radial differential rotation of the Sun: the Leighton and Babcock models (Reid & Hawley 2005). In both theories, the Sun is presumed to have an initially poloidal magnetic field, meaning field lines run parallel to lines of longitude and (in the case of a dipolar field) intersect with the solar surface near the poles (Figure 1.5(a)). Differential rotation shears these poloidal fields into toroidal ones, which run around the Sun parallel to lines of latitude. The toroidal fields then reconnect, and the poloidal field is gradually restored. The mechanism by which the toroidal field turns back into a poloidal field, as well as the location of the differential shear, distinguish the two models.

In the $\alpha\Omega$ dynamo model, first proposed by Parker (1955, 1975), the transformation from poloidal to toroidal fields is caused by differential rotation in the convective zone, and is known as the Ω effect (Parker 1955). The toroidal field itself sits at the base of the convective zone (Parker 1975). Magnetic helicity converts the toroidal field back into a poloidal one, and this is known as the α effect (Deluca & Gilman 1991; Durney et al. 1993). Initially, differential rotation in the outer convective zone was thought to generate the α effect, and constraints from the Solar cycle indicated that rotation speed must increase steeply as one moves into the Sun to produce the necessary shear (Leighton 1969). The Sun's convective zone rotates fairly rigidly at the relevant active latitudes (Schou et al.

1998), however, prompting theorists to re-locate the α effect to the boundary between the rapidly rotating radiative core and the slower outer convective zone (Reid & Hawley 2005). This boundary, called the tachocline, therefore plays a crucial role in the $\alpha\Omega$, or Leighton, dynamo model.

The Babcock (1961) model, in contrast, is a phenomenological one, based on sunspot observations. Here, latitudinal differential rotation stretches the poloidal field into a toroidal one, as the equatorial regions rotate faster than higher latitudes. The toroidal field sinks to the base of the convective zone, and flux tubes rise from there to form sunspots. Sunspots form first at mid-latitudes, then migrate towards the equator, eventually canceling out their toroidal components via reconnection and returning the global field to a dipole (Figure 1.5). Although the Babcock model is primarily motivated by surface features, the tachocline nonetheless plays a significant role as the location of the toroidal magnetic field here as well.

Neither of these models can account for the magnetic properties observed in M dwarfs, as these stars have a deep tachocline or none at all. The radiative core rapidly decreases in size between spectral types M0–M3, and, by definition, does not exist in fully convective mid–late M dwarfs. If the presence of a strong shear layer is necessary for large-scale, ordered fields, then M dwarfs should have only weak, complex fields (Durney et al. 1993). Contrary to this prediction, observations show that most M dwarfs have strong, dipole-dominated fields with a significant amount of flux generated at small scales (Donati & Landstreet 2009; Reiners & Basri 2009). Some M dwarfs have, however, have been observed with weaker, higher-order fields (e.g., Donati & Landstreet 2009;

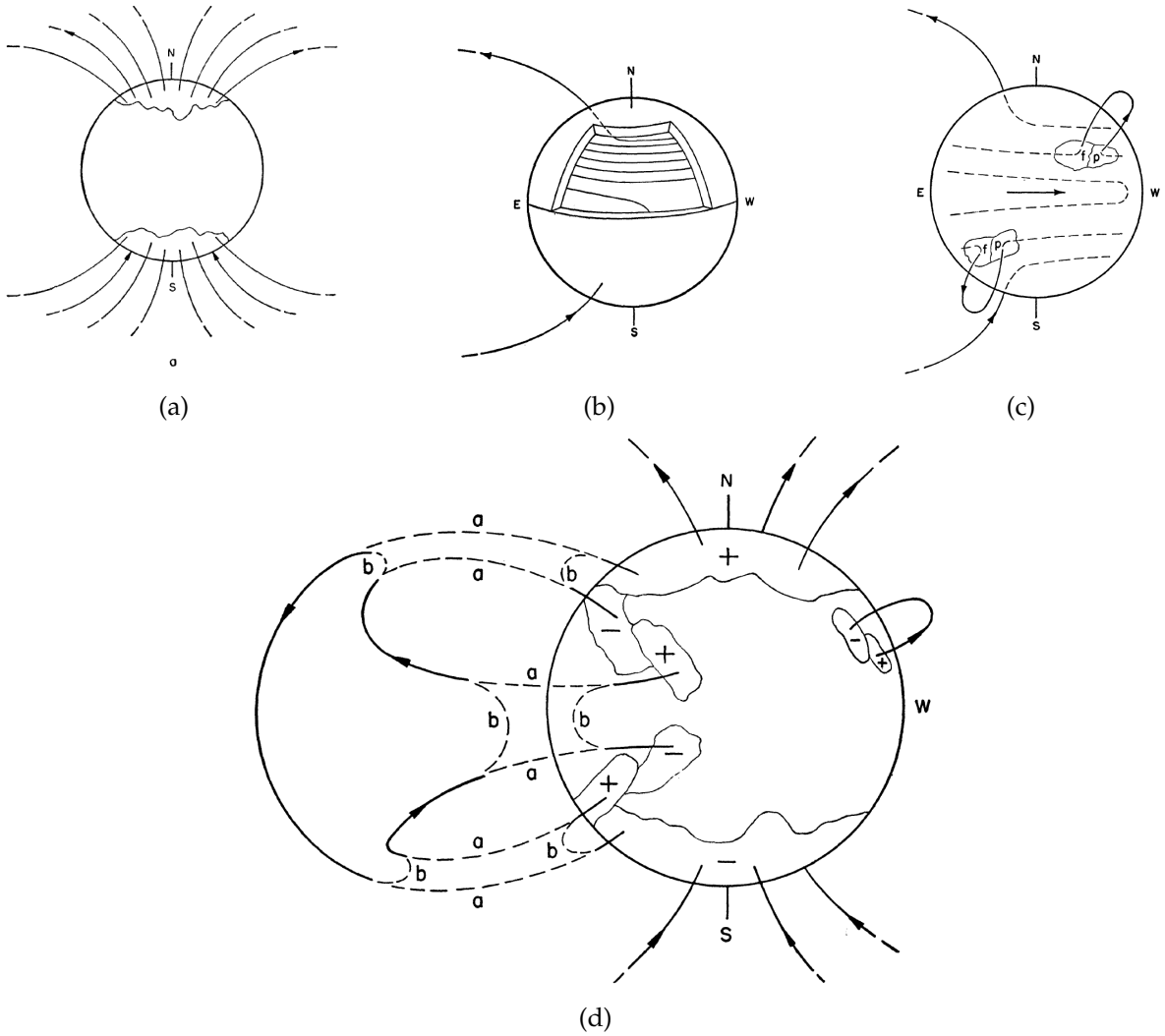

Figure 1.5 The Babcock dynamo model for the Sun. (a) The Sun begins its cycle with a dipolar field configuration. (b) Latitudinal differential rotation drags the poloidal field lines into toroidal fields that encircle the Sun. These toroidal fields sink to the base of the convective zone (the tachocline). (c) Buoyant field loops rise from the tachocline to emerge through the Sun's surface. (d) Loops initial form the configuration labeled 'a', with both ends anchored in the Sun. The loops reconnect to form the configuration labeled 'b', with a new loop ejected outward from the star, and the reconnected loops on the surface contributing to a new dipolar field with opposite polarity from the one in (a). Image Credit: Babcock (1961).

Donati 2011). Furthermore, there appears to be no significant transition in magnetic field properties at the fully convective boundary—a shift in magnetic field strength and

structure instead occurs around 0.5 $M_\odot$ (Reiners & Basri 2007; Donati 2011).

Computational models still struggle to replicate all aspects of M dwarf magnetic fields. The production of large, dipolar fields in magnetohydrodynamic (MHD) simulations requires low density stratification in the interiors of fully convective stars, and increasing stratification shreds the larger fields into smaller ones (Browning 2008; Gastine et al. 2012). Models that use mean-field dynamo theory to parameterize the effect of small-scale fields cannot produce dipole-dominant fields at all (Chabrier & Küker 2006; Shulyak et al. 2015). Yadav et al. (2015a) use a 3D MHD simulation of an Earth-like distributed dynamo to simultaneously produce both large- and small-scale field structures in a fully convective star. The success of this simulation suggests that α^2 or distributed dynamos, rather than $\alpha\Omega$ dynamos relying on a tachocline, can produce strong, dipolar stellar magnetic fields.

1.3.2 Observations of Stellar Magnetism and its Evolution

It is possible to obtain high-resolution measurements of the Sun's magnetic field, but direct observations of magnetic fields on other stars are more complicated and less informative. These direct observations rely on measuring the Zeeman effect, where the magnetic field induces slightly different energies for electrons with different relative spin-orbit states. Zeeman Broadening (ZB) measurements measure the cumulative effect on individual lines (iron is often used, e.g., Reiners & Basri 2007, 2010). Zeeman Doppler Imaging (ZDI), on the other hand, involves tracking the combined effect of the Doppler shift and polarizing effect of starspots as the star rotates (e.g., Donati & Landstreet 2009; Donati

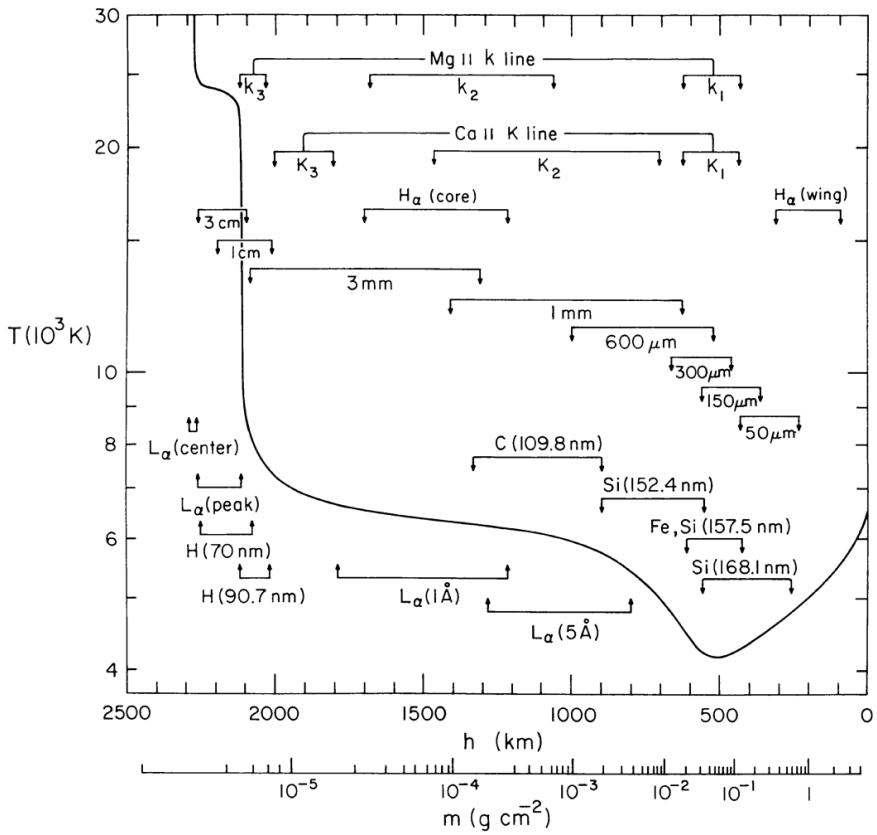

Figure 1.6 The approximate temperature profile for the quiet Sun, with the source locations of various emission and absorption features overlaid. Image Credit: Vernazza et al. (1981).

2011; Vidotto et al. 2014a; Folsom et al. 2016). In either form, therefore, measurements of the Zeeman effect require high-resolution spectra, and ZDI also requires time series spectropolarimetry of (typically) rapid rotators. These requirements mean that direct observations of stellar magnetic fields are limited to the nearest and brightest field stars (Donati & Landstreet 2009).

Fortunately, indirect effects of magnetic fields on stellar atmospheres are also observable, both for the Sun (in resolved and disk-integrated form) and other stars (in integrated light only). Magnetic fields heat stellar atmospheres non-thermally, and the stars then radiate away this excess energy at wavelengths corresponding to particular

line or continuum emission processes (Figure 1.6). The energy of the emitted radiation is roughly associated with the atmospheric height from which it originates (e.g., Vernazza et al. 1981; Reid & Hawley 2005). For solar-type stars, the most common observations of chromospheric activity have been measurements of the emission cores of Ca II H&K lines (e.g., the Mount Wilson Survey; Wilson 1968, 1978), while $H\alpha$ is the more commonly used activity indicator for M dwarfs. UV emission probes the chromosphere, transition region, and lower corona (Vernazza et al. 1981). Finally, the corona proper emits largely in the soft X-rays (Güdel 2004, and references therein). Broadband X-ray observations and optical/NIR line emission are the most commonly used activity indicators, with UV observations limited largely by instrument availability.

Ionized metal lines like Ca II H & K ($\lambda \approx 3900$ Å), Mg II h & k ($\lambda \approx 2800$ Å), and $H\alpha$ ($\lambda = 6563$ Å) are formed by multiple (predominantly collisional) processes in stellar chromospheres (see, e.g., Hall 2008, and references therein). Roughly, the photospheric temperature decreases with increasing atmospheric height until a few hundred km above the photosphere, at which point other local heating sources (i.e., non-radiative heating or downward-directed heating from the chromosphere above) begin to outpace radiative heating from the surface. In this Sun, this leads to a temperature reversal at about $\approx$500 m above the photosphere (Figure 1.6), rising slightly into a temperature plateau where an approximate equilibrium is maintained between collisional excitation and line cooling through recombination in Hydrogen and other singly-ionized metals (i.e., Ca II and Mg II). Broad absorption lines are initially formed near the temperature-minimum region, with emission cores developing through most of the chromosphere (Vernazza et al.

1981). The emission cores are found predominantly in active regions (White & Livingston 1981).

The longest-studied activity indicators are the Ca II H & K lines, due to their prominence in the Solar spectrum and accessibility from the ground. These lines were first cataloged in the Sun by Fraunhofer (Hall 2008), and observed in other stars by Eberhard & Schwarzschild (1913), but the large sample of long-term stellar observations by Wilson (1963, 1978) provide the basis for much of our understanding of chromospheres in solar-type stars. Frazier (1970) and Schrijver et al. (1989) showed that the intensity of the Ca II K-line emission core depends linearly on the local magnetic field strength, making this line ideal for investigating stellar magnetism. Ca II H & K emission probes most of the height of the chromosphere, and each line appears in the stellar spectrum as a chromospheric emission core overlaid on the broader photospheric absorption. Observations of these lines, however, require either careful spectrophotometry, as in the Mount Wilson Survey, or high signal-to-noise spectra with $R \gtrsim 5000$ (and if interstellar absorprtion is potentially a problem, much higher resolution is needed; Giampapa et al. 2006; Curtis 2017).

The Hydrogen Balmer series is the primary mechanism for chromospheric cooling in M dwarfs, and M dwarf activity is most commonly measured using $H\alpha$ emission. $H\alpha$ observations are preferable to Ca II for M dwarfs, both because $H\alpha$ equivalent widths can be measured from lower-resolution spectra than required for Ca II emission core observations, and because these cooler stars emit far more flux at 6563 Å than at ≈3900 Å (Reid & Hawley 2005). Like Ca II in solar-type stars, $H\alpha$ emission correlates with M dwarfs' surface magnetic field strength (as measured by Zeeman broadening; Reiners &

Basri 2007, 2010). It is worth noting, however, that *Hα* and Ca II are only correlated in active main sequence stars (Rauscher & Marcy 2006; Walkowicz & Hawley 2009; Gomes da Silva et al. 2014), and the two lines are formed in slightly different regions of the chromosphere for solar-type stars (Meunier & Delfosse 2009; Vernazza et al. 1981).

Joy & Abt (1974) first divided chromospherically active M dwarfs from inactive ones; these authors defined dMe stars as having "significant" *Hα* emission lines, as compared to inactive dM stars (Reid & Hawley 2005).[5] Initially all M dwarfs later than M5 were found to be active, suggesting that *Hα* emission might be a function of spectral type. Larger surveys eventually find that *Hα* emission is not directly and solely a feature tied to late spectral type, but rather a signature of youth—most dMe stars are kinematically younger than their inactive dM counterparts (Giampapa & Liebert 1986; West & Hawley 2008).

Besides Ca II and *Hα* emission, X-ray observations are the other primary indirect tracer of stellar magnetism. X-rays probe the corona—the hot, diffuse outer regions of the stellar atmosphere. It is still unclear exactly how coronae reach temperatures $>10^6$ Kelvin, but the two primary theories both invoke magnetic fields: Alfvén wave heating (Schatzman 1949) and nanoflaring from magnetic reconnection events (Parker 1987). Despite the lack of a proven physical cause, however, total unsigned magnetic flux and X-ray spectral radiance are correlated over ten orders of magnitude in both parameters, from local observations on the quiet Sun to disk-integrated observations of

[5]The equivalent width that corresponds to *Hα* emission/an active classification varies from study to study. Some recent studies have defined active M dwarfs to be those with *Hα* equivalent widths <-1 Å (e.g., West & Hawley 2008), while Stauffer et al. (1991) appear to define emission as equivalent widths <0.5 Å (taking the convention that negative equivalent widths indicate emission while positive indicate absorption, this means that, technically, the latter authors are defining emission as beginning in the absorption regime). As will be seen in Chapter 2, I define stars with any level of *Hα* emission to be active.

T Tauri and main sequence GKM stars (Pevtsov et al. 2003; Güdel 2004; Reiners 2012), thus making X-rays a good proxy for the large-scale magnetic fields on solar-type and low-mass stars.

X-ray observations are only possible from space, such that a global census of stellar X-ray emitters was not possible until NASA's launch of the Einstein observatory—the first orbiting X-ray satellite with astronomical imaging capabilities—in 1978.[6] FGK dwarfs, and even a few flaring M dwarfs, were detected in the Hyades using Einstein; for more distant clusters like the Pleiades, only stars with spectral types (SpTs) earlier than F were detected (Micela et al. 1988, 1990). Later surveys with ROSAT[7] in the 1990s and NASA's *Chandra*[8] and ESA's *XMM-Newton*[9] observatories in the 2000s have been able to observe fainter stars, even detecting M dwarfs in Praesepe (Franciosini et al. 2003, though many of these M dwarfs have binary companions). Studies of cluster and field stars showed that, like $H\alpha$ and Ca II activity, X-ray emission declines with age (Güdel 2004; Preibisch & Feigelson 2005).

1.4 The (Age-)Rotation-Activity Relation

1.4.1 Magnetic braking on the main sequence

The current interpretation for the observed P_{rot} evolution described in Section 1.2.2.2 is that once stars reach the main sequence, they stop contracting and (in the absence of tides

[6] https://www.cfa.harvard.edu/hea/hm/heaob.html
[7] http://www.dlr.de/dlr/en/desktopdefault.aspx/tabid-10424/
[8] http://chandra.harvard.edu/
[9] http://sci.esa.int/xmm-newton/47370-fact-sheet/

from a companion) magnetic braking primarily drives their further angular momentum evolution (as summarized in Soderblom 2010; Bouvier et al. 2014). As the star loses angular momentum via its wind, it spins more slowly. The slower rotation weakens the stellar dynamo and magnetic fields, and in turn this makes braking less efficient. Spin-down thus decelerates as the star ages, and this feedback loop is thought to be the cause of the observed correlation between weakening activity and slowing rotation. The details of the age-rotation-activity relation, however, are still unclear, particularly the impact of magnetic field topology and the underlying magnetic dynamo on rotational evolution in stars of different masses.

Magnetic fields that emerge through the stellar surface align themselves into two basic structures: loops and open field lines. Loops have both ends rooted in the star itself: bright active regions form when strong loops confine hot plasma along the field lines, while quiet regions of the solar surface are characterized by weak, closed loops. Open field lines, on the other hand, stretch out to infinity, leaving the star. The regions of open field lines are also known as coronal holes, since they appear dark in UV/X-ray images of the Sun when compared to the hot material magnetically confined to strong coronal loops. Most mass and angular momentum loss occurs along the open field lines in coronal holes (Withbroe & Noyes 1977; Withbroe et al. 1991), although recent models suggest that coronal mass ejections (CMEs) may carry away even more angular momentum than stellar winds (e.g., Cranmer 2017).

Magnetized particles accelerate outwards along open field lines until they obtain sufficient speed (the Alfvén speed) to escape the field's influence. At this point, called

the Alfvén critical point, Alfvén radius, or Alfvén surface, the particles continue traveling outwards and can be considered to have left the star, carrying their mass and angular momentum away (Schatzman 1962; Weber & Davis 1967; Réville et al. 2015). Since the particles do not "leave" the star until they are far from the stellar surface, this provides a large lever arm and even low mass loss rates can yield large torques (Bouvier et al. 2014).

When he proposed the first theory of the solar wind, Parker (1958) also proposed that the wind could carry away angular momentum once it had left the solar corona. Based on his assumptions about the wind, however, Parker (1958) claimed the solar wind torque was "not serious" and that the characteristic timescale for spin-down was ≈30 Gyr, far longer than the Sun's main sequence lifetime. Schatzman (1962) and Weber & Davis (1967) generalized the Parker model; when employing observations of the solar wind near Earth as boundary conditions, Weber & Davis (1967) found a characteristic timescale of 7 Gyr. If the radiative core and outer convective envelope are allowed to decouple, then the spin-down timescale drops to 10–100 Myr (Dicke 1964; Deutsch 1967; Kraft 1967). Since these timescales are shorter than the Sun's main sequence lifetime, these studies imply that the solar wind does significantly effect the Sun's rotational evolution.

One of the most frequently cited angular momentum evolution models is that of Kawaler (1988), based on previous work by Mestel (1984). After assuming forms for the dependence of the Alfvén radius on the magnetic field strength B_0, and in turn the dependence of B_0 on P_{rot} and the stellar radius R, Kawaler presents an equation for the torque exerted on a star by its magnetized wind. Assuming an approximately radial field

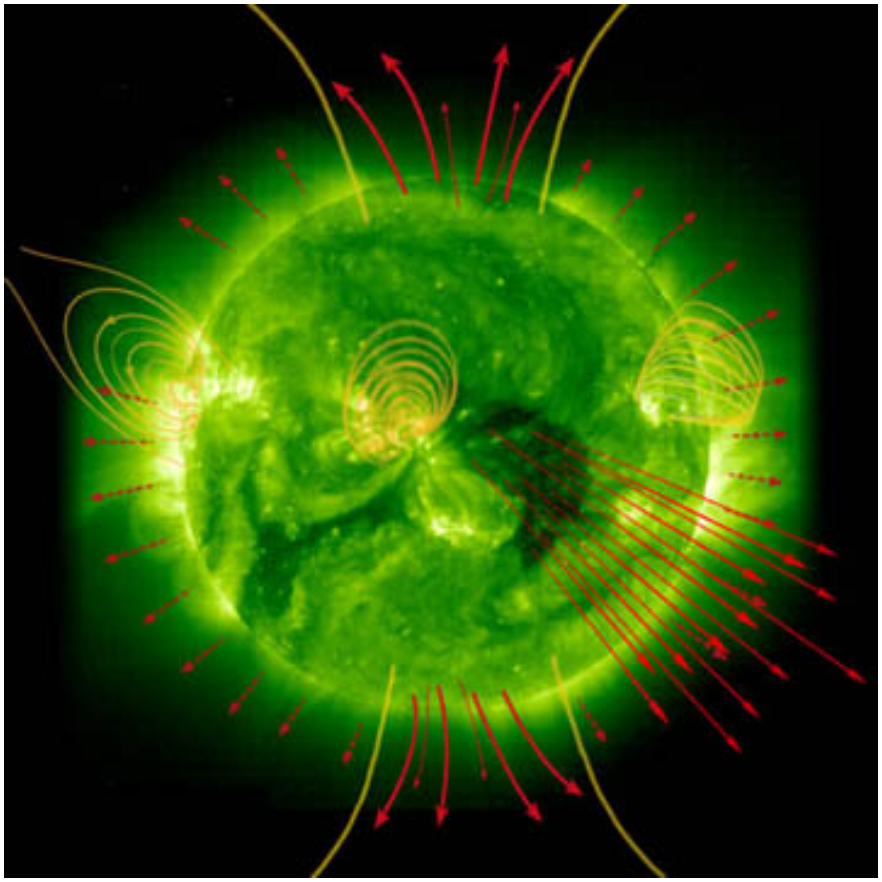

Figure 1.7 The Sun, with magnetic field loops (yellow) and solar wind streams (red) overlaid. The solar wind is slower in areas with mostly loops (short dashed arrows), and fastest through coronal holes (longer solid arrows). Angular momentum loss is maximized along open field lines near the equator. Image Credit: SOHO/ESA/NASA

geometry yields a Skumanich-like spin-down, with the torque on the star given by

$$\frac{dJ}{dt} \propto P_{rot}^{-3} R^{\frac{1}{2}} M^{-\frac{1}{2}} \dot{M} \tag{1.1}$$

where M is the stellar mass and $\dot{M}$ the mass loss rate. Matt et al. (2015) reformat the torque more generally as

$$\frac{dJ}{dt} \propto P_{rot}^{-1} R^{5m+2} M^{-m} \dot{M}^{1-2m} B_0^{4m} \tag{1.2}$$

where m is constant related to the magnetic field geometry. Setting $m = \frac{1}{2}$ and $B_0 \propto R^{-2}P_{rot}^{-1}$ yields the Kawaler (1988) equation for a radial field, but, e.g., Matt et al. (2012b) and Réville et al. (2015) find that the magnetic field is more likely a dipole with a slight quadrupolar component (m = 0.20–0.25).

This illustrates one challenge facing angular momentum evolution models: how to determine B_0 and $\dot{M}$ for each star. Weber & Davis (1967) were able to use observations of the Solar wind to constrain their models, but only ≈20 other main sequence solar-type and low-mass stars have had their mass loss rates measured (Wood et al. 2002, 2005; Fichtinger et al. 2017). Furthermore, mass loss rates in very low mass stars may be an order of magnitude larger than that of the Sun, since low mass stars have stronger magnetic fields and higher-density coronae (Vidotto et al. 2011; Reiners & Mohanty 2012). Vidotto et al. (2014a) also find correlations between R_o , L_X/L_{bol}, and the large-scale magnetic field strength which they suggest could be used instead of the simple assumptions in a Kawaler-like wind law. Despite these observational constraints, many models of angular momentum loss continue to use solar values, simply scaling them by stellar mass and radius (e.g., Reiners & Mohanty 2012; Matt et al. 2015) or using theoretical models that have been tuned to match very limited observations (e.g., Cranmer & Saar 2011).

Since the stellar wind is driven by the magnetic field, understanding field structure is necessary for understanding angular momentum evolution. By simulating 3D winds produced by real stellar magnetic fields (inferred from ZDI), Vidotto et al. (2010, 2014b) find that winds in the plane carry away the most angular momentum, and that angular momentum loss increases with non-axisymmetry; Garraffo et al. (2015c,a) find a similar

result from MHD modelling. Matt & Pudritz (2008), Garraffo et al. (2015c,b), and Réville et al. (2015) also find that mass loss is correlated with more open field geometries, as expected based on observations of the solar wind. This is because open field lines more effectively accelerate particles, increasing the Alfvén radius (at which they "leave" the star), and hence the lever arm for the torque applied. However, these authors also find that faster rotation decreases the Alfvén radius, which in turn decreases the torque on the star. High latitude spots can also close what would otherwise be open field lines, reducing mass and angular momentum loss (Garraffo et al. 2015b). Both large- and small-scale magnetic field topology therefore significantly impacts the wind structure, which in turn affects the efficiency of angular momentum loss.

The internal differential rotation of stars also likely plays an important role in rotational evolution. Beyond the role of differential rotation and/or the tachocline in generating magnetic fields (as discussed in Section 1.3.1), some theories predict that stars' radiative cores and convective outer envelopes may decouple for a period of time after the core forms (Irwin & Bouvier 2009; Reiners & Mohanty 2012). In the core-envelope decoupling theory, when the radiative core first forms, it decouples from the outer convective layer and becomes an invisible reservoir for angular momentum. The convective zone then spins down rapidly due to magnetic braking. Eventually, the core and envelope re-couple, which injects angular momentum back into the outer convective envelope and stalls its braking for a time. After this, the star spins down as a solid body, though it retains some internal differential rotation (Pinsonneault et al. 1989; Epstein & Pinsonneault 2014). The timescale for this re-coupling is 1–2 orders of magnitude longer for slow rotators than it is

for fast rotators (Irwin & Bouvier 2009). Core-envelope decoupling should affect internal mixing, yielding observationally testable consequences on the Lithium abundances in fast vs. slow rotators; fast rotators in the Pleiades appear to have more Lithium than slow rotators, supporting this theory (Soderblom et al. 1993; Bouvier 2008). Collier Cameron & Li (1994) and Matt et al. (2015), however, reproduce the behavior of both rapidly and slowly rotating FGK stars assuming only that magnetic braking efficiency is reduced in rapid rotators; no core-envelope decoupling is required.

One final important modification to the Kawaler (1988) model is the concept of saturation. To explain the simultaneous presence of fast and slow rotators in the Pleiades (van Leeuwen & Alphenaar 1982), MacGregor & Brenner (1991) and Chaboyer et al. (1995) proposed that rapidly rotating stars with P_{rot} shorter than some critical value P_{sat} experience inefficient angular momentum loss. These authors therefore change the Kawaler (1988) equation into two, so that the torque on the star depends only weakly on the P_{rot} in the saturated regime:

$$\frac{dJ}{dt} \propto \begin{cases} P_{rot}^{-1} P_{sat}^{-2} & \text{if } P_{rot} < P_{sat} \text{ (Saturated)} \\ P_{rot}^{-3} & \text{if } P_{rot} \geq P_{sat} \text{ (Unsaturated)} \end{cases} \tag{1.3}$$

(Krishnamurthi et al. 1997; Epstein & Pinsonneault 2014). Observations of mass-dependent timescales for spin-down imply that P_{sat} must be mass-dependent as well (Section 1.2.2.2; Stauffer et al. 1987; Barnes & Sofia 1996; Krishnamurthi et al. 1997). Krishnamurthi et al. (1997) propose using the convective overturn time τ to scale P_{sat} with mass, which also

ties angular momentum loss to activity saturation:

$$P_{sat} = P_{sat,\odot}\frac{\tau}{\tau_\odot} \tag{1.4}$$

where $P_{sat,\odot}$ and $\tau_\odot$ are the values for Sun-like stars. The majority of current theoretical angular momentum evolution models invoke a form of the saturated/unsaturated Kawaler (1988) law (e.g., Barnes & Kim 2010; Reiners & Mohanty 2012; Brown 2014; Matt et al. 2015); one prominent exception is Gallet & Bouvier (2015), who use a single functional form for angular momentum loss across all rotation rates.

1.4.2 Saturation and the Rossby Number

Around the same time that the concept of saturation was being added to models of angular momentum evolution, it was also being observed as a maximum activity level for stars of a given type (e.g., Herbst & Miller 1989; Mathioudakis & Doyle 1992). Eventually, studies of activity and rotation in main sequence FGKM stars found that activity saturates as a function of rotation as well (e.g., Randich et al. 1996). For stars rotating more slowly than some saturation velocity, faster rotation is correlated with increased activity, as measured by the fractional luminosity for a given activity index (e.g., L_X/L_{bol} or $L_{H\alpha}/L_{bol}$ for X-ray and $H\alpha$ activity). In stars that rotate faster than the saturation velocity, however, activity is no longer correlated with rotation rate—instead, all rapid rotators exhibit roughly the same activity levels. This activity-rotation relationship is often parametrized as a flat line in the saturated regime connected to a power law for slower, unsaturated rotators (See

the top panel of Figure 1.8).

Some studies also find that activity decreases again for the very fastest rotators, a phenomenon known as supersaturation. Supersaturation has only been definitively observed for FGK stars in the X-rays (Jeffries et al. 2011; Wright et al. 2011), although it has been sought at lower masses and in chromospheric emission (Marsden et al. 2009; Jackson & Jeffries 2010; Christian et al. 2011). Cook et al. (2014) do find a supersaturation-like effect in some rapidly rotating M6.5–L9 brown dwarfs, but it is not clear that this is a comparable dynamo effect in these ultracool, largely neutral atmospheres. Since the saturation velocity is mass dependent, most modern studies use the Rossby number $R_o = P_{rot}/\tau$ to reduce scatter in the unsaturated regime and to cause all stars to saturate at the same point (typically $R_{o,sat} \approx 0.1$)—this is equivalent to Equation 1.4, which sets $R_{o,sat} = (R_{o,sat})_\odot$ for all stars.[10]

Noyes first used R_o to improve the correlation between Ca II emission and rotation, but they did not observe saturation as their observations only reached $R_o \approx 0.25$ (Noyes 1983; Noyes et al. 1984). Although Noyes et al. (1984) used τ values from Gilman (1980) in their analysis, Noyes (1983) (and later Stepien 1994) computed τ as a function of (B-V) color such that the scatter in the unsaturated activity-R_o plane was minimized. Before Noyes (1983), τ was simply a parameter used to characterize convective zones in stellar structure models. Later studies also computed empirical τ values, but with the intent of forcing stars of different masses to saturate at the same $R_{o,sat}$ value. Pizzolato et al. (2003)

[10]It should be noted that, although this dissertation assumes R_o is the correct ordinate to consider in rotation-activity analysis, Reiners et al. (2014) find that $L_X \propto P_{rot}^{-2}$ (equivalent to $L_X/L_{bol} \propto P_{rot}^{-2}R^{-4}$, where R is the stellar radius) yields a tighter correlation than $L_X/L_{bol} \propto R_o$. However, this requires well calibrated L_X values, and hence accurate distances to the stars in question, which are not always readily available.

and Wright et al. (2011) re-derived τ values solely from observed X-ray data for cluster and field stars, and expand the work of Noyes et al. (1984) and Stepien (1994) to the M dwarf regime. Pizzolato and Wright computed τ as a function of stellar color and/or mass, but both authors also assumed that $L_X/L_{bol} \propto {R_o}^{-2}$ or $L_X/L_{bol} \propto {R_o}^{-2.7}$ in the unsaturated regime. If either L_X/L_{bol} or $L_{H\alpha}/L_{bol}$ are plotted as a function of R_o, then the resulting plot should be mass-independent.

Most studies of saturation for main-sequence stars focus on chromospheric and transition-region activity tracers. Vilhu (1984) demonstrated saturation in main sequence rotators and found that a variety of chromospheric indices in the optical and near-UV (Ca II H & K, C I, C II, O I, plus a combined index for Si IV, C IV, and N V) saturate around $R_{o,sat} \approx 0.1$. The transition region Mg II h & k lines also saturate at $R_{o,sat} \approx 0.1$ in FGK and a few M stars (Doyle 1987; Cardini & Cassatella 2007); these studies primarily focused on field stars, but Cardini & Cassatella (2007) included some open cluster members, including Hyads. Interestingly, Mamajek & Hillenbrand (2008) investigated Ca II emission in field GK stars, and found a shift in activity around $R_o \approx 0.1$–0.2, but did not find definitive evidence for saturation. Astudillo-Defru et al. (2017), on the other hand, found that Ca II H & K emission saturates for K and M dwarfs in the HARPS-N sample. Saturation of the Ca II infrared triplet has also been observed in PMS and ZAMS stars (Marsden et al. 2009; Jackson & Jeffries 2010), and $H\alpha$ emission definitely saturates for field-age M dwarfs (Reiners & Mohanty 2012; Rebassa-Mansergas et al. 2013; Newton et al. 2016). The majority of these studies find that saturation begins at $R_o \approx 0.1$.

Despite the early evidence for chromospheric saturation and lack of evidence for

coronal saturation—Walter (1982) and Vilhu (1984), for example, found a shift in the X-ray activity-rotation relation for rapid rotators, but their data still showed a dependence on rotation—most observational and theoretical studies have instead focused on saturation of soft X-ray emission. Pallavicini et al. (1981) were the first to correlate L_X with rotation, and found that $L_X \propto (vsini)^2$. Noyes et al. (1984), Maggio et al. (1987), and Schmitt et al. (1985) all derived empirical τ values; although their data did not probe the saturated regime, these authors all found that, approximately, $L_X \propto {R_o}^{-2}$. This is likely the root of what Wright et al. (2011) (and others) call "the canonical −2 power-law". Many studies in the 1980s–1990s do identify the presence of saturation in FGK open cluster samples, but these authors rely on $v\sin(i)$ measurements (e.g., Stauffer et al. 1994b; Prosser et al. 1996), only occasionally converting these into R_o values (e.g., Randich et al. 1996, 2000).

1.4.3 Testing theories of saturation

Interestingly, Doyle (1996) claim that no convincing evidence for X-ray saturation existed at that time—within a few years, however, theories explaining X-ray saturation from a magnetic perspective began to be published, with no theories focusing on primarily on chromospheric saturation. Below I discuss several theories which attempt to explain why L_X/L_{bol} saturates and then (in some cases) supersaturates, as well as the potential implications for chromospheric activity which should allow us to test these theories; this section is partly based on the discussion in Jeffries et al. (2011).

The coronal stripping theory, where coronal loops are centrifugally ripped open, was first proposed by Jardine & Unruh (1999) and then developed by James et al. (2000) and

Jardine (2004). These authors posit that, as the star's rotation speed increases, the X-ray emitting volume of the corona is decreased. At speeds faster than the saturation velocity, the decreased volume is balanced by an increase in the emission measure so that the total L_X is preserved. Supersaturation therefore occurs when the corona is stripped so far back that L_X finally begins to decrease. These authors do not make predictions for the effect of coronal stripping on chromospheric activity, but presumably if this mechanism is at work then $L_{H\alpha}/L_{bol}$ will saturate at faster speeds than L_X/L_{bol}, if it saturates at all. It is also possible that rapidly and slowly rotating stars have differently ordered magnetic fields or different dynamo mechanisms altogether.

Another possibility is that the starspot or magnetic flux saturates, causing activity indices to follow suit (Vilhu 1984; Solanki et al. 1997; Stepien et al. 2001). Active regions may cover the entire star in this case, or simply reach a maximum threshold; more recent observations suggest that the maximum covering fraction is ~40–50%. In very rapidly rotating stars, the radiative cores produce additional flux at their poles, which in turn generates increased upward flows in the convective zone at the poles. This sets up meridional currents that drag magnetic field lines towards the poles, leaving the equator bare and decreasing the spot filling factor once again. If this mechanism is responsible for X-ray saturation and supersaturation, then it would also affect chromospheric emission and all activity indices should saturate and supersaturate together.

Finally, the dynamo itself may saturate, and be unable to produce additional magnetic fields despite faster rotation. In this case, the increasing magnetic field strength suppresses differential rotation within the star, which in turn suppresses the generation

of additional (poloidal) fields (Robinson & Durney 1982; Kitchatinov et al. 1994; Rempel 2006). This likely also produces a change in the field topology for fast vs. slow rotators. Collier Cameron & Li (1994) find that dynamo saturation at 15–45× the solar rotation rate can explain activity saturation in young solar-type stars. These authors, along with O'dell et al. (1995), also find that saturation of chromospheric and transition region indices occurs for rotation rates ~5–10× less than dynamo saturation. Based on correlations between the large scale magnetic field strength and L_X/L_{bol} (Vidotto et al. 2014a), X-rays should then saturate with the dynamo at more rapid speeds than chromospheric saturation.

Unfortunately, due in part to the difficulty of measuring $L_{H\alpha}$ and L_X for a statistically significant number of stars with known P_{rot}, tests of the relation between coronal and chromospheric saturation have been inconclusive (Mamajek & Hillenbrand 2008; Marsden et al. 2009; Jackson & Jeffries 2010), and the connection between these manifestations of magnetic activity remains unclear. Meanwhile, evidence for chromospheric supersaturation, especially in M dwarfs, is tenuous at best (Jackson & Jeffries 2010), but is expected if changing field topology is responsible for coronal supersaturation. Jeffries et al. (2011) claim evidence for the coronal stripping theory from L_X/L_{bol} data alone, though Wright et al. (2011) analyze a larger X-ray sample and cannot reach a conclusion on the cause for saturation. Most authors examine mixed samples of field and open cluster stars with a range of masses, however, so it is possible that the magnetic effects are being obscured by a dependence on mass or age.

1.5 Benchmarking Stellar Evolution with Open Clusters

Open clusters are loose collections of a few 100s-1000s of stars. They are located almost exclusively in the disk of the Milky Way (Melotte 1915; Kharchenko et al. 2013, Figure 1.9), and as such they are typically destroyed by the Galaxy's tidal potential with a half-life of 200–300 Myr (Janes et al. 1988; Janes & Phelps 1994; Binney & Tremaine 2008). Older open clusters usually sit slightly above or below the Galactic disk where they can avoid the most destructive effects of passing giant molecular clouds and the overall Galactic tidal potential (Spitzer 1958; Wielen & Fuchs 1988). Therefore, most open clusters are young, and most older open clusters are faint and distant (e.g., Kharchenko et al. 2013; Schmeja et al. 2014).

Unlike the more massive globular clusters, open clusters contain stars which are all the same age. Each cluster undergoes a single burst of star formation which blows away any remaining dust and gas. Recent studies suggest that small age spreads may exist in open clusters: for example, Bonatto et al. (2012) find evidence for star formation over 5–10 Myr. Hillenbrand et al. (2008) and Jeffries et al. (2011), in contrast, find marginal to no evidence for age spreads. More recently, Brandt & Huang (2015a,b) invoke rotational effects to explain the apparent age spread at the main-sequence turnoff in open clusters. However, any potential age spread will only matter during times of rapid stellar evolution, such as the early pre-main sequence or the main sequence turnoff. For solar-type and low-mass main sequence stars, any age spread can be neglected. It is generally assumed, therefore, that open clusters consist of a mono-age, mono-metallicity stellar population, which makes open clusters ideal benchmarks for calibrating stellar properties.

Analysis of a cluster's color-magnitude diagram also yields the cluster's age. As the cluster ages, the most massive stars quickly fuse their reservoir of Hydrogen into Helium and leave the main sequence (Iben 1967, and references therein). Theoretical models produce synthetic color-magnitude diagrams at a given age; these isochrones can be fit to observed cluster data in order to determine absolute ages (e.g., Baraffe et al. 1998). Open clusters with a range of ages can then be placed into an evolutionary sequence of benchmark clusters to measure stellar properties and calibrate their evolution (Soderblom 2010).

As seen in Figure 1.3 and Bouvier et al. (2014), most calibrations of the age-rotation-activity relation rely on either young open clusters or older field stars without well-constrained ages. Few teenaged open clusters are close enough to the Sun to enable in-depth studies of rotation and activity across the FGKM spectral range, and most ground-based P_{rot} surveys primarily reach FGK stars (e.g., in Coma Ber and M37; Collier Cameron et al. 2009; Hartman et al. 2009). As a result, to characterize rotation and activity evolution in the older (t¿1 Gyr) stellar populations, astronomers are restricted to assuming rough ages for older, nearby field stars based on galactic height or other tracers (e.g., Barnes 2003; West & Hawley 2008). This is beginning to change, however: *Kepler* and *K2* have provided light curves for several clusters between 1–4 Gyr (NGC 6811, NGC 6819, M67, and Ruprecht 147; Meibom et al. 2011a, 2015; Barnes et al. 2016, Curtis et al. in prep). Even with *Kepler*'s precision, however, only a dozen or two P_{rot} were measured for FGK stars in NGC 6819, M67, and Ruprecht 147, with a handful of early M dwarfs also detected in the latter (Curtis et al. in prep).

Two of the closest and most well-studied clusters are the Hyades and Praesepe (highlighted in Figure 1.9). At ≈650 Myr, these clusters are teenagers—beyond their star-forming and ZAMS years, but not yet settled into the calmer life of middle-aged stars like the Sun. And at only 47 pc and 181.5 pc, both have been the subject of much scrutiny over the last 50–100 years. The Hyades and Praesepe are also the primary bridge between the aforementioned young clusters and field stars in studies of rotation and magnetic activity (e.g., Skumanich 1972; Bouvier et al. 2014). Thus, precisely calibrating the P_{rot} and activity distributions in these clusters is crucial for extrapolating the behavior of younger stars out to field stars with less precise ages.

1.6 The Hyades and Praesepe Open Clusters

The Hyades (Melotte 25) has been known since ancient times—its four red giant members form the head of Taurus along with the unrelated giant Aldebaraan (Frommert & Kronberg 2001). Melotte (1915) classified it as a Type IV coarse cluster, along with the Pleiades, Alpha Per, Coma Ber, and other clusters that didn't fit into his first three categories (globular clusters, regular loose clusters, and irregular loose clusters). The cluster's proximity makes it a useful benchmark, but also makes determining its membership challenging: the cluster is so close to the Sun that projection effects cause its members to exhibit significantly different proper motions, especially outside the cluster core. The convergent point method is thus necessary for membership studies based on proper motion, as is radial velocity confirmation, which must also take into account the variation in cluster members' projected motion along the line of sight (van Leeuwen 2009). The membership

list has therefore undergone numerous revisions over the last 100 years (e.g., van Bueren 1952; Hanson 1975; Reid 1992; Goldman et al. 2013), with ≈800 confirmed and candidate members known at present.

Praesepe (M44, NGC 2632, or the Beehive) is about three times as far away as the Hyades, with ≈50% more members. Like the Hyades, Praesepe has also been known since ancient times (see Frommert & Kronberg 2007, and references therein for a complete historical treatment), though it was thought to be a faint nebulous object until Galileo resolved it into 40 stars (Galilei 1610). Praesepe was included in Messier's catalog (Frommert & Kronberg 2007), and the first modern proper motion studies were undertaken by van Rhijn (1916) and Klein Wassink (1927). As instrumentation improved, the cluster membership was extended to fainter objects; the major proper motion surveys have included Vanderlinden (1934), Artiukhina (1971), Jones & Cudworth (1983), Jones & Stauffer (1991), Hambly et al. (1995),Adams et al. (2002), and Kraus & Hillenbrand (2007). The cluster was also detected by Kharchenko et al. (2013) in their statistical search for Galactic open clusters.

The Hyades and Praesepe are generally considered to be coeval, although Praesepe may be slightly younger. Using isochrone fitting and a color-magnitude diagram generated using parallaxes from the *Hipparcos*, Perryman et al. (1998) find that the Hyades is 625 ± 50 Myr. Zuckerman & Song (2004) gives the Hyades's age as 600 Myr without an additional citation, and Kraus & Hillenbrand (2007) does the same for Praesepe. Franciosini et al. (2003) also claims that both clusters are 600 Myr. Fossati et al. (2008) find Praesepe to be 590^{+150}_{-120} Myr from isochrone fitting. Using gyrochonology, Delorme et al.

(2011) find that Praesepe is 578 ± 12 Myr, while Kovács (2015) find 665 ± 11 Myr, although these values do not include systematic uncertainties in gyro-ages.

The age of these clusters have come under debate recently, with Brandt & Huang (2015a,b) suggesting that both the Hyades and Praesepe are older than previously thought. Using a statistical method to fit rotating stellar models to the observed color-magnitude diagram, these authors measure the ages of Hyades and Praesepe to be ≈800 Myr, instead of what they term "the consensus age of ~600–650 Myr". However, these authors introduce several sources of systematic uncertainty such as adjusting model parameter values, extrapolating the model grid to super-solar metallicity, and using an incompatible non-rotating model to interpolate between the coarse grid-points of the rotating model. These systematic uncertainties are not included in their final error budget, but based on their discussion, they would increase the uncertainty on their final result and make it consistent with the previously determined age.

In Chapter 2, I assume that both the Hyades and Praesepe were ≈600 Myr old, though in Chapters 3–4 the cluster P_{rot} distributions are a reasonably good match to models at ≈650 Myr.

1.7 Structure of Dissertation

This dissertation focuses on using the Hyades and Praesepe open clusters to benchmark stellar wind-driven angular momentum evolution. I also investigate stellar activity in these two clusters, as part of my analysis of the stellar magnetic field.

Chapter 2 describes my initial investigation of the activity-rotation relation in these

two open clusters. I use ≈800 new and archival optical spectra to investigate the $H\alpha$ -color relations in the two clusters, and demonstrate the importance of a consistent equivalent width measurement technique for inter-cluster comparisons. I then combine this $H\alpha$ data with archival P_{rot} data to measure a saturation-type activity-rotation relationship. Finally, I present a preliminary comparison of the $H\alpha$ and X-ray activity-rotation relations in Praesepe and the Hyades, but this comparison is stymied by the lack of extensive P_{rot} and X-ray surveys of these clusters.

Chapters 3–4 focus on expanding the P_{rot} catalogs in the Hyades and Praesepe, respectively. In each chapter, I describe the *K2* data for the relevant cluster, my P_{rot} measurement methods, and the resulting expanded P_{rot} catalogs. I also discuss existing binary surveys of the clusters and the locations of binaries in the mass-period plane. Finally, I compare my P_{rot} data to models of stellar angular momentum evolution. I conclude in Chapter 5

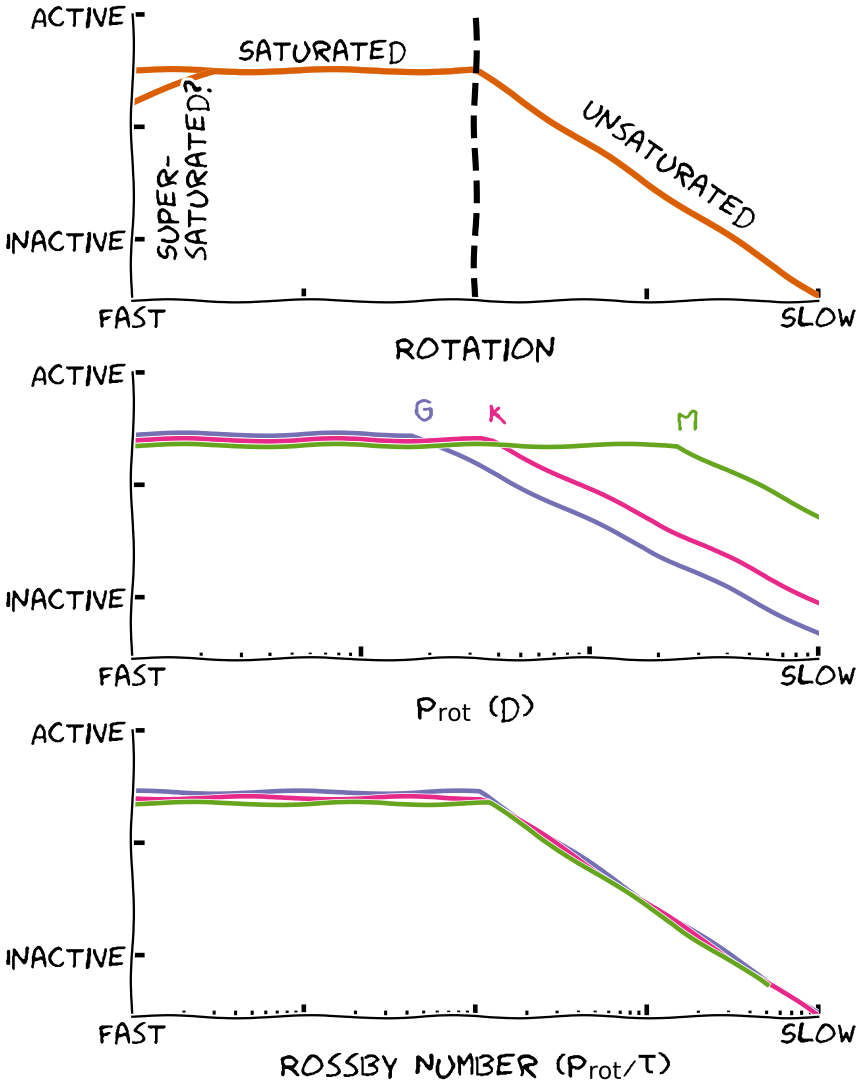

Figure 1.8 Top—Cartoon of the saturation phenomenon. Activity increases with faster rotation in the unsaturated regime. For stars rotating faster than the saturation velocity (vertical dashed line), their activity levels are independent of rotation speed. Some studies find that activity decreases again for the fastest rotators, a phenomenon called supersaturation. Middle—Approximate saturation laws found by Pizzolato et al. (2003) for G, K, and M stars. Lower-mass stars saturate at longer periods. Bottom—The same activity-rotation relations as above, but with P_{rot} converted to the Rossby Number $R_O = P_{rot}/\tau$. Now stars of all different masses saturate at the same point.

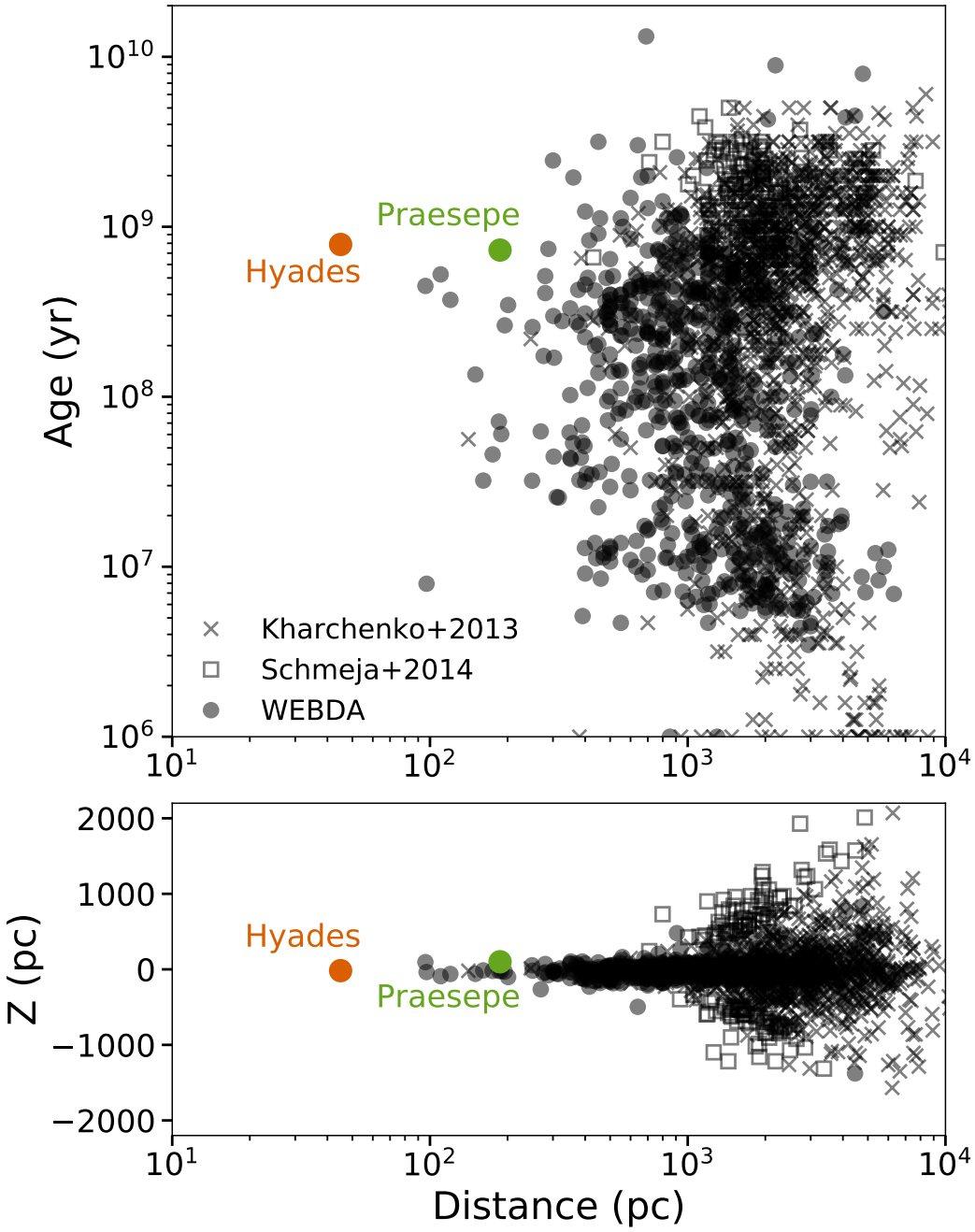

Figure 1.9 Top—Age vs distance from the Sun for open clusters in the WEBDA database and from Kharchenko et al. (2013) and Schmeja et al. (2014). The Hyades and Praesepe are highlighted. Bottom—Galactic height (Z) vs distance from the Sun for the same sample.

Chapter 2

The Factory and The Beehive II. Activity and Rotation in Praesepe and the Hyades

2.1 Introduction

In Agüeros et al. (2011) we reported stellar rotation periods (P_{rot}) for 40 late-K/early-M members of the open cluster Praesepe (α 08 40 24 δ +19 41), also known as the Beehive Cluster, derived from our Palomar Transient Factory (PTF; Law et al. 2009; Rau et al. 2009) observations. By combining these P_{rot} with those obtained by Scholz & Eislöffel (2007), Delorme et al. (2011), and Scholz et al. (2011), we determined that Praesepe's mass-period relation transitions from a well-defined singular relation to a more scattered distribution of P_{rot} at ∼0.6 $M_{\odot}$, or a spectral type (SpT) ∼M0. We found that the location of this

[0]This chapter is a reproduction of a paper that has been published by The Astrophysical Journal. It can be found at `http://iopscience.iop.org/article/10.1088/0004-637X/795/2/161/meta`. The original abstract has been removed and the article has been reformatted for this section. The original appendix to this paper has been moved to Appendix A.

transition is consistent with expectations based on observations of younger clusters and the assumption that stellar spin-down is the dominant mechanism influencing angular momentum evolution at ~600 Myr, the age of Praesepe.

This mass-period relation is one projection of the relationship between stellar age, rotation, and magnetic activity. Numerous studies of open clusters have derived relationships between a star's age and chromospheric or coronal emission, which are manifestations of magnetic activity (e.g., Skumanich 1972; Radick et al. 1987; Hawley et al. 1999; Soderblom et al. 2001). Other studies have used e.g., kinematic information to infer the activity lifetimes of low-mass field stars (e.g., Hawley et al. 1999; West et al. 2008). West et al. (2008) model the dynamical heating of stars in the Galactic disk and use the results to calibrate the age-dependence of the vertical gradient in $H\alpha$ emission strengths, finding that the activity lifetimes of stars with SpTs of M2 or later appear to be >1 Gyr. Because few active early M stars are observed in the field, the activity lifetimes of M0-M1 stars are less well known, but they are likely $\lesssim$600 Myr (West et al. 2008). Thus, we expect that the boundary between $H\alpha$ active and inactive Praesepe members will occur in the M0/M1 spectral range. That this transition occurs at roughly the same mass as that between the singular mass-period relation and a more scattered distribution of P_{rot} strengthens the case for a rotation-activity relation in Praesepe.

In Agüeros et al. (2011), we also compared the mass-period relation for Praesepe to that derived from the rotation data published by Delorme et al. (2011) for the Hyades, which is generally assumed to be coeval with Praesepe. This indicated that the transition to a single-valued mass-period relation occurs at a lower characteristic mass in the Hyades,

implying that this cluster is older than Praesepe. Intriguingly, activity studies do not necessarily agree with this conclusion: in the most recent large-scale spectroscopic survey of the two clusters, Kafka & Honeycutt (2006) found that, as measured by $H\alpha$ emission strength, more massive stars are active in the Hyades than in Praesepe, implying that the Hyades is the younger cluster. (The coronal activity picture is not much clearer: Franciosini et al. (2003) found that the two clusters have similar X-ray luminosity functions, contradicting the earlier findings of Randich & Schmitt (1995).)

In this paper we examine activity and rotation in Praesepe and the Hyades to probe the activity-rotation relation at 600 Myr. Our spectroscopic sample includes new spectra obtained with the 2.4-m Hiltner telescope at MDM Observatory, the WIYN 3.5-m telescope at NOAO, both on Kitt Peak, AZ,[1] and the Magellan Echellette (MagE) Spectrograph[2] on the 6.5-m Clay Telescope, Las Campanas, Chile. To these we add spectra from the literature; in total, we have 720 spectra of 516 high-confidence members of Praesepe, and 139 spectra of 130 high-confidence Hyads. We also make use of the Praesepe P_{rot} reported in Agüeros et al. (2011), as well as those measured by Scholz & Eislöffel (2007), Delorme et al. (2011), and Scholz et al. (2011). And we supplement the Hyades P_{rot} of Delorme et al. (2011) with P_{rot} derived from All Sky Automated Survey (ASAS; Pojmański 2002) data by Cargile et al. (in prep.).

We begin in Section 2.2 by describing our membership catalogs for both clusters, the

[1]The MDM Observatory is operated by Dartmouth College, Columbia University, Ohio State University, Ohio University, and the University of Michigan. The WIYN Observatory is a joint facility of the University of Wisconsin-Madison, Indiana University, Yale University, and the National Optical Astronomy Observatory.

[2]Support for the design and construction of the Magellan Echellette Spectrograph was received from the Observatories of the Carnegie Institution of Washington, the School of Science of the Massachusetts Institute of Technology, and the National Science Foundation in the form of a collaborative Major Research Instrument grant to Carnegie and MIT (AST-0215989).

sources of our photometric data, our spectroscopic sample, and our collection of P_{rot} data. In Section 2.3, we describe our method for measuring $H\alpha$ equivalent widths (EqWs) and for deriving the ratio of the $H\alpha$ line luminosity over the stellar bolometric luminosity ($L_{H\alpha}/L_{bol}$). We also discuss our procedure for calculating masses, identifying binaries, and determining Rossby numbers (R_o). In Section 2.4, we use our $H\alpha$ data to compare chromospheric activity in the two clusters and present an updated 600-Myr mass-period relation that includes data for both clusters. We then examine the relation between $H\alpha$ emission and rotation, and between X-ray emission and rotation, for stars in our sample. We conclude in Section 2.5.

Our χ values were calculated as a function of color using medium-resolution synthetic spectra, and as a function of SpT using field M dwarfs. As they differ from those of Walkowicz et al. (2004) and West & Hawley (2008), in Appendix A we discuss in greater detail our calculations and provide tables of our χ values.

2.2 Data

2.2.1 Membership Catalogs

Kraus & Hillenbrand (2007) calculated proper motions and photometry for several million objects within 7° of the center of Praesepe. The resulting catalog includes 1128 candidate cluster members with membership probabilities $P_{mem} > 50\%$. As in Agüeros et al. (2011), we supplement this catalog with 41 known members that are too bright to be identified as members by Kraus & Hillenbrand (2007).

For the Hyades, we adopt the Röser et al. (2011) membership catalog. These authors identified candidate Hyades members via the convergent point method and confirmed membership using photometry. The Röser et al. (2011) catalog does not include P_{mem} calculations, but the authors list contamination percentages based on distance from the cluster center (d_c): the contamination is 1% for stars with $d_c \leq 9$ pc, 7.5% for $9 < d_c \leq 18$ pc, and 30% for $18 < d_c \leq 30$ pc. We converted these to P_{mem} by subtracting the contamination percentage from 100%. By our calculations, the catalog includes 724 stars with $M \geq 0.12\,M_{\odot}$ and $P_{mem} \geq 70\%$ up to 30 pc from the cluster center. Based on photometric limits, Röser et al. (2011) state that their catalog is complete down to $\sim$0.25 $M_{\odot}$.

We supplement the Röser et al. (2011) catalog with new Hyades members found by Cargile et al. (in prep.), who identify 170 cluster members based on reduced proper motions (μ) and distances obtained by *Hipparcos* (Perryman et al. 1997). Cargile et al. consider stars within 26° and 20 pc of the cluster center and with $-170 < \mu_{\parallel} < -60$ and $-20 < \mu_{\perp} < 20$ mas yr^{-1}. All but 13 of the Hyades members identified in this manner were also identified by Röser et al. (2011). We add these 13 additional members to our catalog, bringing the total number of Hyads to 737.

2.2.2 Photometry

We use ($r' - K$) as our primary proxy for stellar temperature. By selecting an optical-NIR color, we obtain a broader dynamic range than is possible with a narrower color index. For example, in ($J - K$), M-dwarf colors range from roughly 0.9 to 1.2 mag, while this same mass range is spread out from 3.3 to 8.0 mag in ($r' - K$). While nearly all the stars

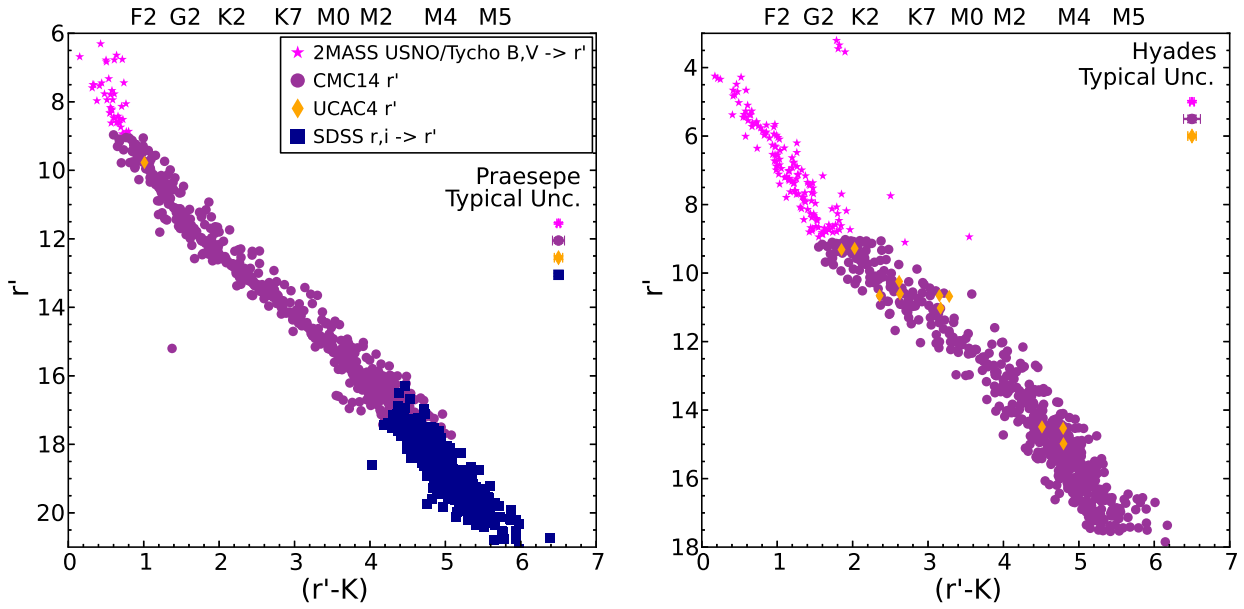

Figure 2.1 CMD for Praesepe (left) and the Hyades (right) indicating the sources of r' photometry. Typical photometric uncertainties for the surveys used in assembling these CMDs are shown for reference. The y-axes are such that stars of similar masses will appear at roughly the same position, despite the different distances to the clusters. SpTs are indicated along the top axes for reference. All stars from the catalogs discussed in Section 2.2.1 are shown. While the r' magnitudes are drawn or transformed from multiple surveys, the cluster sequences are clean and well-defined.

in our sample have Two Micron All Sky Survey (2MASS; Skrutskie et al. 2006) K-band magnitudes, the large range in r' magnitudes (~15 mag) for both clusters meant that we had to obtain this photometry from multiple sources.

The Carlsberg Meridian Catalogue 14 (CMC14; Copenhagen University et al. 2006) provides photometry for approximately 10^8 stars with declinations between $-30°$ and $50°$ and $9 < r' \lesssim 17$ mag. We use CMC14 photometry for stars falling within this magnitude range. The 4$^{\text{th}}$ U.S. Naval Observatory CCD Astrograph Catalog (UCAC4; Zacharias et al. 2012) includes $g'r'i'$ magnitudes from APASS (Henden et al. 2012). In the Hyades, we use the CMC14 magnitudes and errors listed in Röser et al. (2011). CMC14 does not list r'

errors for all stars in Praesepe; in these cases we use the typical errors for the catalog.[3] For a handful of stars with $10 \lesssim r' \lesssim 14$ mag that do not appear in CMC14, we use r' magnitudes from UCAC4.

For stars lacking r' magnitudes, we use the Jester et al. (2005) and Bilir et al. (2008) transformations to convert available r magnitudes to r'.[4]

For stars in Praesepe, we use SDSS photometry to obtain r' for stars with $r > 16$ mag. Our $(r - K)$ color-magnitude diagram (CMD) in Agüeros et al. (2011) indicated that the SDSS r magnitudes could not always be trusted for stars brighter than $r \sim 16$, even in cases where the SDSS flags did not indicate that the star was saturated (see Figure 4 in Agüeros et al. 2011). We use SDSS *ri* photometry to obtain r' using the Jester et al. (2005) equations listed on the SDSS website.[5] Few Hyads are in the SDSS footprint, and many of those in the footprint are saturated; as a result, we do not use any SDSS magnitudes for Hyads.

For stars with $r < 9$ mag in both clusters, we use the Jester et al. (2005) relations to convert the USNO-A2.0 and Tycho 2 Johnson B and V magnitudes included in the 2MASS catalog to SDSS r magnitudes. Since these stars fall into the appropriate color range, we then apply the Bilir et al. (2008) transformation from 2MASS colors to obtain $(r - i)$ for these stars. Finally, we use these r and $(r - i)$ values to obtain r' using the Jester et al. (2005) relation as above. Figure 2.1 shows the r' versus $(r' - K)$ CMDs for both clusters. The

[3] `http://www.ast.cam.ac.uk/ioa/research/cmt/cmc14.html`

[4] We convert r to r' rather than the inverse because CMC14 lacks the i' photometry that would allow us to transform r' into r. Furthermore, the Bilir et al. (2008) relation for $(r - i)$ as a function of 2MASS colors is valid for $(r - i) \lesssim 0.5$, and we could only apply it to the highest mass dwarfs in these clusters. The difference between r and r' is small but not negligible for our purposes.

[5] `http://www.sdss.org/dr7/algorithms/jeg\_photometric\_eq\_dr1.html`

typical photometric uncertainty for these r' magnitudes depends on the source catalog; after applying the convrsions discussed above to 2MASS or SDSS data, the uncertainty is generally $\lesssim$0.1 mag. For CMC14 data, the uncertainty is $\approx$0.1 mag for Hyads and slightly smaller for stars in Praesepe; for UCAC4 data, it is $\approx$0.05 mag.

2.2.3 Spectroscopy

2.2.3.1 New Observations

We used the MDM Observatory Modular Spectrograph (ModSpec) on the Hiltner 2.4-m telescope to obtain spectra of stars in Praesepe and the Hyades over the course of five multi-night runs between 2010 Dec 2 and 2012 Nov 14 (see Table 2.1). ModSpec was configured to provide coverage from 4500 to 7500 Å with ~1.8 Å sampling and a spectral resolution of ~3300. These spectra were reduced with a script written in PyRAF, the Python-based command language for the Image Reduction and Analysis Facility (IRAF).[6] All the spectra were trimmed, overscan- and bias-corrected, cleaned of cosmic rays, flat-fielded, extracted, dispersion-corrected, and flux-calibrated using standard IRAF tasks. After accounting for the quality of the spectra and for those stars that we observed more than once, our sample included 253 spectra for 209 Praesepe stars, of which 226 spectra were for 187 stars with $P_{mem} > 70\%$, as calculated by Kraus & Hillenbrand (2007). Our Hyades sample included 139 spectra for 130 stars with $P_{mem} > 70\%$ (see Section 2.2.1) once the same quality cuts were made.

[6]PyRAF is a product of the Space Telescope Science Institute, which is operated by AURA for NASA. IRAF is distributed by the National Optical Astronomy Observatories, which are operated by the Association of Universities for Research in Astronomy, Inc., under cooperative agreement with the National Science Foundation.

Table 2.1. ModSpec Observations of Praesepe and Hyades Stars

Dates	# of Spectra Praesepe	Hyades
2010 Dec 02-Dec 06	124	···
2011 Feb 08-Feb 11	82	···
2011 Nov 30-Dec 05	···	66
2012 Feb 17-Feb 21	44	13
2012 Nov 11-Nov 14	8	65
Total	258	144

Note. — All dates in Tables 2.1-2.3 are UT.

Table 2.2. Hydra Observations of Praesepe Fields

Date	Field Center	Exposure Time (s)	# of Spectra
2011 Feb 7	08 39 22.3 +20 02 00.0	1380	57
	08 40 24.0 +19 36 00.0	6000	41
	08 39 07.5 +20 44 00.0	6000	24
	08 45 19.0 +19 18 00.0	4200	26
	08 41 51.5 +19 30 00.0	1500	43
2011 Feb 8	08 39 07.5 +20 44 00.0	4200	23
	08 44 35.5 +20 12 00.0	3600	17
Total			231

Table 2.3. MagE Observations of Praesepe Stars

Date	Target	Position	Exposure Time (s)
2011 Mar 19	JS 718[a]	08 40 04.2 +19 24 50.3	1600
	HSHJ 428	08 42 37.6 +19 59 18.9	1800
2011 Mar 20	JS 123[b]	08 36 19.2 +19 53 54.9	900
	JS 298	08 39 31.8 +19 24 17.6	1200
	JS 729	08 41 26.0 +19 59 15.1	900

[a]Identified as a candidate binary system in Agüeros et al. (2011).

[b]Identified as a candidate binary system in this paper.

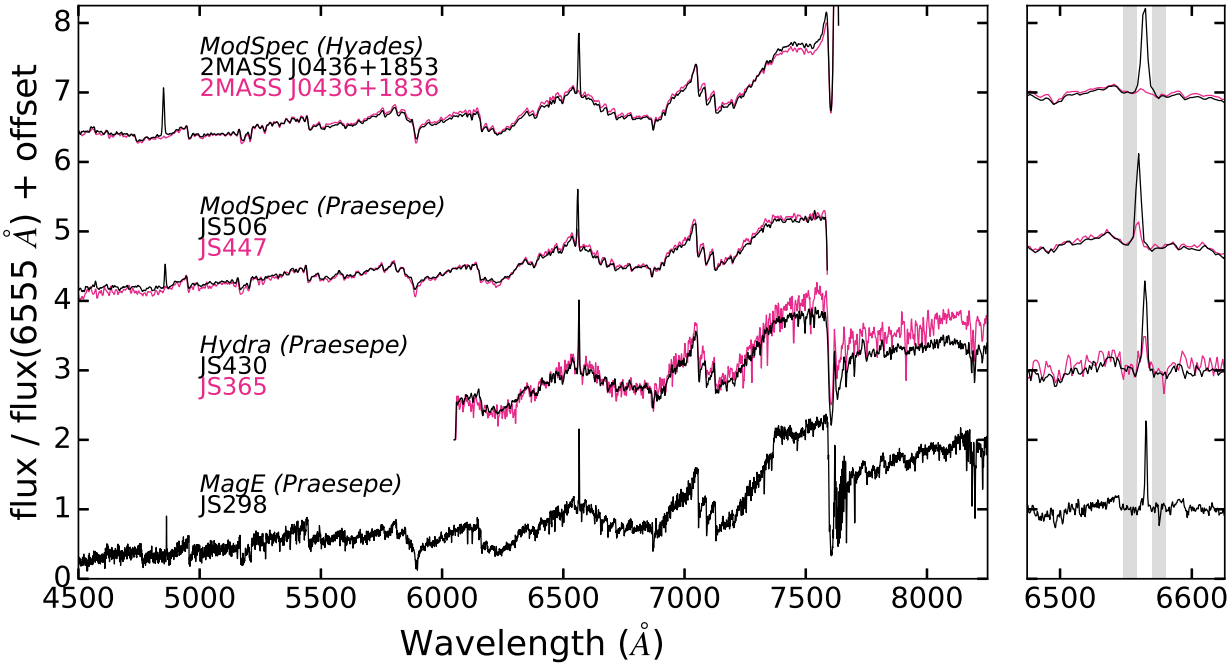

Figure 2.2 Example spectra from our new observations of Praesepe and Hyades stars with ModSpec on MDM, Hydra on WIYN, and MagE on Magellan. The Hyads are both M2 stars, while all the Praesepe stars are M3s. For each cluster/instrument combination, the most active star of that SpT is shown in black, and the least active in pink. The panel to the right shows a close-up of the region around $H\alpha$, with gray shading marking the typical continuum regions for the EqW measurements (see Section 2.3.1).

We also observed Praesepe with the Hydra multi-object spectrograph on the WIYN 3.5-m telescope during the nights of 2011 Feb 7 and 8. We used the bench-mounted spectrograph with the red fiber cable and an échelle grating with 600 lines mm^{-1} set at a blaze angle of 13.9°. This resulted in coverage from 6050 to 8950 Å with ~1.4 Å sampling and a spectral resolution of ~4000. We targeted seven fields that required exposure times ranging from 1380 to 6000 s and were typically divided into three or four sub-exposures for cosmic-ray removal (see Table 2.2). We reduced these spectra using standard routines in the IRAF Hydra package.[7] Each image was trimmed and instrument biases were removed.

[7] `http://iraf.noao.edu/tutorials/dohydra/dohydra.html`

Table 2.4. Final Spectroscopic Sample

Telescope (Instrument)	Hiltner (ModSpec)	WIYN (Hydra)	Magellan (MagE)
Praesepe stars	209	176	5
... with $P_{mem} > 70\%$	187	174	5
... with spectra in literature[a]	42	61	4
Hyades stars	130	···	···
... with $P_{mem} > 70\%$	130	···	···

[a]These are for the stars with $P_{mem} > 70\%$. See Section 2.2.3.2.

The spectra for the individual fibers were extracted, flat-fielded, and dispersion-corrected. Sky spectra from ~30 fibers placed evenly across the field-of-view were combined and subtracted from our target star spectra. We throughput-corrected and flux-calibrated each spectrum using the flux standard G191B2B, which was observed using the same set-up as for our targets. We then combined the sub-exposures for each object to form a high signal-to-noise (S/N) spectrum for each star.

We placed Hydra fibers on 231 targets in Praesepe; 43 of these spectra were too noisy to use for our analysis, so that the total number of usable spectra was 188. Once we accounted for the stars targeted more than once, there were a total of 176 individual Praesepe members with at least one usable Hydra spectrum. 174 of these stars have $P_{mem} > 70\%$ in the Kraus & Hillenbrand (2007) catalog, and we have a total of 186 Hydra spectra for these stars. (We observed 23 stars with both ModSpec and Hydra.)

Finally, five Praesepe rotators were observed with MagE (Marshall et al. 2008) on the 6.5-m Clay Telescope on the nights of 2011 Mar 19 and Mar 20 (see Table 2.3). MagE is a cross-dispersed spectrograph that covers 3000−10500 Å in a single exposure. These

spectra were reduced with the MASE pipeline (Bochanski et al. 2009). All five stars have $P_{mem} > 70\%$.

Example spectra from each observatory are shown in Figure 2.2; Table 2.4 provides the overall statistics for our spectroscopic campaign, and reflects the application of the quality cuts discussed above to the data. In Praesepe, our goal was to obtain spectra for at least twice as many stars of a given SpT without measured periods as for stars with known periods, and we achieved this for stars later than K4. In the Hyades, by contrast, we mostly observed stars with known periods.

2.2.3.2 Archival Spectroscopy

To increase our spectroscopic coverage of Praesepe, we collected spectra from the literature. Allen & Strom (1995) compiled a grid of stellar classification spectra using Hydra on the Mayall 4-m telescope at NOAO, Kitt Peak, and observed 98 stars classified by Kraus & Hillenbrand (2007) as Praesepe members. (They also observed four non-members.) These spectra were flat-fielded and wavelength-calibrated, but were not flux-calibrated and have no associated noise spectrum. We removed two spectra from this sample because they were too noisy for our purposes. Of the remaining spectra, 93 are for stars with $P_{mem} > 70\%$.

Kafka & Honeycutt (2004, 2006) observed 224 K and M dwarfs in Praesepe using Hydra on the WIYN 3.5-m telescope. S. Kafka (pers. comm.) kindly provided us with 185 of these spectra, which are not flux-calibrated or corrected for telluric absorption. After visual inspection, we removed 24 spectra due to incomplete cosmic-ray subtraction and/or

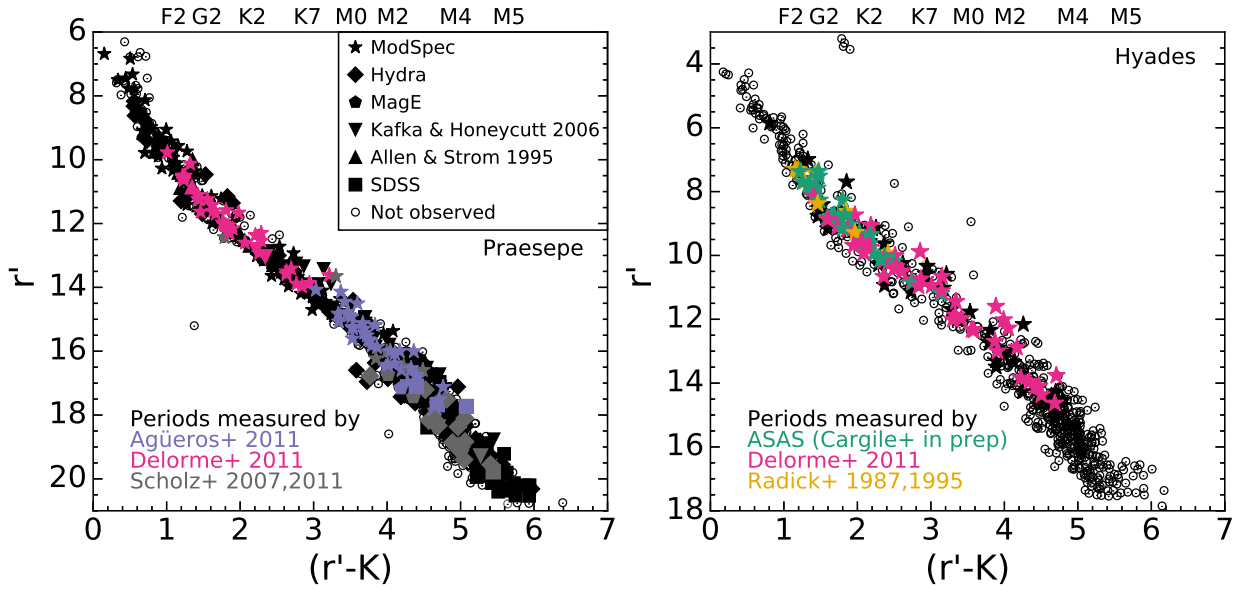

Figure 2.3 CMD for Praesepe (left) and the Hyades (right) showing the completeness of our spectroscopic samples. We have obtained spectra across the full mass range for which P_{rot} have been measured in each cluster.

strong sky lines near $H\alpha$. Of the remaining spectra, 154 are for stars with $P_{mem} > 70\%$.

As of 2013 Feb 14, SDSS had obtained spectra for 66 Praesepe stars. These spectra have been sky-subtracted, corrected for telluric absorption, and spectrophotometrically calibrated, as well as calibrated to heliocentric vacuum wavelengths.[8] We removed two spectra from this sample because they were too noisy for our purposes; 56 of the remaining spectra are for stars with $P_{mem} > 70\%$.

Once the quality cuts described above and the $P_{mem} = 70\%$ threshold was set, and we accounted for stars with multiple spectra, we were left with 720 spectra of 516 Praesepe members and 139 spectra of 130 Hyads. Figure 2.3 gives an overview of our spectral coverage in each cluster, along with the distribution of stars with P_{rot} measured by the surveys discussed below.

[8] `http://www.sdss.org/dr3/products/spectra/`

2.2.4 Rotation Periods

The Palomar Transient Factory is described in detail in Law et al. (2009) and Rau et al. (2009); our first season of PTF observations of Praesepe and subsequent light-curve analysis is described in Agüeros et al. (2011). This analysis produced high-confidence measurements of P_{rot} ranging from 0.52 to 35.85 d for 40 stars. Thirty-seven of these stars have $P_{mem} > 95\%$, as calculated by Kraus & Hillenbrand (2007), with two of the other stars having $P_{mem} > 94\%$.

In Agüeros et al. (2011), we also compiled P_{rot} measurements from the literature, including 52 bright stars (of which 46 have $P_{mem} > 95\%$), whose periods were measured by Delorme et al. (2011), and 54 low-mass Praesepe members with periods reported by Scholz & Eislöffel (2007) and Scholz et al. (2011). As nine of these stars with P_{rot} from the literature also have PTF periods, the total sample of Praesepe rotators is 135 stars. Our spectroscopic sample includes observations of 113 of these stars, of which 111 have $P_{mem} > 70\%$.

Radick et al. (1987, 1995) searched for variability in Hyades stars using differential photometry obtained over several seasons, at least one of which had a five-month baseline. These authors measured P_{rot} for 18 cluster members, all with SpT K8 or earlier.

In addition to their results for Praesepe, Delorme et al. (2011) published 60 P_{rot} for Hyades stars that were also derived from data collected by the SuperWASP search for transiting exoplanets. Delorme et al. (2011) analyzed light curves spanning $\gtrsim$100 d for stars within $\sim$15° of the Hyades's center. Fifty-nine of their rotators have $P_{mem} > 95\%$ according to their analysis.

Cargile et al. (in prep) used the publicly available light curves from ASAS (Pojmański 2002) to measure P_{rot} for Hyades stars. On average, the ASAS data provide 240 observations over a seven-year baseline for $V = 7-13$ mag stars. Cargile et al. measure P_{rot} for 40 Hyads; 18 are new measurements. For the other 22, the agreement with the P_{rot} measured by Radick et al. (1987, 1995) and Delorme et al. (2011) is excellent, with the exception of ASAS 040526+1926.5. For this star, Cargile et al. find a P_{rot} half that published by Delorme et al. (2011); we use this more recent period for our analysis.

Nine Hyades rotators are known binaries, and we remove these stars from the list of rotators for our analysis. There are no known binaries among the Praesepe rotators (see Section 2.3.3). This leaves 87 known rotators in the Hyades, and we have spectra for 83 of those stars.

2.3 Measurements and Derived Quantities

2.3.1 $H\alpha$ Measurements and $L_{H\alpha}/L_{bol}$

We measured the equivalent width (EqW) of the $H\alpha$ line for each spectrum in our sample. We did not correct these measurements for photospheric absorption. Where possible, the continuum flux was taken to be the average flux between 6550−6560 Å and 6570−6580 Å (as shown in the right panel of Figure 2.2). In cases where the line was broad or shifted away from 6563 Å, the continuum flux was measured from 10 Å windows on each side of the line. The window used to measure the line flux varies from spectrum to spectrum, and was adjusted interactively.

In cases where we had multiple spectra for a star, the EqWs were generally consistent at the 1σ level. A few stars appeared to show strongly varying $H\alpha$ emission. We have spectral coverage blueward of $H\alpha$ for a small number of these stars, and these do not appear to be flaring. We therefore simply use the average EqW in all these cases for our analysis.

To estimate the EqW uncertainties, the same person first measured each EqW twice, and we took the difference between the two measurements to be the human error in the interactive measurement. The median difference between the two measurements was 0.22 Å in Praesepe and 0.15 Å in the Hyades.

We then used a Monte Carlo technique to add Gaussian noise to each point in the spectrum and remeasured the EqWs 2500 times in an automated fashion. The continuum and line regions from the initial interactive measurements were re-used. For spectra with an associated uncertainty spectrum, we drew the noise at each point from a Gaussian with width equal to the uncertainty at that point. For stars without an uncertainty spectrum, we drew the noise from a Gaussian distribution with a width equal to the σ of the flux in the continuum region. We took the standard deviation of the EqWs from the Monte Carlo simulation as the error from noise in the spectrum. The two error measurements were added in quadrature to produce the uncertainty in each EqW.

In Figure 2.4, we compare our EqW measurements to those of Kafka & Honeycutt (2006) for all 161 of the usable Praesepe spectra collected by these authors, and to those of Stauffer et al. (1997) for 12 spectra collected by those authors (J. Stauffer, pers. comm.). Kafka & Honeycutt (2006) state that their typical EqW uncertainties are $\sim$ 0.2Å. There is

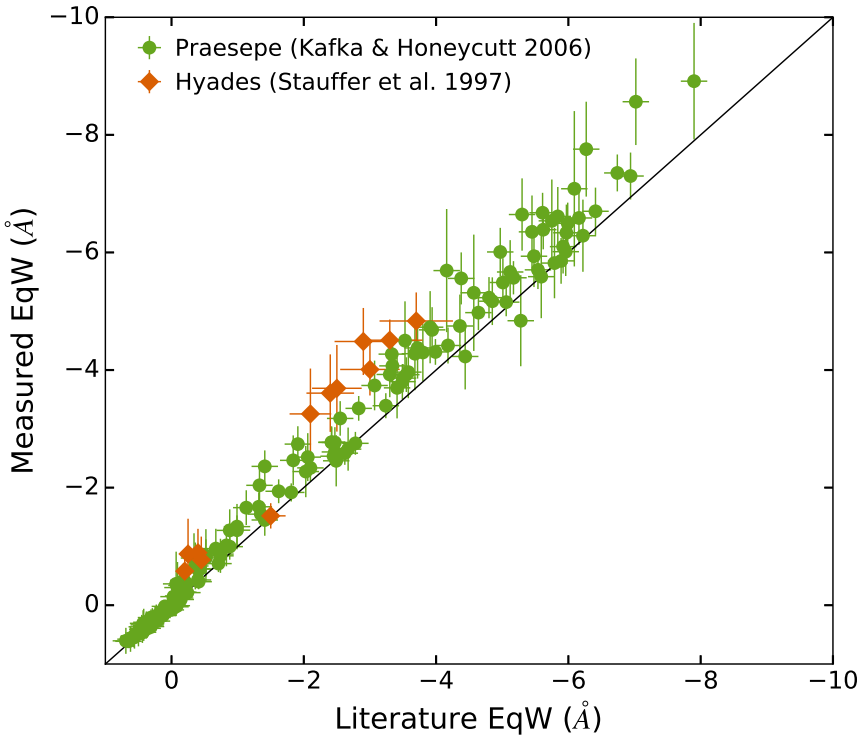

Figure 2.4 Comparison of EqW measurements for the 161 Kafka & Honeycutt (2006) spectra of Praesepe stars and for 12 Stauffer et al. (1997) spectra of Hyades stars. We follow the convention that an EqW < 0 corresponds to emission. We have measured EqWs using the spectra from these two papers, so we are showing the different EqWs obtained using different measurement techniques. Our EqWs are systematically larger, and the difference grows as the EqWs become larger.

no mention of uncertainties in Stauffer et al. (1997), but we assume a 15% measurement uncertainty, as quoted by Stauffer et al. (1994a) in earlier work on the Hyades. While the measurements are broadly consistent with each other, our EqW measurements tend to return values $10-20\%$ larger than those of Kafka & Honeycutt (2006) and $25-35\%$ larger than those of Stauffer et al. (1997).

The Hyades EqW measurements used by Kafka & Honeycutt (2006) come from a variety of sources and therefore potentially very different telescope/spectrograph combinations and EqW-measurement techniques. As shown in Figure 2.4, the difference between

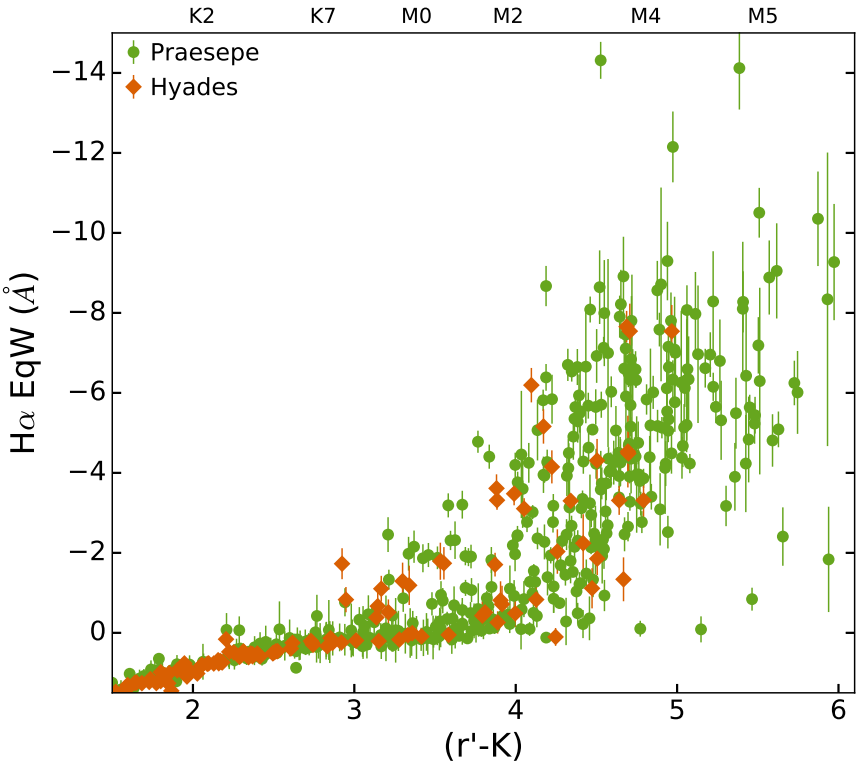

Figure 2.5 $H\alpha$ EqW vs. $(r' - K)$ for stars in Praesepe (green dots) and the Hyades (orange diamonds). For stars with multiple measurements, the average is shown. We do not show higher-mass stars with $(r' - K) < 1.5$, but the trend of consistent levels of $H\alpha$ activity in the two clusters continues to $(r' - K) \approx 1$, the bright limit of our observations in the Hyades. We find no evidence for different levels of activity in the two clusters (see Section 2.4).

our measurements and those of Stauffer et al. (1997) is larger than the difference between our measurements and those of Kafka & Honeycutt (2006). These discrepancies argue for a single, uniform approach to measuring EqWs, as is possible for our spectroscopic sample, to maximize the internal consistency of the results.

Figure 2.5 shows the average EqW for all stars in our sample with $P_{mem} \geq 70\%$; these values can be found in Tables 2.5 (for Praesepe) and 2.6 (for the Hyades).

The ratio of the $H\alpha$ luminosity to the bolometric luminosity of the star, $L_{H\alpha}/L_{bol}$, enables a better comparison of activity between stars of different (low) masses than EqW

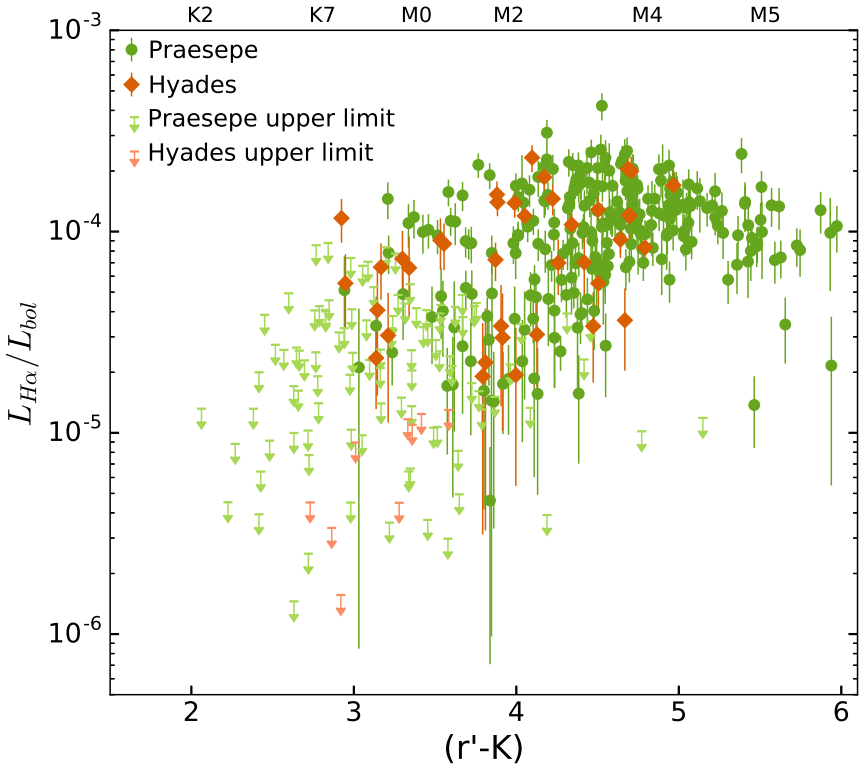

Figure 2.6 $L_{H\alpha}/L_{bol}$ vs. $(r' - K)$ for stars in Praesepe and the Hyades, including upper limits. For stars with multiple measurements, the average $L_{H\alpha}/L_{bol}$ is shown. There are no stars with $(r' - K) \lesssim 3$ with definitive $H\alpha$ emission, and all the stars with $(r' - K) \lesssim 2$ are statistically inconsistent with emission at the 2σ level. The upper envelope of $L_{H\alpha}/L_{bol}$ increases to $(r' - K) \sim 4.5$ before decreasing again; at this color the amount of scatter in $L_{H\alpha}/L_{bol}$ begins to decrease significantly. Our EqW uncertainties are generally smaller for Hyads than for Praesepe stars, placing more stringent upper limits on emission from Hyades stars.

alone. It reflects the importance of the $H\alpha$ flux relative to the star's entire energy output, and not just relative to the continuum flux in a single band, which changes rapidly across the K and M SpTs (Reid & Hawley 2005). Ideally, $L_{H\alpha}/L_{bol}$ would be calculated as

$$\frac{L_{H\alpha}}{L_{bol}} = -W_{H\alpha}\frac{f_0}{f_{bol}}$$

where $W_{H\alpha}$ is the EqW of the $H\alpha$ line, f_0 is the continuum flux for the line, and f_{bol} is

the apparent bolometric flux of the star. However, because some of our spectra are not flux-calibrated, we cannot always measure f_0 directly. We therefore followed Walkowicz et al. (2004) and West & Hawley (2008) in calculating $\chi = f_0/f_{bol}$ as a function of color.

As our sample of active stars includes K and M dwarfs, we could not simply use the χ values of Walkowicz et al. (2004), which were calculated for M0.5-L0 stars. We therefore calculated χ as a function of color and magnitude using medium-resolution model spectra from PHOENIX ACES atmospheres (Husser et al. 2013); we obtained synthetic photometry by convolving these spectra with the SDSS and 2MASS filter curves.[9] Interestingly, our χ values do not match those given in Walkowicz et al. (2004) and West & Hawley (2008); see Appendix A for full discussion. Our χ values are listed as a function of temperature and color in Table A.2.

We then computed $L_{H\alpha}/L_{bol}$ for stars with $H\alpha$ in emission using our EqWs, each star's $(r' - K)$, and the appropriate χ value from our χ versus $(r' - K)$ relation. We also calculated 2σ EqW upper limits for all stars with EqWs consistent with absorption at the 1σ level, and converted those upper limits into $L_{H\alpha}/L_{bol}$ upper limits. (The $L_{H\alpha}/L_{bol}$ values can also be found in Tables 2.5 and 2.6.)

Figure 2.6 shows the average $L_{H\alpha}/L_{bol}$ (along with upper limits) as a function of $(r' - K)$ for $P_{mem} \geq 70\%$ stars. The scatter in $L_{H\alpha}/L_{bol}$ lessens significantly for $(r' - K) \gtrsim 4.5$. The upper envelope of activity appears to increase slightly with color, peaking at $(r' - K) \sim 4$ before decreasing slightly again at the reddest colors.

[9]We calibrated χ as a function of color rather than absolute magnitude because the distances to many of the low-mass Hyads have not been directly determined, and the cluster's extent along the light-of-sight is large enough to introduce significant uncertainties in the luminosities.

Table 2.5. Praesepe Stars

Name	RA	DEC	r' (mag)	r' src[a]	M ($M_\odot$)	R_o	Binary?	$H\alpha$ EqW (Å)	$L_{H\alpha}/L_{bol}$[b] ($\times 10^{-5}$)
JS 466	08:41:58.84	20:06:27.1	12.818 ± 0.002	C	0.80	0.5525	N	0.560 ± 0.223	···
JS 468	08:41:59.35	19:44:45.1	15.631 ± 0.070	C	0.50	0.4641	N	−0.300 ± 0.435	1.363 ± 1.984
HSH J404	08:42:01.59	19:26:46.0	17.878 ± 0.005	S	0.22	···	N	−2.098 ± 0.498	6.101 ± 1.734
AD 3050	08:42:04.48	19:32:42.7	18.834 ± 0.005	S	0.19	0.0086	N	−8.071 ± 0.619	17.136 ± 3.235
AD 3051	08:42:04.69	19:38:00.8	20.784 ± 0.008	S	0.13	0.0060	N	···	···
JS 470	08:42:05.17	20:57:56.5	15.466 ± 0.070	C	0.58	···	Y	−0.456 ± 0.207	1.853 ± 0.876
KW 445	08:42:06.49	19:24:40.4	7.944 ± 0.001	T	2.38	···	Y	···	···
HSH J421	08:42:23.82	19:23:12.5	18.370 ± 0.006	S	0.21	0.0034	N	−4.488 ± 0.507	10.121 ± 2.076
HSH J424	08:42:30.77	19:29:31.0	17.610 ± 0.005	S	0.23	···	N	−1.036 ± 0.503	3.326 ± 1.687
JS 513	08:43:05.28	19:27:54.6	14.765 ± 0.035	C	0.58	···	N	0.139 ± 0.108	···

[a]Source of r' magnitude: T is 2MASS/TYCHO2, U is UCAC4, S is SDSS, and C is CMC14.

[b]Only for stars with $H\alpha$ in emission.

Note. — Only selected lines are shown. The full table, with additional data columns, may be found in the on-line edition of the journal at `http://iopscience.iop.org/0004-637X/795/2/161/suppdata/apj502916t5_mrt.txt`

Table 2.6. Hyades Stars

2MASS J	RA	DEC	r' (mag)	r' src[a]	M ($M_\odot$)	R_o	Binary?	SpT[b]	$H\alpha$ EqW (Å)	$L_{H\alpha}/L_{bol}$[c] ($\times 10^{-5}$)
03014830+3733202	03:01:48.32	37:33:20.3	15.12 ± 0.12	C	0.20	···	N	M4	−4.533 ± 0.897	12.070 ± 3.058
03550142+1229081	03:55:01.36	12:29:08.2	9.74 ± 0.04	C	0.63	0.429	N	K5	0.706 ± 0.030	···
03550647+1659545	03:55:06.41	16:59:54.7	8.74 ± 0.00	T	0.99	0.664	N	K1	1.058 ± 0.103	···
04070122+1520062	04:07:01.15	15:20:06.3	10.03 ± 0.04	C	0.69	0.581	N	K7	0.586 ± 0.153	···
04070323+2016510	04:07:03.25	20:16:50.9	15.58 ± 0.18	C	0.16	···	N	···	···	···
04084015+2333257	04:08:40.18	23:33:25.6	12.34 ± 0.04	C	0.59	···	Y	M2	−0.510 ± 0.430	2.235 ± 1.908
04142562+1437300	04:14:25.59	14:37:30.3	8.27 ± 0.00	T	1.03	···	N	F9	1.692 ± 0.030	···
04151038+1423544	04:15:10.34	14:23:54.6	10.96 ± 0.04	C	0.48	0.370	N	K7	0.333 ± 0.167	···
04322565+1306476	04:32:25.59	13:06:47.8	10.58 ± 0.04	C	0.97	···	N	M0	−1.728 ± 0.387	11.650 ± 2.858
04343992+1512325	04:34:39.94	15:12:32.6	11.77 ± 0.04	C	0.61	···	Y	M1	−1.790 ± 0.463	9.048 ± 2.575

[a]Source of r' magnitude: T is 2MASS/TYCHO2, U is UCAC4, and C is CMC14.

[b]SpTs are from the output of the Hammer.

[c]Only for stars with $H\alpha$ in emission.

Note. — Only selected lines are shown. The full table, with additional data columns, may be found in the on-line edition of the journal at `http://iopscience.iop.org/0004-637X/795/2/161/suppdata/apj502916t6_mrt.txt`

2.3.2 Stellar Masses

We estimated masses for every star in our sample using the mass-absolute K magnitude (M_K) relation assembled by Kraus & Hillenbrand (2007), who provided masses and spectral energy distributions (SEDs) for B8-L0 stars. We chose this method over the mixed empirical and model-based method used in Agüeros et al. (2011) because Kraus & Hillenbrand (2007) accounted for observations that models under-predict masses for stars $<0.5\ M_\odot$. This also had the advantage of giving us a single source for mass calculations across our entire sample.

For Praesepe, we calculated M_K using a *Hipparcos*-derived cluster distance of 181.5±6.0 pc (van Leeuwen 2009). For the Hyades, we used *Hipparcos* parallaxes (Perryman et al. 1997) where possible to determine distances to individual stars. When *Hipparcos* parallaxes were not available, we used the secular parallaxes published by Röser et al. (2011). The 13 Cargile et al. stars that are not in the Röser et al. (2011) catalog do not have *Hipparcos* parallaxes, and for these stars we assumed a distance of 47 pc (van Leeuwen 2009).

We determined each star's mass by linearly interpolating between the M_K and mass points given by Kraus & Hillenbrand (2007). The resulting Praesepe masses used in this paper differ by $0.02-0.07\ M_\odot$ from those listed in Agüeros et al. (2011). Masses for all stars in our sample are given in Tables 2.5 and 2.6. Figure 2.7 shows the combined mass-period data for Praesepe and the Hyades, along with the typical mass uncertainties that result from the distance and photometric uncertainties in Praesepe.

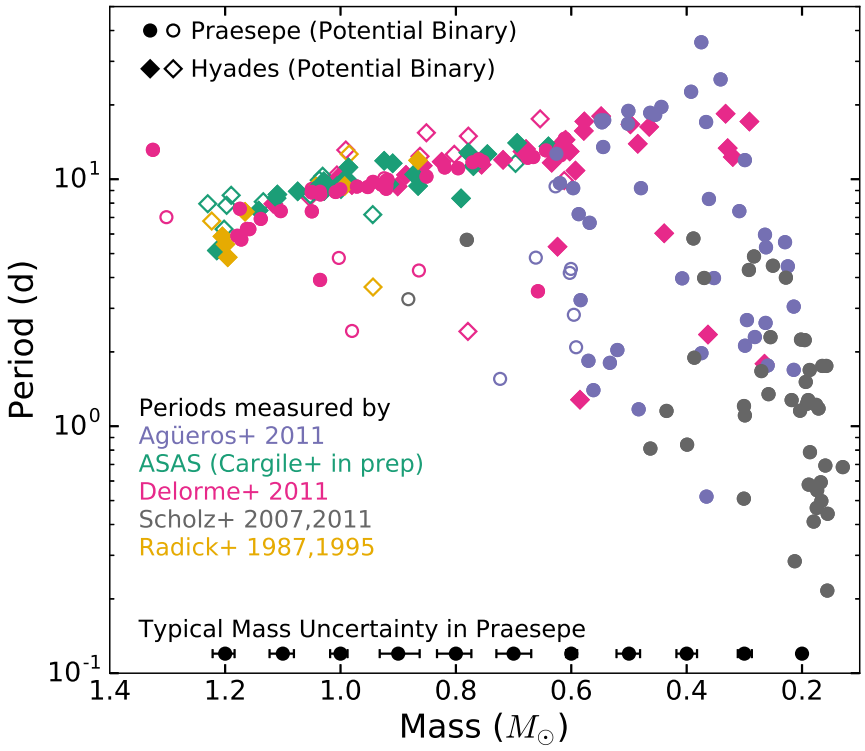

Figure 2.7 Mass-period diagram for Praesepe and the Hyades. Confirmed binaries from the literature are not shown. The black points with error bars show the typical mass uncertainties that result from the distance uncertainty and photometric uncertainties for Praesepe members. All but three stars with $M \gtrsim 0.7\ M_\odot$ that have not joined their fellow cluster members on the slow-rotator sequence are photometrically identified potential binaries. The three exceptions may be binaries with smaller mass ratios, or they may host giant planets on close orbits (Poppenhaeger & Wolk 2014; Kovács et al. 2014).

2.3.3 Binary Identification

In Agüeros et al. (2011), we followed Steele & Jameson (1995) in identifying a binary main sequence in the Praesepe CMD offset by 0.75 mag for a given color from that of single stars. We then labeled as candidate binary systems stars that lie above the midpoint between the single-star and binary main sequences (Hodgkin et al. 1999).

We applied the same method to both of our CMDs here, but only for stars with $(r' - K) < 4$. To the red of this value, the binary main sequence is no longer as apparent,

so determining candidate binaries requires more information than a single color and magnitude. We identified 15 and 29 potential binary systems among known rotators in Praesepe and the Hyades, respectively; these stars are flagged in Tables 2.5 and 2.6. Four of the possible binary systems in Praesepe were similarly flagged in Agüeros et al. (2011). Since no color cut was imposed on potential binaries in Agüeros et al. (2011), there were 14 stars flagged as potential binary systems in Agüeros et al. (2011) which we did not flag here. Radial velocity monitoring is required to confirm that these are actually binaries. For now, these stars are shown as open symbols in Figure 2.7 and we removed them when appropriate for our analysis.

Finally, we searched the literature for any confirmed binaries amongst stars with measured P_{rot}. We did not find any known binaries in Praesepe. Eight Hyades members were identified in SIMBAD as spectroscopic binaries or as having a M dwarf companion. Delorme et al. (2011) also listed an additional spectroscopic binary. We removed these nine stars from our sample for our analysis.

2.3.4 Rossby Numbers

Stellar activity evolves with rotation in a mass-dependent way. For stars of a given mass, those rotating above a threshold velocity show emission independent of rotation rate, while below this saturation velocity stars show decreasing activity with decreasing rotation. The saturation velocity depends on stellar mass (Pizzolato et al. 2003). Analysis of activity as a function of Rossby number, $R_o = P_{rot}/\tau$, where τ is the convective overturn time, removes this mass-dependence of the rotation-activity relation. To calculate R_o for

stars in our sample, we used the equation of Wright et al. (2011) for τ as a function of mass. These authors calculated τ such that the turnover point for L_X/L_{bol} occurs at the same R_o regardless of stellar mass. This produces an empirical scaling factor that removes the mass-dependence of the turnover point; we note that this is different from obtaining τ from comparisons to models. Tables 2.5 and 2.6 include R_o values for rotators in the two clusters.

2.4 Results and Discussion

2.4.1 Comparing Chromospheric Activity in the Two Clusters

The data in Figure 2.5 indicate that Praesepe and the Hyades have similar levels of chromospheric activity. Stars with $2 < (r' - K) < 3$ do not have statistically significant levels of $H\alpha$ emission; some stars in this range have $H\alpha$ EqWs consistent with emission, but many of those are potential binaries. Emission is more reliably detected starting at $(r' - K) \sim 3$, or SpTs of ~K7. All stars with $(r' - K) \gtrsim 4.5$ (later than ~M3) appear to be active, and the two clusters visually appear to have similar upper and lower envelopes of activity.

Figure 2.6 is a comparison between the $L_{H\alpha}/L_{bol}$ for both clusters; the clusters also appear to have consistent levels of activity by this measure. The upper limits in Figure 2.6 are slightly misleading because our Hyades stars have smaller EqW errors, likely because stars of the same mass have apparent magnitudes ~3 mag brighter in the Hyades than in Praesepe (see Figure 2.1). The correspondingly higher S/N for those spectra allows us to

place more stringent upper limits on $H\alpha$ emission in the Hyades than in Praesepe.

Figure 2.8 shows the average EqW for each cluster as a function of binned $(r' - K)$. It also includes EqWs for nearly 2800 SDSS M dwarfs; we constructed this sample by cross-matching the West et al. (2011) M-dwarf catalog with the "high quality" sample of SDSS/2MASS photometry from Covey et al. (2007).[10] We use logarithmic bins in $(r' - K)$ because we have more high-mass stars than low-mass stars in the Hyades; the bins increase in size for redder colors but still contain approximately the same number of stars (between eight and 20).

Kolmogorov-Smirnov (KS) tests in each color bin find that for $(r' - K) > 1$, the EqWs for the cluster stars are consistent with coming from the same distribution. Furthermore, for $(r' - K) > 2.6$, these EqWs are inconsistent with the distribution of EqWs for the low-activity (and on average, older) field-stars. (The exception is the $2.6 < (r' - K) < 3.2$ bin, where the Hyads are consistent with the field stars (p = 0.14).) It is therefore appropriate to treat the two clusters as a single-aged cluster for purposes of analysis, as we do below.

Figure 2.8 also shows clearly that the late-type cluster stars are systematically more active than their SDSS counterparts. The field star ages are not known, but they presumably range between 2−10 Gyr. These data therefore illustrate nicely the overall decay of magnetic activity with time (as noted by e.g., Skumanich 1972; Radick et al. 1987; Soderblom et al. 2001).

How do our results compare to previous authors' comparisons of chromospheric activity in Praesepe and the Hyades? Pace & Pasquini (2004) found that solar-type stars in the two clusters have similar levels of chromospheric activity, as measured by CaII K

[10]This sample includes two Praesepe stars.

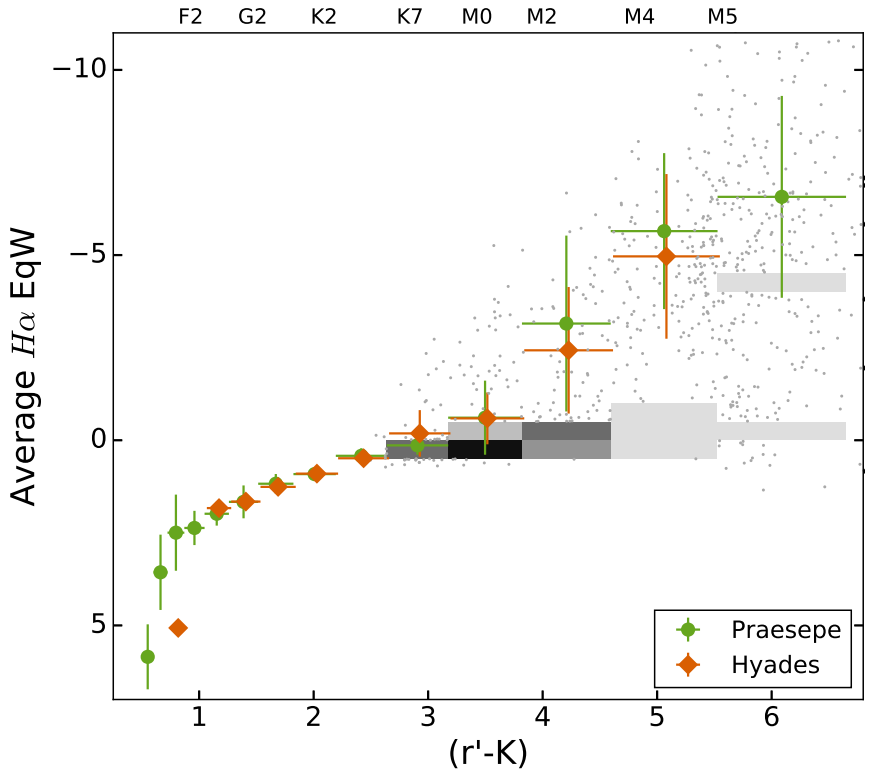

Figure 2.8 Average $H\alpha$ EqW vs. logarithmically binned color for stars in Praesepe and the Hyades. The vertical bars show the standard deviation within the bin, and the horizontal bars show the extent of the bin. The ~2800 SDSS M dwarfs (Covey et al. 2007; West et al. 2011) are shown as a greyscale histogram when more than 25 stars fell into a bin, and as gray points otherwise. The inactive region of the histogram includes 2059 stars. KS tests indicate that, for $(r' - K) \gtrsim 2$, the EqWs for Praesepe and the Hyades are consistent with coming from the same distribution, and are inconsistent with the distribution for the field-star sample.

emission. Our data are consistent with this result, and extend it to later-type stars.

However, Kafka & Honeycutt (2006) found that $H\alpha$ activity in the Hyades began at bluer colors than in Praesepe. Kafka & Honeycutt (2006) also found that the Hyads in their sample became completely active at a bluer color than those in Praesepe. Because these authors combined their $H\alpha$ measurements in Praesepe with literature EqWs for both clusters, it is possible that the disagreement is due to inconsistencies in the methods

used to measure EqWs. As discussed in Section 2.3.1, our $H\alpha$ EqWs are systematically 0.1−1 Å larger than those measured by Kafka & Honeycutt (2006) for the same stars in Praesepe. Shifting the upper envelope of Praesepe EqWs up by ∼0.5 Åin figure 7 of Kafka & Honeycutt (2006) would essentially remove the difference in the location of the transition between inactive and active stars in the two clusters reported by these authors. Such a shift, however, would not change the color at which all of the Praesepe stars become active.

2.4.2 Activity and Measurements of Periodic Variability

Active stars may have higher spot coverage and might therefore show stronger photometric modulation than non-active stars, which would bias our sample of rotators toward stars with stronger $H\alpha$ emission. If $H\alpha$ active stars are more likely to exhibit periods, then the age-rotation-activity relation derived from stars with measured periods (rotators) may not apply to stars without measured periods.

On the other hand, periodic variability may not be detected for a variety of reasons. Stars without measured P_{rot} may have photometric variability that falls below the detection threshold of a given survey, which in turn may be due to lack of spots or symmetrical spot coverage across the stellar surface. They may also have P_{rot} that is too short or too long to be detected by that survey.

Figure 2.9 shows a comparison of the $H\alpha$ EqW as a function of $(r' - K)$ for stars in our sample with and without detected P_{rot}. To test the similarity between these two samples, we determine the probability that the stars with detected P_{rot} are drawn from the same

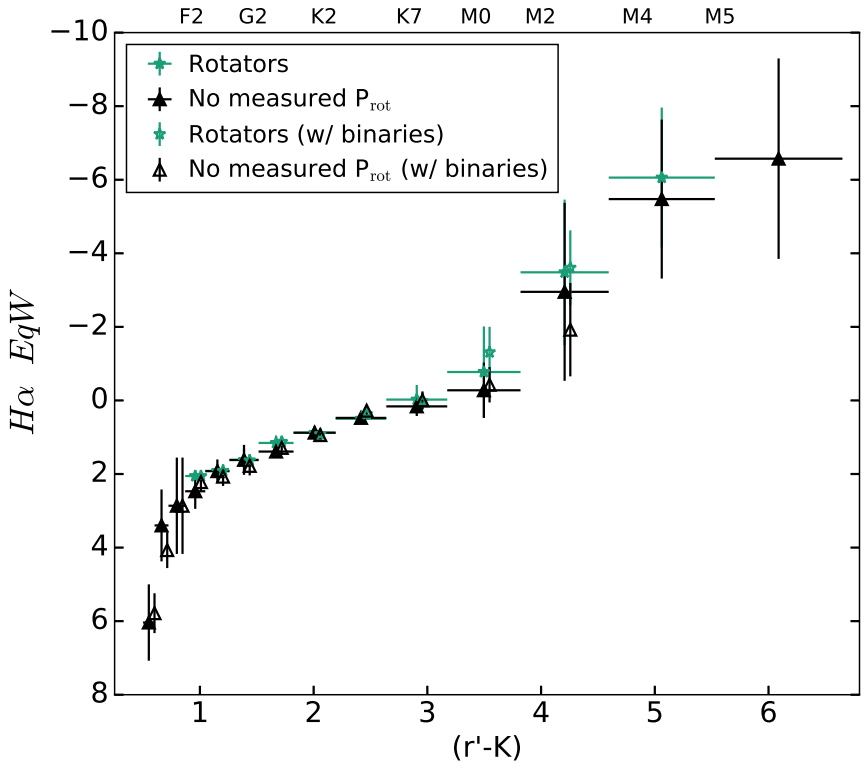

Figure 2.9 $H\alpha$ EqWs for stars with and without measured P_{rot}, using the same logarithmic color bins as in Figure 2.8. The data with potential binaries included (open symbols) have been offset slightly for clarity. KDE tests show that our sample of rotators is not biased toward more active stars: the distribution of $H\alpha$ EqWs is similar regardless of whether the stars have a measured P_{rot}.

distribution as the stars without detected P_{rot} using the procedure outlined in Cargile et al. (2014). To begin, we derive the probability distribution function (PDF) for both EqW-color distributions using the gaussian kernel density estimation (KDE) function from the SciPy package.[11] Instead of binning the data, KDE uses a kernel function to smooth over all the data points and produce a continuous distribution (see Silverman 1986, for details). We use an automatic bivariate bandwidth determination based on "Scott's rule" (Scott 1992) to choose the kernel width.

[11] **scipy.stats.gaussian_kde, `http://www.scipy.org/`**

Once we have the two PDFs, we multiply them together and integrate the product over the full parameter space. This gives a metric that describes the overall correlation between the distributions of stars with and without detected P_{rot}. If potential binaries are included in the test, $p_{0,all} = 0.0420$, but $p_{0,no\ bin} = 0.03798$ if potential binaries are removed.

To find the significance of this metric, we use Monte Carlo simulations. First, we randomly draw 10^5 subsamples of 194 stars without P_{rot} measurements (the same number as the rotators distribution) and compare this to the full distribution of stars without P_{rot}. This shows what metric results if the rotators are actually drawn from the same distribution as the stars without P_{rot} measurements. Then we randomly draw 10^5 subsamples of 194 stars from a flat distribution over the observed space and calculate the average probability metric again. This shows what metric results if the rotators come from a random distribution. The average probability metric in the first case is $p_{1,all} = 0.0365$, and in the second case it is $p_{2,all} = 0.0067$. If potential binaries are excluded, we find $p_{1,no\ bin} = 0.0336$ and $p_{2,no\ bin} = 0.0066$. Thus, we can determine that the rotator distribution is more likely to be drawn from the non-rotator distribution than from a random distribution in the same observed space.

This implies that our sample of rotators is not biased toward stars with stronger $H\alpha$ activity. We can therefore use our sample of rotators for which we have measured $H\alpha$ EqWs to characterize the relationship between activity and rotation for all 600 Myr stars, regardless of whether they exhibit periodic behavior at any given epoch.

2.4.3 The Relationship Between $H\alpha$ Emission and Rotation

We have assembled a large sample of stars from Praesepe and the Hyades to test the rotation-activity relation at 600 Myr. As Figure 2.7 shows, the only notable difference between the two clusters' period-mass distributions is that there are no known <0.26 $M_{\odot}$ rotators in the Hyades, and only two ≤0.3 $M_{\odot}$. By contrast, our lowest-mass Praesepe rotator has $M = 0.15\,M_{\odot}$, and we have spectra for 28 Praesepe stars with $0.15 \leq M \leq 0.3\,M_{\odot}$. We therefore are dependent mostly on Praesepe stars for any analysis of activity and rotation in fully convective stars at this age. However, since the distributions of activity versus color are consistent between the two clusters (Section 2.4.1), and our sample of rotators is not biased toward more active stars (Section 2.4.2), we can use the combined sample as a proxy for all 600 Myr stars. In Figure 2.10, we reproduce the mass-period diagram for both clusters and highlight $H\alpha$ active and fully convective ($M < 0.3\,M_{\odot}$) stars.

The top panel of Figure 2.11 shows $L_{H\alpha}/L_{bol}$ as a function of R_o for all observed rotators with $P_{mem} \geq 70\%$; it includes 2σ upper limits for stars whose $H\alpha$ EqW is consistent with absorption. Stars above $M > 0.3\,M_{\odot}$ appear to follow a saturation-type rotation-activity relation: for $R_o \lesssim 0.11$, the activity is approximately constant. This result is consistent with prior results that stars from mid-F to early-M SpTs exhibit a saturation-type relationship between rotation and chromospheric activity (Noyes et al. 1984; Delfosse et al. 1998; Jackson & Jeffries 2010).

At larger R_o, activity decreases with increasing P_{rot} and increasing R_o. However, our data hint that this may not be a smooth power-law decline: the slowly rotating stars with $R_o \gtrsim 0.45$ suggest a sharp decrease in chromospheric activity over a small range in R_o.

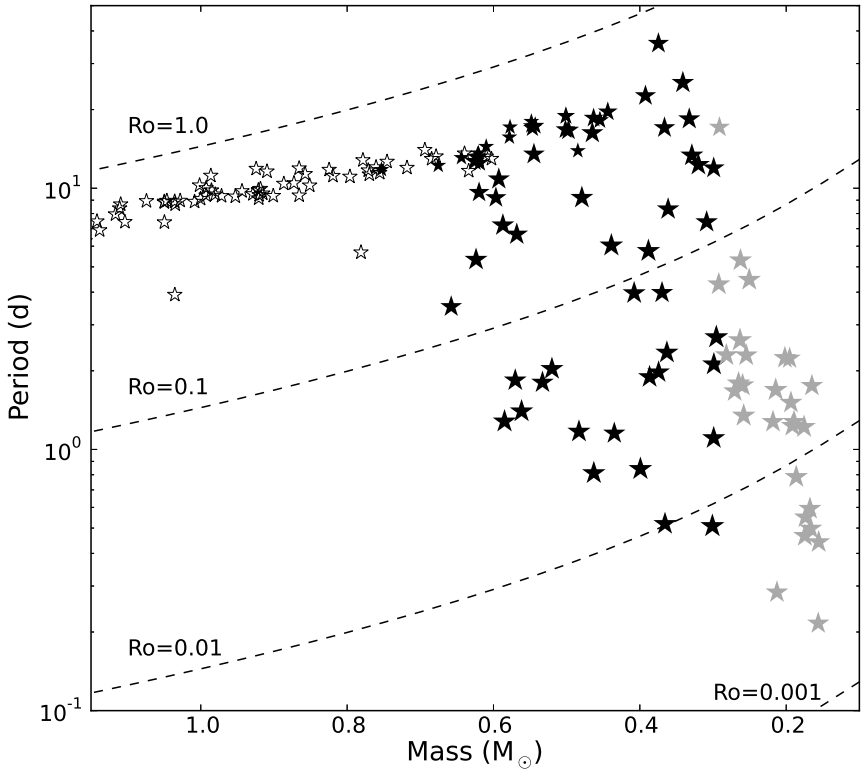

Figure 2.10 Mass-period diagram for Praesepe and Hyades stars with measured P_{rot} and $H\alpha$ EqW and $P_{mem} \geq 70\%$ (known and candidate binaries are not included). Fully convective stars ($\leq$0.3 $M_\odot$) are in gray. Solid symbols indicate stars with $H\alpha$ in emission; nearly all stars with $M \lesssim 0.6\ M_\odot$ are active. Lines of constant R_o are plotted for reference. Only one fully convective star has $R_o > 0.1$; given the uncertainties in the masses, it may well have $M > 0.3\ M_\odot$.

Because we can only give upper limits on $L_{H\alpha}/L_{bol}$ for most of these stars, our data do not allow us to confidently claim this change in behavior, and further activity measurements are required to investigate activity for slow rotators.

Nearly all the fully convective stars in our sample have $R_o \leq 0.07$ and saturated levels of $H\alpha$ activity. One has $R_o > 0.2$; it is the slowest rotator among the <0.3 $M_\odot$ stars in Figure 2.10. This outlier has $M = 0.291\ M_\odot$. However, given the uncertainties in the masses, it may well have $M > 0.3\ M_\odot$, and its rotation-activity behavior is consistent with

that of the higher-mass stars. Aside from this outlier, all the stars with $M \leq 0.3\ M_{\odot}$ are rotating fast enough to have saturated levels of activity.

We therefore parametrize the rotation-activity relationship for our stars as a flat region connected to a power-law. Below the turnover point ($R_{o,sat}$), activity is constant and equal to $(L_{H\alpha}/L_{bol})_{sat}$. Above $R_{o,sat}$, activity declines as a power-law with index β. Functionally, this corresponds to

$$\frac{L_{H\alpha}}{L_{bol}} = \begin{cases} \left(\frac{L_{H\alpha}}{L_{bol}}\right)_{sat}, & \text{if } R_o \leq R_{o,sat} \\ C{R_o}^{\beta}, & \text{if } R_o > R_{o,sat} \end{cases} \tag{2.1}$$

where C is a constant. This model has been widely used in the literature (e.g., Randich 2000; Wright et al. 2011).

We use the open-source Markov-chain Monte Carlo (MCMC) package *emcee* (Foreman-Mackey et al. 2013) to fit the three-parameter model described above to our data. The fit derives posterior probability distributions over each parameter. The posterior distributions are shown in Figure 2.12. Figure 2.11 includes 200 random models drawn from these distributions; each grey line represents a model that fits the datapoints, though it may not be the most probable model. Figure 2.11 also shows the maximum *a posteriori* model, which is the most probable model.

The parameters corresponding to the maximum *a posteriori* model are $(L_{H\alpha}/L_{bol})_{sat} = (1.26 \pm 0.04) \times 10^{-4}$, $R_{o,sat} = 0.11^{+0.02}_{-0.03}$, and $\beta = -0.73^{+0.16}_{-0.12}$, where the stated values correspond to the 50$^{\text{th}}$ quantile of the results and the uncertainties correspond to the 16$^{\text{th}}$ and 84$^{\text{th}}$ quantiles, respectively. We selected these quantiles to be consistent with 1σ Gaussian uncertainties, even though our 1D posterior probability distributions are not Gaussian.

We also note that $R_{o,sat}$ and β are highly anti-correlated: a lower $R_{o,sat}$ results in a shallower β, and vice versa. We find a turnover point $R_{o,sat}$ consistent with that found in the literature (e.g., Wright et al. 2011), but the β we derive is inconsistent with literature values (e.g., Jackson & Jeffries 2010) by $2-11\sigma$.

2.4.4 Chromospheric and Coronal Activity-Rotation Relations at 600 Myr

A number of authors have also derived power-laws to describe the unsaturated rotation-activity regime for other activity indices. Jackson & Jeffries (2010) observed a saturation-type relationship between chromospheric emission (measured using CaII) and rotation in early M dwarfs in the younger, ≈150 Myr-old cluster NGC 2516. Their figure 9 shows saturated activity below $R_{o,sat} \approx 0.1$; above that, activity decreases as a power-law with $\beta \approx -1$. In her summary of *ROSAT* results for open clusters and field stars, Randich (2000) found that the data for $R_o \gtrsim 0.16$ were best fit by a $\beta = -2.1 \pm 0.09$ power-law. More recently, Wright et al. (2011) found that, for $R_o > 0.13$, the decline in coronal activity followed a slightly steeper $\beta = -2.18 \pm 0.16$ power-law; furthermore, these authors calculated $\beta = -2.70 \pm 0.13$ for a set of solar-type stars.

Our $H\alpha$ data are best fit by a power-law that is clearly shallower than and inconsistent with the three power-laws described above, as shown in the top panel of Figure 2.11. The Jackson & Jeffries (2010) value of $\beta = -1$, which also describes chromospheric activity for young, low-mass stars, comes closest to describing our data. Our data, however, are inconsistent with this value at the 2σ level, and are better fit by an even shallower

power-law.

The bottom panel of Figure 2.11 shows L_X/L_{bol}, calculated using the X-ray data for Praesepe and Hyades stars published by Wright et al. (2011), as a function of R_o. The shallower power-laws we find best describe our $L_{H\alpha}/L_{bol}$ data are not consistent with the behavior of L_X/L_{bol} for most X-ray-emitting stars in these clusters, which appear to follow a steeper power-law relation: our $L_{H\alpha}/L_{bol}$ data are inconsistent with the Randich et al. (2000) and Wright et al. (2011) relationships for unsaturated stars at the 7-11σ level.

This is not entirely surprising: Preibisch & Feigelson (2005) and Stelzer et al. (2013) found that X-ray emission declines more rapidly than chromospheric activity indicators with age, both for solar-type stars and M dwarfs. In our sample, one possible explanation for the difference in the unsaturated behavior of $L_{H\alpha}/L_{bol}$ and L_X/L_{bol} for stars is that the subsets with $H\alpha$ and X-ray detections have different mass distributions. The unsaturated $H\alpha$-emitters in the top panel of Figure 2.11 range from $\approx$0.4$-$0.7 $M_\odot$, while the unsaturated X-ray-emitting stars in the bottom panel are mostly $\approx$1 $M_\odot$.

The few X-ray-emitting stars in the bottom panel of Figure 2.11 that have $M < 0.7\,M_\odot$ and $R_o > R_{o,sat}$ also suggest a mass-dependent rotation-activity relationship; these stars lie closer to the shallow power-laws derived for chromospheric emission from low-mass stars. Although using R_o should provide a mass-independent way to examine rotation and activity (Pizzolato et al. 2003; Wright et al. 2011), it may not remove this dependence entirely: unsaturated emission may decline with increasing R_o at different rates for stars of different masses.

As noted by Covey et al. (2008), a separate problem with these comparisons is that

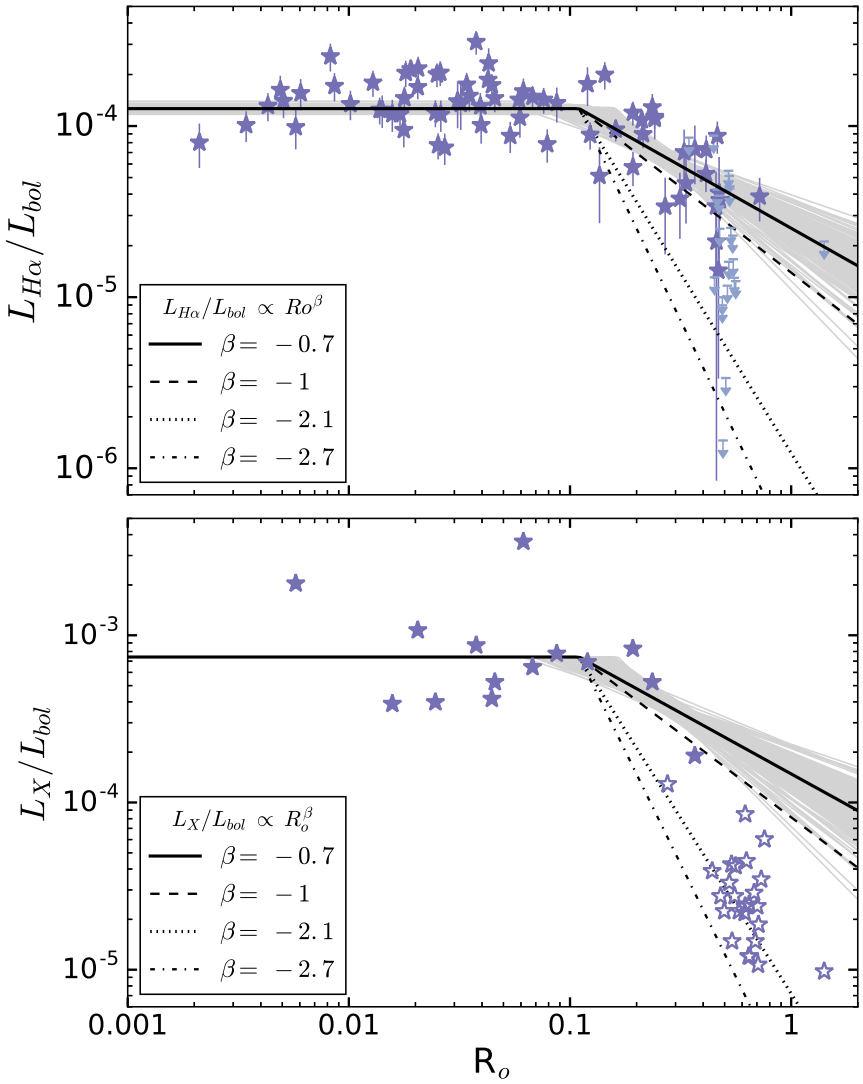

Figure 2.11 *Top* — $L_{H\alpha}/L_{bol}$ vs. R_o for Praesepe and Hyades stars with various power-laws for the unsaturated regime overlaid (for $R_o \gtrsim 0.11$). The results from the fit discussed in the text are also shown: the gray region shows 200 models drawn randomly from the posterior probability distribution, and the solid black line is the maximum *a posteriori* model. Upper limits are shown but not included in the fit. The broken black lines show power-laws from the literature. *Bottom* — L_X/L_{bol} vs. R_o for Praesepe and Hyades stars (data from Wright et al. 2011). Empty symbols indicate stars >0.68 $M_\odot$, the highest mass at which $H\alpha$ emission is detected. The $H\alpha$ data are consistent with a shallow decline of activity with rotation ($\propto R_o^{-1}$), while X-ray activity appears to decline in a manner more consistent with the steeper Randich (2000) or Wright et al. (2011) power-laws ($\propto R_o^{-2.1}$ and $R_o^{-2.7}$, respectively).

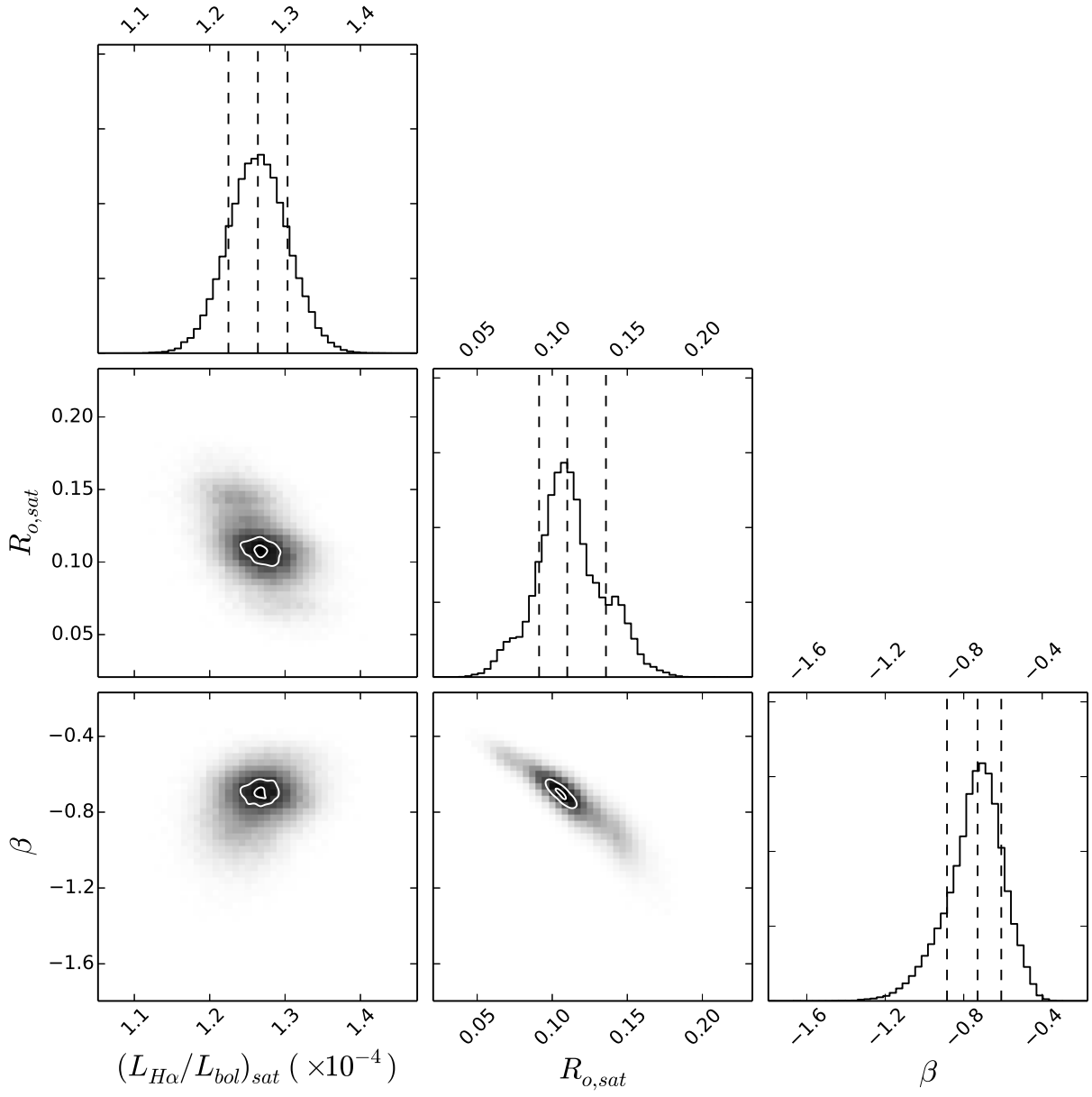

Figure 2.12 The marginalized posterior probability distributions from the MCMC analysis using *emcee*. The peaks of the 1D distributions correspond to the maximum *a posteriori* model, and the 2D distributions illustrate covariances between parameters. The vertical lines on the 1D histograms indicate the median and 68-percentile values; the contours on the 2D histograms indicate the 99.5- and 68-percentile of the distributions.

these are non-simultaneous $H\alpha$ and X-ray measurements. The Wright et al. (2011) sample may be preferentially selecting stars in an X-ray flare state, while the $H\alpha$ measurements may have been taken when the star has returned to a quiescent state. While our data hint at underlying mass- and age-related differences in the evolution of chromospheric and coronal emission, our sample is small. A larger sample of X-ray measurements in Praesepe and the Hyades, ideally made simultaneously with $H\alpha$ measurements, is required to draw firmer conclusions.

2.5 Conclusion

1. We have collected 720 spectra of 516 high-confidence Praesepe members, and 139 spectra of 130 high-confidence Hyads; more than half of the Praesepe spectra and all of the Hyades spectra are new observations. We have measured $H\alpha$ EqWs for all of these spectra, estimating the EqW uncertainties by accounting for both human measurement error and for photon noise.

2. To convert these $H\alpha$ EqWs into mass-independent $L_{H\alpha}/L_{bol}$ values, we have computed our own χ factors. $\chi = f_0/f_{bol}$, where f_0 is the continuum flux level for the $H\alpha$ line and f_{bol} is the apparent bolometric flux. Our values differ from those presented in Walkowicz et al. (2004) and West & Hawley (2008); see Appendix A for details.

3. We have found that Praesepe and the Hyades follow a nearly identical color-activity relation, implying that they have very similar ages. This contradicts the results of Kafka & Honeycutt (2006), who found that activity in the Hyades began at bluer

colors than in Praesepe, and that Hyads became completely active at a bluer color than stars in Praesepe. Because Kafka & Honeycutt (2006) combined their $H\alpha$ measurements in Praesepe with literature EqWs for both clusters, it is possible that the disagreement is due to inconsistencies in the methods used to measure EqWs. Our results are consistent with the finding of Pace & Pasquini (2004) that solar-type stars in the two clusters have similar levels of chromospheric activity, as measured by CaII K emission.

4. We gathered P_{rot} for 135 Praesepe members and 87 Hyads from PTF observations and from the literature. Taking the two clusters as a single-aged sample, we constructed a combined mass-period distribution for stars at 600 Myr. We examined the $H\alpha$ EqWs of known rotators and of stars without a measured P_{rot} in our sample, finding that the known rotators are not more active, on average, than the stars without measured periods. We can therefore use our sample of rotators for which we have measured $H\alpha$ EqWs to characterize the relationship between activity and rotation for all 600 Myr stars.

5. We have demonstrated the presence of a $R_o \approx 0.11$ chromospheric activity threshold for low-mass stars at 600 Myr. Stars rotating below this threshold show saturated levels of activity, and stars with slower rotation speeds show declining activity levels.

6. We have presented preliminary evidence that chromospheric activity (as measured by $H\alpha$) and coronal activity (measured by X-ray emission) decline differently as a function of R_o.

Jackson & Jeffries (2010) found that, at 150 Myr, fully convective M dwarfs showed CaII emission at levels roughly independent of rotation. These observations of saturated, fully convective M dwarfs at 150 Myr, and now at 600 Myr, differ somewhat from what is seen in the field. Some field M dwarfs with $M \lesssim 0.3\ M_{\odot}$ have longer P_{rot} and follow an unsaturated rotation-activity relationship for $R_o \gtrsim 0.1$ (Mohanty & Basri 2003; Wright et al. 2011). Low-mass members of Praesepe and the Hyades are young enough to rotate faster than the saturation velocity for fully convective M dwarfs. As they age, these stars should begin to spin down into the unsaturated regime observed for field stars. Similar studies of older clusters are essential to map out fully the evolution of the chromospheric activity-rotation relation for these low-mass stars.

However, while a dozen open clusters with ages $\lesssim$600 Myr have been extensively surveyed both for tracers of magnetic activity and for rotation, few clusters older than the Hyades and Praesepe and younger than field stars, whose ages are imprecisely known but range from 2-10 Gyr, have been studied in the same detail. Recent work on NGC 752 (Bowsher et al., in prep) and on the three open clusters in the *Kepler* field of view (including NGC 6811; Meibom et al. 2011a) will add to our knowledge of stellar properties at $\gtrsim$1 Gyr. For now, the clusters at ≈600 Myr anchor the transition from young open clusters to more rare evolved clusters and field stars. The results of our examination of activity and rotation in the Hyades and Praesepe are therefore an essential data point in the study of the evolution of these properties.

Chapter 3

K2 Rotation Periods for low-mass Hyads and the Implications for Gyrochronology

3.1 Introduction

As the nearest open cluster to the Sun (≈47 pc; van Leeuwen 2009), the Hyades is a benchmark for understanding stellar properties. Many brighter Hyads were targeted by *Hipparcos* (Perryman et al. 1997, 1998), allowing for precise astrometric and absolute photometric calibration. The cluster has also been surveyed for binary stars (e.g., Griffin et al. 1988; Patience et al. 1998; Reid & Mahoney 2000; Duchêne et al. 2013) and for planets (e.g., Cochran et al. 2002; Paulson et al. 2004; Quinn et al. 2014). Hyads have been used to test stellar models (e.g., Castellani et al. 2001) and to calibrate gyrochronology and

[0]This chapter is a reproduction of a paper that has been published by The Astrophysical Journal. It can be found at `http://iopscience.iop.org/article/10.3847/0004-637X/822/1/47`. The article has been reformatted for this section.

metallicity scales (e.g., Skumanich 1972; Barnes 2003; Paulson et al. 2003; Delorme et al. 2011).

The Hyades's age also contributes to its benchmark status: at 625±50 Myr (Perryman et al. 1998), it is the oldest nearby open cluster.[1] The cluster's canonical age, however, has been called into question by Brandt & Huang (2015a,b), who fit rotating stellar models to main-sequence turnoff Hyads and find that the cluster is 750±100 Myr.[2] If the Hyades is older than previously thought, then the stellar evolution scales that it anchors, including gyrochronology, will need to be re-calibrated.

The Hyades's proximity aids observations of individual members, but presents challenges for studying the population as a whole. The ≈750 cluster members are scattered widely across the sky, covering $\gtrsim$3600 deg^2. Ground-based observations designed to measure rotation periods (P_{rot}) typically have small fields-of-view ($\lesssim$1 deg^2), which would prevent them from obtaining light curves for more than one or two Hyads at a time. Previous campaigns to measure P_{rot} in the Hyades have therefore been limited to observations of individual targets (Radick et al. 1987, 1995; Prosser et al. 1995) or to shallower large-area surveys designed to discover transiting exoplanets or other transients (e.g., SuperWASP and HATNet; Delorme et al. 2011; Hartman et al. 2011). These surveys have generally focused on solar-type stars ($0.7 - 1.2\ M_\odot$), with almost no sensitivity to fully convective stars ($\lesssim 0.3\ M_\odot$).

After the second of its four reaction wheels failed, the *Kepler* spacecraft could no

[1]The next nearest, older cluster is the ≈3-Gyr-old Ruprecht 147. At $D \approx 300$ pc and in the direction of the Galactic Bulge, it is far harder to study (Curtis et al. 2013).

[2]However, Brandt & Huang (2015a,b) mention several potential sources of ≈100 Myr systematic uncertainties, and these are not included in their final quoted uncertainties.

longer maintain pointing toward its original field. However, by observing in the ecliptic, stable pointing can be maintained using the two functioning reaction wheels to balance the torque on the spacecraft due to sunlight. The *K2* mission (Howell et al. 2014) stares at fields of view along the ecliptic, observing each for approximately 80 days. The Hyades was targeted in *K2*'s Campaign 4, and the spacecraft's ≈100 deg^2 field-of-view provided an unprecedented opportunity to measure P_{rot} for a large number of Hyads. Light curves were obtained simultaneously for 65 Hyads, and *Kepler*'s sensitivity enabled the first assembly of light curves for fully convective Hyads.

We present the results of our analysis of these *K2* data, including the first measurements of P_{rot} for fully convective Hyads.[3] We describe the existing data used in our study, including membership catalogs, photometry, archival P_{rot}, and studies of multiplicity, in Section 3.2. We present our mass measurements in Section 3.3 and our *K2* data analysis in Section 3.4. Our results are in Section 3.5, and we discuss their potential implications for gyrochronology in Section 3.6. We conclude in Section 3.7.

3.2 Archival Data

3.2.1 Membership

We draw Hyades members primarily from the Goldman et al. (2013) catalog, which is an updated version of the Röser et al. (2011) catalog used in Chapter 2. Goldman et al. (2013) and Röser et al. (2011) identified candidate Hyads via the convergent point method and

[3]Hartman et al. (2011) assign a Prosser et al. (1995) rotator $M_* \approx 0.22\ M_\odot$, but we find $M_* = 0.36\ M_\odot$, and the star is a known visual binary (WDS J04288+1617B; Mason et al. 2001).

confirmed their membership using photometry: Röser et al. (2011) combined *JHK* data from the Two Micron All-Sky Survey (2MASS; Skrutskie et al. 2006) with *r'* photometry from the Carlsberg Meridian Catalogue 14 (CMC14; Copenhagen University et al. 2006).

Goldman et al. (2013) added *ugriz* photometry from the Sloan Digital Sky Survey (SDSS) Data Release 8 (Aihara et al. 2011), $g_{P1}r_{P1}i_{P1}z_{P1}y_{P1}$ photometry from Pan-STARRS 1 (Kaiser et al. 2002; Tonry et al. 2012), and data from all four bands from the Wide-field Infrared Survey Explorer (WISE; Wright et al. 2010). The Pan-STARRS 1 and WISE data allow these authors to extend the cluster's membership to the stellar/sub-stellar boundary. Goldman et al. (2013) also reject 13 stars that were identified as Hyads by Röser et al. (2011) and add 62 low-mass stars and brown dwarfs. The final Goldman et al. (2013) catalog contains 773 members.

Röser et al. (2011) estimate contamination to their catalog based on distance from the cluster center (d_c): it is 1% for stars with $d_c \leq 9$ pc, 7.5% for $9 < d_c \leq 18$ pc, and 30% for $18 < d_c \leq 30$ pc. In Chapter 2, we converted these percentages to membership probabilities, P_{mem}, by subtracting the contamination percentage from 100%.

Goldman et al. (2013) simulate field star contamination as a function of d_c and absolute K magnitudes (M_K) but do not give their full results, stating only that the contamination is <10% for $d_c \leq 18$ pc, ≤17% for stars with $18 < d_c \leq 30$ pc and $7.5 < M_K < 9.5$ mag, and ≤30% for $d_c \leq 30$ pc and $M_K = 9$. These contamination rates appear consistent with those from Röser et al. (2011). Therefore, we also calculate distance-based P_{mem} for the new Goldman et al. (2013) members using the method described in Section 2.2.1.

We supplement the Goldman et al. (2013) catalog with new Hyades members found

by our analysis of All Sky Automated Survey (ASAS; Pojmański 2002) data (Cargile et al., in prep.). We follow the method outlined by van Leeuwen (2009) and consider stars within 26° and 20 pc of the cluster center. We identify 170 cluster members with reduced proper motions (μ) satisfying $-170 < \mu_{\parallel} < -60$ and $-20 < \mu_{\perp} < 20$ mas yr^{-1} and distances distances obtained by *Hipparcos* (Perryman et al. 1997). We add stars from the Radick et al. (1987) and Delorme et al. (2011) catalogs that were too bright or too faint to be included in the *Hipparcos* survey, so that this catalog includes 209 stars, all of which are listed in Table 6 of Chapter 2. All but 13 of the Hyads identified in this manner were also identified by Röser et al. (2011) and Goldman et al. (2013). We add these 13 stars to our final Hyades catalog, resulting in a membership catalog of 786 stars with $P_{mem} \geq 70\%$.

3.2.2 Photometry

As in Chapter 2, we use $(r' - K)$ as our primary proxy for stellar temperature. Optical-near infrared (NIR) colors allow a broader dynamic range than is possible with a narrower color index, particularly for lower-mass stars. For example, when using NIR photometry alone, M dwarfs only show colors $0.9 \lesssim (J - K) \lesssim 1.2$ mag, but stars in this same mass range are spread across $3.3 < (r' - K) < 8.0$. While nearly all the stars in our catalog have 2MASS K-band magnitudes, the large range in r' magnitudes ($\approx$15 mag) for these objects meant that we had to obtain this photometry from multiple sources.

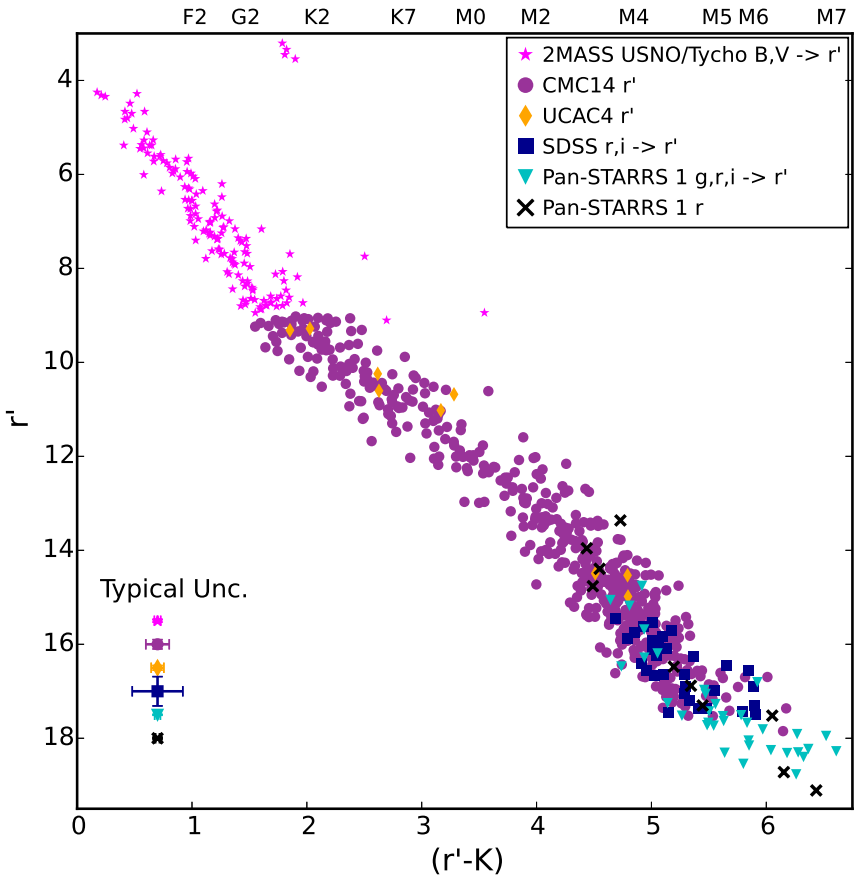

Figure 3.1 CMD for the Hyads in our final catalog. The symbols represent different sources of photometry, and whether conversions were necessary to obtain the r' magnitudes. We could not convert r_{P1} into r' for a subset of the Goldman et al. (2013) stars (see Section 3.2.2), so we retain the r_{P1} magnitudes and mark these stars with crosses. The typical uncertainty (propagated from the source photometry) is shown in the lower left.

CMC14 includes r' measurements for $\approx 10^8$ stars with declinations between $-30°$ and $50°$ and $9 < r' \lesssim 17$ mag. We use this photometry for 522 Hyads falling within this magnitude range; for the members identified by Röser et al. (2011), we use the CMC14 magnitudes and errors listed in that catalog. For 17 Hyads with $10 \lesssim r' \lesssim 14$ mag that do not appear in CMC14, we use r' magnitudes from the 4$^{\text{th}}$ U.S. Naval Observatory CCD Astrograph Catalog (UCAC4; Zacharias et al. 2012), which includes $g'r'i'$ magnitudes from

APASS (Henden et al. 2012). In total, 539 Hyads have r' data from CMC14 or UCAC4.

The remaining Hyads are too bright or too faint to appear in CMC14 or UCAC4. We convert photometry from other systems into r' magnitudes for these stars.

• Thirty-three new Goldman et al. (2013) members have SDSS *ri* photometry. We convert those magnitudes to r' using transformation equations from Jester et al. (2005) and documented online.[4]

• For 44 new Goldman et al. (2013) members with photometry in all three Pan-STARRS 1 $g_{P1}r_{P1}i_{P1}$ bands, we use appropriate equations from Tonry et al. (2012) and Jester et al. (2005) to convert these magnitudes to SDSS r and i magnitudes, and from there to r'.

• Eighteen new members identified by Goldman et al. (2013) were detected in only one or two Pan-STARRS 1 bands, and lack the photometry needed for a conversion to r'. The seven stars with detections only in g_{P1} or i_{P1} do not have previous P_{rot} measurements, nor are they *K2* targets, so the lack of r' photometry does not impact our analysis. Eleven stars were only detected in r_{P1}; this includes one *K2* target, EPIC 210489654. We retain the unconverted r_{P1} magnitude for these stars.

• For 152 bright stars with $r < 9$ mag, we use the Jester et al. (2005) relations to convert the USNO-A2.0 and Tycho 2 Johnson B and V magnitudes included in the 2MASS catalog to SDSS r magnitudes. Fortuitously, these stars fall into the appropriate color range for which the Bilir et al. (2008) transformation from 2MASS colors to $(r-i)$ can be used. Finally, we use these r and $(r-i)$ values to obtain r' by applying the Jester et al. (2005) relation, as above.

[4] `http://www.sdss.org/dr7/algorithms/jeg\_photometric\_eq\_dr1.html`

The typical uncertainty for these r' magnitudes depends on the source catalog. After applying the conversions discussed above to 2MASS and SDSS photometry, the uncertainties are generally $\lesssim$0.1 and $\approx$0.3 mag, respectively. For CMC14 photometry, the uncertainty is $\approx$0.1 mag; for UCAC4, $\approx$0.05 mag. The sources for all of our photometry are shown in the color-magnitude diagram (CMD) for the cluster presented in Figure 3.1.

3.2.3 Archival Rotation Periods

In Chapter 2 we assembled P_{rot} measurements for Hyads from Radick et al. (1987, 1995); Delorme et al. (2011); and from an analysis of ASAS data (Cargile et al., in prep) into a catalog of 87 rotators. We now restore eight additional stars with measured P_{rot} that are confirmed binaries, bringing the total number of known rotators from these studies to 95.

We then add P_{rot} measured by Hartman et al. (2011) for stars in our catalog of likely members. These authors used light curves from the HATNet survey to search for photometric variability among nearby field K and M dwarfs. Hartman et al. (2011) present P_{rot} measured at two different stages in their analysis: after applying external parameter decorrelation and then after applying a trend filtering algorithm. We required that the quality flags on both periods be 0 and that the periods Hartman et al. (2011) measured at both stages agree to within one day. Although nine Hartman et al. (2011) targets match objects in our Hyades catalog, two had bad quality flags, and another showed different periods after the two different filtering algorithms were applied; we add the six remaining P_{rot} to our catalog

Table 3.1. Hyads with multiple P_{rot} measurements

Roser No.	Object Name	Prosser et al. (1995) P_{rot} (d)	Delorme et al. (2011) P_{rot} (d)	ASAS-derived P_{rot} (d)[a]	*K2*-derived P_{rot} (d)
68[b]	HIP 16908	···	10.57	11.17	···
78	EPIC 210865372	···	12.30	···	12.32
85[b]	EPIC 211058178	···	···	8.37	12.57
125[b]	EPIC 210772796	···	11.45	···	11.60
133	EPIC 210771915	···	13.51	7.19[c]	13.85
140[d]	HIP 19207	···	11.98	14.03	···
144[b]	HIP 19263	···	12.30	11.60	···
148	EPIC 211049709	···	9.35	···	9.39
202	EPIC 210744818	···	12.95	···	12.84
203	EPIC 210470484	···	2.35	···	2.38
267[b]	EPIC 210786154	···	9.90	9.96	10.02
288	EPIC 210674406	···	11.60	11.87	11.47
303[b]	EPIC 210741091	···	10.84	···	10.97
339[b]	2M J0427+1415	···	12.78	12.81	···
345[b]	HIP 20827	···	9.70	10.28	···
355[b]	EPIC 210651981	2.42	2.42	···	2.44
428	HIP 21256	···	12.69	13.59	···
438[b]	2M J0434+1133	···	11.03	11.59	···
486	HIP 21723	···	10.85	11.30	···
514[b]	2M J0443+1704	···	10.31	10.18	···
558[b]	HIP 22350	···	9.69	9.92	···

Table 3.1—Continued

Roser No.	Object Name	Prosser et al. (1995) P_{rot} (d)	Delorme et al. (2011) P_{rot} (d)	ASAS-derived P_{rot} (d)[a]	*K2*-derived P_{rot} (d)
564[b]	HIP 22394	···	6.90	7.07	···

Note. — EPIC 210359769 and EPIC 210675409 also have P_{rot} measurements from Delorme et al. (2011) and were targeted by *K2*, but we were unable to measure a new P_{rot} for either (see Table 3.4). There was no overlap between the listed samples and those from Radick et al. (1987, 1995) and Hartman et al. (2011)

[a]Cargile et al. (in prep)

[b]Confirmed binary

[c]Half-period harmonic

[d]Planet host; $P_{orb} \approx 6.09$ d (Quinn et al. 2014). In Chapter 2 we chose to use the ASAS-derived P_{rot} value for this star, and for consistency we use that value here as well.

Finally, we add two rotation periods from Prosser et al. (1995). These authors observed stars from several open clusters and searched for periodic variability. They targeted three Hyads, and found two to be variable.

In total, we have 102 Hyads with P_{rot} measurements from the literature. However, 48 are confirmed binaries, and eight more are candidate binaries (see discussion below). This leaves 44 single[5] Hyads with measured P_{rot} before the addition of the *K2* data. The mass-period relationship for these 102 Hyads is shown in Figure 3.2.

3.2.4 Companions

Close companions impact the rotational evolution of stars, potentially biasing our analysis. Additional flux from a companion star could also contaminate our mass calculations.

[5]Because not all of these have been surveyed for binarity, this is an upper limit on the true number of single stars in this sample.

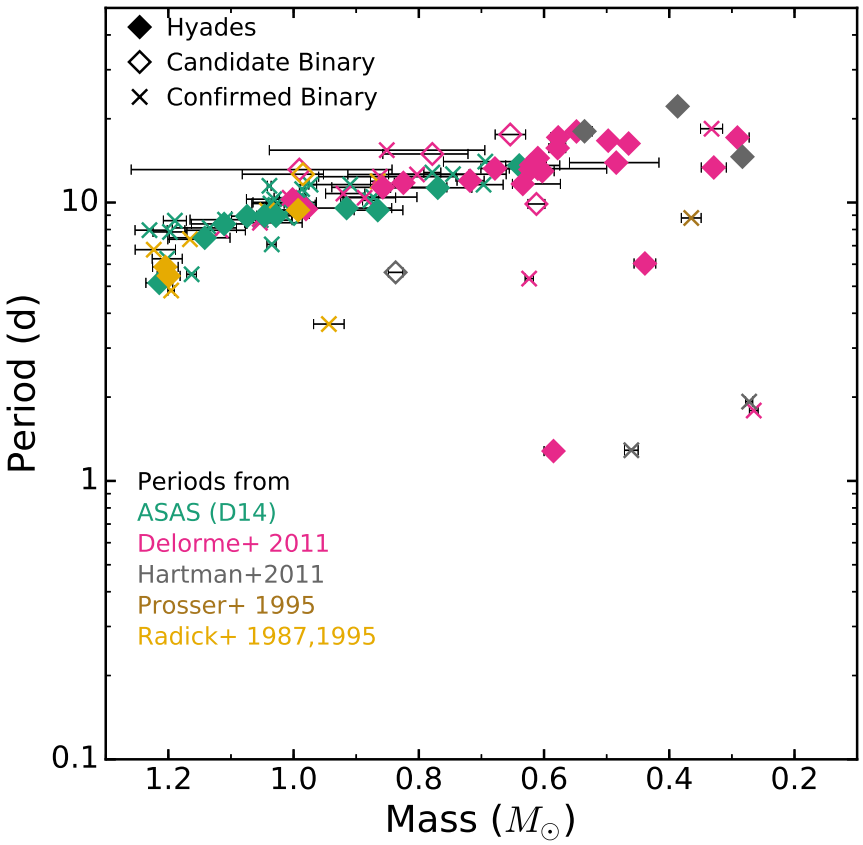

Figure 3.2 Mass-period distribution for Hyads with period measurements in the literature. The color indicates the source of the P_{rot}; empty diamonds and crosses denote photometrically identified candidate binaries and confirmed binaries, respectively. We also include the mass uncertainties; in general, $\sigma_{M*} \approx 2-3\%$, which is smaller than or comparable to the symbol size. Distance uncertainties dominate the M_* uncertainties; the stars with large σ_{M_*} have $\sigma_D \approx 10-20$ pc. The error bars only represent systematic uncertainties from our mass calculation, and do not reflect, e.g., systematics in the model or excess K-band flux due to an unresolved companion.

Therefore, we try to identify all confirmed or candidate binaries and remove these from our gyrochronology analysis.

In Chapter 2, we used SIMBAD and Delorme et al. (2011) to identify nine binaries in the Hyades. We now carry out a more thorough search of the literature for binaries among known Hyades rotators and *K2* targets.

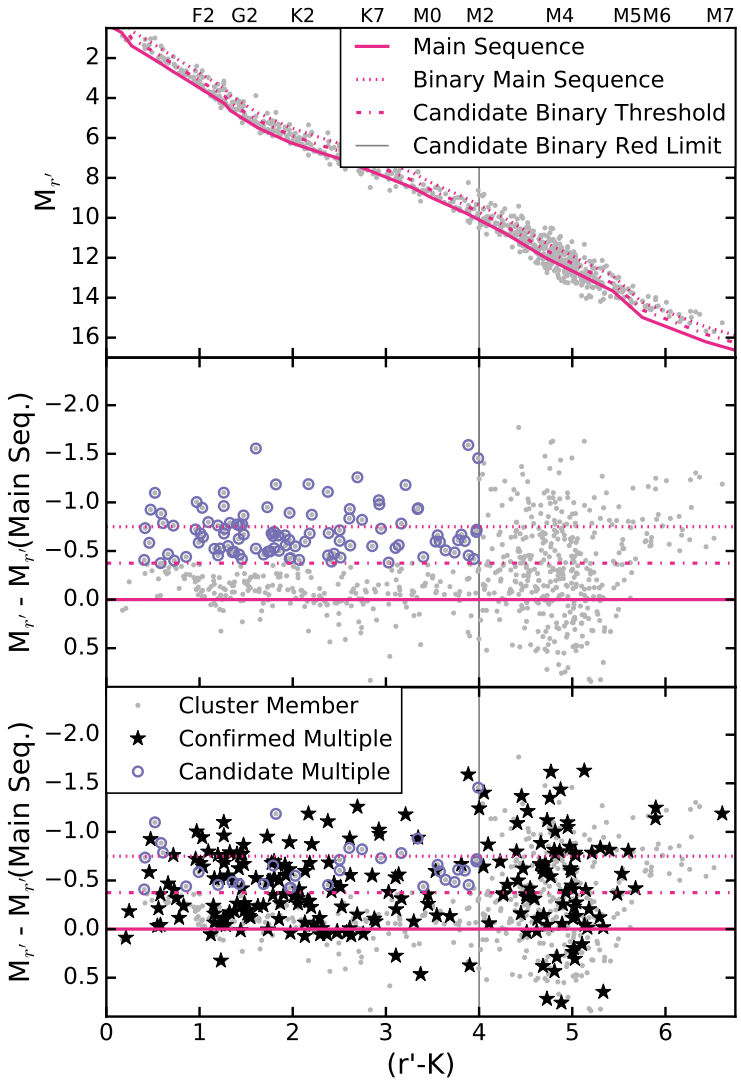

Figure 3.3 *Top* — CMD of the Hyades. The solid line traces out the main sequence, identified using the SEDs assembled by Kraus & Hillenbrand (2007), and the dotted line the binary main sequence. We label any star lying above the dot-dashed line halfway between these two sequences as a candidate binary (as in Hodgkin et al. 1999). Stars with $(r' - K) \gtrsim 4$ have a wider range of magnitudes at a given color, and do not show an easily identified main sequence, so we do not search for photometric binaries in this color range. *Middle* — Residuals between each star's $M_{r'}$ and the model main-sequence magnitude. Photometrically identified candidate binaries are shown as purple circles. This method is primarily sensitive to ≈equal-mass binaries. *Bottom* — Same as above, with confirmed binaries from the literature shown as black stars (identifications are only complete for stars with measured P_{rot}). Confirmed binaries can be found at all distances from the main sequence, illustrating the limitations of this approach to binary identification.

Table 3.2. Confirmed and candidate binary and planetary systems among the *K2* targets and Hyads with measured P_{rot}

Roser	HIP	2MASS J	EPIC	Cand?[a]	P_{orb} (d)	Source[b]
			Binaries			
207	···	04174767+1339422	210408563	N	···	Guenther et al. (2005)
214	···	04181077+2317048	211019716	Y	1.88	Griffin et al. (1982); Pourbaix et al. (2004); Kopytova et al. (2016)
216	···	04181926+1605181	···	Y	···	···
267	20482	04232283+1939312	210786154	Y	···	Morzinski (2011)
270	20485	04232526+1545474	···	Y	···	Morzinski (2011)
275	···	04235070+0912193	···	N	5.26	Griffin (2012)
284	20553	04241244+1445295	···	Y	···	Patience et al. (1998); Kopytova et al. (2016)
293	20577	04242831+1653103	···	Y	···	Patience et al. (1998); Kopytova et al. (2016)
303	···	04251456+1858250	210741091	N	···	Morzinski (2011)
			Planets			
140	19207	04070122+1520062	···	N	6.09	Quinn et al. (2014)
169	···	04130560+1514520	210490365	N	3.48	Mann et al. (2016); David et al. (2016)

[a]Photometric candidate binary identified in Section 3.2.4.

[b]If no source is given, we have identified the star as a photometric candidate binary, but its multiplicity is not confirmed.

Note. — This table is available in its entirety in a machine-readable form in the online journal at `http://iopscience.iop.org/0004-637X/822/1/47/suppdata/apj523231t2_mrt.txt`. A portion is shown here for guidance regarding its form and content.

We begin with the catalog compiled by Kopytova et al. (2016). These authors combined the results of several multiplicity surveys (Patience et al. 1998; Mason et al. 2001; Mermilliod et al. 2009; Morzinski 2011; Duchêne et al. 2013), to which they added their own AstraLux lucky imaging observations and visual companions identified in archival Hubble Space Telescope (HST) images. Of 724 Röser et al. (2011) Hyads, Kopytova et al. (2016) identify 213 as binary or multiple systems.

We add confirmed binaries from Barrado y Navascues & Stauffer (1996), Tokovinin (1997), Reid & Gizis (1997), Paulson et al. (2004), Pourbaix et al. (2004), Guenther et al. (2005), Delorme et al. (2011), Griffin (2012), and Janson et al. (2014). Other known rotators and/or *K2* targets were included in previous surveys, but these did not resolve any companions (Gizis & Reid 1995; Patience et al. 1998; Reid & Mahoney 2000; Mason et al. 2001; Richichi & Percheron 2002; Paulson et al. 2004; Duchêne et al. 2013). There are also two confirmed planets in the Hyades; both have short orbital periods (Quinn et al. 2014; Mann et al. 2016). In total, we find two planet hosts and 70 confirmed multiple systems among the known rotators and *K2* targets.

As in Chapter 2, we also identify candidate unresolved binaries that are overluminous for their color (see Figure 3.3). We use model stellar SEDs assembled by Kraus & Hillenbrand (2007) to identify the single-star main sequence, then identify a binary main sequence offset by 0.75 mag for a given color from that of single stars (as in Steele & Jameson 1995). We then label stars with $(r' - K) < 4$ as candidate binaries if they lie above the midpoint between the single-star and binary main sequences (Hodgkin et al. 1999). This method is biased toward binaries with equal masses, so that we are certainly missing candidate binaries with lower mass ratios. Indeed, the bottom panel of Figure 3.3 shows confirmed binaries at all distances from the main sequence. While further observations are required to confirm the binary status of all cluster members, this photometric approach does allow the identification of a significant number of binaries.

We only apply this method to stars with $(r' - K) < 4$ because the single-star main sequence is less apparent for stars redder than this value. The observed spread in mag-

nitudes could be due to binary systems at a variety of mass ratios, or to uncertainties in distance or magnitude for these faint red stars. Identifying even candidate binaries in this regime therefore requires more information than just photometry.

In total, after our analysis of the *K2* data (Section 3.4), we find that 63 Hyads with measured periods are confirmed binaries, two are confirmed planet hosts, and eight are candidate binaries. Another six *K2* targets for which we could not measure P_{rot} are confirmed binaries, and one is a candidate. We list all confirmed and candidate binaries in Table 3.2, and exclude them from our gyrochronology analysis in Section 3.6.

3.3 Stellar masses

As in Chapter 2, we estimate stellar masses (M_*) by linearly interpolating between the M_K and M_* points given by Kraus & Hillenbrand (2007), who list M_* and spectral energy distributions (SEDs) for B8-L0 stars.

We calculate M_K using *Hipparcos* parallaxes (Perryman et al. 1997) where possible to determine distances (D) to individual stars. When *Hipparcos* parallaxes are not available, we use the secular parallaxes published by Röser et al. (2011) or Goldman et al. (2013). The 13 ASAS stars that are not in the Röser et al. (2011) or Goldman et al. (2013) catalogs do not have *Hipparcos* parallaxes, and for these stars we assume D = 47 pc (van Leeuwen 2009) with an uncertainty $\sigma_D = \pm 10$ pc.

We calculate the M_K uncertainties by propagating the m_K and D uncertainties for each star, and then determine the M_* uncertainties by passing the $\pm 1 \sigma_{M_K}$ values through the same M_* calculation as above. Most of the uncertainties are small ($\sigma_{M*} \approx 2 - 3\%$), but in

a few cases, significant distance uncertainties lead to $\sigma_{M*} \approx 20 - 30\%$. Figure 3.2 includes these σ_M values. These are simply the systematic uncertainties from our calculation, and do not reflect other sources of uncertainty, such as our choice of model or *K*-band excesses due to a binary companion.

3.4 *K2* data

The pointing in *K2* is held in an unstable equilibrium against solar pressure by the two functioning reaction wheels. The spacecraft rolls about the boresight by up to 1 pixel at the edge of the focal plane. To correct for this, thrusters can be fired every 6 hours (if needed) to return the spacecraft to its original position. This drift causes stars to move on the focal plane in a diagonal pattern, inducing sawtooth-like signal in the 75-day light curve for each star (Van Cleve et al. 2016).

For stars with intrinsic long-timescale, high-amplitude variability, the drift has minimal impact on measurements of P_{rot}. For rotational variability on short timescales ($\lesssim$1 d) or with low amplitudes, we must use caution to avoid removing or distorting the rotational signature while applying instrumental corrections to the light curves.

We analyze *K2* Campaign 4 data for 65 Hyads identified in Section 3.2.1 and with *Kepler* magnitudes $K_p > 9$ mag (see Figure 3.4). Sixty-two of these stars have $P_{mem} > 90\%$ as calculated in Section 3.2.1. We exclude an additional 14 Hyads with $K_p < 9$, as they are saturated and therefore not amenable to our light-curve extraction method. The K_p values in the EPIC catalog are only approximate—they are computed from survey photometry—so among the 65 Hyads are a few stars with $9 \lesssim K_p \lesssim 10$ that also are too bright for our

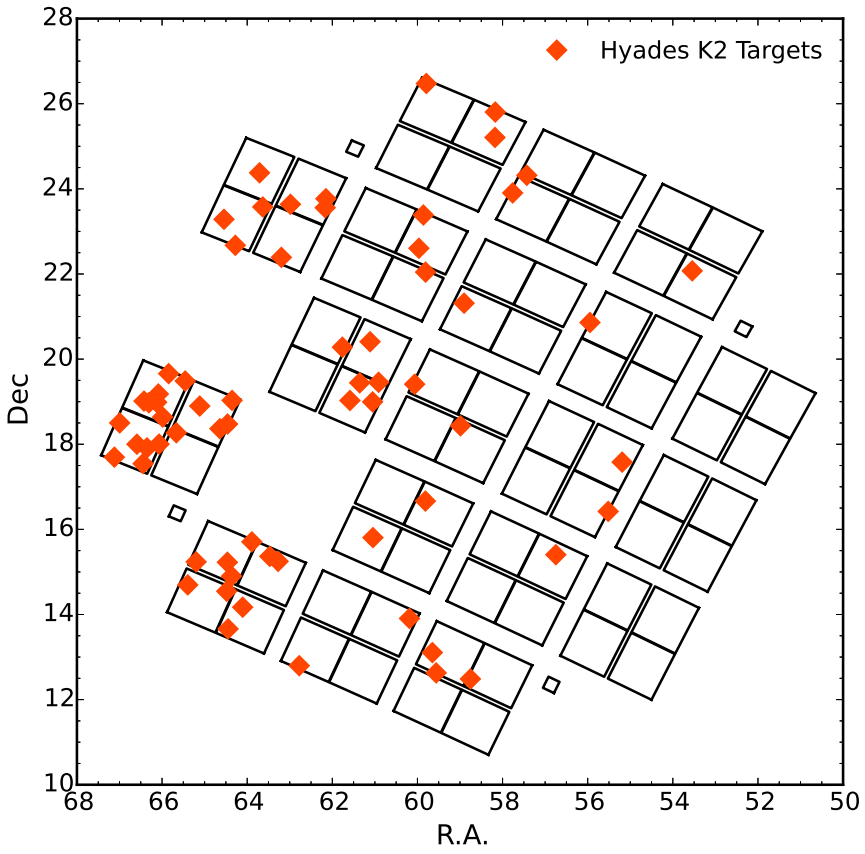

Figure 3.4 The *K2* Campaign 4 field of view, with our 65 Hyades targets shown as orange diamonds. Because the cluster is so large on the sky, many targets are near the edges of the field of view, and therefore have distorted PSFs. Two of the spacecraft's detector modules are no longer functioning.

method (see Table 3.4).

We describe how we extract light curves in Section 3.4.1, how we account for nearby stars in Section 3.4.2, and how we remove instrumental signatures in Section 3.4.3.[6]

[6]Our python code for light curve extraction can be found at `https://github.com/stephtdouglas/k2phot/tree/hyades_paper/` and our python code for detrending/P_{rot} measurement can be found at `https://github.com/stephtdouglas/k2spin/tree/hyades_paper/`.

3.4.1 Light Curve Extraction

All 65 of our targets were observed in long-cadence, meaning exposures lasted 29.4 min. Eight of our targets were also observed in short-cadence (58.89 s exposures), but we restrict our analysis to the long-cadence data.

The *K2* data are provided as target pixel files, which include basic information about the target, individual exposure frames for each time point, pipeline-calculated background counts, and quality flags for each exposure. Quality flags indicate problems with the exposure, noting for example when data were obtained during the thruster fires. Before further analysis, we remove any exposures with quality flags not equal to 0.

The Campaign 4 data processed by the *K2* pipeline is background-subtracted, but the pipeline background calculation is not reliable. The background is determined by fitting a low-order polynomial to the global background, which misses smaller local variations, especially those caused by dust near the Pleiades.[7]

We therefore perform our own background subtraction after adding the pipeline-calculated background flux back to the data. We compute the median flux of all pixels in each exposure, rejecting pixels identified as 3σ outliers over three iterations. After three iterations, the sigma-clipped median generally matches the levels in a visibly source-free region, and we take this value as the background level.

We calculate a flux-weighted centroid to determine the star's position in each exposure. We follow Howell (2006) in using a nine-by-nine pixel box around the nominal target position given by the exposure's header. We then place soft-edged circular apertures on

[7]See `http://keplerscience.arc.nasa.gov/k2-data-release-notes.html#k2-campaign-4`

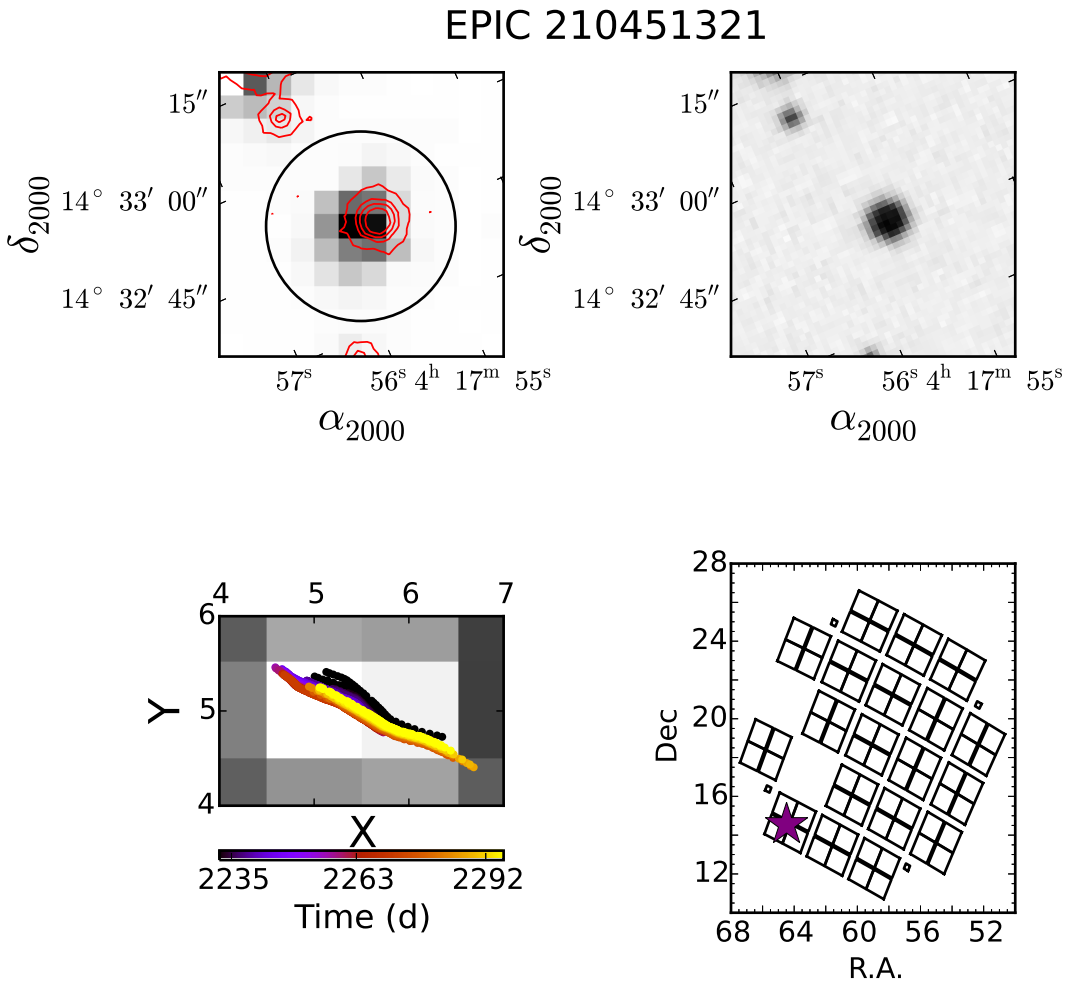

Figure 3.5 Diagnostic plots for EPIC 210451321; plots for all other *K2* Hyades targets are found in the electronic edition of the journal at `http://iopscience.iop.org/article/10.3847/0004-637X/822/1/47/meta#apj523231f5`. *Top left* — *K2* data in greyscale with the aperture selected in Section 3.4.3 shown in black. The DSS2 red image of the target is overlaid as red contours. The WCS in the *K2* target pixel files does not perfectly match the WCS in the DSS images, particularly near the edges of the field of view where distortion is significant. *Top right* — DSS2 red image of the target, rotated to match the orientation of the *K2* data. In this case, nearby companions are clearly visible within the *K2* pixel stamp, but they are excluded from the aperture used to extract the light curve. *Bottom left* — *K2* data in greyscale (colors reversed from above), with the centroid drift overlaid. *Bottom right* — The *K2* footprint for Campaign 4; the purple star indicates the position of the target.

the star's position that we calculated for each exposure, so that the aperture moves to follow the star. Tracking the motion of the star in this manner does not entirely remove variations in pixel sensitivity, but it does prevent nearby stars from entering the aperture. The soft-edged apertures include a fraction of the counts in pixels that are not entirely within the aperture. This fraction is equal to the fraction of the pixel covered by the aperture.

We carry out all aperture photometry and some source detection using the *photutils* package.[8] We extract light curves for each target using aperture radii r ranging from $2 \leq r \leq 6.5$ pixels in 0.5 pixel increments. The optimal light curve for analysis is chosen at a later stage.

3.4.2 Accounting for Nearby Stars

We co-add the individual images for each star and search for any nearby sources automatically and by eye. These co-added images are included in our diagnostic plots for each target (Figure 3.5).

First, we use the *daofind* function from *photutils*[9] with a low threshold for detecting nearby stars. We set *sharphi*=5, *sharplo*=0.1, and *FWHM*=2.5. Because the flux-weighted method will simply find the brightest spot in the frame, we also extract light curves for all detected objects using *daofind* to track the centroids.

When the sources are well separated on the chip (i.e., the neighbor's centroid is $\gtrsim 2-3$ pixels), we did not find any significant variability in the neighbors' light curves. Therefore,

[8] `https://github.com/astropy/photutils`, Version 0.2
[9] This is a Python implementation of the IRAF DAOFIND routine.

we simply restrict the maximum aperture radius for the primary target so that light from the neighbor does not affect further analysis of the target star.

We also search by eye for any sources in the coadded image that were missed by *daofind*. All the neighboring stars are real objects that also appear on archival images, but are either too faint or too close to the edge of the pixel stamp to be detected by *daofind*. Our moving aperture method for constructing light curves requires that sources be automatically detected either by daofind or a flux-weighted centroid, so that the source's centroid position can be used to define the source's aperture in each exposure. We are therefore unable to produce light curves for faint neighbors that *daofind* cannot detect. As above, in cases where we visually identify a faint neighbor, we restrict the maximum aperture radius for the primary target to exclude these neighbors wherever possible.

We deviate from our standard extraction procedure in two cases where a bright neighbor on the chip biases the flux-weighted centroid of the target. For EPIC 210736105, we simply use a smaller five-by-five pixel box to calculate the flux-weighted centroid, which yields the correct position for the star. We also reduce the maximum aperture size to 2.0 pixels. The neighbor shows no evidence of periodic variability (Figure 3.6).

Restricting the centroid calculation box for EPIC 210963067 does not remove the bias towards the brighter neighbor, and the neighbor is also variable (Figure 3.7). We therefore track the centroid of both the target and its neighbor using *daofind*. This is the only star for which we significantly change our light curve extraction technique based on a neighboring star.

We also must account for the *K2* imager's large pixel scale (4''), which can produce

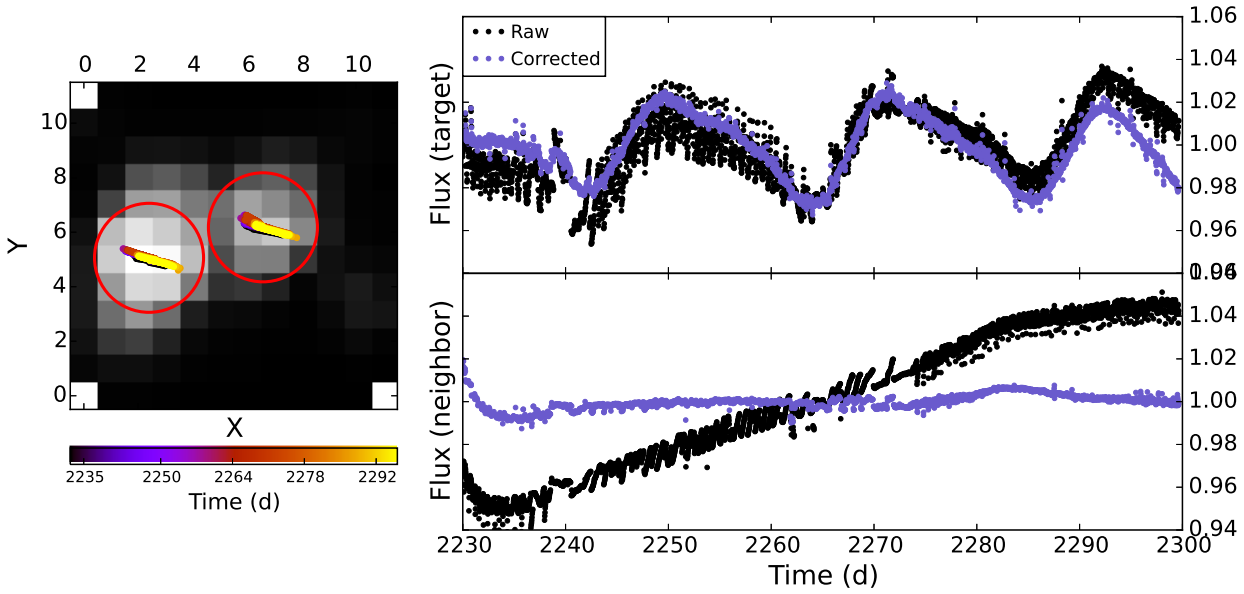

Figure 3.6 *Left* — Co-added *K2* images of EPIC 210736105 (center) and its nearby neighbor (left). We track the centroids with the *daofind* function in *photutils* and extract light curves through circular apertures with $r = 2$ pixels (red). The centroid positions are colored by date; black points were taken at the beginning of the campaign and yellow at the end. *Right* — *K2* light curves of EPIC 210736105 (top) and its nearby neighbor (bottom). The raw light curves are shown in black and corrected light curves in purple. Although the light curves are noisy, the periodic signature of the target clearly dominates any signal from the neighbor. Therefore, we simply restrict the centroid box and aperture size to extract a final light curve for EPIC 210736105.

blended point spread functions (PSFs) even when nearby objects are well-resolved in other surveys. We therefore compare the *K2* images by eye to Digital Sky Survey (DSS), SDSS (when available), and 2MASS images of our targets.[10] A DSS or SDSS image of each target is shown in Figure 3.5, rotated into the frame of the *K2* image. In many cases these neighboring stars are too close to our target to be separated, and we flag these targets as having blended neighbors.

Flags indicating whether a companion was identified by eye and whether it is blended

[10]We use the IRSA/IPAC finder chart application to obtain these images: `http://irsa.ipac.caltech.edu/applications/finderchart/`.

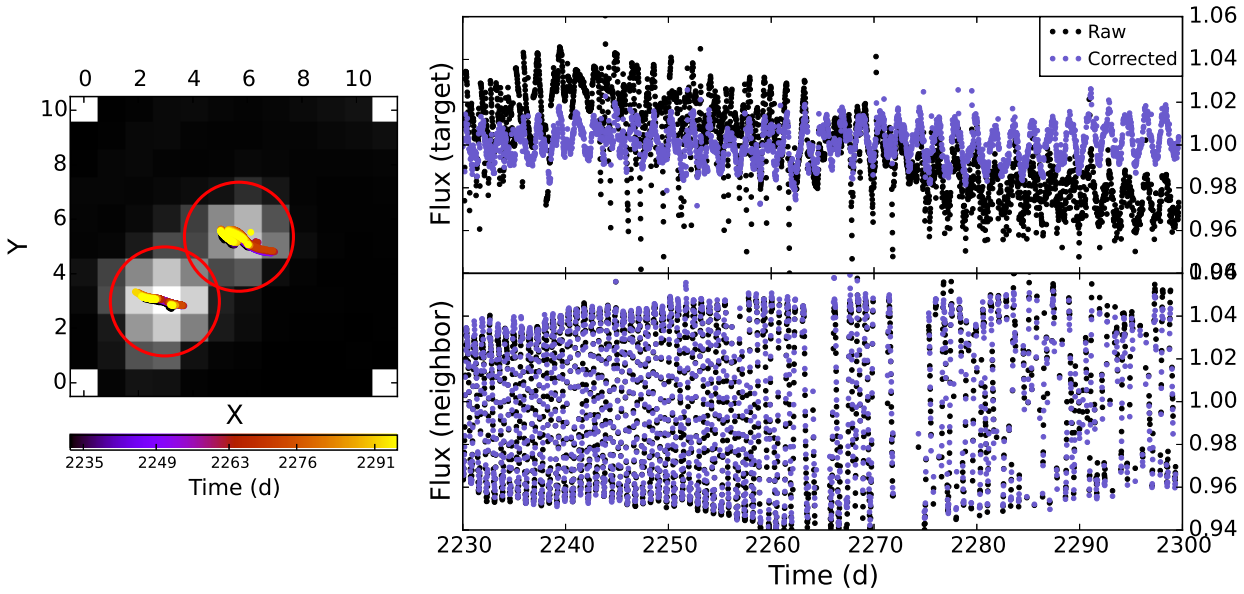

Figure 3.7 Same as Figure 3.6, but for EPIC 210963067 and its nearby neighbor (at center and lower left, respectively, in postage stamp at left). In this case both the target and neighbor show periodic variability on different timescales. Furthermore, restricting the centroid box does not prevent the brighter neighbor from biasing the centroid. Therefore, we use the light curves shown above, which were extracted using *daofind* centroid, for our analysis in Section 3.4.3.

in the target aperture are given in Table 3.3. A neighbor flag of "Y" indicates that a neighbor was identified. For these targets, a blended flag of "Y" indicates that the neighbor is definitely inside the *K2* aperture, "M" indicates that there is possible contamination or overlapping PSFs that can still be separated, and "N" indicates that the neighbor is well-separated.

3.4.3 Detrending Light Curves and Measuring P_{rot}

As noted earlier, *K2* light curves contain instrumental signals that can hinder measurements of intrinsic stellar variability. Given the 6-hour timescale for the dominant in-

strumental signature in *K2* light curves, however, disentangling intrinsic variability from instrumental effects can be difficult for stars with short-period, low-amplitude astrophysical signals. To decouple these signatures as best we can, we adopt an iterative approach that first removes intrinsic stellar signals from the light curve, so that instrumental effects can be isolated and corrected before further analyzing the stellar variability.

We describe this iterative approach in detail below, but the steps are to:

1. remove the long-timescale variability;
2. measure the initial periodic signal;
3. select the light curve with the optimal photometric aperture;
4. remove periodic stellar signals from the optimal-aperture light curve;
5. infer and correct for instrumental signatures;
6. refine the initial period measurement and consider secondary periodic signatures.

This procedure, which is similar to that used by Kraus et al. (2015) to remove instrumental and out-of-eclipse variability from the *K2* light curve for UScoCTIO 5, a spectroscopic binary in the Upper Scorpius star-forming region, is illustrated in Figure 3.8.

We also test a modified version of the Vanderburg & Johnson (2014) algorithm. Unlike the original Vanderburg & Johnson (2014) algorithm, the modified version removes as much periodic signal as possible before fitting for the instrumental drift. While this method produced light curves consistent with our own, there were some differences. First, our method rejects outliers, and is therefore less sensitive to transits or flares. Second, the modified Vanderburg & Johnson (2014) algorithm introduces jumps in the light curves

for stars with longer P_{rot}. Our method also more aggressively removes long-term trends from the light curves, but these trends are not periodic and likely not from rotation.

3.4.3.1 Removing long-timescale variability

We begin by computing a low-power smoothed version of the raw light curve using *supersmoother*, a Python implementation of the SuperSmoother non-parametric adaptive smoothing algorithm (Friedman 1984).[11] SuperSmoother selects the best local smoothing window for each point in a data series. The degree of smoothing can be set using the bass-enhancement value α: low values of α retain more local variability, while high values of α only retain long term trends. We set the bass-enhancement value to the maximum possible value of $\alpha = 10$. In most cases, the smoothed curve is effectively linear, but in some cases the data include slow trends, and this method accounts for these trends. This smoothed curve is overlaid on the raw light curve in the top panel of Figure 3.8. We divide the data by this smoothed curve to produce the detrended light curve, shown in green in the second panel of Figure 3.8.

3.4.3.2 Measuring the initial periodic signal

We measure rotation periods using the fast Lomb-Scargle function from the *gatspy* package.[12] This is an implementation of the FFT-based algorithm from Press & Rybicki (1989). We compute the periodogram power for $3{\times}10^4$ periods ranging from 0.1 d to 70.8 d (the length of the Campaign), though in practice we only consider periods <40 d in our

[11] `https://github.com/jakevdp/supersmoother`
[12] `https://github.com/astroML/gatspy`

analysis.

At every step, we calculate minimum significance levels for periodogram peaks using non-parametric bootstrap resampling. We generate 1000 simulated light curves for each source by holding the observation times fixed and randomly re-drawing the flux values with replacement. We compute a periodogram for each simulated light curve, and record the maximum power in each periodogram. The 99.9-percentile value of the maximum peak serves as the 0.1% significance level for peak detection.

In general, the minimum significance levels for our periodogram are extremely low. The grey line representing the 0.1% significance level is rarely visible in the periodograms in Figure 3.8. This is likely due to *K2*'s high observation cadence. If a periodic signal is present, randomly reshuffling the data will almost certainly destroy it, leaving no significant peaks in the periodogram (the 30-min observing cadence is outside our search range). Even the 6-hour thruster firing timescale will be wiped out in this resampling. Therefore, most periodic signals we find in our analysis are likely real, though we must still distinguish between stellar and instrumental sources.

We compute periodograms for both the raw and the detrended light curves, and select for further analysis the light curve with the highest peak in its periodogram. For this comparison, we only consider peaks at less than 40 d that do not correspond to a low multiple of the 6-hour thruster firing period; the periodogram peaks that fail these cuts likely correspond to the instrumental signatures or long trends in the raw light curve that we are trying to remove.

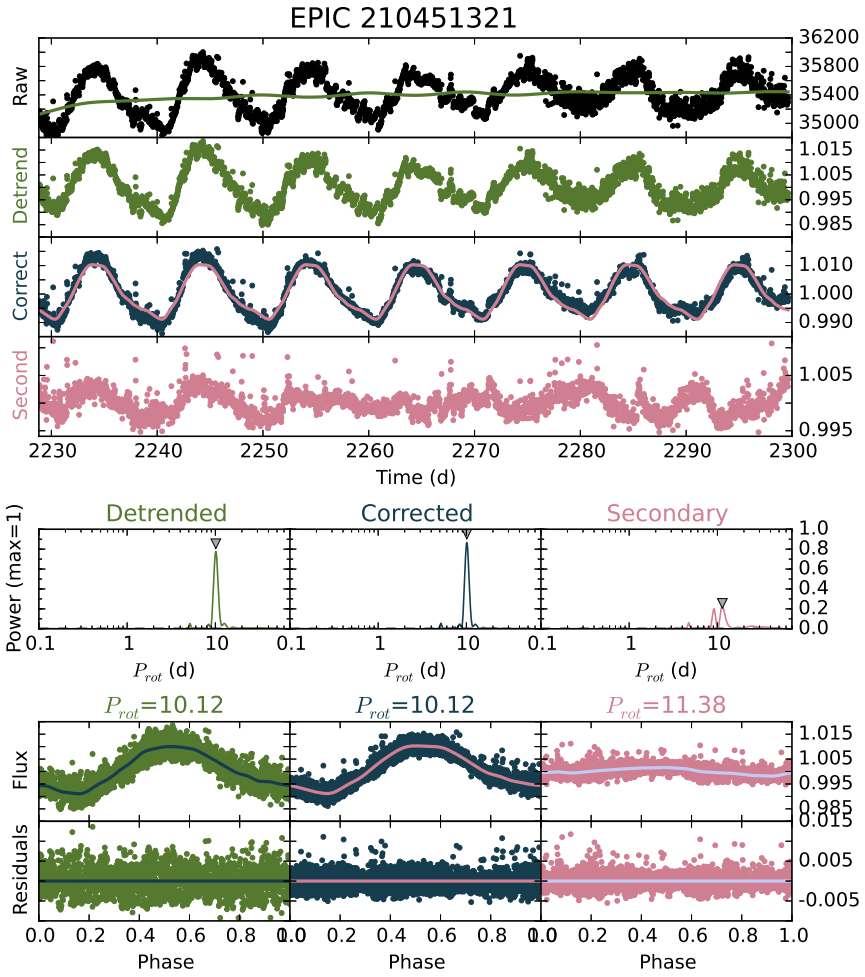

Figure 3.8 Analysis of the *K2* light curve for EPIC 210451321; plots for all other *K2* Hyades targets are found in the electronic edition. The top four rows show the light curve at different stages of processing. The center row shows periodograms for each light curve; the corresponding 99.9% significance levels (dot-dashed grey line) are generally too close to 0 to be visible. The second-to-last row shows the phased light curves with a smoothed version overlaid, and bottom row shows the residuals between those two. We divide the raw light curve (top, black) by a smoothed, low-power version (green line) to produce the detrended light curve (second panel, green). Either the raw or detrended light curve is chosen for further analysis based on which has the highest periodogram peak between 0.1−40 d; the corresponding periodogram is shown in the left column. We then account for the effect of the spacecraft drift, producing the corrected light curve (blue, third row and center column). We also look for additional periods by smoothing the phased, corrected light curve and dividing the periodic signal away, producing the secondary light curve (pink, fourth row and right column). In general, the period derived from the corrected light curve is the final period, but in a few cases, the period from the secondary light curve is more likely the true period.

3.4.3.3 Selecting the optimal photometric aperture

Initially, we detrend all raw light curves for each target using the process described above, and then select from among all possible apertures the light curve with the highest periodogram peak after the raw/detrended selection. An aperture that is too small will not contain a star's full PSF, decreasing the signal to noise, while a larger aperture may include nearby stars that contaminate the light curve. By selecting the light curve with the strongest initial peak, we begin with the cleanest possible light curve. We refer to the light curve selected for further analysis as the initial light curve.

In some cases, we restrict the maximum possible aperture to exclude nearby stars; see Section 3.4.2 for details.

3.4.3.4 Removing periodic stellar signals

We iteratively smooth the initial light curve selected in the previous step before correcting for the centroid drift across the detector. We phase-fold the light curve on the best period, and use *supersmoother* again to produce a smoothed version of the periodic signal. We then divide the light curve by the smoothed periodic light curve. We repeat this process up to six times, or until one of two conditions is met: either the maximum periodogram power falls below 10% of the initial power, or the highest remaining peak is a harmonic of the 6-hour thruster firing period. This produces a flattened light curve that should only contain instrumental signals.

3.4.3.5 Inferring and correcting for instrumental signatures

Once all significant periodic signals have been removed from the light curve, leaving it relatively flat, we use it to correct the initial light curve for instrumental signals. At each epoch in the light curve, we find the 21 other epochs with the closest centroid positions (in detector coordinates) to the epoch being corrected. We then divide each point in the initial light curve by the median of the flattened light curve at those 21 neighboring points. This produces the corrected light curve shown in dark blue in the third panel of Figure 3.8; for most of our targets, the P_{rot} measured from the corrected light curve is selected as the final P_{rot}.

The P_{rot} measured from the initial and corrected light curves are in general consistent with each other (Figure 3.9). There are four exceptions, where the P_{rot} measured from both the initial and corrected light curves are spurious, representing non-periodic trends.

3.4.3.6 Refining the initial period measurement

After correcting for instrumental effects, we also remove the dominant periodic signal to search for any additional signals. We phase-fold the corrected light curve and then use *supersmoother* to produce a smoothed version of the periodic signal, shown in pink in the third panel of Figure 3.8. We then divide the corrected light curve by this smoothed periodic curve to produce the secondary light curve, shown in the fourth panel of Figure 3.8.

We examine by eye the light curves produced for each object at each stage in the analysis. We note quality flags, any evidence of spot evolution and/or multiple periods,

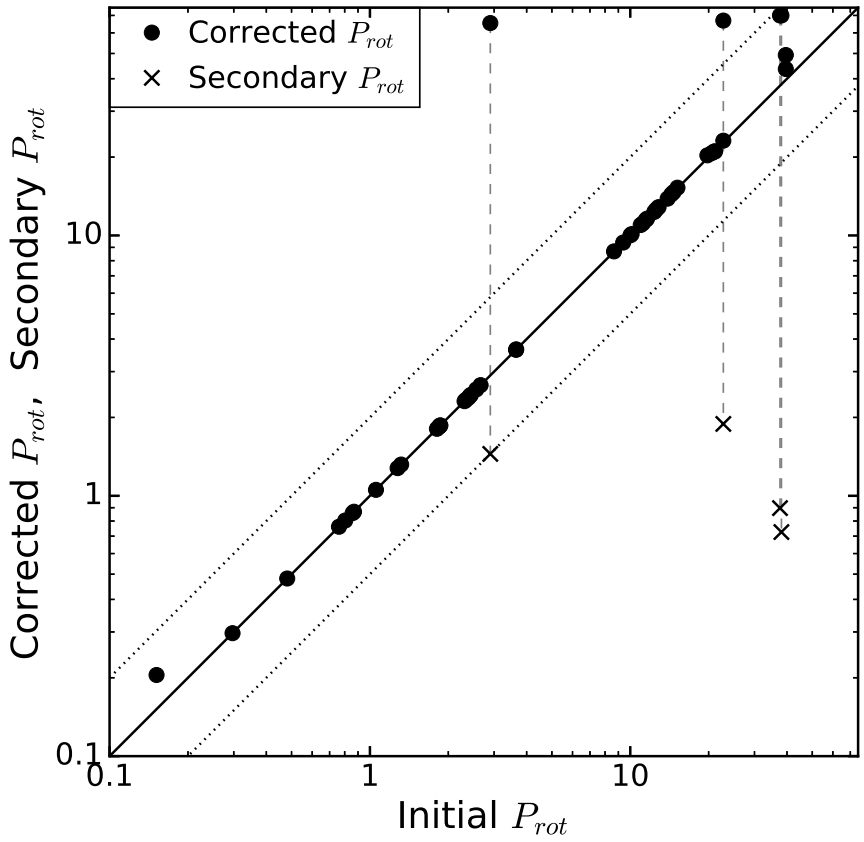

Figure 3.9 Comparison of P_{rot} measured at different stages of our analysis. The solid line corresponds to a one-to-one match; the dotted lines represent double- and half-period harmonics. In general, the P_{rot} measured from the initial and corrected light curves are consistent (black dots). In four cases, the corrected P_{prot} is extremely long, and likely represents long-term but non-periodic noise in the corrected light curve. Lines connect each of these P_{rot} values to the crosses that represent the secondary P_{rot}, which is more likely the true period (see also Figure 3.10).

and select the final P_{rot} from either the corrected or secondary light curve.

Our visual inspection of the periodograms and phased light curves prevents instrumental signals from contaminating our sample. We tested our algorithm on 3600 other Campaign 4 targets with $9 \leq K_p \leq 16.5$, and we detect periods between 20-25 d in $\approx 20\%$ of the corrected light curves. These periodogram peaks are typically wide, and appear with other wide peaks around 40 d and 70 d. We believe these to be low frequency noise

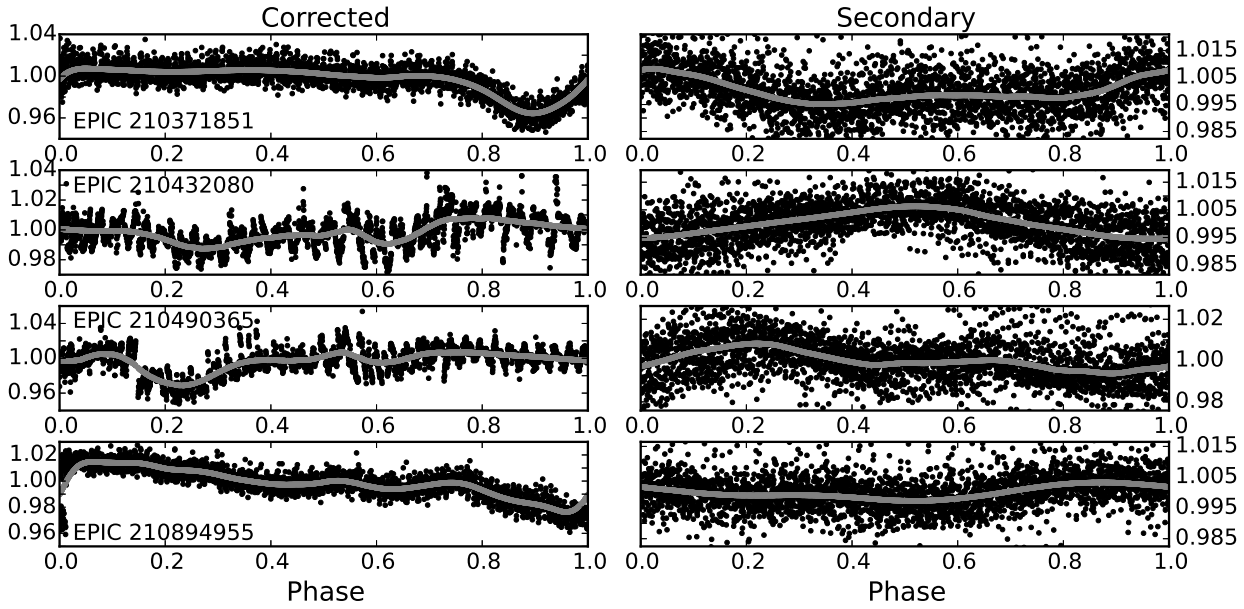

Figure 3.10 Four light curves for which the P_{rot} measured from the secondary light curve is more likely the true value. The corrected light curves (left) show non-periodic structures that dominate the periodogram. This is removed by dividing out the smoothed curve (grey), which produces the secondary light curves (right).

and/or a harmonic with the 70 d campaign length, and they appear particularly (though not exclusively) in light curves where the spacecraft drift is the only signal. Our visual inspection allows us to separate these spurious detections from genuine sinusoidal rotational variability, and we are confident in the $\approx$ 20 d rotation periods that we identify for four Hyads.[13]

We flag the light-curve quality on a scale of 0–2: 0 is a confident detection, 1 indicates significant residual noise in the light curve that may affect the final period measurement, or confusion about which periodogram peak corresponds to the dominant period, and 2 indicates that the spacecraft drift pattern dominates the light curve or that there is some

[13]See Figures 8.28, 8.32, 8.49, and 8.56 for the light curves of EPIC 210704853, EPIC 210736105, EPIC 210941195, and EPIC 211036776.

other fatal problem with the period measurement.

We also add flags for the presence of spot evolution and multiple periodic signals in the light curve. For spot evolution and multiperiodic signals, we use "Y," "M," and "N" flags, for "Yes," "Maybe," and "No." When there is significant power at half or twice the chosen period, we phase-fold the light curve at those harmonics and note in Table 3.3 whether they could be the true period. We also note in Table 3.3 when there are two clear peaks in the periodogram and there is confusion over which is the dominant period, or when any visible periodic signals are not picked up in our analysis.

In most cases, the secondary period is a harmonic of either the thruster-firing period or the fundamental period, or a clear, unrelated signal. In four cases, however, the period from the corrected light curve is spurious, and the period from the secondary light curve is selected as the real period. These four corrected light curves, shown in Fig. 3.10 show structure that was not removed by the initial low-power detrending, but which was removed by the smoothing used to produce the secondary light curve. The periods measured from the initial and corrected light curves appear to be an instrumental signal, and the secondary period looks more like a rotational signal (see Figures 3.9 and 3.10).

3.4.4 Light Curves With Multiple Periodic Signals

A subset of Hyades light curves in our sample show multiple significant periodogram peaks. The secondary peaks can generally be classified into two categories: harmonics of the fundamental period that appear due to symmetric spot coverage or spot evolution (21 cases) or a real secondary period (eight cases).

Spot evolution and double-dip light curves due to symmetric spot distributions have been observed in many *Kepler* stars (e.g., Walkowicz et al. 2013; McQuillan et al. 2013). All 11 Hyads with P_{rot} from the literature and this work show at least some evidence for spot evolution in their *K2* light curves. In two of these cases we find a different rotation period than in the literature (see Section 3.5.1 below), and spot evolution is the likely culprit for this discrepancy.

The cause of two distinct signals in the light curve is more difficult to untangle, but likely comes from an unresolved second star on the chip. Of the 11 stars with light curves that definitely or possibly contain multiple periodic signals, seven are confirmed binaries and one has a neighbor that is unresolved on the *K2* chip.

3.5 Results

We present P_{rot} measurements for 48 Hyades members, including 37 members with no prior P_{rot} measurement. Our P_{rot} values, flags, and analysis outputs are found in Table 3.3, where we also note whether we initially choose the raw or detrended light curve for analysis, and whether the final period is selected from the corrected or secondary light curve. Our new rotation periods, along with literature values, are shown as a function of stellar mass in Figure 3.11.

Nearly all of these new periods are for Hyads with $M_* \lesssim 0.7\ M_\odot$, and the majority are for fully convective, $\lesssim$0.3 $M_\odot$ Hyads. These are the first P_{rot} measurements for a set of Hyades members with $0.1 \lesssim M_* \lesssim 0.3\ M_\odot$.

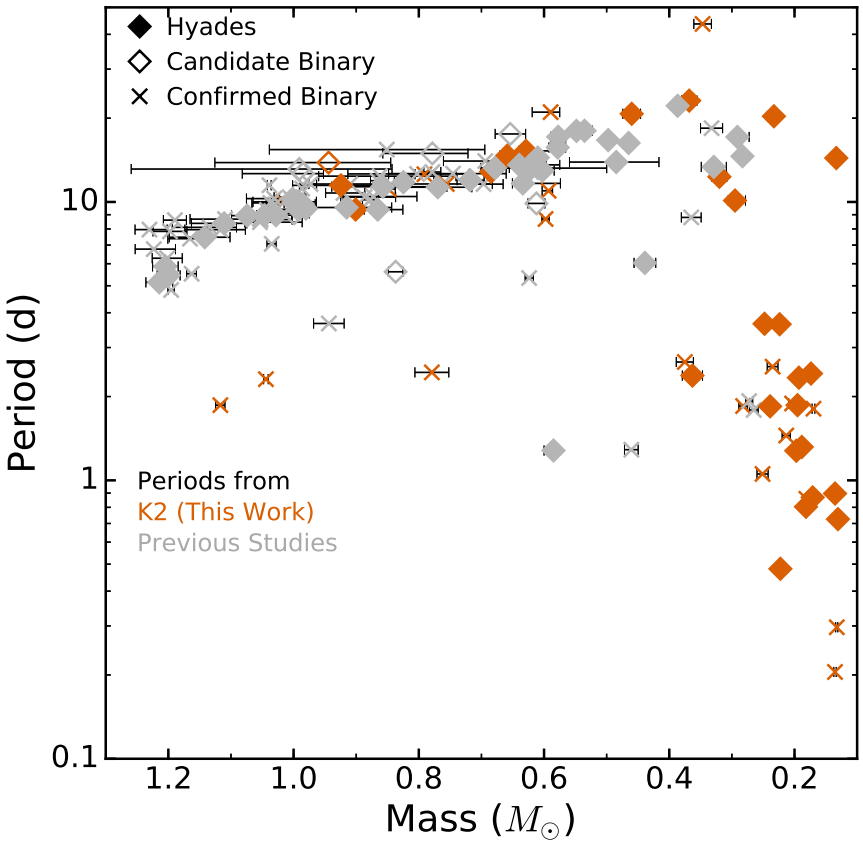

Figure 3.11 Mass-period distribution for all Hyads with measured periods. Grey symbols represent literature P_{rot}, and orange symbols denote new P_{rot} measured from *K2* data. Empty diamonds and crosses denote photometrically identified candidate binaries and confirmed binaries, respectively.

Table 3.3. Rotation periods measured from *K2* data

Ros. No.[a]	EPIC	RA	Dec	K_p Mag	Prev. P_{rot}[b]	*K2* P_{rot} (d)	Peak Power	Q[c]	Bin[d]	Spot Evol.[e]	Multi P_{rot}[f]	notes
64	210942999	03:34:10.57	+22:04:21.17	13.7	-	1.81	0.86	0	2	N	N	···
78	210865372	03:43:47.09	+20:51:36.25	13.4	D	12.32	0.63	0	0	Y	N	···
80	210499476	03:46:59.57	+15:24:16.93	14.2	-	0.86	0.75	0	2	N	N	not quite sinusoidal pattern
85	211058178	03:51:03.11	+23:54:13.14	9.8	A	12.57	0.56	0	2	Y	N	amplitude drops to almost 0 as the campaign progresses
86	211169647	03:52:41.02	+25:48:16.21	10.6	-	14.66	0.63	0	0	Y	M	···
87	211137806	03:52:42.71	+25:12:26.03	15.4	-	14.38	0.72	0	0	Y	N	···
98	210894955	03:55:36.90	+21:18:48.29	14.6	-	0.73	0.09	1	0	N	N	using secondary P_{rot}
104	210365286	03:58:14.38	+12:37:40.88	14.1	-	0.87	0.31	0	0	N	N	···
108	211201094	03:59:09.65	+26:28:34.43	10.9	-	15.26	0.85	0	0	N	N	···
111	210579563	03:59:15.03	+16:39:51.94	14.5	-	1.28	0.79	0	0	N	N	···

Note. — This table is available in its entirety in a machine-readable form in the online journal at `http://iopscience.iop.org/0004-637X/822/1/47/suppdata/apj523231t4_mrt.txt`. A portion is shown here for guidance regarding its form and content.

[a]Röser et al. (2011)

[b]Gives source of previous P_{rot} measurement, if any. P is Prosser et al. (1995), D is Delorme et al. (2011), and A is from our analysis of ASAS data (Cargile et al. in prep). There is no overlap between the Radick et al. (1987, 1995), Hartman et al. (2011) and *K2* samples.

[c]Quality flag. 0 is a confident detection, 1 indicates residual noise or confusion in the periodogram.

[d]Indicated binary status (Section 3.2.4, Table 3.2). 0 indicates a single star (to the best of our knowledge), 1 is a photometrically identified candidate binary, and 2 is a confirmed binary from the literature.

[e]Indicates visible spot evolution over several cycles. "Y," "M," and "N" flags indicate "Yes," "Maybe," and "No."

[f]Indicates multiple periods in the periodogram. "Y," "M," and "N" flags indicate "Yes," "Maybe," and "No."

We could not measure P_{rot} for the 17 *K2* targets listed in Table 3.4. In two cases, nearby bright stars contaminate the PSF. The PSF of another target extends beyond the pixel stamp; the estimated K_p magnitude was likely too faint. Six other stars with nearby neighbors show periodic signals in light curves extracted with apertures of $r = 4-6$ pixels, but exhibit mostly noise when the aperture is restricted to exclude these faint neighbors. Thus, it is possible that a neighbor is the source of the periodic variability rather than the target star. Finally, in two cases, the signal looks sinusoidal, but the measured P_{rot} is too close to the 6-hour thruster firing period to be sure that it is a stellar signal.

For the remaining six stars, however, the light curves are dominated by instrumental noise caused by the pointing drift. Although some of our faintest targets are among these 16, the noise-dominated light curves come from stars across the full brightness range of our sample. Thus, these noisy stars are likely to have very small amplitude variability, and our inability to extract periods for these stars does not necessarily imply a failure of our method for faint stars.

3.5.1 Consistency With Prior P_{rot} Measurements

Eleven *K2* targets have P_{rot} measured by previous authors; the measurements are generally consistent (see Table 3.1), with two exceptions.

Delorme et al. (2011) measure $P_{rot} = 13.51$ d for EPIC 210771915, while our analysis of ASAS data gave us $P_{rot} = 7.19$ d. In D14, we used the shorter ASAS-derived period, but our analysis of the *K2* data shows that the longer Delorme et al. (2011) period is correct. The *K2* light curve for this star shows a prominent double-dip feature and evidence for

Table 3.4. *K2* targets for which P_{rot} could not be measured

EPIC	RA	Dec	*Kp* (mag)	Prev. P_{rot} (d)[a]	Bin[b]	Notes
210643507	03:40:45.81	17:34:47.77	16.64	-	0	noise
210563410	03:42:04.44	16:25:18.29	15.13	-	0	periodicity in large aperture light curve, may be from neighbor
211084463	03:49:42.70	24:19:07.80	14.99	-	0	much brighter blended neighbor
210359769	03:55:01.44	12:29:08.10	9.76	D	0	periodicity in large aperture light curve, may be from neighbor
210384590	03:58:35.82	13:06:18.11	9.17	-	1	noise; unclear if true stellar signal
210976212	03:59:51.83	22:36:13.45	14.41	-	0	noise
210835395	04:04:27.04	20:24:30.43	15.16	-	2	period close to firing period
210827030	04:07:03.25	20:16:50.87	13.81	-	0	period close to firing period
211037886	04:14:32.32	23:34:29.80	9.05	A	0	saturated and bleeds out of pixel stamp (estimated K_p is too faint)
211088189	04:14:50.19	24:22:37.52	16.02	-	0	noise
210517837	04:15:33.69	15:42:22.57	10.46	-	2	noise
210707811	04:17:50.63	18:28:30.69	12.81	-	2	periodicity in large aperture light curve, may be from neighbor
210693497	04:22:39.56	18:16:09.61	12.13	-	0	periodicity in large aperture light curve, may be from neighbor
210754620	04:24:20.95	19:10:50.66	14.40	-	0	noise
210742017	04:24:30.59	18:59:12.82	15.15	-	2	periodicity in large aperture light curve, may be from neighbor
210667985	04:25:25.03	17:54:55.23	10.62	-	2	saturation strip from brighter star crosses PSF
210743724	04:25:41.84	19:00:47.57	13.80	-	2	periodicity in large aperture light curve, may be from neighbor

Note. — For details on the light curve analysis of these stars, see the electronic version of Table 3.3 at `http://iopscience.iop.org/0004-637X/822/1/47/suppdata/apj523231t4_mrt.txt`.

[a]Source of previous P_{rot} measurement: "D" for Delorme et al. (2011) and "A" for our ASAS analysis (Cargile et al. in prep).

[b]Binary status (Section 3.2.4, Table 3.2): 0 indicates a single star (to the best of our knowledge), 1 is a photometrically identified candidate binary, and 2 is a confirmed binary from the literature.

spot evolution. The shorter period we initially derived is a half-period harmonic of the true period.

In our analysis of ASAS stars, we measure P_{rot} = 8.37 d for EPIC 211058178, while we measure P_{rot} = 12.32 d with *K2* data. The *K2* light curve for this star shows rapid

evolution on timescales close to and shorter than the rotation period, and the amplitude of variability drops from nearly 1% to ≈0.1% over the course of Campaign 4. The star is also a confirmed spectroscopic binary (Paulson et al. 2004), and is therefore excluded from our gyrochronology analysis.

Overall, however, the P_{rot} measurements are consistent from study to study. For example, one Prosser et al. (1995) target was also observed by Delorme et al. (2011) and by *K2*, and the three derived P_{rot} agree at the 1% level. The variation among P_{rot} measured by different surveys for the same star are frequently of order a few percent, and usually <10% (see Table 3.1). This overall consistency is a good sign for future rotation studies, especially since *K2*'s baseline and cadence do allow us to identify two instances where sampling likely affected earlier results.

3.5.2 Stellar Rotation and Multiplicity at 625 Myr

Based on previous studies, we expect Hyades members with $M_* \gtrsim 0.6 - 0.7\ M_\odot$ to be confined to a single-valued $M_*(P_{rot})$ relation that also defines the upper envelope of rotation for lower-mass stars, while less massive stars to show a wide spread in P_{rot} (Barnes 2003; Irwin & Bouvier 2009; Agüeros et al. 2011). We refer to the upper envelope of P_{rot} values as the slow-rotator sequence, and the lower envelope as the rapid rotator sequence (labelled the "I sequence" and "C sequence," respectively, by Barnes 2003). We also expect all fully convective stars to be rapidly rotating at this age, with a break in the slow-rotator sequence around the transition between partially and fully convective stars (Irwin & Bouvier 2009; Newton et al. 2016).

The upper envelope of rotation in the Hyades is consistent with previous observations of rotation in open clusters. One notable exception, EPIC 210489654 ($M_* = 0.35\ M_\odot$, $P_{rot} = 45$ d), lies well above the rest of the Hyads. It is a confirmed binary (Janson et al. 2014), which may be the cause of its unusually slow P_{rot} for this age, or it may be an older field star whose proper motion happens to match the Hyades's. Besides this outlier, the Hyades slow-rotator sequence is well-defined for $M_* \gtrsim 0.3\ M_\odot$ stars, with P_{rot} increasing slightly toward lower masses.

Once binary systems are excluded, we do not see strong evidence for a transition in rotation properties at $M_* \approx 0.6\ M_\odot$. Only three rapid rotators with $0.6 \gtrsim M_* \gtrsim 0.3\ M_\odot$ remain, and none has been surveyed for binary companions. Therefore, we cannot rule out multiplicity (Morgan et al. 2012) or closely orbiting giant planets (Poppenhaeger & Wolk 2014) as the cause for their more rapid rotation. These outliers should be priority targets for future multiplicity surveys; they are most likely binaries, meaning that the period-mass relation for single stars is single-valued for $M_* \gtrsim 0.3\ M_\odot$

It is also possible that the reported P_{rot} for these three remaining rapid rotators with $0.6 \gtrsim M_* \gtrsim 0.3\ M_\odot$ are aliases of longer periods. All three have P_{rot} derived from the same survey (Delorme et al. 2011), and these authors note that they are sensitive to P_{rot} between $1 - 20$ d. Although only a few *K2* targets fall within the $0.6 \gtrsim M_* \gtrsim 0.3\ M_\odot$ range, we are sensitive to the full range of possible P_{rot} values. However, we only detect long ($\gtrsim$10 d) rotation periods for stars in this mass range.

The break in the slow-rotator sequence around the transition to full convection ($\approx$0.3 $M_\odot$) is hard to quantify due to a pair of slowly rotating mid-M dwarfs. EPIC

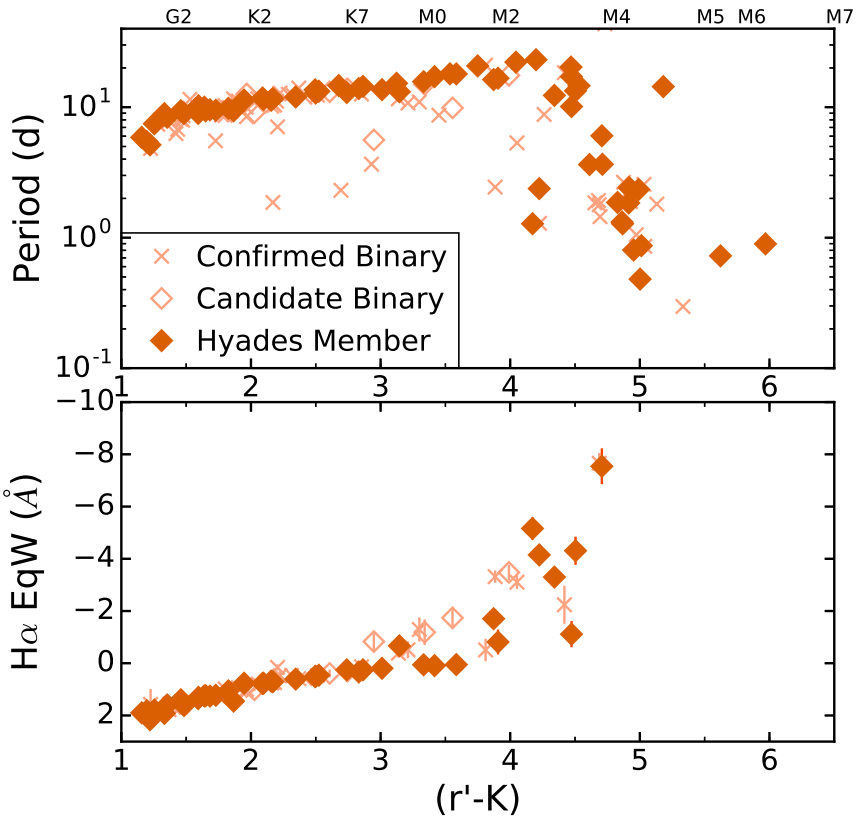

Figure 3.12 *Top* — P_{rot} as a function of color for all Hyads with measured periods. Empty diamonds and crosses denote photometrically identified candidate binaries and confirmed binaries, respectively. *Bottom* — $H\alpha$ emission as a function of color for Hyads with optical spectra in Chapter 2. Negative equivalent widths indicate emission. We find the same pattern in activity that we find in rotation. Most stars bluer than $(r' - K) \approx 4$ lie along a sequence of slow rotation/low activity, with only a few rapid rotators or active stars among them. Most of these outliers are confirmed or candidate binaries. Redward of $(r' - K) \approx 4$, both P_{rot} and equivalent width values show much more scatter.

211137806 ($M_* = 0.13\ M_\odot$, $P_{rot} = 14.38$ d) is newly identified as a candidate Hyad by Röser et al. (2011). EPIC 210736105 ($M_* = 0.23\ M_\odot$, $P_{rot} = 20.31$ d) was cataloged as a cluster member by Reid (1992), but it has not been surveyed for multiplicity.[14] Based on their

[14]EPIC 210736105 also has an angular light curve with a fast rise and slow decline reminiscent of a Cepheid variable (Figure 3.6). However, period-luminosity relationships for Classical or Type II Cepheids imply a distance of ≈24 kpc or ≈7 kpc, respectively (Gieren et al. 1998; Matsunaga et al. 2009), which is too far away to account for the observed proper motion. There is also a brighter star nearby, but that star does not show evidence of periodic variability (Figure 3.6).

slow rotation periods, these stars are likely either unresolved multiple systems or older field interlopers, but we cannot confirm this without radial velocity or high-resolution imaging data.

Despite these two outliers, nearly all Hyads with $M_* \lesssim 0.3\ M_\odot$ have $P_{rot} < 5$ d. This is consistent with existing evidence that fully convective M dwarfs stay spinning rapidly for several Gyr (Newton et al. 2016). The fastest fully convective rotators are confirmed binary systems, similar to the effect observed in more massive stars.

3.6 Discussion

3.6.1 Implications for Gyrochronology

As described above, empirical studies of rotation in open clusters identify two regimes in the $P_{rot}(M_*)$ plane for partially convective stars: above a particular mass, most stars are confined to a single-valued $P_{rot}(M_*)$ sequence, and below this mass, stars exhibit a wide range of P_{rot} values (Barnes 2003). Gyrochronology studies typically focus on the evolution of the slow-rotator sequence, which is unaffected by our results. The same studies make predictions for the age-dependent location of the transition between the single-valued sequence and the wider spread in P_{rot} values. Previous work on the Hyades and the co-eval Praesepe cluster suggests that this transition occurs around $0.6 - 0.7\ M_\odot$ for ≈600 Myr-old stars (Agüeros et al. 2011, Chapter 2).

Our results indicate that, after confirmed binaries are removed, the sequence of slowly rotating likely single-star Hyades members breaks down at ≈0.3 $M_\odot$. This is has

important consequences for models of stellar spin-down. If single $\gtrsim$0.3 $M_{\odot}$ stars converge onto the slow-rotator sequence by the age of the Hyades, then this will skew empirical gyrochronological relations (i.e., Barnes 2003), which are currently calibrated such that this transition occurs at $\approx$0.6 $M_{\odot}$ in the Hyades.

Since rotation and activity are generally correlated, we would expect that any behavior observed in the mass-period plane would be reflected when analyzing the strength of the $H\alpha$ line (a chromospheric proxy for the magnetic-field strength) for these same stars. Specifically, if rapid rotators $\gtrsim$0.3 $M_{\odot}$ are all binaries, then $H\alpha$ emitters above that threshold mass should predominantly be binaries as well. In D14 we found that, for stars in the Hyades and the co-eval Praesepe cluster, both P_{rot} and $H\alpha$ activity transitioned from a mostly single-valued sequence to a wider spread in P_{rot} or equivalent width at about $0.6 - 0.7\ M_{\odot}$, or spectral types K7-M0. However, we did not consider the binary status of Praesepe and Hyades members in that analysis.

Because binary companions will add excess K-band flux and impact our mass calculations, we now re-examine this transition as a function of $(r' - K)$ rather than mass. Using color keeps equal-mass binaries closer to the correct location for their spectral type, although low-mass companions could still redden a star's colors.

We find that the transition in activity and P_{rot} occurs around $(r' - K) \approx 4$, corresponding to spectral types of M2-M3 or $M_* \approx 0.3 - 0.4\ M_{\odot}$ (Figure 3.12). Bluer stars with higher-than-average $H\alpha$ equivalent widths or rotating more rapidly than average are nearly all binaries. This provides further evidence that binaries have contaminated previous studies of P_{rot} evolution in open clusters.

The Hyades's proximity means it has been extensively studied for multiplicity, and may be the best current example of how binaries affect the period-mass plane. Other, more distant clusters may not have received the same attention. Roughly 45% of Hyads with measured P_{rot} are confirmed binaries, and in total $\gtrsim$30% of all Hyads are confirmed binaries. The co-eval Praesepe cluster, in contrast, has ≈1200 members (Kraus & Hillenbrand 2007) compared to the Hyades's ≈800, but <20% Praesepe stars have confirmed companions. While experiments like *K2* are providing many new P_{rot} measurements for open cluster stars, complementary binary surveys are needed to investigate the impact of multiplicity on current age-rotation relations.

3.6.2 Implications for Magnetic Braking Models

Reiners & Mohanty (2012) derive a model for the angular momentum lost by a rotating solid sphere due to magnetic braking. These authors initialize their model using P_{rot} and masses measured for 5-Myr-old stars in the Orion Nebula Cluster and NGC 2264, then evolve these stars forward in time. They show that their model broadly reproduces the shape of the mass-period plane at 625 Myr as defined by then-available P_{rot} for Praesepe and the Hyades, but a detailed comparison to these data shows several discrepancies. The upper envelope of slow rotators in the Reiners & Mohanty (2012) model has a different slope than the data; these authors attribute this to the effects of core-envelope coupling, which their model does not include. The Reiners & Mohanty (2012) model also predicts shorter P_{rot} values than is observed for $M_* \lesssim 0.6\ M_\odot$ (Figure 3.13).

Matt et al. (2015) also derive a model for the spin-down of a solid sphere due to

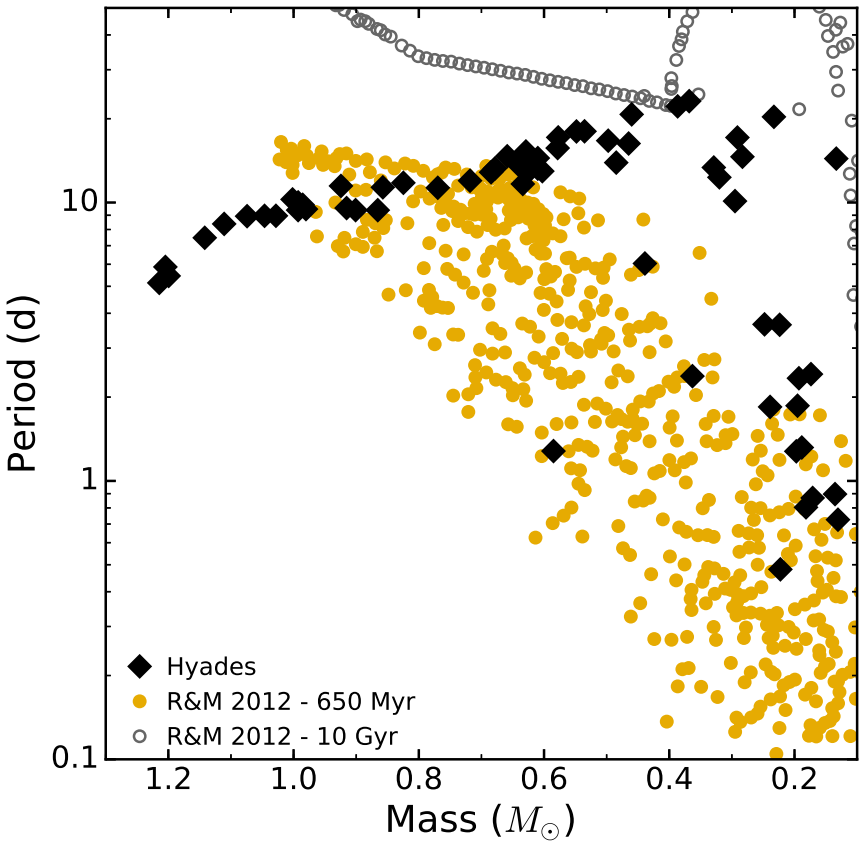

Figure 3.13 Mass-period distribution for single Hyads (black diamonds; includes both confirmed single stars and stars that have not been surveyed for multiplicity) compared to Reiners & Mohanty (2012) model data for 650-Myr-old (yellow closed circles) and 10-Gyr-old (grey open circles) stars.

magnetic braking. These authors' initial conditions approximate the distribution of P_{rot} observed for 2 – 5 Myr-old stars, but are not drawn directly from observations. They also allow the stellar radius and moment of inertia to evolve with time following evolutionary tracks. The Matt et al. (2015) model better predicts the mass dependence of the slow-rotator sequence for Hyads with $M_* \gtrsim 0.6\,M_\odot$ (Figure 3.14).

Matt et al. (2015) find that their model at 573 Myr fails to predict a set of rapid rotators in Praesepe with $0.7 \lesssim M_* \lesssim 1.0\,M_\odot$, and these authors attribute the discrepancy to a change

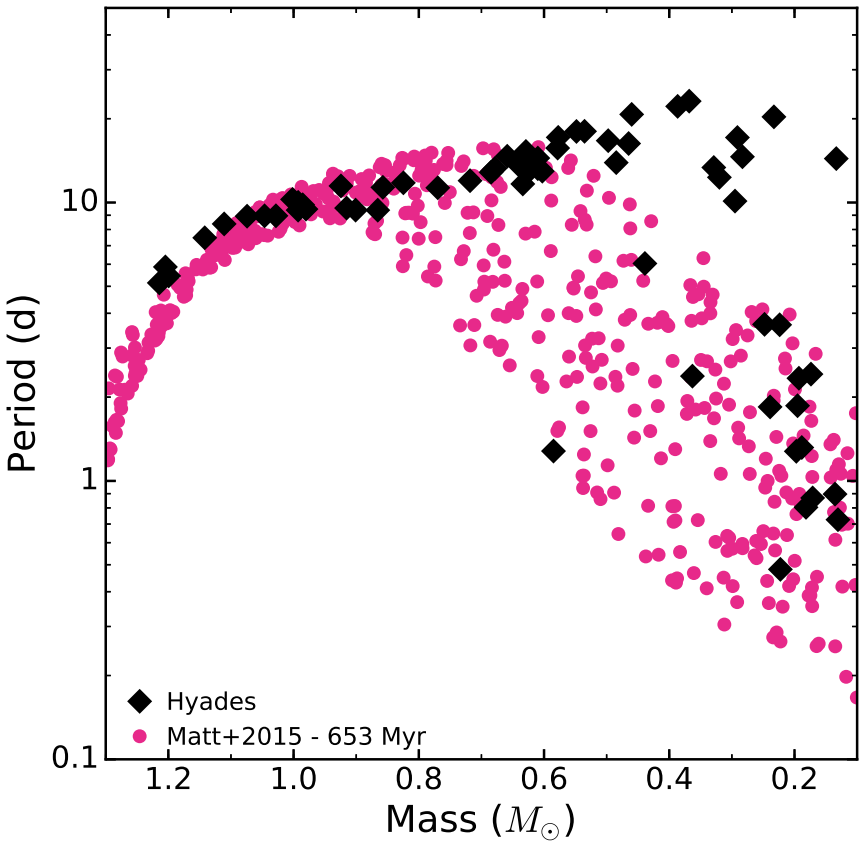

Figure 3.14 Mass-period distribution for single Hyads (black diamonds; includes both confirmed single stars and stars that have not been surveyed for multiplicity) compared to the Matt et al. (2015) model data for 653-Myr-old stars (pink circles).

in the magnetic torque exerted on these stars. However, we find that any rapidly rotating Hyads in that mass regime are known multiple systems, and most of the rapidly rotating Praesepe members at those masses are identified as candidate binaries in Chapter 2.

Both models predict more rapid rotators than observed for $\lesssim$0.9 $M_\odot$ Hyads, which indicates that magnetized winds more effectively brake stellar rotation than the models predict. These discrepancies are most pronounced for $M_* \lesssim 0.6\ M_\odot$, and suggest two transition points in braking behavior: one around the beginning of the M-dwarf regime, and one at the boundary to full convection.

Hyads with $0.3 \lesssim M_* \lesssim 0.6\ M_\odot$ rotate more slowly than either model predicts, extending the slow-rotator sequence to the fully convective boundary. Matt et al. (2015) suggest that this is due to internal angular momentum transport that is not included in their models.

Alternately, a change in magnetic field geometry could increase the braking efficiency for M dwarfs relative to the prescriptions of Matt et al. (2015), which match G and K stars well. Zeeman Doppler imaging studies find a transition in magnetic field properties at around 0.5 $M_\odot$, not at the transition to fully convective stars (Donati & Landstreet 2009; Donati 2011). Most M dwarfs have much stronger and more poloidal fields than their more massive counterparts with the same P_{rot}, though some still have weaker and/or more toroidal fields. Poloidal fields should lead to more effective magnetic braking because they allow for larger magnetic wind torques due to a larger Alfvén radius and more efficient mass loss in the equatorial plane, compared to more complex fields (Garraffo et al. 2015c,a). This could explain why the models fail to reproduce the population of slow rotators with $0.3 \lesssim M_* \lesssim 0.6\ M_\odot$ in the Hyades and Praesepe; future models will need to account for the enhanced braking efficiency in this mass range.

A second transition point occurs around the fully convective boundary, where core-envelope coupling becomes irrelevant. Since these stars have no core to decouple from their convective zone, the solid-body model used by Reiners & Mohanty (2012) and Matt et al. (2015) should match these $\lesssim$0.3 $M_\odot$ stars best, and the stellar wind model is a likely culprit for the observed discrepancy. The discrepancy with observations is more pronounced in the Reiners & Mohanty (2012) model, where the model P_{rot} distribution

appears to be shifted down by a factor of $3-4$ relative to observations. The Matt et al. (2015) model extends to slightly faster P_{rot} than we observe in this mass range, but overall does a better job of replicating the fully convective Hyads. This indicates that, despite the discrepancy with early M dwarfs, the Matt et al. (2015) model better captures the overall internal angular momentum and wind loss rates for fully convective stars.

3.7 Conclusions

1. We have extracted and analyzed *K2* light curves for 65 Hyades members. We measure rotation periods for 48 of these, including 37 Hyads without previous P_{rot}. This is the first time rotation periods have been measured for single Hyades members that definitively fall below the fully convective boundary ($M_* \lesssim 0.3\ M_\odot$). A total of 139 Hyades members now have measured P_{rot}.

2. We have assembled binary information from the literature for all Hyads with measured P_{rot} and for those targeted by *K2*. We find that 63 of 139 stars with measured P_{rot} are confirmed binary or multiple systems. This ensures that, to the best of present knowledge, our gyrochronological analysis is based on a sample of single stars.

3. We find that most, if not all, rapid rotators with $M_* \gtrsim 0.3\ M_\odot$ are multiple systems. Most single stars have spun down to a single-valued mass-period relationship, indicating that multiplicity must be considered when analyzing the mass-period plane.

4. We find that magnetic braking models predict more rapid rotation at this age than

observed over a range of masses. The discrepancy in the fully convective regime in particular indicates that magnetic braking is more efficient than predicted.

The Hyades's large apparent size on the sky has limited surveys for rotation in the cluster, and the mass range where rotators appear to be missing is at the faint end of previous surveys. This is compounded by a dip in membership numbers around $0.4 \lesssim M_* \lesssim 0.6\ M_\odot$. Even if our data suggest more fundamental theoretical challenges, at this time we cannot rule out these selection effects as being responsible for points 3–4 above.

Additional P_{rot} measurements, both for the Hyades and the co-eval Praesepe cluster, are needed to rule out these selection effects. *K2* observed ≈700 Praesepe members in Campaign 5; those data are the focus of Chapter 4. Furthermore, *K2* is slated to return to the Hyades in Campaign 13, and the planned field position could yield ≈100 additional P_{rot} for cluster members.

More binary surveys are also needed in both clusters to match these P_{rot} samples and confirm the effect of multiplicity on the period-mass plane at ≈600 Myr. The remaining rapidly rotating $M_* \gtrsim 0.3\ M_\odot$ Hyads have not been surveyed for companions, and many planned Campaign 13 targets are also missing from existing multiplicity studies. Comparable P_{rot} and multiplicity samples are also needed in other clusters to further investigate how binarity impacts age-rotation relations.

Chapter 4

Poking the Beehive from Space: *K2* Rotation Periods for Praesepe

4.1 Introduction

In examining the evolution of angular momentum and activity in late-type stars, the Hyades and Praesepe (α = 04:27, δ = +15:52 and α = 08:40:24, δ = +19:41, respectively), two ≈650-Myr-old open clusters, form a crucial bridge between young open clusters (such as the Pleiades, at ≈125 Myr; e.g., Covey et al. 2016; Rebull et al. 2016a) and older field dwarfs (≥2 Gyr; e.g., Kiraga & Stepien 2007). This paper is the fourth in our study of these linchpin clusters.

In Agüeros et al. (2011), we presented new rotation periods (P_{rot}) for 40 late-K to mid-

[0]This chapter is a reproduction of a paper that has been accepted by The Astrophysical Journal. It can currently be found at `https://arxiv.org/abs/1704.04507`. The article has been reformatted for this section. The original appendix to this paper has been moved to Appendix B.

M Praesepe members measured from Palomar Transient Factory (PTF; Law et al. 2009; Rau et al. 2009) data. We also tested models of angular-momentum evolution, which describe the evolution of stellar P_{rot} as a function of color and mass. We used the semi-empirical relations of Barnes & Kim (2010) and Barnes (2010) to evolve the sample of Praesepe periods. Comparing the resulting predictions to periods measured in M35 and NGC 2516 ($\approx$150 Myr) and for kinematically selected young and old field star populations (1.5 and 8.5 Gyr, respectively), we found that stellar spin-down may progress more slowly than described by these relations.

In Chapter 2, we extended our analysis to the Hyades, combining new P_{rot} measured with All Sky Automated Survey (Pojmański 2002) data (Cargile et al. in prep) with those obtained by Radick et al. (1987, 1995), Scholz & Eislöffel (2007), Scholz et al. (2011), and Delorme et al. (2011). We combined these data with new and archival optical spectra to show that the transition between magnetically inactive and active stars happens at the same mass in both clusters, as does the transition from a partially active population to one where every star is active. Furthermore, we determined that Praesepe and the Hyades are following identical rotation-activity relations, and that the mass-period relation for the combined clusters transitions from an approximately single-valued sequence to a wide spread in P_{rot} at a mass $M_* \approx 0.6{-}0.7\ M_\odot$, or a spectral type SpT $\approx$ M0.

In Chapter 3, however, after adding P_{rot} from Prosser et al. (1995), Hartman et al. (2011), and our observations with the re-purposed *Kepler* mission (*K2*; Howell et al. 2014), and after removing all confirmed and candidate binaries from the Hyades's mass-period plane, we found that nearly all *single* Hyads with $M_* \gtrsim 0.3\ M_\odot$ are slowly rotating. We

also found that the more recent, theoretical models for rotational evolution of Reiners & Mohanty (2012) and Matt et al. (2015) predict faster rotation than is actually observed at ≈650 Myr for $\lesssim$0.9 $M_\odot$ stars. The dearth of single $\gtrsim$0.3 $M_\odot$ rapid rotators indicates that magnetic braking is more efficient than previously thought, and that age-rotation studies must account for multiplicity.

We now present P_{rot} measurements for 677 Praesepe members measured from *K2* data. We describe the membership catalog and archival P_{rot} we used in Section 4.2, and our *K2* light curves and period-measuring algorithm in Section 4.3. To examine the impact of multiplicity on the mass-period plane, we attempt to identify binaries in Praesepe; we discuss these efforts in Section 4.4. We present our results, including their potential implications for calibrating angular momentum evolution, in Section 4.5. We conclude in Section 4.6.

4.2 Existing Data

4.2.1 Cluster Catalog

We continue to use the Praesepe membership catalog presented in Chapter 2, which includes 1130 cluster members with membership probabilities $P_{mem} \geq 50\%$ as calculated by Kraus & Hillenbrand (2007) and 39 previously identified members too bright to be included by those authors in their catalog for the cluster. We assign these bright stars $P_{mem} = 100\%$. We also continue to use the photometry and stellar masses presented in Table 2.5. For most of our analysis, as in that work, we include only the 1099 stars with

$P_{mem} \geq 70\%$.

4.2.2 Archival Rotation Periods

In Agüeros et al. (2011) and Chapter 2, we combined P_{rot} measurements from PTF data with P_{rot} measurements from Scholz & Eislöffel (2007), Scholz et al. (2011), and Delorme et al. (2011) to produce a catalog of 135 known rotators in Praesepe.[1] Eighty-three of these stars have a Kraus & Hillenbrand (2007) $P_{mem} > 95\%$.

To this catalog we now add 180 P_{rot} measurements from Kovács et al. (2014); 174 of these stars have $P_{mem} \geq 70\%$. Forty-four stars have previous P_{rot} measurements by other authors: the majority of these measurements are consistent to within 0.5 d, but 13 stars have significantly discrepant P_{rot} measurements (see Table 4.1). In all 13 cases, Kovács et al. (2014) measure the P_{rot} to be at least twice as long as previous authors. This discrepancy undermines the validity of the other Kovács et al. (2014) P_{rot} values, and we therefore retain the previous literature P_{rot} wherever possible.

In total, we add 136 rotators with non-*K2* P_{rot} to our Praesepe catalog, including 131 with $P_{mem} > 70\%$. The mass-period data for Praesepe members with existing P_{rot} measurements is shown in Figure 4.1.

[1]For details on these data, see Chapter 2 and the original papers.

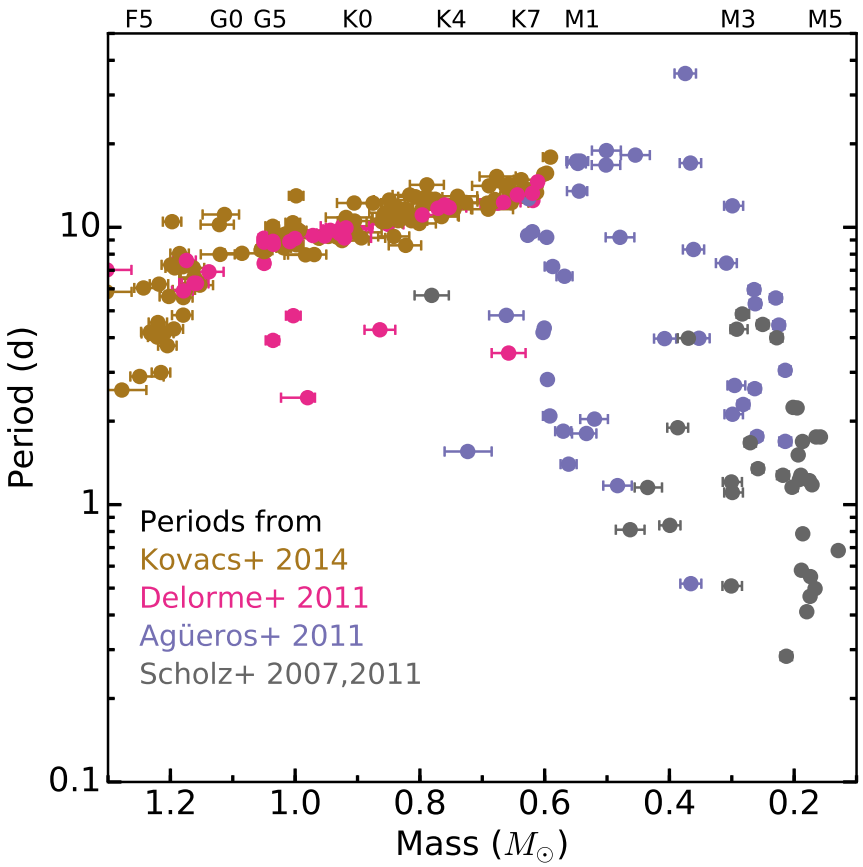

Figure 4.1 Praesepe mass-period plane showing all literature P_{rot} before the addition of the new *K2* data. Periods for F, G, and K dwarfs were measured from all-sky surveys by Kovács et al. (2014, brown) and Delorme et al. (2011, pink), while periods for M dwarfs were measured from targeted surveys of the cluster by Agüeros et al. (2011, purple), Scholz & Eislöffel (2007), and Scholz et al. (2011, both grey). Approximate spectral types corresponding to the plotted masses are indicated at the top of the plot.

Table 4.1. Praesepe members with discrepant P_{rot} measurements

Name[a]	EPIC	Agüeros et al. 2011 P_{rot} (d)	Delorme et al. 2011 P_{rot} (d)	Scholz et al. 2007, 2011 P_{rot} (d)	Kovacs et al. 2014 P_{rot} (d)	*K2* P_{rot} (d)
···	211885995	9.20	···	···	18.13	9.16
AD 1508	212009427	1.55	···	···	11.22	1.56
AD 1512	···	9.64	···	···	19.15	···
AD 2182	211734093	···	···	···	15.87	18.22
AD 2509	211970613	···	···	0.50	···	1.01
AD 2527	211939989	···	···	0.47	···	0.92
AD 2552	211989299	25.36	···	···	···	12.84
AD 2802	211980450	···	···	0.51	···	1.02
AD 3128	···	···	3.52	···	14.17	···
AD 3663	211773459	···	···	···	17.91	5.94
HSHJ 15	211971354	9.36	···	···	17.46	8.26
HSHJ229	211938988	···	···	2.29	···	1.09
HSHJ421	211944193	···	···	0.28	···	0.48
HSHJ436	211988700	···	···	4.87	···	6.46
JS140	211930699	···	···	···	13.35	6.74
JS298	211945362	···	···	4.29	···	9.16

Table 4.1—Continued

Name[a]	EPIC	Agüeros et al. 2011 P_{rot} (d)	Delorme et al. 2011 P_{rot} (d)	Scholz et al. 2007, 2011 P_{rot} (d)	Kovacs et al. 2014 P_{rot} (d)	*K2* P_{rot} (d)
JS313	211992053	···	···	5.76	···	5.08
JS379	212013132	···	4.27	···	12.78	2.13
JS418	211954582	···	···	3.27	12.75	3.19
JS432	···	2.09	···	···	8.36	···
JS503	212019252	···	9.95	···	···	11.26
JS547	211923502	···	···	···	10.73	12.07
JS655	211896596	···	···	···	5.85	2.97
JS719	211989620	···	···	1.21	···	0.88
KW 30	211995288	···	3.91	···	7.97	7.80
KW141	211940093	···	9.42	···	9.79	4.89
KW172	211975426	···	···	···	12.22	6.26
KW256	211920022	···	4.80	···	9.76	4.67
KW267	211970147	···	···	5.68	11.89	11.60
KW301	211936906	···	···	···	7.58	8.76
KW304	211996831	···	···	···	8.79	4.37
KW336	211911846	···	8.89	···	9.12	4.30

Table 4.1—Continued

Name[a]	EPIC	Agüeros et al. 2011 P_{rot} (d)	Delorme et al. 2011 P_{rot} (d)	Scholz et al. 2007, 2011 P_{rot} (d)	Kovacs et al. 2014 P_{rot} (d)	*K2* P_{rot} (d)
KW367	211975006	···	···	···	6.04	3.07
KW401	211909748	···	2.43	···	9.61	2.42
KW434	211935518	···	···	···	8.27	4.18
KW533	211954532	···	···	···	8.29	9.27
KW563	211970427	4.33	···	4.85	···	4.38
KW566	211988628	···	···	···	15.25	7.95
KW570	211983725	4.18	···	4.27	16.81	4.22

Note. — Only cluster members with at least two P_{rot} measurements that differ by at least 10% are shown here. An additional 215 cluster members have at least two P_{rot} measurements that agree to within 10%.

[a] Literature name given in Kraus & Hillenbrand (2007). All are standard SIMBAD identifiers, except AD####, which correspond to stars in Adams et al. (2002).

4.3 Measuring Rotation Periods with K2

K2 targeted Praesepe in its Campaign 5. We analyze the resulting long-cadence data for 794 Praesepe members identified in Section 4.2.1 and with *Kepler* magnitudes $K_p > 9$ mag and masses $M_* < 1.5\ M_\odot$. These limits exclude saturated stars as well as stars with radiative outer layers, which are outside of the scope of this work. The distribution of targets on the *K2* imager is shown in Figure 4.2. Of the 794 targets, 749 have a Kraus & Hillenbrand (2007) $P_{mem} > 70\%$.

4.3.1 K2 Light Curves

The pointing in *K2* is held in an unstable equilibrium against solar pressure by the two functioning reaction wheels. The spacecraft rolls about the boresight by up to 1 pixel at the edge of the focal plane. To correct for this, thrusters can be fired every 6 hr (if needed) to return the spacecraft to its original position. This drift causes stars to move in arcs on the focal plane, inducing a sawtooth-like signal in the 75-d light curve for each star (Van Cleve et al. 2016).

Several groups have developed methods for extracting photometry and removing the effect of the pointing drift from the raw light curve. We tested the light curves produced using several detrending methods (Vanderburg & Johnson 2014; Aigrain et al. 2016; Luger et al. 2016), as well as our own (see Section 3.4). We chose to use the light curves generated by the *K2* Systematics Correction method (K2SC; Aigrain et al. 2016) for our analysis, as this approach does the best job of removing systematics and long-period trends, which can bias period measurements or completely wash out periodic signals.

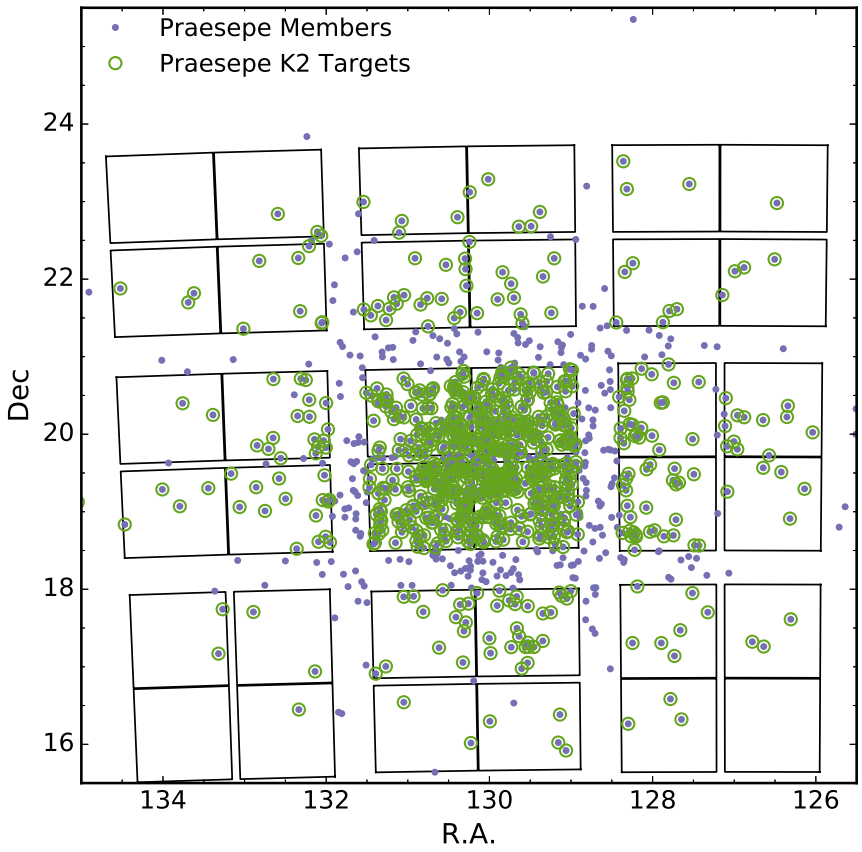

Figure 4.2 All Praesepe members (blue dots) and 794 K2 targets (green circles), with the *K2* chip edges overlaid. The entire cluster fits within the *K2* field-of-view, although many members still fall in the chip gaps. Two of the detector modules were no longer functioning by the time Campaign 5 started, but no Praesepe members fell on these modules.

Aigrain et al. (2016) use a semi-parametric Gaussian process model to correct for the spacecraft motion. These authors begin with the light curves and centroid positions produced by the *Kepler* Science Operations Center pipeline. They then simultaneously model the position-dependent, time-dependent, and white-noise components of the light curve. The time-dependent component should describe the intrinsic variability of the star, and the position-dependent component should describe the instrumental signal resulting from the spacecraft roll. In cases where a significant period between 0.05 and 20 d is

detected in the raw light curve, Aigrain et al. (2016) use a quasi-periodic kernel to describe the time-dependent trend; otherwise these authors use a squared-exponential kernel.

Since we wish to measure stellar variability, we remove only the position-dependent trend. The provided light-curve files include the position-dependent, time-dependent, and white-noise components in separate columns for both the simple aperture photometry (SAP) and pre-search data conditioning (PDC) pipeline light curves (Van Cleve et al. 2016). We use the PDC light curves, and compute the final light curve for our analysis by adding the white noise and time-dependent components, and then subtracting the median of the time-dependent component.[2]

4.3.2 Measuring Rotation Periods

We use the Press & Rybicki (1989) FFT-based Lomb-Scargle algorithm[3] to measure rotation periods. We compute the Lomb-Scargle periodogram power for $3{\times}10^4$ periods ranging from 0.1 to 70 d (approximately the length of the Campaign).

The periodogram power, which is normalized so that the maximum possible power is 1.0, is the first measurement of detection quality. The normalized power, P_{LS}, is related to the ratio of χ^2 for the sinusoidal model to χ^2_0 for a pure noise model (Ivezić et al. 2013):

$$P_{LS} = 1 - \frac{\chi^2}{\chi^2_0}. \tag{4.1}$$

A higher P_{LS} indicates that the signal is more likely sinusoidal, and a lower P_{LS}

[2] `https://archive.stsci.edu/missions/hlsp/k2sc/hlsp_k2sc_k2_llc_all_kepler_v1_readme.txt`
[3] Implemented as *lomb_scargle_fast* in the *gatspy* package; see `https://github.com/astroML/gatspy`.

indicates that it is more likely noise. Therefore, P_{LS} gives some information about the relative contributions of noise and periodic modulation to the light curve. We do not impose a global minimum value for P_{LS}. Instead, we compute a minimum significance threshold for each light curve.

We identify periodogram peaks using the *scipy.signal.argrelextrema* function, and define a peak as any point in the periodogram higher than at least 100 of the neighboring points. This value was chosen after some trial and error, and has the benefit of automatically rejecting most long period trends, because the periodogram is logarithmically sampled and has fewer points at long periods. Long period trends appear as a peak near 60–70 d with a series of harmonic peaks; these are generally rejected by *argrelextrema*. When there is a sinusoidal stellar signal in the light curve, it dominates the periodogram above any trends and is detected by *argrelextrema*.

We determine minimum significance thresholds for the periodogram peaks using bootstrap re-sampling, as in Section 3.4.3.1. We hold the observation epochs fixed and randomly redraw and replace the flux values to produce new scrambled light curves. We then compute a Lomb-Scargle periodogram for the scrambled light curve, and record the maximum periodogram power. We repeat this process 1000 times, and take the 99.9^{th} percentile of peak powers as our minimum significance threshold for that light curve. A peak in our original light curve is significant if its power is higher than this minimum threshold, which is listed in Table 4.3. We take the highest significant peak as our default P_{rot} value; twenty-three of our targets show no significant periodogram peaks.

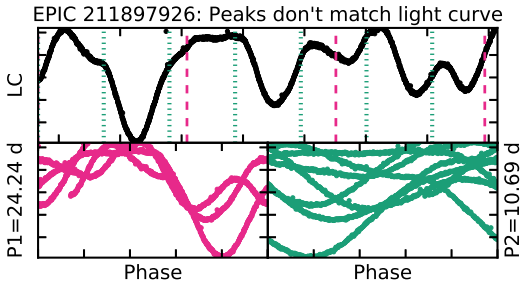

(a) Neither detected period matches the observable repeats in the full light curve; this may be a case of rapid spot evolution or differential rotation. We set Q = 2 as we cannot determine the correct period.

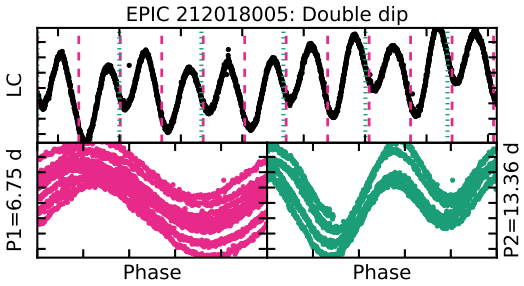

(b) Double-dip structure, periodogram selects half of the likely true period. We select the longer period and set Q = 0.

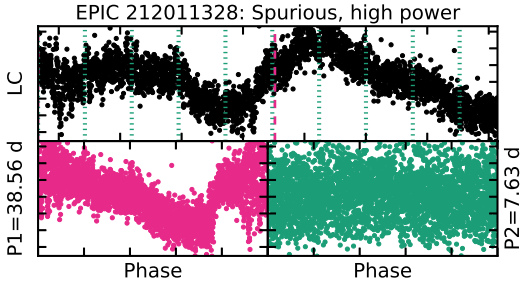

(c) A non-repeating trend is detected with high periodogram power; we set Q = 2.

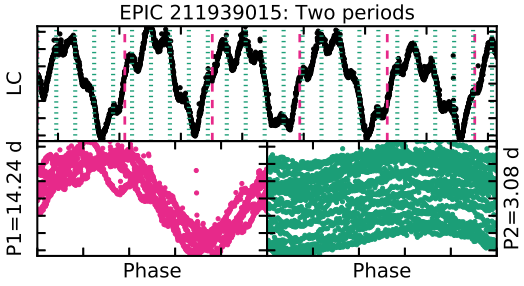

(d) There are two clear periods in the light curve. We set Q = 0, and we flag this target as definitely multiperiodic and therefore a candidate binary.

Figure 4.3 Examples of the light curve effects discussed in Section 4.3.3. Vertical lines at intervals of the detected period are overlaid on each full light curve, as in Figure 4.5. The phase-folded light curves corresponding to the first and second highest periodogram peaks are also shown.

4.3.3 Validating the Measured Rotation Periods

We combine automated and by-eye quality checks to validate the P_{rot}. The automated check comes from the peak periodogram power along with the number of, and power in, periodogram peaks beyond the first. Following Covey et al. (2016), we label a periodogram as clean if there are no peaks with more than 60% of the primary peak's power. The presence of such peaks may indicate that the P_{rot} measurement is incorrect. The clean flag

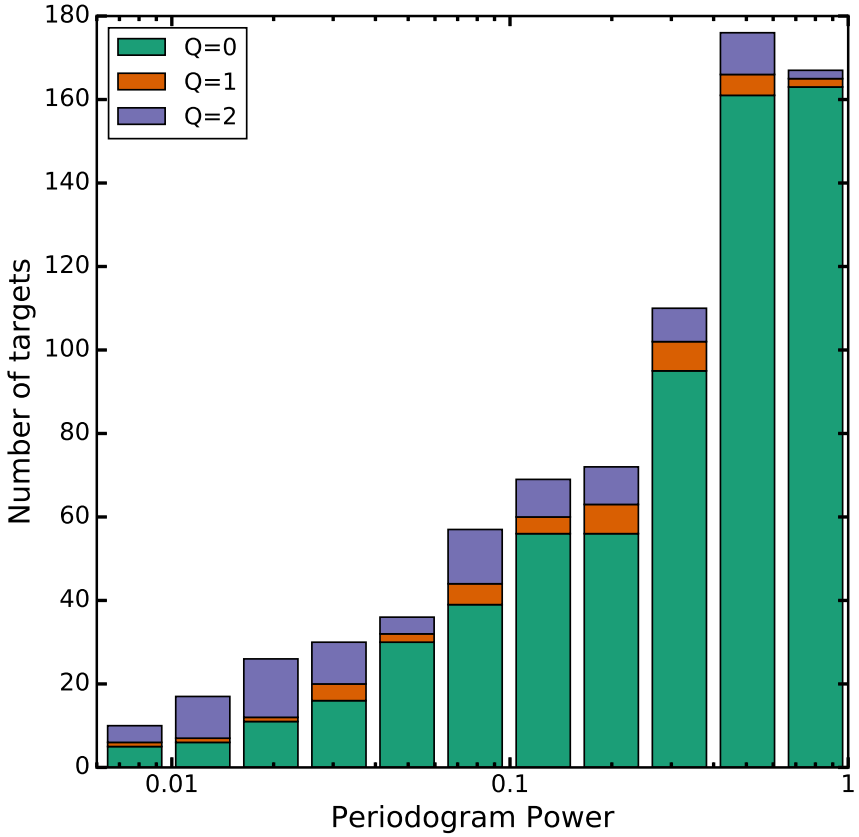

Figure 4.4 Histogram of periodogram powers from our sample; colors correspond to the flags assigned during our visual inspection of all P_{rot} detections. Spurious detections (Q = 2, purple) occur at a low rate across the full range of periodogram powers, motivating our visual inspection.

is included in Table 4.3; only 46 *K2* detections are not clean.

In addition, since instrumental signals can occasionally be detected at high significance, we inspect the periodograms and phase-folded light curves by eye to confirm detections. Clearly spurious detections are flagged as Q = 2, and questionable detections as Q = 1. This is similar to the approach used in Chapter 2, but we are more generous here and try to identify only the most obvious bad detections. In total, we remove 94 light curves. Additionally, a Q = 3 flag indicates that there were no significant periodogram

peaks; as noted earlier, this occurred for 23 stars.

The Q flag is separate from the clean/not-clean classification, and we do not change the Q value based on the clean/not-clean classification. We consider P_{rot} measurements with a clean periodogram and Q = 0 to be high-quality detections. In cases where we measure a *K2* P_{rot} for a star with a P_{rot} in the literature, the agreement is generally excellent (see Section 4.5.1). This indicates that our methods produce reasonable and valid P_{rot} measurements.

Following McQuillan et al. (2013), we plot the full light curve and, for $P_{rot} > 2$ d, vertical dashed lines at intervals of the detected period. We check that light curve features repeat over several intervals. We identify six cases where the phased light curve looks reasonable, but the pattern identified by eye does not match that detected in the periodogram (see Figure 4.5 and top panel of Figure 4.3), and we flag these with Q = 2.

We also identify 13 light curves where the dominant periodogram peak is likely for half of the true period and there is double-dip structure in the light curve (see second panel, Figure 4.3). There is typically a periodogram peak at this longer period that is weaker than the dominant peak. This feature is common in stellar light curves and usually attributed to symmetrical spot configurations and/or an evolving spot pattern on the stellar surface (McQuillan et al. 2013).

In most Q = 2 cases, the phase-folded light curve does not look sinusoidal (third panel, Figure 4.3), and the light curve is likely just noise. We also remove three stars where the saturation strip from a nearby star crosses the target pixel stamp, and one where the target is extended and likely a galaxy based on its Sloan Digital Sky Survey

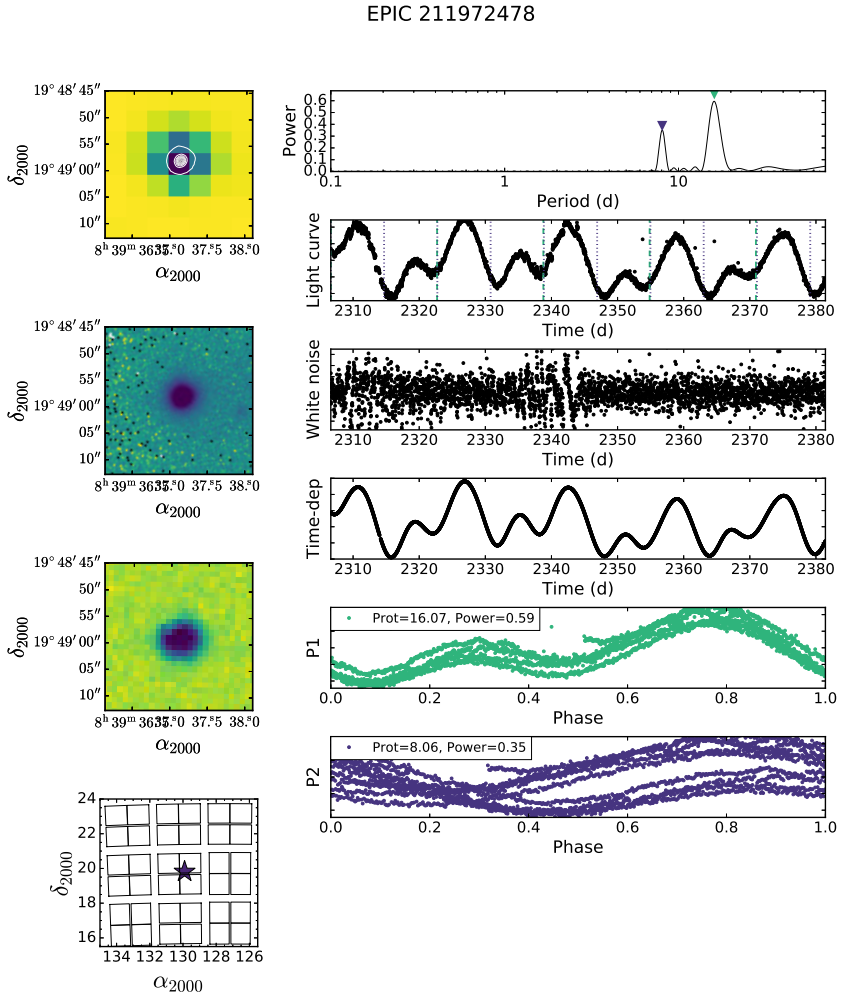

Figure 4.5 Example of the plots used to inspect period detections and check for neighboring stars. Left column, top to bottom: *K2* pixel stamp with SDSS *r*-band image overlaid as a contour; SDSS *r*-band image rotated into the *K2* frame; DSS red image rotated into the *K2* frame; and the target's position within the *K2* Campaign 5 field of view. Right column, top to bottom: Lomb-Scargle periodogram with (up to) the three highest significant peaks indicated by inverted triangles; the light curve corrected for spacecraft drift; the white-noise component of the light curve; the time-dependent component; and the light curve phase-folded on (up to) the three most significant periods. The colors of the markers indicating the peaks in the periodogram correspond to the colors of the phase-folded light curves. Versions of this plot for every *K2* target analyzed are available as an electronic figure set.

Data Release 12 (SDSS DR12; Alam et al. 2015) image.

As part of our visual inspection, we also note cases where two or more periods are detected, i.e., due to multiple stars being present in the aperture (fourth panel, Figure 4.3), or where there we find evidence for spot evolution (second panel, Figure 4.3). We assign flags for targets with multiple periods and with spot evolution: "Y" for yes, "M" for maybe, and "N" for no.

Finally, we note any other interesting light curve features, typically transits or eclipses (see Appendix B for discussion of the latter light curves). An example set of our inspection plots is shown in Figure 4.5, and the plots for all of our objects are available as an electronic figure set.

4.3.4 Photometric Amplitudes

We measure the amplitude of variability for a given star using the 10^{th} and 90^{th} percentiles (P_{10} and P_{90}) of the light curve in counts. We calculate the amplitude in magnitudes as

$$2.5 \times \frac{\left[\log_{10}\left(P_{90}\right) - \log_{10}\left(P_{10}\right)\right]}{2}. \tag{4.2}$$

This number may be slightly misleading, however, in cases where the median flux level varies over the course of the Campaign (a minor example is shown in the second panel of Figure 4.3). Therefore, we also calculate a smoothed version of the phase-folded light curve, and measure the amplitude as the percent difference between the maximum and minimum values of the smoothed light curve. This method, already used in Chapter 3,

tends to underpredict the amplitude of very fast rotators. We list both amplitudes in Table 4.3, but use the amplitude calculated using Equation 4.2 for all analysis below. Our results do not change significantly when using the amplitudes calculated by either method.

4.4 Binary Identification

We identify as many binary systems as possible among our *K2* targets, both to account for tidal effects and the more mundane impact of two (or more) stars blended on the chip. We denote all confirmed and candidate binaries in our analysis below.

Binary companions may impact rotational evolution via gravitational or magnetic interactions. Stars in very close binaries can exert tidal forces on each other, spinning them up or down more rapidly than predicted for a single star (e.g., Meibom & Mathieu 2005; Zahn 2008). These systems are also close enough for one star to interact with the other's large-scale magnetic field. And at the earliest evolutionary stages, a companion may truncate the protoplanetary disk, minimizing the impact of magnetic braking and allowing the young star to spin faster than its single counterparts (e.g., Rebull et al. 2004; Meibom et al. 2007; Cieza et al. 2009). Any of these effects could result in different angular-momentum evolution paths for stars with and without companions.

Furthermore, binaries may contaminate our analysis of P_{rot} distributions. If two stars are blended in ground-based images as well, the additional flux from the companion may cause us to overestimate L_{bol} and M_*. A companion may also dilute the rotational signal, leading to underestimated photometric amplitudes or masking the rotation of the fainter component altogether. In the case of two detected periods, it is impossible to tell

which signal comes from which star. These effects can cause stars to be misplaced in the mass-period plane, leading us to misidentify trends or transition periods.

4.4.1 Visual Identification

We examine a co-added *K2* image, a Digital Sky Survey (DSS) red image, and an SDSS (Alam et al. 2015) *r*-band image of each target to look for neighboring stars (see Figure 4.5). We use a flag of "Y" for yes, "M" for maybe, and "N" for no to indicate whether the target and a neighbor have blended PSFs on the *K2* chip. Stars flagged as "Y" are labeled candidate binaries; we find 159 such targets, or 23% of stars with *K2* P_{rot}.

To determine the likelihood that these are chance alignments, we offset the cluster positions by 15° in both RA and Dec and search for neighbors in the SDSS DR12. We restrict this search to objects with $g \leq 22$ mag, the SDSS 95% completeness limit. We find an SDSS object within 10'' (20'') of 8% (13%) of these offset positions. This suggests that at least 10% of Praesepe members have a very wide but bound companion, with separations on the order of 10^3–10^4 AU at Praesepe's distance (181.5±6 pc; van Leeuwen 2009). The other neighboring stars are likely background stars that could still contribute flux to the *K2* light curve. Lacking the observations to confirm which neighboring stars are actually bound companions, we consider all these stars to be candidate binaries in our analysis.

4.4.2 Photometric Identification

As in previous work, we identify candidate unresolved binaries that are overluminous for their color (see Figure 4.6). We identify a binary main sequence (MS) offset by 0.75 mag

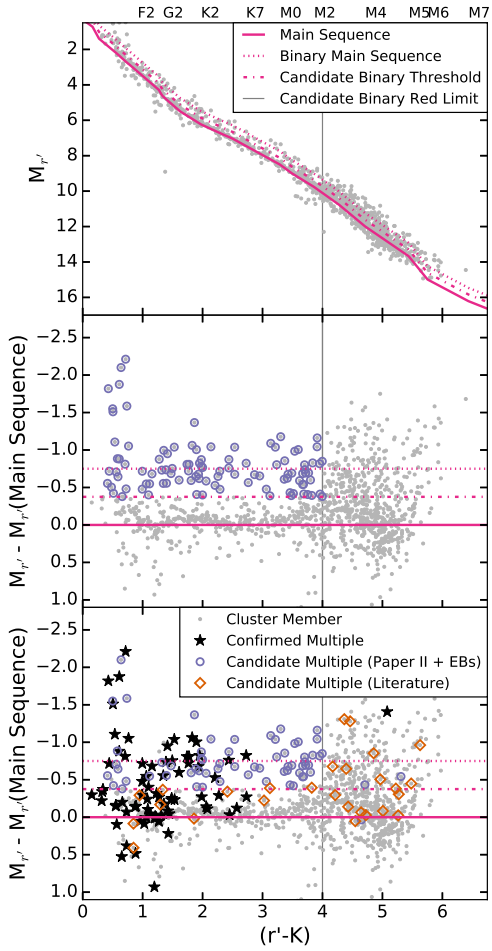

Figure 4.6 *Top* — CMD of Praesepe. The solid line is the single-star MS, identified using the spectal energy distributions assembled by Kraus & Hillenbrand (2007), and the dotted line the binary MS. We label any star above the dot-dashed line halfway between these two sequences as a candidate binary (as in Hodgkin et al. 1999). Stars with $(r' - K) \gtrsim 4$ have a wider range of magnitudes at a given color, and do not show an obvious MS, so we do not identify candidate photometric binaries in this color range. *Middle* — Residuals between each star's $M_{r'}$ and the model MS magnitude. Photometrically identified candidate binaries are shown as purple circles. This method is primarily sensitive to ≈equal-mass binaries. *Bottom* — Same as above, with confirmed and candidate binaries from the literature shown as black stars and open orange diamonds, respectively. Confirmed binaries can be found at all distances from the MS, illustrating the limitations of this approach to binary identification.

for a given color from that of single stars (as in Steele & Jameson 1995). We then label as candidate binary systems stars with $(r' - K) < 4$ that lie above the midpoint between the

single-star and binary MSs (Hodgkin et al. 1999). This method is biased towards binaries with equal masses, so that we are certainly missing candidate binaries with lower mass ratios. Indeed, confirmed multiples appear at all distances from the putatively single MS (as shown in Figure 4.6; also see Figure 3.3 for a similar analysis in the better-surveyed Hyades). Further observations and analysis are required to confirm the binary status of all cluster members.

We only apply this method to stars with $(r' - K) < 4$ because the single-star MS is less apparent for stars redder than this value. The observed spread in magnitudes could be due to binary systems at a variety of mass ratios, or to increased photometric uncertainties for these faint red stars. Identifying candidate binaries in this regime requires more information than just photometry.

4.4.3 Literature Identifications

Surveys for multiple systems in Praesepe have been undertaken using lunar occulations (Peterson & White 1984; Peterson et al. 1989), spectroscopy (Mermilliod et al. 1990; Bolte 1991; Abt & Willmarth 1999; Mermilliod & Mayor 1999; Halbwachs et al. 2003), speckle imaging (Mason et al. 1993; Patience et al. 2002), adaptive optics imaging (Bouvier et al. 2001), and time-domain photometry (e.g., Pepper et al. 2008). Spectroscopic binaries in Praesepe have also been identified through larger radial velocity (RV) surveys (Pourbaix et al. 2004; Mermilliod et al. 2009). Several of these surveys also note RV-variable or candidate binary systems. Bolte (1991) and Hodgkin et al. (1999) identify candidate binary systems by their position above the cluster main sequence (similar to our method

above).

Three planets have been detected from RV observations of two Praesepe members (Quinn et al. 2012; Malavolta et al. 2016), including one hot Jupiter in each system. One confirmed and eight candidate transiting planets have also been discovered from the *K2* data for the cluster (Pope et al. 2016; Barros et al. 2016; Libralato et al. 2016; Obermeier et al. 2016; Mann et al. 2016).

4.4.4 Binaries Identified from K2 Data

No eclipsing binaries in Praesepe have been published from the *K2* data so far, but we identify four likely eclipsing binaries and two single-transit events by eye; see Appendix B for details. One of these candidate eclipsing binaries was previously identified from PTF data, and has been confirmed with RVs (Kraus et al. in prep.). We consider the other three eclipsing binaries to be candidate binaries until we can confirm that the eclipses are not from a background system.

We also consider stars with multiple periods visible in the *K2* light curve to be candidate binaries if the two peaks are separated by at least 20% of the primary period. In other words, if

$$\frac{|P_{rot,1} - P_{rot,2}|}{P_{rot,1}} > 0.2, \tag{4.3}$$

we consider the target to be a candidate binary. This threshold is based on the maximum period separation for differentially rotating spot groups on the Sun (c.f. Rebull et al. 2016a). Fifty-eight *K2* targets have a second period detected in their periodogram, and nine more have a second period identified by eye only, giving 67 (10%) multiperiodic

Table 4.2. Companions to Praesepe members with measured P_{rot}

Name[a]	EPIC	2MASS	Binary Type	Triple Type	Source
KW350	211980142	J08405693+1956055	SB2	···	Dickens et al. (1968); Patience et al. (2002)
JS401	211896450	J08405866+1840303	Phot.	···	Douglas et al. (2014)
JS402	···	J08405968+1822045	Phot.	···	Douglas et al. (2014)
KW365	211923188	J08410737+1904165	SB1	SB1	Bolte (1991); Mermilliod et al. (1994); Mermilliod & Mayor (1999) Bouvier et al. (2001); Patience et al. (2002); Halbwachs et al. (2003) Mermilliod et al. (2009)
KW367	211975006	J08410961+1951187	SB1	SB1	Mermilliod et al. (1994); Mermilliod & Mayor (1999) Halbwachs et al. (2003); Mermilliod et al. (2009); Douglas et al. (2014)
KW371	211952381	J08411002+1930322	Phot.	···	Mermilliod & Mayor (1999); Patience et al. (2002)
KW368	211972627	J08411031+1949071	SB1	···	Mermilliod & Mayor (1999); Halbwachs et al. (2003) Mermilliod et al. (2009)
JS418	211954582	J08411319+1932349	Phot.	···	Hodgkin et al. (1999); Douglas et al. (2014)
KW375	211979345	J08411377+1955191	SB	···	Johnson (1952)
KW385	211935741	J08411840+1915395	Visual	···	Patience et al. (2002); Douglas et al. (2014)

Note. — This table is available in its entirety in a machine-readable form in the online journal. A portion is shown here for guidance regarding its form and content.

[a] Literature name given in Kraus & Hillenbrand (2007). All are standard SIMBAD identifiers, except AD####, which correspond to stars in Adams et al. (2002).

targets out of the 677 *K2* targets with measured P_{rot}.

In total, we find 82 confirmed binaries or triples, 92 candidate systems from our photometric analysis and the literature, and 170 additional candidate systems identified from our *K2* analysis. Table 4.2 lists the binary members and their relevant properties, and they are also flagged in Table 4.3. Aside from the M-dwarf eclipsing binary noted above, however, confirmed binaries in Praesepe are only found above 0.72 $M_{\odot}$, which limits our

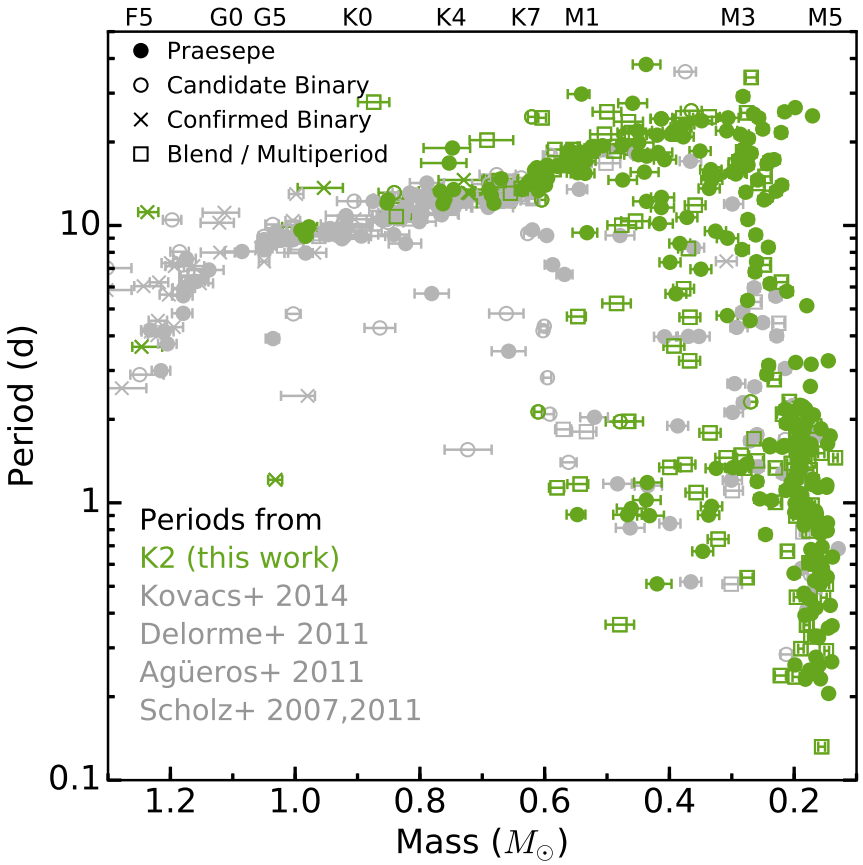

Figure 4.7 Praesepe mass-period plane showing literature (grey) and previously unpublished high-quality *K2* (green) P_{rot} for stars with $P_{mem} > 70\%$. We also mark confirmed and candidate binaries: crosses indicate confirmed binaries, open circles indicate photometric or spectroscopic candidate binaries, and open squares indicate *K2* targets with a blended neighbor or a second period in the light curve. Approximate spectral types are indicated along the top.

ability to analyze the impact of binaries on rotation and activity in low-mass Praesepe members.

4.5 Results and Discussion

We measure P_{rot} for 677 Praesepe members with *K2*, or 85% of the 794 Praesepe members with $P_{mem} > 50\%$ and *K2* light curves. Of these, 471 are new measurements, and 398 (84%) of these are considered high quality, meaning the periodogram is clean and our by-eye quality flag Q = 0 (see Section 4.3.3). This sample excludes 94 P_{rot} detections (12% of the original sample) that we flag as spurious and remove, along with 23 stars (3%) whose periodograms lack significant peaks. The cluster's updated mass-period distribution is shown in Figure 4.7. In addition to confirmed and candidate photometric or spectroscopic binaries, we also indicate cases where two or more stars may be contributing to the *K2* light curves: open squares are targets with blended neighbors or that show multiple periodic signals.

Table 4.3. P_{rot} measurements for Praesepe stars targeted in K2

Name[a]	EPIC	$P_{rot,1}$	Power$_1$	Q_1	Clean	Threshold	$P_{rot,2}$	Power$_2$	Q_2	Multi	Spot	Blend	Bin.	Ampl.(mag)
JC201	211930461	14.59	0.83910	0	Y	0.00816	···	···	···	N	Y	Y	Conf	0.00934
···	212094548	6.60	0.00890	1	N	0.00521	···	···	···	N	N	N	···	0.04953
···	211907293	···	···	2	···	···	···	···	···	···	···	···	0	···
KW222	211988287	3.29	0.20730	0	N	0.00861	···	···	···	M	Y	N	···	0.00281
KW238	211971871	2.96	0.66740	0	Y	0.00747	···	···	···	N	Y	N	···	0.01633
KW239	211992776	1.18	0.30260	0	Y	0.00791	···	···	···	M	Y	N	···	0.00109
KW282	211990908	2.56	0.25900	0	Y	0.00802	···	···	···	Y	Y	Y	Conf	0.00497
AD 2305	212100611	1.34	0.44670	0	Y	0.00776	1.8001	0.18730	0	Y	N	M	···	0.03630
AD 2482	211795467	15.49	0.23690	0	Y	0.00794	···	···	···	N	Y	N	···	0.01088
JS352	211913532	16.33	0.09270	0	Y	0.00723	2.8027	0.01060	0	Y	Y	N	Cand	0.01570

Note. — This table is available in its entirety in a machine-readable form in the online journal. A portion is shown here for guidance regarding its form and content.

[a] Literature name given in Kraus & Hillenbrand (2007). All are standard SIMBAD identifiers, except AD####, which correspond to stars in Adams et al. (2002).

4.5.1 Consistency of P_{rot} Measured from Different Surveys

There are 207 Praesepe members with P_{rot} measured both from *K2* data and from at least one ground-based survey. Another 51 members have P_{rot} measured by multiple ground-based surveys, but not by *K2*. The 43 stars with P_{rot} from at least two studies that differ by >10% are listed in Table 4.1. Overall, the agreement between *K2* and literature P_{rot} measurements is excellent: half of our *K2* measurements are consistent with previous measurements to within 2%, and >75% are consistent to within 5%.

Discrepant measurements are typically $\frac{1}{2}\times$ or $2\times$ harmonics of each other. All but two stars with discrepant P_{rot} show evidence of evolving spot configurations: either a double-dip light-curve structure or a varying amplitude of modulation over the course of the campaign. This signature is usually better resolved in the *K2* light curves, allowing us to measure the correct period even if it is not the highest periodogram peak.

Additionally, four stars with discrepant P_{rot} values show evidence for two periods in the light curve. The PTF and *K2* periods for EPIC 211937872 and EPIC 211971354 are $\approx$1 d apart; both *K2* light curves show a second $\approx$1 d period superimposed on the primary period, in addition to evidence of spot evolution. Two periods are detected in the *K2* data for EPIC 212013132: $P_{rot,1}$ = 2.13 d, half of the SWASP P_{rot} = 4.27 d, and $P_{rot,2}$ = 12.32 d, consistent with the Kovács et al. (2014) P_{rot} = 12.78 d. Finally, two periods are also detected in the *K2* light curve of EPIC 211734093: $P_{rot,1}$ = 18.22 d and $P_{rot,2}$ = 7.74 d. The latter of these is half of the Kovács et al. (2014) P_{rot} = 15.87 d. In all four cases, the second period in the light curve, possibly with additional spot evolution effects, accounts for the discrepancy between our *K2* P_{rot} values and those in the literature.

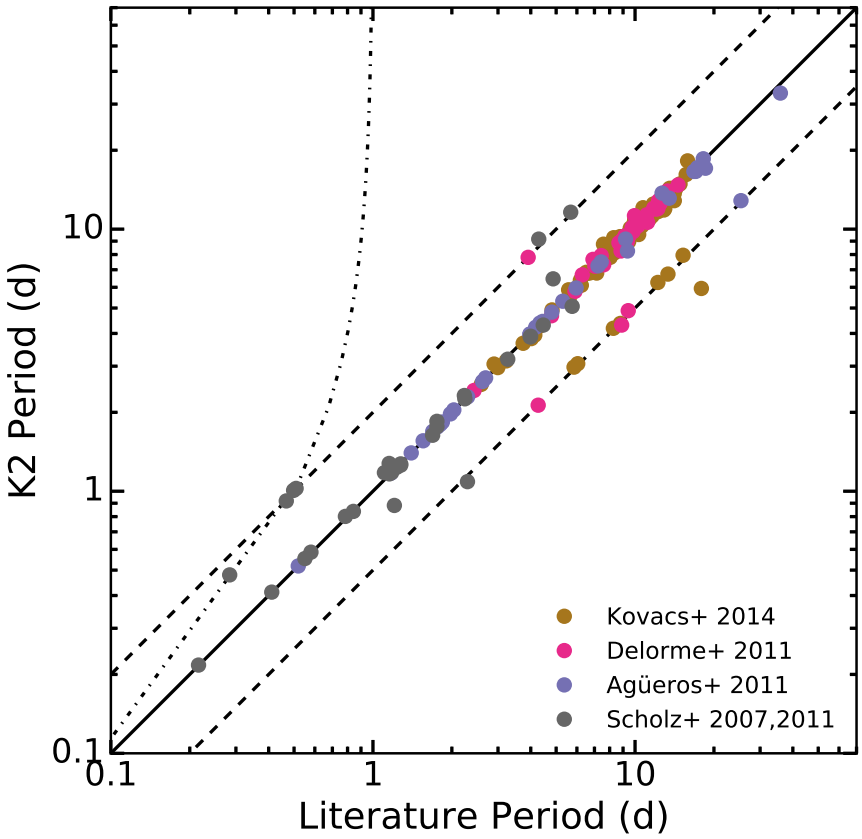

Figure 4.8 P_{rot} from *K2* compared to literature P_{rot} for the same stars. Colors are the same as in Figure 4.1. Our new P_{rot} are generally consistent with literature P_{rot}, except for a handful of cases where the older P_{rot} is a harmonic (dashed lines) or 1-d alias (dot-dashed line) of the *K2* P_{rot}.

In three cases, the P_{rot} measured by Scholz & Eislöffel (2007) and Scholz et al. (2011) is potentially a 1-d alias of the *K2* period. Scholz & Eislöffel (2007) surveyed Praesepe over three observing runs lasting three to five nights each, and Scholz et al. (2011) surveyed the cluster again for nine nights. Measurements over such short baselines are more prone to aliasing, particularly when the periods are so close to 0.5 or 1 d.

We find no strong evidence that the Praesepe stars with literature P_{rot} have larger photometric amplitudes (Figure 4.9), which has often been invoked to explain low P_{rot}

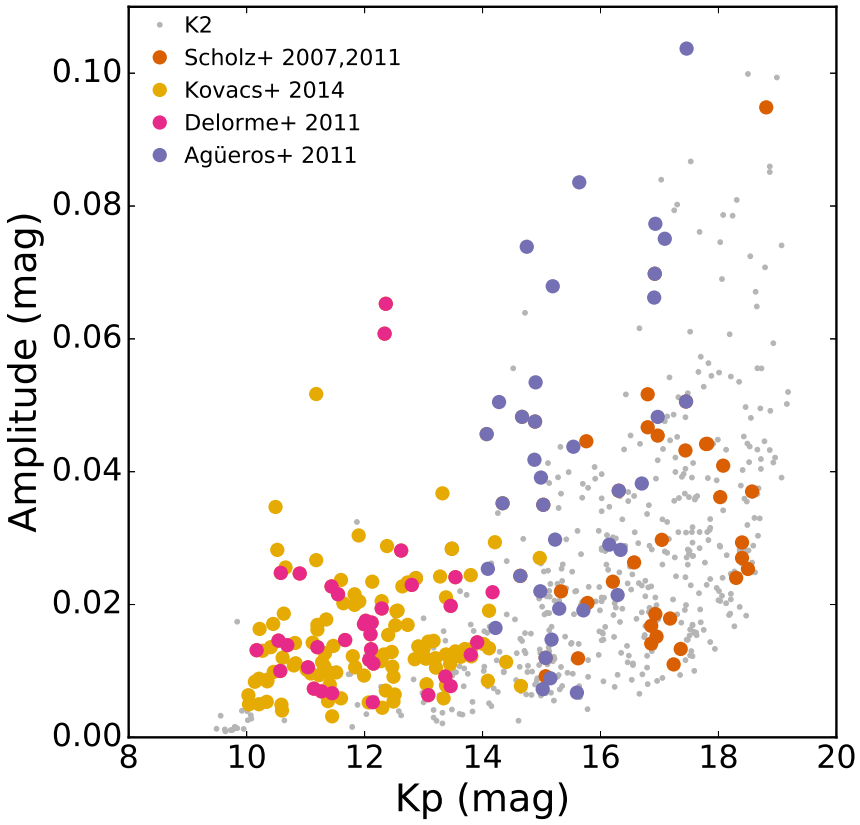

Figure 4.9 Amplitude of the *K2* light curve as a function of K_p; colors indicate stars with literature P_{rot} and are the same as in Figure 4.1. We find no strong evidence that stars with P_{rot} measured by ground-based surveys have higher amplitudes. Two targets with amplitudes >0.2 mag are not shown for clarity.

yields from ground-based surveys. The only partial exception to this are the PTF data: in Agüeros et al. (2011), we could only measure P_{rot} for stars with amplitudes $\gtrsim$0.02 mag ($\gtrsim$1%) for $K_p > 16$. Aside from this handful of PTF stars, small photometric amplitude—i.e., less contrast between starspots and the stellar photosphere—does not explain the incompleteness of ground-based surveys.

Overall, 86% of Praesepe *K2* targets have detectable P_{rot}, suggesting that non-detections in ground-based surveys are due primarily to limitations of those surveys rather than to inclination effects or spot coverage. Our Praesepe and Hyades *K2* P_{rot} are nearly all

consistent with previous measurements (Figure 4.8 and Section 3.5.1). We conclude that ground-based P_{rot} measurements are reasonably reliable, and that these surveys are merely limited by trade-offs between photometric precision, cadence, baseline, and number of targets; interruptions due to daylight and weather; and variable spot patterns on the stars themselves. Further comparisons of the *K2* data with ground-based light curves and survey techniques are needed to determine why previous surveys did not detect the rotators with new P_{rot} measured here.

Nonetheless, the overall agreement between the *K2* measurements and those of previous surveys indicates that our P_{rot} measurement procedures provide accurate results. It also bodes well for future ground-based surveys: while *K2*'s superior precision allows us to resolve detailed light-curve features, it appears that in general, ground-based surveys produce valid and reproducible P_{rot} measurements.

4.5.2 Binaries in the Mass-Period Plane

In Chapter 3, we found that nearly all the rapid rotators in the Hyades with $M_* \gtrsim 0.3\ M_\odot$ were confirmed or candidate binary systems. Of the three remaining rapid rotators, none had been surveyed for companions. The Hyades as a whole has been extensively surveyed for companions: >30% of all Hyads are confirmed binaries, including ≈45% of Hyads with measured P_{rot}. This suggested that all single stars with $M_* \gtrsim 0.3\ M_\odot$ have converged onto the slow-rotator sequence by ≈650 Myr.

For Praesepe stars, we define the cutoff between the slow-rotator sequence and more rapid rotators by computing the 75$^{\text{th}}$ percentile of periods for stars with $1.1 \gtrsim M_* \gtrsim 0.3\ M_\odot$,

and then lowering this threshold by 30%. This produces the orange line shown in Figure 4.10. We find that half of all rapidly rotating Praesepe stars are confirmed or candidate binaries.

Despite the far more extensive P_{rot} catalog in Praesepe relative to the Hyades, however, we are currently unable to confirm our result from Chapter 3 because Praesepe lacks a similarly rich binary catalog. Only 7% of all cluster members are confirmed binaries, and (with the exception of one eclipsing M-dwarf binary) these are restricted to $M_* \gtrsim 0.72\ M_\odot$. Our identification of candidate systems is also likely incomplete. Confident analysis of the impact of binaries on the mass-period plane requires additional binary searches in Praesepe.

Many stars on the slow-rotator sequence are also candidate binaries. This might suggest that companions have minimal impact on angular-momentum evolution. It could also indicate that different subsets of binaries undergo different rotational evolution.

The rapidly and slowly rotating binaries likely have different separation distributions, due to the impact of disk disruption on their initial angular-momentum content. Single stars experience braking due to their protoplanetary disks (Rebull et al. 2004). Binaries wider than 40 AU are unlikely to disrupt each others' protoplanetary disks (Cieza et al. 2009; Kraus et al. 2016) and are far too wide to be affected by tides—these systems will therefore evolve as (two) single stars. Binaries closer than 40 AU, on the other hand, are far more likely to have disrupted disks, which would allow the component stars to spin up without the losing angular momentum to their disks. These systems will arrive on the MS spinning more rapidly, and eventually spin down to converge with single stars. We expect

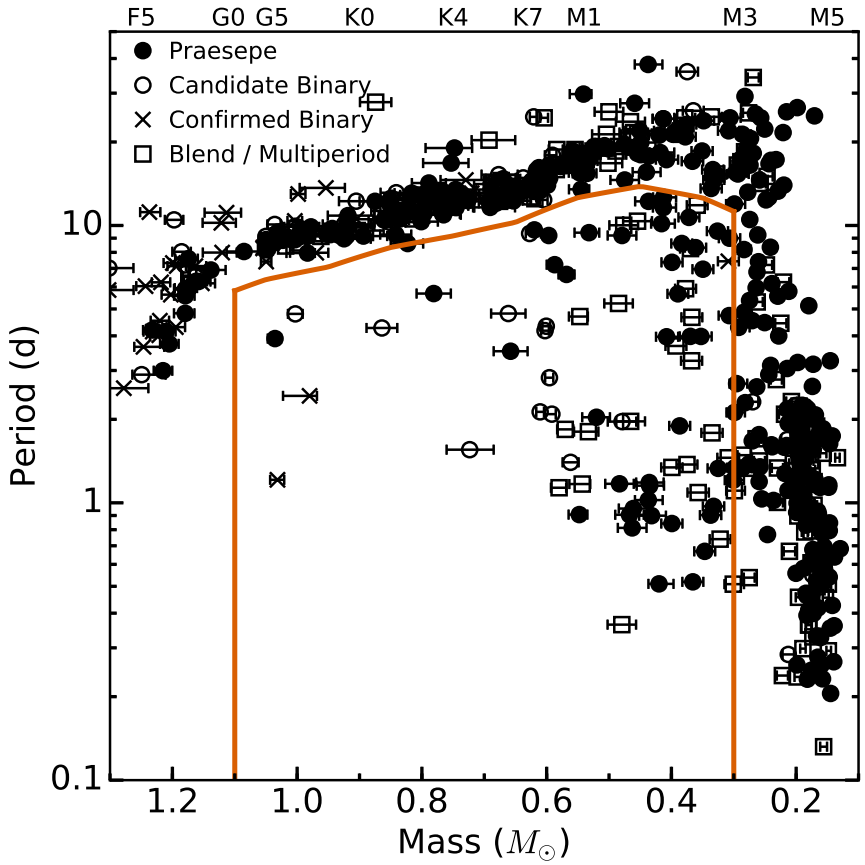

Figure 4.10 Mass-period plane with the region that defines $M_* > 0.3\ M_\odot$ rapid rotators outlined in orange. Half of the rapid rotators are confirmed or candidate binaries.

that future studies of Praesepe will find that binaries with slowly-rotating components are wider than 40 AU (≈0.2″ at ≈180 pc), while the rapidly rotating stars have companions at closer separations.

4.5.3 Comparison with Models of Rotation Evolution

In Chapter 3, we found that the Reiners & Mohanty (2012) and Matt et al. (2015) models for angular-momentum evolution predicted faster rotation than observed for 0.9−0.3 $M_\odot$ stars. However, this comparison was limited by the number of Hyads with P_{rot}. We

therefore compare our far richer Praesepe sample with the models of Matt et al. (2015) and Brown (2014), which were generously provided by these authors (S. Matt, private communication, 2015; T. Brown, private communication, 2017).

4.5.3.1 Matt et al. (2015)

Matt et al. (2015) derive a model for the angular-momentum evolution of a rotating solid sphere due to magnetic braking. These authors' initial conditions approximate the distribution of P_{rot} observed for 2−5-Myr-old stars, but are not drawn directly from observations. Matt et al. (2015) allow the stellar radius to evolve according to model evolutionary tracks. Their prescription for the angular momentum lost via stellar winds is based on the Kawaler (1988) and Matt et al. (2012a) solar-wind models, and the angular-momentum loss scales with stellar mass and radius. Matt et al. (2015) also use explicitly different spin-down rates for stars in the saturated and unsaturated regime.

The Matt et al. (2015) model accurately predicts the mass dependence of the slow-rotator sequence for Hyades and Praesepe stars with $M_* \gtrsim 0.8\,M_\odot$, with the exception of a handful of binary stars (see Figures 4.11–4.12). This indicates that, as in our comparison to the Hyades alone, the stellar-wind prescription used by Matt et al. (2015) is correct for solar-type stars.

The lower envelope of P_{rot} predicted by Matt et al. (2015) approximates that observed in Praesepe, although the distribution of rapidly rotating stars with $M_* \lesssim 0.8\,M_\odot$ is much more sparse than predicted by the model. Using the division between the slow sequence and faster rotators defined in Section 4.5.2, we observe that 26% of stars with masses

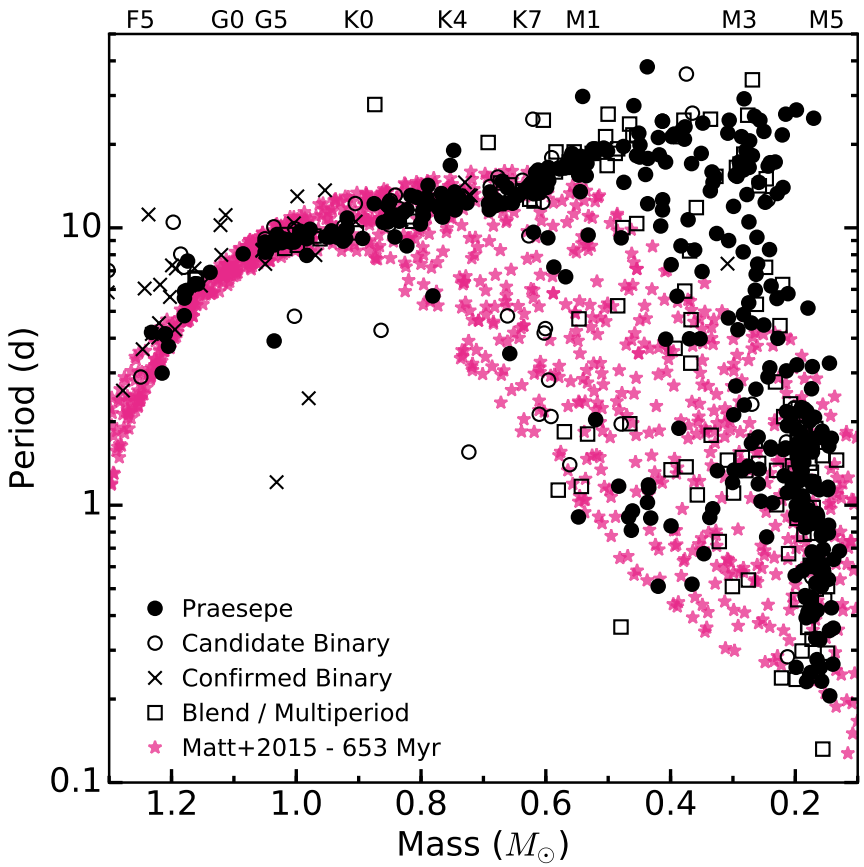

Figure 4.11 Comparison of P_{rot} in Praesepe (black; symbols are as in Figure 4.7) with the P_{rot} distribution predicted by Matt et al. (2015) at 653 Myr (purple stars). Only literature P_{rot} and clean, Q = 0 *K2* detections are shown. The model matches the slow-rotator sequence for single >0.8 $M_\odot$ stars, but fails to predict that the majority of 0.6−0.3 $M_\odot$ stars are slowly rotating.

0.3−0.8 $M_\odot$ are rapidly rotating, relative to 77% of model stars. In Figure 4.13, we have binned the model and data P_{rot} distributions by mass to allow for easier comparisons of the period distribution. Below ≈0.8 $M_\odot$, the Matt et al. (2015) model predicts a broader distribution of periods than is observed, while the observed P_{rot} are more concentrated at slow periods with a tail of fast rotators. This suggests that although the Matt et al. (2015) model may work for some 0.8−0.3 $M_\odot$ stars, it fails to predict the efficiency with which

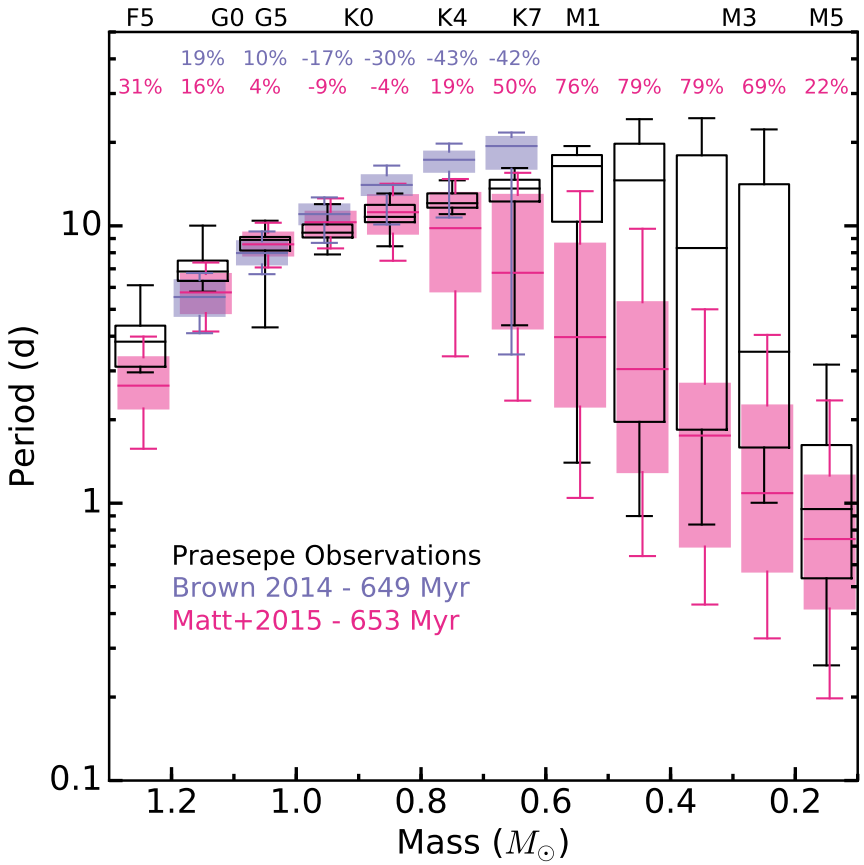

Figure 4.12 A box-and-whiskers plot of the Praesepe mass-period plane (black) compared to predictions by Brown (2014, purple) and Matt et al. (2015, pink). The boxes extend to the 25th and 75th percentiles, and the whiskers extend to the 5th and 95th percentiles. The percentage differences between the data and model medians are printed across the top of the plot. The Matt et al. (2015) models fail to predict the slow rotation periods for the majority of <0.6 $M_\odot$ stars.

<50% of stars in this mass range spin down.

The most obvious discrepancy between the Matt et al. (2015) models and our data occurs for slowly rotating early M stars with masses ≈0.6−0.3 $M_\odot$, as was previously noted in Matt et al. (2015) and Chapter 3. In our observations, more than half of the 0.6−0.3 $M_\odot$ stars have converged to the slow-rotator sequence, which extends fairly smoothly from ≈1−0.3 $M_\odot$ (see Figure 4.12), and more than half of the remaining rapid rotators are binaries

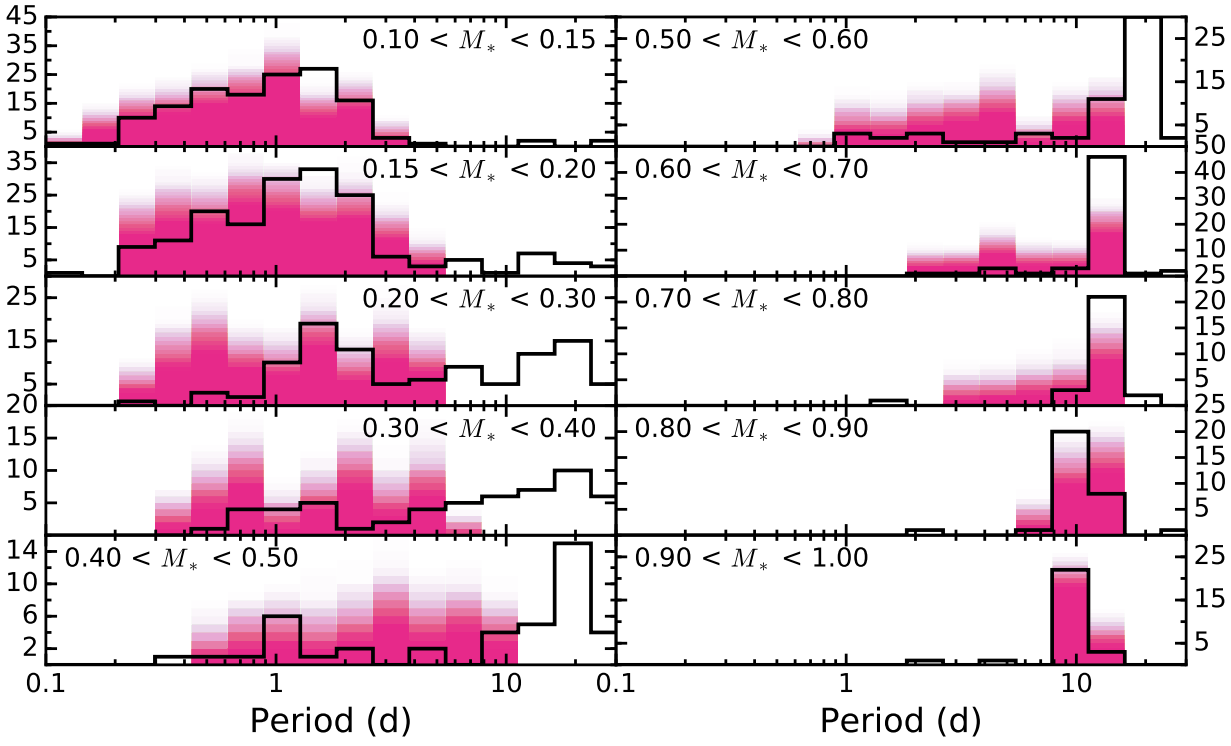

Figure 4.13 Praesepe P_{rot} distribution (solid line) compared to that predicted by Matt et al. (2015, shaded) for different mass bins. The mass bins are smaller at the lowest masses and larger for solar-type stars. The histograms represent 200 randomly drawn sets of modeled points; each set contains the same number of stars observed in that mass bin. These random subsets are plotted with transparency, so that the model histograms are darker when they are more frequently produced at that height. The model accurately tracks the slow-rotator sequence for >0.6 $M_\odot$ stars, but fails to predict the majority of slowly rotating M dwarfs.

(Figure 4.11).

By contrast, the model predicts an end to the slow-rotator sequence around 0.6 $M_\odot$, with the slowest rotators at lower masses being significantly faster than the slow rotators observed in our data. The median P_{rot} we observe for 0.6−0.3 $M_\odot$ stars is >75% slower than predicted (Figure 4.12). Furthermore, >60% of stars in this mass range rotate more slowly than the maximum P_{rot} predicted for their mass (Figure 4.13). It appears that real early M dwarfs brake far more efficiently than predicted by Matt et al. (2015).

This discrepancy suggests that most M dwarfs undergo enhanced angular-momentum loss relative to their higher mass counterparts. This could be due to a change in the structure of the magnetic field , i.e., a larger, less complex field with more open field lines near the star's equator that would allow the star to more efficiently shed angular momentum (i.e., Donati 2011; Garraffo et al. 2015c). It could also indicate a departure from solid-body rotation, which is assumed by Matt et al. (2015), for early M dwarfs. We could be observing an effect of the deepening convective zone for M dwarfs, through a change in the moment of inertia or in the dynamo as the radiative core shrinks with decreasing mass.

Despite the failure of the Matt et al. (2015) model to predict the observed behavior of early M dwarfs, this model does reasonably well in reproducing the distribution of rapidly rotating, fully convective 0.1−0.2 $M_{\odot}$ stars. This suggests that whatever is to blame for the discrepancy with observed early M dwarfs, the physical assumptions of Matt et al. (2015) do apply to fully convective stars.

4.5.3.2 Brown (2014): The Metastable Dynamo Model

Brown (2014) derives an empirical model for the generation and evolution of the fast and slow rotator sequences, called the Metastable Dynamo Model (MDM). He models all stars as solid bodies that are born with weak coupling between their dynamos and stellar winds, leading to minimal spin-down. The stars then spontaneously and permanently switch into a strong coupling mode where they spin down rapidly. Brown (2014) does not employ a critical P_{rot} for this switch—it is purely stochastic, with a mass-dependent probability of switching by a given stellar age. Taking as its starting point the distribution

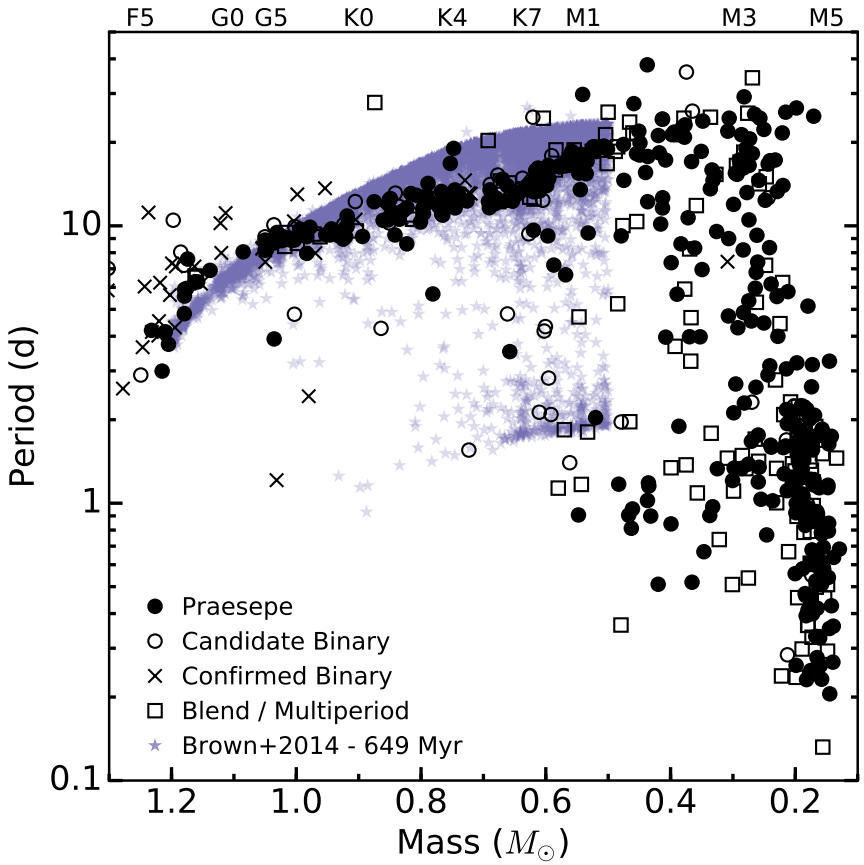

Figure 4.14 Comparison of P_{rot} in Praesepe (black; symbols are as in Figure 4.7) with the P_{rot} distribution predicted by Brown (2014) at 649 Myr (purple stars). Only literature P_{rot} and clean, Q = 0 *K2* detections are shown. This model only covers ≈1.2−0.5 $M_\odot$, and predicts a bimodal P_{rot} distribution. However, we do not observe a strongly bimodal distribution in Praesepe, and the model fails to predict the rapidly rotating Praesepe stars with $M_* \approx 0.6\,M_\odot$ and $P_{rot} \approx 1$ d.

of periods in the 13-Myr-old cluster h Per, the MDM generates a bimodal distribution at older ages: a fast sequence and a slow sequence separated by a gap, similar to the distribution observed by Barnes (2003).

The Brown (2014) model approximately reproduces the overall morphology of the mass-period plane in Praesepe: there is a clear sequence of slowly rotating stars with some faster rotators. A more careful comparison, however, indicates that the model and

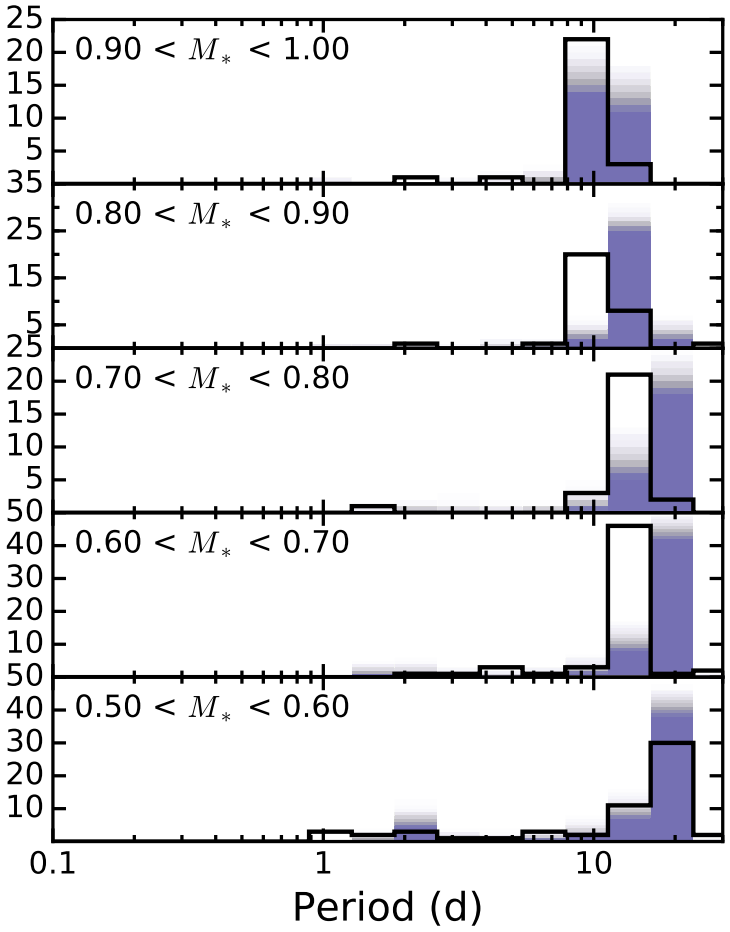

Figure 4.15 Praesepe P_{rot} distribution (solid line) compared to that predicted by Brown (2014, shaded) for different mass bins. Here again the mass bins are not even, and this model does not extend below 0.5 $M_\odot$. The histograms represent 200 randomly drawn sets of the modeled points; each set contains the same number of stars observed in that mass bin. This model correctly predicts that most stars will have converged onto the slow-rotator sequence by this age, but fails to predict the evolution of faster rotators.

data are discrepant. Specifically, the bimodality is not obvious in the data for Praesepe >0.5 $M_\odot$ stars, which is the mass regime covered by the MDM (Figures 4.14-4.15). The rapidly rotating Praesepe stars in this mass range are not strongly concentrated at any particular P_{rot}, nor is there an obvious gap at intermediate P_{rot}. Furthermore, using the division between slow and fast stars defined in Section 4.5.2, we find that 15% of observed

0.9−0.5 $M_\odot$ Praesepe stars are rapidly rotating, compared to only 7% in the model.

We do observe stronger bimodality for 0.25−0.5 $M_\odot$ stars, below the mass range modeled by the Brown (2014). The observed morphology does not match the predictions for >0.5 $M_\odot$ stars, however: the rapid rotators extend to $P_{rot} \approx \frac{1}{2}$ d and show a wider range of fast P_{rot}, in contrast to the clear lower limit of ≈1.5 d in the current model. Our observations of early M stars in Praesepe therefore support the Brown (2014) model's prediction of bimodality in the mass-period morphology, but adjustments are needed to extend the MDM to this mass range.

Finally, the predicted locations of the fastest and slowest rotators at a given mass do not match the observations. The slow-rotator sequence is too slow, while a handful of early M dwarfs with $0.5 \lesssim M_* \lesssim 0.6\ M_\odot$ rotate faster than predicted by the MDM. The offset of the slow sequence is visible in figure 6 of Brown (2014), who points out that more complicated physics is likely needed to explain the exact evolution of slow rotators. The too-fast rotators are not obvious in that figure, however, due to the use of a linear P_{rot} axis and the inclusion of only a few dozen P_{rot} from Delorme et al. (2011) and WEBDA, compared to the hundreds of P_{rot} included here.

4.6 Conclusions

We analyze *K2* light curves for 794 members of the Praesepe open cluster, and present P_{rot} for 677 *K2* targets. Of these, 471 are new measurements, bringing the total number of P_{rot} measurements for Praesepe members to 732.

We find that half of the rapidly rotating stars with $M_* \gtrsim 0.3\ M_\odot$ are confirmed or

candidate binary systems. The remaining $\gtrsim$0.3 $M_{\odot}$ fast rotators are not confirmed single stars, as they have not been searched for binary companions. We previously found that all rapidly rotating $\gtrsim$0.3 $M_{\odot}$ Hyads are binaries (Chapter 3), but we require deeper binary searches in Praesepe to confirm whether binaries in the two co-eval clusters have different P_{rot} distributions.

We also compare the P_{rot} distribution in Praesepe to that predicted by Matt et al. (2015) and Brown (2014) for ≈650 Myr-old stars. We find that Matt et al. (2015) correctly predict the slow rotator sequence for >0.8 $M_{\odot}$ stars, but that >60% of ≈0.6−0.3 $M_{\odot}$ stars are rotating more slowly than predicted. This suggests that a change in braking efficiency occurs for early M dwarfs, causing them to spin down more quickly than predicted using a scaled solar-wind model. We do not observe a clear bimodality in P_{rot} for Praesepe stars with $M_{*} > 0.5\ M_{\odot}$, in contrast with the Brown (2014) model predictions. We do observe stronger bimodality for 0.25−0.5 $M_{\odot}$ stars, but adjustments will likely be needed to extend the model to this mass range.

Binaries likely impact our comparison with these models, which assume that stars evolve in isolation. This should work well for actual single stars, of course, as well as for wider binaries that never interact, but not for closer binaries, many of which have yet to be identified in these open clusters. If most or all rapidly rotating stars are binaries, and particularly if their rapid rotation is due to increased initial angular-momentum content, then it is unsurprising that models struggle to replicate simultaneously the distributions of slow and rapid rotators. Theorists may be attempting to match a population of stars reflecting a set of initial conditions that do not match their assumptions. Confirmed single

stars will be better calibrators for these models, and binary surveys of Praesepe will be crucial for obtaining a proper benchmark sample.

Chapter 5

Conclusions

5.1 Distribution of rotation periods at 600 Myr

My work with *K2* data dramatically expands our knowledge of the distribution of rotation periods for ≈650 Myr-old stars. Just 10 years ago, only a few dozen stars in Praesepe and the Hyades had measured photometric rotation periods. 2011-2014 saw an explosion of new rotation studies, bringing the total number of P_{rot} in the two clusters to 363. Still, selection biases prevented us from being certain about the true distribution of P_{rot} at this age, especially since there was a dearth of P_{rot} detections for M dwarfs In Chapters 3-4, I measure rotation periods for 725 Hyades and Praesepe stars, including the first P_{rot} measurements ever for fully convective Hyads. My work brings the total number of P_{rot} measurements at 650 Myr to 871, more than twice the number that existed before *K2*.

In Praesepe especially, this new P_{rot} data enables us to see, for the first time, the full distribution of P_{rot} for M dwarfs. Rather than simply outlining the boundaries for fast and

slow rotation at this age, we can look more deeply at how periods are distributed at a given mass. The vast majority of F, G, and K stars with masses 0.6–1.3 $M_{\odot}$are concentrated on a single-valued sequence of slow rotators, and any remaining rapid rotators are binaries. In the Hyades, this sequence of single slow rotators extends almost down to the fully convective boundary, while the lack of binary identifications in Praesepe means that we cannot rule out a spread in P_{rot} for early M dwarfs. Finally, nearly all fully convective M dwarfs in the cluster are rapidly rotating.

I compare these new, detailed P_{rot} distributions to several models of rotational evolution and determined where the models still require improvement. Thus far, no model can replicate perfectly the mass-period distribution in the Hyades and Praesepe. Reiners & Mohanty (2012) vaguely reproduce the transition from a single-valued sequence to a spread of rapid rotators, but their predictions are too slow for solar-type stars and too fast for M dwarfs. They also predict the wrong slope altogether for the slow rotator sequence. The MDM reproduces a slow rotator sequence using largely statistical methods, but the sequence is in the wrong place compared to ≈650 Myr-old stars (Brown 2014). Matt et al. (2015) most closely match both solar-type stars and fully convective M dwarfs, but predict far too rapid rotation for early M dwarfs.

This discrepancy with early M dwarfs, found in both the Reiners & Mohanty (2012) and Matt et al. (2015) models, provides an intriguing puzzle for understanding stellar angular momentum evolution. Both models use Solar mass-loss values scaled by stellar mass and radius to predict mass-loss rates for stars of all masses. This works well to cause FGK stars to converge to the slow-rotator sequence by this age, but scaled Solar

mass-loss rates are insufficient for predicting the degree of spin-down in early M dwarfs Nonetheless, these authors' assumption for saturation in M dwarfs correctly predicts that all fully-convective stars at this are rapidly rotating, so either the insufficiency of the scaled Solar torques will not appear until later times, or these torques are in fact correct to use for fully convective stars.

5.2 Consistent Activity Distributions in the Hyades and Praesepe

Though often assumed to be co-eval, previous analysis of Praesepe and the Hyades conflicted on whether the two clusters actually show similar behavior. The most prominent of these, Kafka & Honeycutt (2006), compared new $H\alpha$ equivalent widths for Praesepe members to those measured for Hyades stars from a variety of spectra by several different authors. There are several ways to measure equivalent widths, and not all previous authors may have used the same method. Thus, previous authors were not comparing consistent samples when comparing the Hyades to Praesepe.

However, in Chapter 2, I show that the relation between $H\alpha$ emission and color in the Hyades is consistent with that observed for Praesepe stars. Figure 2.4 shows that, even when two authors claim to use the same measurement technique on the same spectra, their results can differ. By analyzing all spectra in our sample using the same method, I am able to bring the two clusters' $H\alpha$ activity-color relations into agreement, and Figure 2.5 demonstrates that stars in these clusters do in fact have comparable activity levels.

5.3 The activity-rotation relation at 650 Myr

In Chapter 2, I measure that $L_{H\alpha}/L_{bol}$ for known rotators in Praesepe and the Hyades, and fit a saturation-type model to this data. For slow rotators in these clusters, I find a power-law relation for $L_{H\alpha}/L_{bol}$ vs. R_o that is completely inconsistent with those derived from L_X/L_{bol} vs. R_o . What little archival data existed for Praesepe and the Hyades in 2014 is consistent with power laws derived for X-ray emission in a mixed-age sample of stars. This observation of different unsaturated activity-rotation relations appears to favor the coronal stripping theory. However, it is unclear whether this was due to the differences between chromospheric and coronal activity or simply to different mass ranges in the two samples.

I am currently measuring L_X/L_{bol} for low-mass stars using nine *XMM-Newton* observations of Praesepe and 40 *XMM-Newton* and Swift snapshot observations of Hyads. This will yield X-ray and $H\alpha$ activity samples that cover the same mass range, allowing a more robust comparison of these two activity tracers. If stars in the same mass range exhibit different X-ray and $H\alpha$ activity-rotation relations, this will support the theory that saturation is caused by centrifugal stripping of the corona. Because this work will illuminate the underlying magnetic field topology, it will also help improve models of stellar wind-driven rotational evolution.

5.4 Investigating the rotational evolution of binary stars

In my pre-*K2* work on the Hyades and Praesepe clusters, I find that most stars with $M_* \gtrsim 0.6\,M_\odot$ had spun down (Chapter 2. Using *K2*'s subsequent surveys of these clusters, however, I measure P_{rot} for 48 Hyads, including the first P_{rot} for fully convective members, and for 677 Praesepe stars (Chapters 3-4). I combine these P_{rot} with literature data to investigate how binaries impact the mass–period distribution at 650 Myr.

I find that when binaries are removed from the Hyades mass–period plane, nearly all the remaining stars with masses $\gtrsim$0.3 $M_\odot$ are slowly rotating. Removing binaries lowers the transition from a single-valued mass–period sequence by a factor of two in stellar mass. Approximately half of the rapid rotators in the same mass range in Praesepe are also candidate binaries, but without RV confirmation this result is tentative. It appears that the only thing keeping $M_* \gtrsim 0.3\,M_\odot$ Hyads spinning rapidly is a companion; studies of P_{rot} evolution must therefore account for binaries.

I am not the first to find that rapidly rotating stars tend to have companions. Most of the fastest rotators in M35 (150 Myr) are binaries, even when tidally locked systems are removed (Meibom et al. 2007). Pye et al. (1994), Patience et al. (2002) and Stauffer et al. (2016) also find indirect evidence that binary stars rotate more rapidly than their single counterparts in the Hyades, α Per (100 Myr), and the Pleiades (125 Myr). These studies focus on zero-age main sequence (ZAMS) clusters (i.e., α Per, Pleiades, and M35) and/or on indirect signatures of rotation, however, and could not investigate any dependence of rotation on binary orbital separations. My dissertation work contributes to mounting evidence that single stars and binaries have different P_{rot} distributions. For my post-

doctoral work, I will search for binaries—at all orbital radii, even beyond the classical tidal limit—to accompany our new wealth of P_{rot} in open clusters and test the impact of companions on rotation evolution.

Bibliography

Abazajian, K. N., Adelman-McCarthy, J. K., Agüeros, M. A., Allam, S. S., Allende Prieto, C., An, D., Anderson, K. S. J., Anderson, S. F., Annis, J., Bahcall, N. A., Bailer-Jones, C. A. L., Barentine, J. C., Bassett, B. A., Becker, A. C., Beers, T. C., Bell, E. F., Belokurov, V., Berlind, A. A., Berman, E. F., Bernardi, M., Bickerton, S. J., Bizyaev, D., Blakeslee, J. P., Blanton, M. R., Bochanski, J. J., Boroski, W. N., Brewington, H. J., Brinchmann, J., Brinkmann, J., Brunner, R. J., Budavári, T., Carey, L. N., Carliles, S., Carr, M. A., Castander, F. J., Cinabro, D., Connolly, A. J., Csabai, I., Cunha, C. E., Czarapata, P. C., Davenport, J. R. A., de Haas, E., Dilday, B., Doi, M., Eisenstein, D. J., Evans, M. L., Evans, N. W., Fan, X., Friedman, S. D., Frieman, J. A., Fukugita, M., Gänsicke, B. T., Gates, E., Gillespie, B., Gilmore, G., Gonzalez, B., Gonzalez, C. F., Grebel, E. K., Gunn, J. E., Györy, Z., Hall, P. B., Harding, P., Harris, F. H., Harvanek, M., Hawley, S. L., Hayes, J. J. E., Heckman, T. M., Hendry, J. S., Hennessy, G. S., Hindsley, R. B., Hoblitt, J., Hogan, C. J., Hogg, D. W., Holtzman, J. A., Hyde, J. B., Ichikawa, S.-i., Ichikawa, T., Im, M., Ivezić, Ž., Jester, S., Jiang, L., Johnson, J. A., Jorgensen, A. M., Jurić, M., Kent, S. M., Kessler, R., Kleinman, S. J., Knapp, G. R., Konishi, K., Kron, R. G., Krzesinski, J., Kuropatkin, N., Lampeitl, H., Lebedeva, S., Lee, M. G., Lee, Y. S., French Leger, R., Lépine, S., Li, N., Lima, M., Lin, H., Long, D. C., Loomis, C. P., Loveday, J., Lupton, R. H., Magnier, E., Malanushenko, O., Malanushenko, V., Mandelbaum, R., Margon, B., Marriner, J. P., Martínez-Delgado, D., Matsubara, T., McGehee, P. M., McKay, T. A., Meiksin, A., Morrison, H. L., Mullally, F., Munn, J. A., Murphy, T., Nash, T., Nebot, A., Neilsen, Jr., E. H., Newberg, H. J., Newman, P. R., Nichol, R. C., Nicinski, T., Nieto-Santisteban, M., Nitta, A., Okamura, S., Oravetz, D. J., Ostriker, J. P., Owen, R., Padmanabhan, N., Pan, K., Park, C., Pauls, G., Peoples, Jr., J., Percival, W. J., Pier, J. R., Pope, A. C., Pourbaix, D., Price, P. A., Purger, N., Quinn, T., Raddick, M. J., Re Fiorentin, P., Richards, G. T., Richmond, M. W., Riess, A. G., Rix, H.-W., Rockosi, C. M., Sako, M., Schlegel, D. J., Schneider, D. P., Scholz, R.-D., Schreiber, M. R., Schwope, A. D., Seljak, U., Sesar, B., Sheldon, E., Shimasaku, K., Sibley,

V. C., Simmons, A. E., Sivarani, T., Allyn Smith, J., Smith, M. C., Smolčić, V., Snedden, S. A., Stebbins, A., Steinmetz, M., Stoughton, C., Strauss, M. A., SubbaRao, M., Suto, Y., Szalay, A. S., Szapudi, I., Szkody, P., Tanaka, M., Tegmark, M., Teodoro, L. F. A., Thakar, A. R., Tremonti, C. A., Tucker, D. L., Uomoto, A., Vanden Berk, D. E., Vandenberg, J., Vidrih, S., Vogeley, M. S., Voges, W., Vogt, N. P., Wadadekar, Y., Watters, S., Weinberg, D. H., West, A. A., White, S. D. M., Wilhite, B. C., Wonders, A. C., Yanny, B., Yocum, D. R., York, D. G., Zehavi, I., Zibetti, S., & Zucker, D. B. 2009, The Astrophysical Journal Supplement Series, 182, 543

Abney, W. D. W. 1877, Monthly Notices of the Royal Astronomical Society, 37, 278

Abt, H. A. & Willmarth, D. W. 1999, The Astrophysical Journal, 521, 682

Adams, J. D., Stauffer, J. R., Skrutskie, M. F., Monet, D. G., Portegies Zwart, S. F., Janes, K. A., & Beichman, C. A. 2002, The Astronomical Journal, 124, 1570

Agüeros, M. A., Covey, K. R., Lemonias, J. J., Law, N. M., Kraus, A., Batalha, N., Bloom, J. S., Cenko, S. B., Kasliwal, M. M., Kulkarni, S. R., Nugent, P. E., Ofek, E. O., Poznanski, D., & Quimby, R. M. 2011, The Astrophysical Journal, 740, 110

Aigrain, S., Parviainen, H., & Pope, B. J. S. 2016, Monthly Notices of the Royal Astronomical Society, 459, 2408

Aihara, H., Allende Prieto, C., An, D., Anderson, S. F., Aubourg, É., Balbinot, E., Beers, T. C., Berlind, A. A., Bickerton, S. J., Bizyaev, D., Blanton, M. R., Bochanski, J. J., Bolton, A. S., Bovy, J., Brandt, W. N., Brinkmann, J., Brown, P. J., Brownstein, J. R., Busca, N. G., Campbell, H., Carr, M. A., Chen, Y., Chiappini, C., Comparat, J., Connolly, N., Cortes, M., Croft, R. A. C., Cuesta, A. J., da Costa, L. N., Davenport, J. R. A., Dawson, K., Dhital, S., Ealet, A., Ebelke, G. L., Edmondson, E. M., Eisenstein, D. J., Escoffier, S., Esposito, M., Evans, M. L., Fan, X., Femenía Castellá, B., Font-Ribera, A., Frinchaboy, P. M., Ge, J., Gillespie, B. A., Gilmore, G., González Hernández, J. I., Gott, J. R., Gould, A., Grebel, E. K., Gunn, J. E., Hamilton, J.-C., Harding, P., Harris, D. W., Hawley, S. L., Hearty, F. R., Ho, S., Hogg, D. W., Holtzman, J. A., Honscheid, K., Inada, N., Ivans, I. I., Jiang, L., Johnson, J. A., Jordan, C., Jordan, W. P., Kazin, E. A., Kirkby, D., Klaene, M. A., Knapp, G. R., Kneib, J.-P., Kochanek, C. S., Koesterke, L., Kollmeier, J. A., Kron, R. G., Lampeitl, H., Lang, D., Le Goff, J.-M., Lee, Y. S., Lin, Y.-T., Long, D. C., Loomis, C. P., Lucatello, S., Lundgren, B., Lupton, R. H., Ma, Z., MacDonald, N., Mahadevan, S., Maia, M. A. G., Makler, M., Malanushenko, E., Malanushenko, V., Mandelbaum, R., Maraston,

C., Margala, D., Masters, K. L., McBride, C. K., McGehee, P. M., McGreer, I. D., Ménard, B., Miralda-Escudé, J., Morrison, H. L., Mullally, F., Muna, D., Munn, J. A., Murayama, H., Myers, A. D., Naugle, T., Neto, A. F., Nguyen, D. C., Nichol, R. C., O'Connell, R. W., Ogando, R. L. C., Olmstead, M. D., Oravetz, D. J., Padmanabhan, N., Palanque-Delabrouille, N., Pan, K., Pandey, P., Pâris, I., Percival, W. J., Petitjean, P., Pfaffenberger, R., Pforr, J., Phleps, S., Pichon, C., Pieri, M. M., Prada, F., Price-Whelan, A. M., Raddick, M. J., Ramos, B. H. F., Reylé, C., Rich, J., Richards, G. T., Rix, H.-W., Robin, A. C., Rocha-Pinto, H. J., Rockosi, C. M., Roe, N. A., Rollinde, E., Ross, A. J., Ross, N. P., Rossetto, B. M., Sánchez, A. G., Sayres, C., Schlegel, D. J., Schlesinger, K. J., Schmidt, S. J., Schneider, D. P., Sheldon, E., Shu, Y., Simmerer, J., Simmons, A. E., Sivarani, T., Snedden, S. A., Sobeck, J. S., Steinmetz, M., Strauss, M. A., Szalay, A. S., Tanaka, M., Thakar, A. R., Thomas, D., Tinker, J. L., Tofflemire, B. M., Tojeiro, R., Tremonti, C. A., Vandenberg, J., Vargas Magaña, M., Verde, L., Vogt, N. P., Wake, D. A., Wang, J., Weaver, B. A., Weinberg, D. H., White, M., White, S. D. M., Yanny, B., Yasuda, N., Yeche, C., & Zehavi, I. 2011, The Astrophysical Journal Supplement Series, 193, 29

Alam, S., Albareti, F. D., Allende Prieto, C., Anders, F., Anderson, S. F., Anderton, T., Andrews, B. H., Armengaud, E., Aubourg, É., Bailey, S., Basu, S., Bautista, J. E., Beaton, R. L., Beers, T. C., Bender, C. F., Berlind, A. A., Beutler, F., Bhardwaj, V., Bird, J. C., Bizyaev, D., Blake, C. H., Blanton, M. R., Blomqvist, M., Bochanski, J. J., Bolton, A. S., Bovy, J., Shelden Bradley, A., Brandt, W. N., Brauer, D. E., Brinkmann, J., Brown, P. J., Brownstein, J. R., Burden, A., Burtin, E., Busca, N. G., Cai, Z., Capozzi, D., Carnero Rosell, A., Carr, M. A., Carrera, R., Chambers, K. C., Chaplin, W. J., Chen, Y.-C., Chiappini, C., Chojnowski, S. D., Chuang, C.-H., Clerc, N., Comparat, J., Covey, K., Croft, R. A. C., Cuesta, A. J., Cunha, K., da Costa, L. N., Da Rio, N., Davenport, J. R. A., Dawson, K. S., De Lee, N., Delubac, T., Deshpande, R., Dhital, S., Dutra-Ferreira, L., Dwelly, T., Ealet, A., Ebelke, G. L., Edmondson, E. M., Eisenstein, D. J., Ellsworth, T., Elsworth, Y., Epstein, C. R., Eracleous, M., Escoffier, S., Esposito, M., Evans, M. L., Fan, X., Fernández-Alvar, E., Feuillet, D., Filiz Ak, N., Finley, H., Finoguenov, A., Flaherty, K., Fleming, S. W., Font-Ribera, A., Foster, J., Frinchaboy, P. M., Galbraith-Frew, J. G., García, R. A., García-Hernández, D. A., García Pérez, A. E., Gaulme, P., Ge, J., Génova-Santos, R., Georgakakis, A., Ghezzi, L., Gillespie, B. A., Girardi, L., Goddard, D., Gontcho, S. G. A., González Hernández, J. I., Grebel, E. K., Green, P. J., Grieb, J. N., Grieves, N., Gunn, J. E., Guo, H., Harding, P., Hasselquist, S., Hawley, S. L., Hayden, M., Hearty, F. R., Hekker, S., Ho, S., Hogg, D. W., Holley-Bockelmann, K., Holtzman, J. A., Honscheid, K., Huber, D., Huehnerhoff, J., Ivans, I. I., Jiang, L., Johnson, J. A., Kinemuchi, K., Kirkby, D., Kitaura,

F., Klaene, M. A., Knapp, G. R., Kneib, J.-P., Koenig, X. P., Lam, C. R., Lan, T.-W., Lang, D., Laurent, P., Le Goff, J.-M., Leauthaud, A., Lee, K.-G., Lee, Y. S., Licquia, T. C., Liu, J., Long, D. C., López-Corredoira, M., Lorenzo-Oliveira, D., Lucatello, S., Lundgren, B., Lupton, R. H., Mack, III, C. E., Mahadevan, S., Maia, M. A. G., Majewski, S. R., Malanushenko, E., Malanushenko, V., Manchado, A., Manera, M., Mao, Q., Maraston, C., Marchwinski, R. C., Margala, D., Martell, S. L., Martig, M., Masters, K. L., Mathur, S., McBride, C. K., McGehee, P. M., McGreer, I. D., McMahon, R. G., Ménard, B., Menzel, M.-L., Merloni, A., Mészáros, S., Miller, A. A., Miralda-Escudé, J., Miyatake, H., Montero-Dorta, A. D., More, S., Morganson, E., Morice-Atkinson, X., Morrison, H. L., Mosser, B., Muna, D., Myers, A. D., Nandra, K., Newman, J. A., Neyrinck, M., Nguyen, D. C., Nichol, R. C., Nidever, D. L., Noterdaeme, P., Nuza, S. E., O'Connell, J. E., O'Connell, R. W., O'Connell, R., Ogando, R. L. C., Olmstead, M. D., Oravetz, A. E., Oravetz, D. J., Osumi, K., Owen, R., Padgett, D. L., Padmanabhan, N., Paegert, M., Palanque-Delabrouille, N., Pan, K., Parejko, J. K., Paris, I., Park, C., Pattarakijwanich, P., Pellejero-Ibanez, M., Pepper, J., Percival, W. J., Perez-Fournon, I., Prez-Rafols, I., Petitjean, P., Pieri, M. M., Pinsonneault, M. H., Porto de Mello, G. F., Prada, F., Prakash, A., Price-Whelan, A. M., Protopapas, P., Raddick, M. J., Rahman, M., Reid, B. A., Rich, J., Rix, H.-W., Robin, A. C., Rockosi, C. M., Rodrigues, T. S., Rodríguez-Torres, S., Roe, N. A., Ross, A. J., Ross, N. P., Rossi, G., Ruan, J. J., Rubiño-Martín, J. A., Rykoff, E. S., Salazar-Albornoz, S., Salvato, M., Samushia, L., Sánchez, A. G., Santiago, B., Sayres, C., Schiavon, R. P., Schlegel, D. J., Schmidt, S. J., Schneider, D. P., Schultheis, M., Schwope, A. D., Scóccola, C. G., Scott, C., Sellgren, K., Seo, H.-J., Serenelli, A., Shane, N., Shen, Y., Shetrone, M., Shu, Y., Silva Aguirre, V., Sivarani, T., Skrutskie, M. F., Slosar, A., Smith, V. V., Sobreira, F., Souto, D., Stassun, K. G., Steinmetz, M., Stello, D., Strauss, M. A., Streblyanska, A., Suzuki, N., Swanson, M. E. C., Tan, J. C., Tayar, J., Terrien, R. C., Thakar, A. R., Thomas, D., Thomas, N., Thompson, B. A., Tinker, J. L., Tojeiro, R., Troup, N. W., Vargas-Magaña, M., Vazquez, J. A., Verde, L., Viel, M., Vogt, N. P., Wake, D. A., Wang, J., Weaver, B. A., Weinberg, D. H., Weiner, B. J., White, M., Wilson, J. C., Wisniewski, J. P., Wood-Vasey, W. M., Ye'che, C., York, D. G., Zakamska, N. L., Zamora, O., Zasowski, G., Zehavi, I., Zhao, G.-B., Zheng, Z., Zhou, X., Zhou, Z., Zou, H., & Zhu, G. 2015, The Astrophysical Journal Supplement Series, 219, 12

Allen, L. E. & Strom, K. M. 1995, The Astronomical Journal, 109, 1379

Artiukhina, N. M. 1971, Soobshcheniya Gosudarstvennogo Astronomicheskogo Instituta, 172, 3

Astropy Collaboration, Robitaille, T. P., Tollerud, E. J., Greenfield, P., Droettboom, M., Bray, E., Aldcroft, T., Davis, M., Ginsburg, A., Price-Whelan, A. M., Kerzendorf, W. E., Conley, A., Crighton, N., Barbary, K., Muna, D., Ferguson, H., Grollier, F., Parikh, M. M., Nair, P. H., Unther, H. M., Deil, C., Woillez, J., Conseil, S., Kramer, R., Turner, J. E. H., Singer, L., Fox, R., Weaver, B. A., Zabalza, V., Edwards, Z. I., Azalee Bostroem, K., Burke, D. J., Casey, A. R., Crawford, S. M., Dencheva, N., Ely, J., Jenness, T., Labrie, K., Lim, P. L., Pierfederici, F., Pontzen, A., Ptak, A., Refsdal, B., Servillat, M., & Streicher, O. 2013, Astronomy and Astrophysics, 558, A33

Astudillo-Defru, N., Delfosse, X., Bonfils, X., Forveille, T., Lovis, C., & Rameau, J. 2017, Astronomy and Astrophysics, 600, A13

Attridge, J. M. & Herbst, W. 1992, The Astrophysical Journal Letters, 398, L61

Babcock, H. W. 1961, The Astrophysical Journal, 133, 572

Bailer-Jones, C. A. L. & Mundt, R. 2001, Astronomy and Astrophysics, 367, 218

Baliunas, S., Sokoloff, D., & Soon, W. 1996, The Astrophysical Journal Letters, 457, L99

Baraffe, I., Chabrier, G., Allard, F., & Hauschildt, P. H. 1998, Astronomy & Astrophysics, 337, 403

Barnes, J. R. 2005, Monthly Notices of the Royal Astronomical Society, 364, 137

Barnes, S. & Sofia, S. 1996, The Astrophysical Journal, 462, 746

Barnes, S., Sofia, S., & Pinsonneault, M. 2001, The Astrophysical Journal, 548, 1071

Barnes, S. A. 2003, The Astrophysical Journal, 586, 464

—. 2010, The Astrophysical Journal, 722, 222

Barnes, S. A. & Kim, Y.-C. 2010, The Astrophysical Journal, 721, 675

Barnes, S. A., Weingrill, J., Fritzewski, D., Strassmeier, K. G., & Platais, I. 2016, The Astrophysical Journal, 823, 16

Barrado y Navascues, D. & Stauffer, J. R. 1996, Astronomy and Astrophysics, 310, 879

Barros, S. C. C., Demangeon, O., & Deleuil, M. 2016, Astronomy and Astrophysics, 594, A100

Bilir, S., Ak, S., Karaali, S., Cabrera-Lavers, A., Chonis, T. S., & Gaskell, C. M. 2008, Monthly Notices of the Royal Astronomical Society, 384, 1178

Binney, J. & Tremaine, S. 2008, Galactic Dynamics, 2nd edn., Princeton Series in Astrophysics (Princeton, NJ: Princeton University Press)

Bochanski, J. J., Hennawi, J. F., Simcoe, R. A., Prochaska, J. X., West, A. A., Burgasser, A. J., Burles, S. M., Bernstein, R. A., Williams, C. L., & Murphy, M. T. 2009, Publications of the Astronomical Society of the Pacific, 121, 1409

Boesgaard, A. M. & Hagen, W. 1974, The Astrophysical Journal, 189, 85

Bolte, M. 1991, The Astrophysical Journal, 376, 514

Bonatto, C., Lima, E. F., & Bica, E. 2012, Astronomy and Astrophysics, 540, A137

Borucki, W. J., Koch, D., Basri, G., Batalha, N., Brown, T., Caldwell, D., Caldwell, J., Christensen-Dalsgaard, J., Cochran, W. D., DeVore, E., Dunham, E. W., Dupree, A. K., Gautier, T. N., Geary, J. C., Gilliland, R., Gould, A., Howell, S. B., Jenkins, J. M., Kondo, Y., Latham, D. W., Marcy, G. W., Meibom, S., Kjeldsen, H., Lissauer, J. J., Monet, D. G., Morrison, D., Sasselov, D., Tarter, J., Boss, A., Brownlee, D., Owen, T., Buzasi, D., Charbonneau, D., Doyle, L., Fortney, J., Ford, E. B., Holman, M. J., Seager, S., Steffen, J. H., Welsh, W. F., Rowe, J., Anderson, H., Buchhave, L., Ciardi, D., Walkowicz, L., Sherry, W., Horch, E., Isaacson, H., Everett, M. E., Fischer, D., Torres, G., Johnson, J. A., Endl, M., MacQueen, P., Bryson, S. T., Dotson, J., Haas, M., Kolodziejczak, J., Van Cleve, J., Chandrasekaran, H., Twicken, J. D., Quintana, E. V., Clarke, B. D., Allen, C., Li, J., Wu, H., Tenenbaum, P., Verner, E., Bruhweiler, F., Barnes, J., & Prsa, A. 2010, Science, 327, 977

Bouvier, J. 2008, Astronomy and Astrophysics, 489, L53

Bouvier, J., Duchêne, G., Mermilliod, J.-C., & Simon, T. 2001, Astronomy and Astrophysics, 375, 989

Bouvier, J., Matt, S. P., Mohanty, S., Scholz, A., Stassun, K. G., & Zanni, C. 2014, in Protostars and Planets VI, Space Science Series (University of Arizona Press), 433–450

Boyajian, T. S., von Braun, K., van Belle, G., McAlister, H. A., ten Brummelaar, T. A., Kane, S. R., Muirhead, P. S., Jones, J., White, R., Schaefer, G., Ciardi, D., Henry, T., López-Morales, M., Ridgway, S., Gies, D., Jao, W.-C., Rojas-Ayala, B., Parks, J. R., Sturmann,

L., Sturmann, J., Turner, N. H., Farrington, C., Goldfinger, P. J., & Berger, D. H. 2012, The Astrophysical Journal, 757, 112

Brandt, T. D. & Huang, C. X. 2015a, The Astrophysical Journal, 807, 24

—. 2015b, The Astrophysical Journal, 807, 58

Brown, T. M. 2014, The Astrophysical Journal, 789, 101

Browning, M. K. 2008, The Astrophysical Journal, 676, 1262

Cardini, D. & Cassatella, A. 2007, The Astrophysical Journal, 666, 393

Cargile, P. A., James, D. J., Pepper, J., Kuhn, R. B., Siverd, R., & Stassun, K. G. 2014, The Astrophysical Journal, 782, 29

Carrington, R. C. 1859, Monthly Notices of the Royal Astronomical Society, 19, 81

Casagrande, L., Flynn, C., & Bessell, M. 2008, Monthly Notices of the Royal Astronomical Society, 389, 585

Castellani, V., Degl'Innocenti, S., & Prada Moroni, P. G. 2001, Monthly Notices of the Royal Astronomical Society, 320, 66

Chaboyer, B., Demarque, P., & Pinsonneault, M. H. 1995, The Astrophysical Journal, 441, 876

Chabrier, G. & Küker, M. 2006, Astronomy and Astrophysics, 446, 1027

Choi, P. I. & Herbst, W. 1996, The Astronomical Journal, 111, 283

Christian, D. J., Mathioudakis, M., Arias, T., Jardine, M., & Jess, D. B. 2011, The Astrophysical Journal, 738, 164

Cieza, L., Padgett, D. L., Stapelfeldt, K. R., Augereau, J.-C., Harvey, P., Evans, II, N. J., Merín, B., Koerner, D., Sargent, A., van Dishoeck, E. F., Allen, L., Blake, G., Brooke, T., Chapman, N., Huard, T., Lai, S.-P., Mundy, L., Myers, P. C., Spiesman, W., & Wahhaj, Z. 2007, The Astrophysical Journal, 667, 308

Cieza, L. A., Padgett, D. L., Allen, L. E., McCabe, C. E., Brooke, T. Y., Carey, S. J., Chapman, N. L., Fukagawa, M., Huard, T. L., Noriga-Crespo, A., Peterson, D. E., & Rebull, L. M. 2009, The Astrophysical Journal Letters, 696, L84

Cochran, W. D., Hatzes, A. P., & Paulson, D. B. 2002, The Astronomical Journal, 124, 565

Collier Cameron, A., Davidson, V. A., Hebb, L., Skinner, G., Anderson, D. R., Christian, D. J., Clarkson, W. I., Enoch, B., Irwin, J., Joshi, Y., Haswell, C. A., Hellier, C., Horne, K. D., Kane, S. R., Lister, T. A., Maxted, P. F. L., Norton, A. J., Parley, N., Pollacco, D., Ryans, R., Scholz, A., Skillen, I., Smalley, B., Street, R. A., West, R. G., Wilson, D. M., & Wheatley, P. J. 2009, Monthly Notices of the Royal Astronomical Society, 400, 451

Collier Cameron, A. & Li, J. 1994, Monthly Notices of the Royal Astronomical Society, 269, 1099

Cook, B. A., Williams, P. K. G., & Berger, E. 2014, The Astrophysical Journal, 785, 10

Copenhagen University, O., Institute, A. O., Cambridge, Uk, & Real Instituto Y Observatorio de La Armada, F. E. S. 2006, VizieR Online Data Catalog, 1304, 0

Covey, K. R., Agüeros, M. A., Green, P. J., Haggard, D., Barkhouse, W. A., Drake, J., Evans, N., Kashyap, V., Kim, D.-W., Mossman, A., Pease, D. O., & Silverman, J. D. 2008, The Astrophysical Journal Supplement Series, 178, 339

Covey, K. R., Agüeros, M. A., Law, N. M., Liu, J., Ahmadi, A., Laher, R., Levitan, D., Sesar, B., & Surace, J. 2016, The Astrophysical Journal, 822, 81

Covey, K. R., Ivezić, v., Schlegel, D., Finkbeiner, D., Padmanabhan, N., Lupton, R. H., Agüeros, M. A., Bochanski, J. J., Hawley, S. L., West, A. A., Seth, A., Kimball, A., Gogarten, S. M., Claire, M., Haggard, D., Kaib, N., Schneider, D. P., & Sesar, B. 2007, The Astronomical Journal, 134, 2398

Cranmer, S. R. 2017, The Astrophysical Journal, 840, 114

Cranmer, S. R. & Saar, S. H. 2011, The Astrophysical Journal, 741, 54

Curtis, J. L. 2017, The Astronomical Journal, 153, 275

Curtis, J. L., Wolfgang, A., Wright, J. T., Brewer, J. M., & Johnson, J. A. 2013, The Astronomical Journal, 145, 134

David, T. J., Conroy, K. E., Hillenbrand, L. A., Stassun, K. G., Stauffer, J., Rebull, L. M., Cody, A. M., Isaacson, H., Howard, A. W., & Aigrain, S. 2016, The Astronomical Journal, 151, 112

Delfosse, X., Forveille, T., Perrier, C., & Mayor, M. 1998, Astronomy & Astrophysics, 331, 581

Delorme, P., Collier Cameron, A., Hebb, L., Rostron, J., Lister, T. A., Norton, A. J., Pollacco, D., & West, R. G. 2011, Monthly Notices of the Royal Astronomical Society, 413, 2218

Deluca, E. E. & Gilman, P. A. 1991, in Solar Interior and Atmosphere, 275–303

Deutsch, A. J. 1967, Science, 156, 236

Dicke, R. H. 1964, Nature, 202, 432

Dickens, R. J., Kraft, R. P., & Krzeminski, W. 1968, The Astronomical Journal, 73, 6

Donati, J.-F. 2011, in Astrophysical Dynamics: From Stars to Galaxies, Proceedings from IAU Symposium 271, Vol. 271, 23–31

Donati, J.-F. & Landstreet, J. D. 2009, Annual Review of Astronomy and Astrophysics, 47, 333

Dotter, A., Chaboyer, B., Jevremović, D., Kostov, V., Baron, E., & Ferguson, J. W. 2008, The Astrophysical Journal Supplement Series, 178, 89

Douglas, S. T., Agüeros, M. A., Covey, K. R., Bowsher, E. C., Bochanski, J. J., Cargile, P. A., Kraus, A., Law, N. M., Lemonias, J. J., Arce, H. G., Fierroz, D. F., & Kundert, A. 2014, The Astrophysical Journal, 795, 161

Doyle, J. G. 1987, Monthly Notices of the Royal Astronomical Society, 224, 1P

—. 1996, Astronomy and Astrophysics, 307, 162

Duchêne, G., Bouvier, J., Moraux, E., Bouy, H., Konopacky, Q., & Ghez, A. M. 2013, Astronomy and Astrophysics, 555, A137

Durney, B. R., De Young, D. S., & Roxburgh, I. W. 1993, Solar Physics, 145, 207

Eberhard, G. & Schwarzschild, K. 1913, The Astrophysical Journal, 38

Edwards, S., Strom, S. E., Hartigan, P., Strom, K. M., Hillenbrand, L. A., Herbst, W., Attridge, J., Merrill, K. M., Probst, R., & Gatley, I. 1993, The Astronomical Journal, 106, 372

Epstein, C. R. & Pinsonneault, M. H. 2014, The Astrophysical Journal, 780, 159

Fang, X.-S., Zhao, G., Zhao, J.-K., Chen, Y.-Q., & Bharat Kumar, Y. 2016, Monthly Notices of the Royal Astronomical Society, 463, 2494

Fichtinger, B., Güdel, M., Mutel, R. L., Hallinan, G., Gaidos, E., Skinner, S. L., Lynch, C., & Gayley, K. G. 2017, Astronomy and Astrophysics, 599, A127

Folsom, C. P., Petit, P., Bouvier, J., Lèbre, A., Amard, L., Palacios, A., Morin, J., Donati, J.-F., Jeffers, S. V., Marsden, S. C., & Vidotto, A. A. 2016, Monthly Notices of the Royal Astronomical Society, 457, 580

Foreman-Mackey, D., Hogg, D. W., Lang, D., & Goodman, J. 2013, Publications of the Astronomical Society of the Pacific, 125, 306

Fossati, L., Bagnulo, S., Landstreet, J., Wade, G., Kochukhov, O., Monier, R., Weiss, W., & Gebran, M. 2008, Astronomy and Astrophysics, 483, 891

Franciosini, E., Randich, S., & Pallavicini, R. 2003, Astronomy & Astrophysics, 405, 551

Frazier, E. N. 1970, Solar Physics, 14, 89

Friedman, J. H. 1984, A Variable Span Scatterplot Smoother, Technical Report 5, Laboratory for Computational Statistics, Stanford University, Laboratory for Computational Statistics, Stanford University

Frommert, H. & Kronberg, C. 2001, The Hyades, Melotte 25, `http://messier.seds.org/Mdes/dm044.html`

—. 2007, Messier 44: Observations and Descriptions, `http://messier.seds.org/Mdes/dm044.html`

Galilei, G. 1610, Sidereus Nuncius Magna, Longeque Admirabilia Spectacula Pandens Lunae Facie, Fixis Innumeris, Lacteo Circulo, Stellis Nebulosis, ... Galileo Galileo : Nuper a Se Reperti Beneficio Sunt Observata in Apprime Vero in Quatuor Planetis circa Iovis Stellam Disparibus Intervallis, Atque Periodis, Celeritate Mirabili Circumvolutis ... Atque Medicea Sidera Nuncupandos Decrevit

Gallet, F. & Bouvier, J. 2015, Astronomy and Astrophysics, 577, A98

Garraffo, C., Drake, J. J., & Cohen, O. 2015a, The Astrophysical Journal, 813, 40

—. 2015b, The Astrophysical Journal Letters, 807, L6

Garraffo, C., Drake, J. J., & Cohen, O. 2015c, in , eprint: arXiv:1408.1965, 177–182

Gastine, T., Duarte, L., & Wicht, J. 2012, Astronomy and Astrophysics, 546, A19

Giampapa, M. S., Hall, J. C., Radick, R. R., & Baliunas, S. L. 2006, The Astrophysical Journal, 651, 444

Giampapa, M. S. & Liebert, J. 1986, The Astrophysical Journal, 305, 784

Gieren, W. P., Fouqué, P., & Gómez, M. 1998, The Astrophysical Journal, 496, 17

Gilman, P. A. 1980, in Lecture Notes in Physics, Berlin Springer Verlag, Vol. 114, IAU Colloq. 51: Stellar Turbulence, ed. D. F. Gray & J. L. Linsky, 19–37

Gizis, J. & Reid, I. N. 1995, The Astronomical Journal, 110, 1248

Goldman, B., Röser, S., Schilbach, E., Magnier, E. A., Olczak, C., Henning, T., Jurić, M., Schlafly, E., Chen, W. P., Platais, I., Burgett, W., Hodapp, K., Heasley, J., Kudritzki, R. P., Morgan, J. S., Price, P. A., Tonry, J. L., & Wainscoat, R. 2013, Astronomy & Astrophysics, 559, A43

Gomes da Silva, J., Santos, N. C., Boisse, I., Dumusque, X., & Lovis, C. 2014, Astronomy and Astrophysics, 566, A66

Griffin, R. F. 2012, Journal of Astrophysics and Astronomy, 33, 29

Griffin, R. F., Griffin, R. E. M., Gunn, J. E., & Zimmerman, B. A. 1988, The Astronomical Journal, 96, 172

Griffin, R. F., Mayor, M., & Gunn, J. E. 1982, Astronomy and Astrophysics, 106, 221

Güdel, M. 2004, Astronomy and Astrophysics Review, 12, 71

Guenther, E. W., Paulson, D. B., Cochran, W. D., Patience, J., Hatzes, A. P., & Macintosh, B. 2005, Astronomy and Astrophysics, 442, 1031

Halbwachs, J. L., Mayor, M., Udry, S., & Arenou, F. 2003, Astronomy and Astrophysics, 397, 159

Hall, D. S. 1972, Publications of the Astronomical Society of the Pacific, 84, 323

Hall, J. C. 2008, Living Reviews in Solar Physics, 5, 2

Hambly, N. C., Steele, I. A., Hawkins, M. R. S., & Jameson, R. F. 1995, Astronomy and Astrophysics Supplement Series, 109

Hanson, R. B. 1975, The Astronomical Journal, 80, 379

Hartman, J. D., Bakos, G. Á., Kovács, G., & Noyes, R. W. 2010, Monthly Notices of the Royal Astronomical Society, 408, 475

Hartman, J. D., Bakos, G. Á., Noyes, R. W., Sipőcz, B., Kovács, G., Mazeh, T., Shporer, A., & Pál, A. 2011, The Astronomical Journal, 141, 166

Hartman, J. D., Gaudi, B. S., Pinsonneault, M. H., Stanek, K. Z., Holman, M. J., McLeod, B. A., Meibom, S., Barranco, J. A., & Kalirai, J. S. 2009, The Astrophysical Journal, 691, 342

Hawley, S. L., Tourtellot, J. G., & Reid, I. N. 1999, The Astronomical Journal, 117, 1341

Henden, A. A., Levine, S. E., Terrell, D., Smith, T. C., & Welch, D. 2012, Journal of the American Association of Variable Star Observers (JAAVSO), 40, 430

Henderson, C. B. & Stassun, K. G. 2012, The Astrophysical Journal, 747, 51

Herbst, W., Bailer-Jones, C. A. L., & Mundt, R. 2001, The Astrophysical Journal Letters, 554, L197

Herbst, W., Bailer-Jones, C. A. L., Mundt, R., Meisenheimer, K., & Wackermann, R. 2002, Astronomy and Astrophysics, 396, 513

Herbst, W. & Miller, J. R. 1989, The Astronomical Journal, 97, 891

Hillenbrand, L. A., Bauermeister, A., & White, R. J. 2008, in Proceedings of the 14th Cambridge Workshop on Cool Stars, Stellar Systems, and the Sun, Vol. 384, eprint: arXiv:astro-ph/0703642, 200

Hodgkin, S. T., Pinfield, D. J., Jameson, R. F., Steele, I. A., Cossburn, M. R., & Hambly, N. C. 1999, Monthly Notices of the Royal Astronomical Society, 310, 87

Howell, S. B. 2006, Handbook of CCD Astronomy, 2nd edn., Cambridge Observing Handbooks for Research Astronomers (Cambridge University Press)

Howell, S. B., Sobeck, C., Haas, M., Still, M., Barclay, T., Mullally, F., Troeltzsch, J., Aigrain, S., Bryson, S. T., Caldwell, D., Chaplin, W. J., Cochran, W. D., Huber, D., Marcy, G. W., Miglio, A., Najita, J. R., Smith, M., Twicken, J. D., & Fortney, J. J. 2014, Publications of the Astronomical Society of the Pacific, 126, 398

Hunter, J. D. 2007, Computing in Science Engineering, 9, 90

Husser, T.-O., Wende-von Berg, S., Dreizler, S., Homeier, D., Reiners, A., Barman, T., & Hauschildt, P. H. 2013, Astronomy & Astrophysics, 553, A6

Iben, Jr., I. 1967, Annual Review of Astronomy and Astrophysics, 5, 571

Irwin, J., Aigrain, S., Hodgkin, S., Irwin, M., Bouvier, J., Clarke, C., Hebb, L., & Moraux, E. 2006, Monthly Notices of the Royal Astronomical Society, 370, 954

Irwin, J., Berta, Z. K., Burke, C. J., Charbonneau, D., Nutzman, P., West, A. A., & Falco, E. E. 2011, The Astrophysical Journal, 727, 56

Irwin, J. & Bouvier, J. 2009, in IAU Symposium, Vol. 258, IAU Symposium, ed. E. E. Mamajek, D. R. Soderblom, & R. F. G. Wyse, 363–374

Irwin, J., Hodgkin, S., Aigrain, S., Bouvier, J., Hebb, L., Irwin, M., & Moraux, E. 2008a, Monthly Notices of the Royal Astronomical Society, 384, 675

Irwin, J., Hodgkin, S., Aigrain, S., Bouvier, J., Hebb, L., & Moraux, E. 2008b, Monthly Notices of the Royal Astronomical Society, 383, 1588

Irwin, J., Hodgkin, S., Aigrain, S., Hebb, L., Bouvier, J., Clarke, C., Moraux, E., & Bramich, D. M. 2007, Monthly Notices of the Royal Astronomical Society, 377, 741

Ivezić, Ż., Connolly, A., VanderPlas, J., & Gray, A. 2013, Statistics, Data Mining, and Machine Learning in Astronomy, Princeton Series in Modern Observational Astronomy (Princeton, NJ: Princeton University Press)

Jackson, R. J. & Jeffries, R. D. 2010, Monthly Notices of the Royal Astronomical Society, 407, 465

James, D. J., Jardine, M. M., Jeffries, R. D., Randich, S., Collier Cameron, A., & Ferreira, M. 2000, Monthly Notices of the Royal Astronomical Society, 318, 1217

Janes, K. A. & Phelps, R. L. 1994, The Astronomical Journal, 108, 1773

Janes, K. A., Tilley, C., & Lynga, G. 1988, The Astronomical Journal, 95, 771

Janson, M., Bergfors, C., Brandner, W., Kudryavtseva, N., Hormuth, F., Hippler, S., & Henning, T. 2014, The Astrophysical Journal, 789, 102

Jardine, M. 2004, Astronomy and Astrophysics, 414, L5

Jardine, M. & Unruh, Y. C. 1999, Astronomy and Astrophysics, 346, 883

Jeffries, R. D., Jackson, R. J., Briggs, K. R., Evans, P. A., & Pye, J. P. 2011, Monthly Notices of the Royal Astronomical Society, 411, 2099

Jester, S., Schneider, D. P., Richards, G. T., Green, R. F., Schmidt, M., Hall, P. B., Strauss, M. A., Vanden Berk, D. E., Stoughton, C., Gunn, J. E., Brinkmann, J., Kent, S. M., Smith, J. A., Tucker, D. L., & Yanny, B. 2005, The Astronomical Journal, 130, 873

Johnson, H. L. 1952, The Astrophysical Journal, 116, 640

Jones, B. F. & Cudworth, K. 1983, The Astronomical Journal, 88, 215

Jones, B. F. & Stauffer, J. R. 1991, The Astronomical Journal, 102, 1080

Jones, E., Oliphant, T., Peterson, P., & and others. 2001, {SciPy}: Open Source Scientific Tools for {Python}

Joy, A. H. & Abt, H. A. 1974, The Astrophysical Journal Supplement Series, 28, 1

Kafka, S. & Honeycutt, R. K. 2004, Astronomische Nachrichten, 325, 413

—. 2006, The Astronomical Journal, 132, 1517

Kaiser, N., Aussel, H., Burke, B. E., Boesgaard, H., Chambers, K., Chun, M. R., Heasley, J. N., Hodapp, K.-W., Hunt, B., Jedicke, R., Jewitt, D., Kudritzki, R., Luppino, G. A., Maberry, M., Magnier, E., Monet, D. G., Onaka, P. M., Pickles, A. J., Rhoads, P. H. H., Simon, T., Szalay, A., Szapudi, I., Tholen, D. J., Tonry, J. L., Waterson, M., & Wick, J. 2002, in Proceedings of the SPIE 4836, Vol. 4836, 154–164

Kasting, J. F., Whitmire, D. P., & Reynolds, R. T. 1993, Icarus, 101, 108

Kawaler, S. D. 1988, The Astronomical Journal, 333, 236

—. 1989, The Astrophysical Journal Letters, 343, L65

Kharchenko, N. V., Piskunov, A. E., Schilbach, E., Röser, S., & Scholz, R.-D. 2013, Astronomy and Astrophysics, 558, A53

Kiraga, M. & Stepien, K., K. 2007, Acta Astronomica, 57, 149

Kitchatinov, L. L., Ruediger, G., & Kueker, M. 1994, Astronomy and Astrophysics, 292, 125

Klein Wassink, W. J. 1927, Publications of the Kapteyn Astronomical Laboratory Groningen, 41, 1

Koenigl, A. 1991, The Astrophysical Journal Letters, 370, L39

Konigl, A. & Pudritz, R. E. 2000, Protostars and Planets IV, 759

Kopytova, T. G., Brandner, W., Tognelli, E., Prada Moroni, P. G., Da Rio, N., Röser, S., & Schilbach, E. 2016, Astronomy and Astrophysics, 585, A7

Kovács, G. 2015, Astronomy and Astrophysics, 581, A2

Kovács, G., Hartman, J. D., Bakos, G. A., Quinn, S. N., Penev, K., Latham, D. W., Bhatti, W., Csubry, Z., & de Val-Borro, M. 2014, Monthly Notices of the Royal Astronomical Society, 442, 2081

Kraft, R. P. 1967, The Astrophysical Journal, 150, 551

Kraus, A. L., Cody, A. M., Covey, K. R., Rizzuto, A. C., Mann, A. W., & Ireland, M. J. 2015, The Astrophysical Journal, 807, 3

Kraus, A. L. & Hillenbrand, L. A. 2007, The Astronomical Journal, 134, 2340

Kraus, A. L., Ireland, M. J., Huber, D., Mann, A. W., & Dupuy, T. J. 2016, The Astronomical Journal, 152, 8

Krishnamurthi, A., Pinsonneault, M. H., Barnes, S., & Sofia, S. 1997, The Astrophysical Journal, 480, 303

Lamm, M. H., Bailer-Jones, C. A. L., Mundt, R., Herbst, W., & Scholz, A. 2004, Astronomy and Astrophysics, 417, 557

Law, N. M., Kulkarni, S. R., Dekany, R. G., Ofek, E. O., Quimby, R. M., Nugent, P. E., Surace, J., Grillmair, C. C., Bloom, J. S., Kasliwal, M. M., Bildsten, L., Brown, T., Cenko, S. B., Ciardi, D., Croner, E., Djorgovski, S. G., van Eyken, J., Filippenko, A. V., Fox, D. B.,

Gal-Yam, A., Hale, D., Hamam, N., Helou, G., Henning, J., Howell, D. A., Jacobsen, J., Laher, R., Mattingly, S., McKenna, D., Pickles, A., Poznanski, D., Rahmer, G., Rau, A., Rosing, W., Shara, M., Smith, R., Starr, D., Sullivan, M., Velur, V., Walters, R., & Zolkower, J. 2009, Publications of the Astronomical Society of the Pacific, 121, 1395

Leggett, S. K., Allard, F., Berriman, G., Dahn, C. C., & Hauschildt, P. H. 1996, The Astrophysical Journal Supplement Series, 104, 117

Leighton, R. B. 1969, The Astrophysical Journal, 156, 1

Libralato, M., Nardiello, D., Bedin, L. R., Borsato, L., Granata, V., Malavolta, L., Piotto, G., Ochner, P., Cunial, A., & Nascimbeni, V. 2016, Monthly Notices of the Royal Astronomical Society, 463, 1780

Lichtenegger, H. I. M., Lammer, H., Grießmeier, J.-M., Kulikov, Y. N., von Paris, P., Hausleitner, W., Krauss, S., & Rauer, H. 2010, Icarus, 210, 1

Lockwood, G. W., Thompson, D. T., Radick, R. R., Osborn, W. H., Baggett, W. E., Duncan, D. K., & Hartmann, L. W. 1984, Publications of the Astronomical Society of the Pacific, 96, 714

Luger, R., Agol, E., Kruse, E., Barnes, R., Becker, A., Foreman-Mackey, D., & Deming, D. 2016, The Astronomical Journal, 152, 100

MacGregor, K. B. & Brenner, M. 1991, The Astrophysical Journal, 376, 204

Maggio, A., Sciortino, S., Vaiana, G. S., Majer, P., Bookbinder, J., Golub, L., Harnden, Jr., F. R., & Rosner, R. 1987, The Astrophysical Journal, 315, 687

Malavolta, L., Nascimbeni, V., Piotto, G., Quinn, S. N., Borsato, L., Granata, V., Bonomo, A. S., Marzari, F., Bedin, L. R., Rainer, M., Desidera, S., Lanza, A. F., Poretti, E., Sozzetti, A., White, R. J., Latham, D. W., Cunial, A., Libralato, M., Nardiello, D., Boccato, C., Claudi, R. U., Cosentino, R., Covino, E., Gratton, R., Maggio, A., Micela, G., Molinari, E., Pagano, I., Smareglia, R., Affer, L., Andreuzzi, G., Aparicio, A., Benatti, S., Bignamini, A., Borsa, F., Damasso, M., Di Fabrizio, L., Harutyunyan, A., Esposito, M., Fiorenzano, A. F. M., Gandolfi, D., Giacobbe, P., González Hernández, J. I., Maldonado, J., Masiero, S., Molinaro, M., Pedani, M., & Scandariato, G. 2016, Astronomy and Astrophysics, 588, A118

Mamajek, E. 2014, The Sun Rotates Normally for Its Age

—. 2015, http://www.pas.rochester.edu/ Emamajek/Sun.Txt, http://www.pas.rochester.edu/~emamajek/sun.txt

Mamajek, E. E. & Hillenbrand, L. A. 2008, The Astrophysical Journal, 687, 1264

Mann, A. W., Gaidos, E., Mace, G. N., Johnson, M. C., Bowler, B. P., LaCourse, D., Jacobs, T. L., Vanderburg, A., Kraus, A. L., Kaplan, K. F., & Jaffe, D. T. 2016, The Astrophysical Journal, 818, 46

Marsden, S. C., Carter, B. D., & Donati, J.-F. 2009, Monthly Notices of the Royal Astronomical Society, 399, 888

Marshall, J. L., Burles, S., Thompson, I. B., Shectman, S. A., Bigelow, B. C., Burley, G., Birk, C., Estrada, J., Jones, P., Smith, M., Kowal, V., Castillo, J., Storts, R., & Ortiz, G. 2008, in Society of Photo-Optical Instrumentation Engineers (SPIE) Conference Series, Vol. 7014, Ground-Based and Airborne Instrumentation for Astronomy II

Mason, B. D., Hartkopf, W. I., McAlister, H. A., & Sowell, J. R. 1993, The Astronomical Journal, 106, 637

Mason, B. D., Wycoff, G. L., Hartkopf, W. I., Douglass, G. G., & Worley, C. E. 2001, The Astronomical Journal, 122, 3466

Mathioudakis, M. & Doyle, J. G. 1992, Astronomy and Astrophysics, 262, 523

Matsunaga, N., Feast, M. W., & Menzies, J. W. 2009, Monthly Notices of the Royal Astronomical Society, 397, 933

Matt, S. & Pudritz, R. E. 2005a, The Astrophysical Journal Letters, 632, L135

—. 2005b, Monthly Notices of the Royal Astronomical Society, 356, 167

—. 2008, The Astrophysical Journal, 678, 1109

Matt, S. P., Brun, A. S., Baraffe, I., Bouvier, J., & Chabrier, G. 2015, The Astrophysical Journal Letters, 799, L23

Matt, S. P., MacGregor, K. B., Pinsonneault, M. H., & Greene, T. P. 2012a, The Astrophysical Journal Letters, 754, L26

Matt, S. P., Pinzón, G., Greene, T. P., & Pudritz, R. E. 2012b, The Astrophysical Journal, 745, 101

McQuillan, A., Aigrain, S., & Mazeh, T. 2013, Monthly Notices of the Royal Astronomical Society, 432, 1203

McQuillan, A., Mazeh, T., & Aigrain, S. 2014, The Astrophysical Journal Supplement Series, 211, 24

Meibom, S., Barnes, S. A., Latham, D. W., Batalha, N., Borucki, W. J., Koch, D. G., Basri, G., Walkowicz, L. M., Janes, K. A., Jenkins, J., Van Cleve, J., Haas, M. R., Bryson, S. T., Dupree, A. K., Furesz, G., Szentgyorgyi, A. H., Buchhave, L. A., Clarke, B. D., Twicken, J. D., & Quintana, E. V. 2011a, The Astrophysical Journal Letters, 733, L9

Meibom, S., Barnes, S. A., Platais, I., Gilliland, R. L., Latham, D. W., & Mathieu, R. D. 2015, Nature, 517, 589

Meibom, S. & Mathieu, R. D. 2005, The Astrophysical Journal, 620, 970

Meibom, S., Mathieu, R. D., & Stassun, K. G. 2007, The Astrophysical Journal Letters, 665, L155

—. 2009, The Astrophysical Journal, 695, 679

Meibom, S., Mathieu, R. D., Stassun, K. G., Liebesny, P., & Saar, S. H. 2011b, The Astrophysical Journal, 733, 115

Melotte, P. J. 1915, Memoirs of the Royal Astronomical Society, 60, 175

Mermilliod, J.-C., Duquennoy, A., & Mayor, M. 1994, Astronomy and Astrophysics, 283, 515

Mermilliod, J.-C. & Mayor, M. 1999, Astronomy & Astrophysics, 352, 479

Mermilliod, J.-C., Mayor, M., & Udry, S. 2009, Astronomy and Astrophysics, 498, 949

Mermilliod, J.-C., Weis, E. W., Duquennoy, A., & Mayor, M. 1990, Astronomy and Astrophysics, 235, 114

Messina, S., Parihar, P., Koo, J.-R., Kim, S.-L., Rey, S.-C., & Lee, C.-U. 2010, aap, 513, A29+

Mestel, L. 1984, in Proceedings of the Third Cambridge Workshop on Cool Stars, Stellar Systems, and the Sun, ed. S. L. Baliunas & L. Hartman, Vol. 193 (Berlin Heidelberg New York: Springer-Verlag), 49

Metcalfe, T. S., Egeland, R., & van Saders, J. 2016, The Astrophysical Journal Letters, 826, L2

Meunier, N. & Delfosse, X. 2009, Astronomy and Astrophysics, 501, 1103

Micela, G., Sciortino, S., Vaiana, G. S., Harnden, Jr., F. R., Rosner, R., & Schmitt, J. H. M. M. 1990, The Astrophysical Journal, 348, 557

Micela, G., Sciortino, S., Vaiana, G. S., Schmitt, J. H. M. M., Stern, R. A., Harnden, Jr., F. R., & Rosner, R. 1988, The Astrophysical Journal, 325, 798

Mohanty, S. & Basri, G. 2003, The Astrophysical Journal, 583, 451

Moraux, E., Artemenko, S., Bouvier, J., Irwin, J., Ibrahimov, M., Magakian, T., Grankin, K., Nikogossian, E., Cardoso, C., Hodgkin, S., Aigrain, S., & Movsessian, T. A. 2013, Astronomy and Astrophysics, 560, A13

Morgan, D. P., West, A. A., Garcés, A., Catalán, S., Dhital, S., Fuchs, M., & Silvestri, N. M. 2012, The Astronomical Journal, 144, 93

Morzinski, K. M. 2011, PhD thesis, University of California, Santa Cruz

Mullally, F., Barclay, T., & Barentsen, G. 2016, Astrophysics Source Code Library, ascl:1601.009

Newton, E. R., Irwin, J., Charbonneau, D., Berta-Thompson, Z. K., Dittmann, J. A., & West, A. A. 2016, The Astrophysical Journal, 821, 93

Noyes, R. W. 1983, in Solar and Stellar Magnetic Fields: Origins and Coronal Effects; Proceedings of the Symposium, Vol. 102, 133–146

Noyes, R. W., Weiss, N. O., & Vaughan, A. H. 1984, The Astrophysical Journal, 287, 769

Obermeier, C., Henning, T., Schlieder, J. E., Crossfield, I. J. M., Petigura, E. A., Howard, A. W., Sinukoff, E., Isaacson, H., Ciardi, D. R., David, T. J., Hillenbrand, L. A., Beichman, C. A., Howell, S. B., Horch, E., Everett, M., Hirsch, L., Teske, J., Christiansen, J. L., Lépine, S., Aller, K. M., Liu, M. C., Saglia, R. P., Livingston, J., & Kluge, M. 2016, The Astronomical Journal, 152, 223

Ochsenbein, F., Bauer, P., & Marcout, J. 2000, The Astrophysical Journal Supplement Series, 143, 23

O'dell, M. A., Panagi, P., Hendry, M. A., & Collier Cameron, A. 1995, Astronomy and Astrophysics, 294, 715

Pace, G. & Pasquini, L. 2004, Astronomy and Astrophysics, 426, 1021

Pallavicini, R., Golub, L., Rosner, R., Vaiana, G. S., Ayres, T., & Linsky, J. L. 1981, The Astrophysical Journal, 248, 279

Parker, E. N. 1955, The Astrophysical Journal, 122, 293

—. 1958, The Astrophysical Journal, 128, 664

—. 1975, The Astrophysical Journal, 198, 205

Parker, E. N. 1987, in NASA-Goddard Space Flight Center, Theoretical Problems in High Resolution Solar Physics, Vol. 2483

Patience, J., Ghez, A. M., Reid, I. N., & Matthews, K. 2002, The Astronomical Journal, 123, 1570

Patience, J., Ghez, A. M., Reid, I. N., Weinberger, A. J., & Matthews, K. 1998, The Astronomical Journal, 115, 1972

Paulson, D. B., Cochran, W. D., & Hatzes, A. P. 2004, The Astronomical Journal, 127, 3579

Paulson, D. B., Sneden, C., & Cochran, W. D. 2003, The Astronomical Journal, 125, 3185

Pepper, J., Stanek, K. Z., Pogge, R. W., Latham, D. W., DePoy, D. L., Siverd, R., Poindexter, S., & Sivakoff, G. R. 2008, The Astronomical Journal, 135, 907

Perez, F. & Granger, B. E. 2007, Computing in Science Engineering, 9, 21

Perryman, M. A. C., Brown, A. G. A., Lebreton, Y., Gomez, A., Turon, C., Cayrel de Strobel, G., Mermilliod, J. C., Robichon, N., Kovalevsky, J., & Crifo, F. 1998, Astronomy and Astrophysics, 331, 81

Perryman, M. A. C., Lindegren, L., Kovalevsky, J., Hoeg, E., Bastian, U., Bernacca, P. L., Crézé, M., Donati, F., Grenon, M., Grewing, M., van Leeuwen, F., van der Marel, H., Mignard, F., Murray, C. A., Le Poole, R. S., Schrijver, H., Turon, C., Arenou, F., Froeschlé, M., & Petersen, C. S. 1997, Astronomy and Astrophysics, 323, L49

Peterson, D. M., Baron, R., Dunham, E. W., Mink, D., Aldering, G., Klavetter, J., & Morgan, R. 1989, The Astronomical Journal, 98, 2156

Peterson, D. M. & White, N. M. 1984, The Astronomical Journal, 89, 824

Pevtsov, A. A., Fisher, G. H., Acton, L. W., Longcope, D. W., Johns-Krull, C. M., Kankelborg, C. C., & Metcalf, T. R. 2003, The Astrophysical Journal, 598, 1387

Pinsonneault, M. H., Kawaler, S. D., Sofia, S., & Demarque, P. 1989, The Astrophysical Journal, 338, 424

Pizzolato, N., Maggio, A., Micela, G., Sciortino, S., & Ventura, P. 2003, Astronomy and Astrophysics, 397, 147

Pojmański, G. 2002, Acta Astronomica, 52, 397

Pope, B. J. S., Parviainen, H., & Aigrain, S. 2016, Monthly Notices of the Royal Astronomical Society, 461, 3399

Poppenhaeger, K. & Wolk, S. J. 2014, Astronomy and Astrophysics, 565, L1

Pourbaix, D., Tokovinin, A. A., Batten, A. H., Fekel, F. C., Hartkopf, W. I., Levato, H., Morrell, N. I., Torres, G., & Udry, S. 2004, Astronomy and Astrophysics, 424, 727

Preibisch, T. & Feigelson, E. D. 2005, The Astrophysical Journal Supplement Series, 160, 390

Press, W. H. & Rybicki, G. B. 1989, The Astrophysical Journal, 338, 277

Prosser, C. F., Randich, S., Stauffer, J. R., Schmitt, J. H. M. M., & Simon, T. 1996, The Astronomical Journal, 112, 1570

Prosser, C. F., Shetrone, M. D., Dasgupta, A., Backman, D. E., Laaksonen, B. D., Baker, S. W., Marschall, L. A., Whitney, B. A., Kuijken, K., & Stauffer, J. R. 1995, Publications of the Astronomical Society of the Pacific, 107, 211

Pye, J. P., Hodgkin, S. T., Stern, R. A., & Stauffer, J. R. 1994, Monthly Notices of the Royal Astronomical Society, 266, 798

Quinn, S. N., White, R. J., Latham, D. W., Buchhave, L. A., Cantrell, J. R., Dahm, S. E., Fűrész, G., Szentgyorgyi, A. H., Geary, J. C., Torres, G., Bieryla, A., Berlind, P., Calkins, M. C., Esquerdo, G. A., & Stefanik, R. P. 2012, The Astrophysical Journal Letters, 756, L33

Quinn, S. N., White, R. J., Latham, D. W., Buchhave, L. A., Torres, G., Stefanik, R. P., Berlind, P., Bieryla, A., Calkins, M. C., Esquerdo, G. A., Fűrész, G., Geary, J. C., & Szentgyorgyi, A. H. 2014, The Astrophysical Journal, 787, 27

Radick, R. R., Lockwood, G. W., Skiff, B. A., & Thompson, D. T. 1995, The Astrophysical Journal, 452, 332

Radick, R. R., Mihalas, D., Hartmann, L., Worden, S. P., Africano, J. L., Klimke, A., & Tyson, E. T. 1982, Publications of the Astronomical Society of the Pacific, 94, 934

Radick, R. R., Thompson, D. T., Lockwood, G. W., Duncan, D. K., & Baggett, W. E. 1987, The Astrophysical Journal, 321, 459

Randich, S. 2000, in Astronomical Society of the Pacific Conference Series, Vol. 198, Stellar Clusters and Associations: Convection, Rotation, and Dynamos, ed. R. Pallavicini, G. Micela, & S. Sciortino, 401

Randich, S., Pasquini, L., & Pallavicini, R. 2000, Astronomy and Astrophysics, 356, L25

Randich, S. & Schmitt, J. H. M. M. 1995, Astronomy and Astrophysics, 298, 115

Randich, S., Schmitt, J. H. M. M., Prosser, C. F., & Stauffer, J. R. 1996, Astronomy and Astrophysics, 305, 785

Rau, A., Kulkarni, S. R., Law, N. M., Bloom, J. S., Ciardi, D., Djorgovski, G. S., Fox, D. B., Gal-Yam, A., Grillmair, C. C., Kasliwal, M. M., Nugent, P. E., Ofek, E. O., Quimby, R. M., Reach, W. T., Shara, M., Bildsten, L., Cenko, S. B., Drake, A. J., Filippenko, A. V., Helfand, D. J., Helou, G., Howell, D. A., Poznanski, D., & Sullivan, M. 2009, Publications of the Astronomical Society of the Pacific, 121, 1334

Rauscher, E. & Marcy, G. W. 2006, Publications of the Astronomical Society of the Pacific, 118, 617

Rebassa-Mansergas, A., Schreiber, M. R., & Gänsicke, B. T. 2013, Monthly Notices of the Royal Astronomical Society, 429, 3570

Rebull, L. M. 2001, The Astronomical Journal, 121, 1676

Rebull, L. M., Stauffer, J. R., Bouvier, J., Cody, A. M., Hillenbrand, L. A., Soderblom, D. R., Valenti, J., Barrado, D., Bouy, H., Ciardi, D., Pinsonneault, M., Stassun, K., Micela, G., Aigrain, S., Vrba, F., Somers, G., Christiansen, J., Gillen, E., & Collier Cameron, A. 2016a, The Astronomical Journal, 152, 113

Rebull, L. M., Stauffer, J. R., Bouvier, J., Cody, A. M., Hillenbrand, L. A., Soderblom, D. R., Valenti, J., Barrado, D., Bouy, H., Ciardi, D., Pinsonneault, M., Stassun, K., Micela, G., Aigrain, S., Vrba, F., Somers, G., Gillen, E., & Collier Cameron, A. 2016b, The Astronomical Journal, 152, 114

Rebull, L. M., Stauffer, J. R., Megeath, S. T., Hora, J. L., & Hartmann, L. 2006, The Astrophysical Journal, 646, 297

Rebull, L. M., Wolff, S. C., & Strom, S. E. 2004, The Astronomical Journal, 127, 1029

Reid, I. N. & Gizis, J. E. 1997, The Astronomical Journal, 114, 1992

Reid, I. N. & Hawley, S. L. 2005, New Light on Dark Stars: Red Dwarfs, Low–Mass Stars, Brown Dwarfs, Springer–Praxis books in astrophysics and astronomy. (Praxis Publishing Ltd)

Reid, I. N., Hawley, S. L., & Gizis, J. E. 1995, aj, 110, 1838

Reid, I. N. & Mahoney, S. 2000, Monthly Notices of the Royal Astronomical Society, 316, 827

Reid, N. 1992, Monthly Notices of the Royal Astronomical Society, 257, 257

Reiners, A. 2012, Living Reviews in Solar Physics, 9

Reiners, A. & Basri, G. 2007, The Astrophysical Journal, 656, 1121

—. 2009, Astronomy and Astrophysics, 496, 787

—. 2010, The Astrophysical Journal, 710, 924

Reiners, A. & Mohanty, S. 2012, The Astrophysical Journal, 746, 43

Reiners, A., Schüssler, M., & Passegger, V. M. 2014, The Astrophysical Journal, 794, 144

Rempel, M. 2006, The Astrophysical Journal, 647, 662

Réville, V., Brun, A. S., Matt, S. P., Strugarek, A., & Pinto, R. F. 2015, The Astrophysical Journal, 798, 116

Richichi, A. & Percheron, I. 2002, Astronomy and Astrophysics, 386, 492

Robinson, E. L. & Kraft, R. P. 1974, The Astronomical Journal, 79, 698

Robinson, R. D. & Durney, B. R. 1982, Astronomy and Astrophysics, 108, 322

Röser, S., Schilbach, E., Piskunov, A. E., Kharchenko, N. V., & Scholz, R.-D. 2011, Astronomy and Astrophysics, 531, A92

Schatzman, E. 1949, Annales d'Astrophysique, 12, 203

—. 1962, Annales d'Astrophysique, 25, 18

Schmeja, S., Kharchenko, N. V., Piskunov, A. E., Röser, S., Schilbach, E., Froebrich, D., & Scholz, R.-D. 2014, Astronomy and Astrophysics, 568, A51

Schmidt, S. J., West, A. A., Bochanski, J. J., Hawley, S. L., & Kielty, C. 2014, Publications of the Astronomical Society of the Pacific, 126, 642

Schmitt, J. H. M. M., Golub, L., Harnden, Jr., F. R., Maxson, C. W., Rosner, R., & Vaiana, G. S. 1985, The Astrophysical Journal, 290, 307

Scholz, A. & Eislöffel, J. 2007, Monthly Notices of the Royal Astronomical Society, 381, 1638

Scholz, A., Irwin, J., Bouvier, J., Sipocz, B. M., Hodgkin, S., & Eislöffel, J. 2011, Monthly Notices of the Royal Astronomical Society, 413, 2595

Schou, J., Antia, H. M., Basu, S., Bogart, R. S., Bush, R. I., Chitre, S. M., Christensen-Dalsgaard, J., Di Mauro, M. P., Dziembowski, W. A., Eff-Darwich, A., Gough, D. O., Haber, D. A., Hoeksema, J. T., Howe, R., Korzennik, S. G., Kosovichev, A. G., Larsen, R. M., Pijpers, F. P., Scherrer, P. H., Sekii, T., Tarbell, T. D., Title, A. M., Thompson, M. J., & Toomre, J. 1998, The Astrophysical Journal, 505, 390

Schrijver, C. J., Cote, J., Zwaan, C., & Saar, S. H. 1989, The Astrophysical Journal, 337, 964

Scott, D. W. 1992, Multivariate Density Estimation

Segura, A., Walkowicz, L. M., Meadows, V., Kasting, J., & Hawley, S. 2010, Astrobiology, 10, 751

Shkolnik, E. L. & Barman, T. S. 2014, The Astronomical Journal, 148, 64

Shu, F., Najita, J., Ostriker, E., Wilkin, F., Ruden, S., & Lizano, S. 1994, The Astrophysical Journal, 429, 781

Shulyak, D., Sokoloff, D., Kitchatinov, L., & Moss, D. 2015, Monthly Notices of the Royal Astronomical Society, 449, 3471

Silverman, B. W. 1986, Density Estimation for Statistics and Data Analysis

Skrutskie, M. F., Cutri, R. M., Stiening, R., Weinberg, M. D., Schneider, S., Carpenter, J. M., Beichman, C., Capps, R., Chester, T., Elias, J., Huchra, J., Liebert, J., Lonsdale, C., Monet, D. G., Price, S., Seitzer, P., Jarrett, T., Kirkpatrick, J. D., Gizis, J. E., Howard, E., Evans, T., Fowler, J., Fullmer, L., Hurt, R., Light, R., Kopan, E. L., Marsh, K. A., McCallon, H. L., Tam, R., Van Dyk, S., & Wheelock, S. 2006, The Astronomical Journal, 131, 1163

Skumanich, A. 1972, The Astrophysical Journal, 171, 565

Smith, A. M. S. & WASP Consortium. 2014, Contributions of the Astronomical Observatory Skalnate Pleso, 43, 500

Snodgrass, H. B. & Ulrich, R. K. 1990, The Astrophysical Journal, 351, 309

Soderblom, D. R. 2010, Annual Review of Astronomy and Astrophysics, 48, 581

Soderblom, D. R., Jones, B. F., Balachandran, S., Stauffer, J. R., Duncan, D. K., Fedele, S. B., & Hudon, J. D. 1993, The Astronomical Journal, 106, 1059

Soderblom, D. R., Jones, B. F., & Fischer, D. 2001, The Astrophysical Journal, 563, 334

Solanki, S. K., Motamen, S., & Keppens, R. 1997, Astronomy and Astrophysics, 324, 943

Spitzer, Jr., L. 1958, The Astrophysical Journal, 127, 17

Stassun, K. G., Mathieu, R. D., Mazeh, T., & Vrba, F. J. 1999, The Astronomical Journal, 117, 2941

Stauffer, J., Rebull, L., Bouvier, J., Hillenbrand, L. A., Collier-Cameron, A., Pinsonneault, M., Aigrain, S., Barrado, D., Bouy, H., Ciardi, D., Cody, A. M., David, T., Micela, G., Soderblom, D., Somers, G., Stassun, K. G., Valenti, J., & Vrba, F. J. 2016, The Astronomical Journal, 152, 115

Stauffer, J. R., Balachandran, S. C., Krishnamurthi, A., Pinsonneault, M., Terndrup, D. M., & Stern, R. A. 1997, The Astrophysical Journal, 475, 604

Stauffer, J. R., Giampapa, M. S., Herbst, W., Vincent, J. M., Hartmann, L. W., & Stern, R. A. 1991, The Astrophysical Journal, 374, 142

Stauffer, J. R., Hartmann, L. W., & Latham, D. W. 1987, The Astrophysical Journal Letters, 320, L51

Stauffer, J. R., Liebert, J., Giampapa, M., Macintosh, B., Reid, N., & Hamilton, D. 1994a, The Astronomical Journal, 108, 160

Stauffer, J. R., Prosser, C. F., Hartmann, L., & McCaughrean, M. J. 1994b, The Astronomical Journal, 108, 1375

Steele, I. A. & Jameson, R. F. 1995, Monthly Notices of the Royal Astronomical Society, 272, 630

Stelzer, B., Damasso, M., Scholz, A., & Matt, S. P. 2016, Monthly Notices of the Royal Astronomical Society

Stelzer, B., Marino, A., Micela, G., López-Santiago, J., & Liefke, C. 2013, Monthly Notices of the Royal Astronomical Society, 431, 2063

Stepien, K. 1994, Astronomy and Astrophysics, 292, 191

Stepien, K., Schmitt, J. H. M. M., & Voges, W. 2001, Astronomy and Astrophysics, 370, 157

Strassmeier, K. G. 2002, Astronomische Nachrichten, 323, 309

—. 2009, Astronomy and Astrophysics Review, 17, 251

Terndrup, D. M., Stauffer, J. R., Pinsonneault, M. H., Sills, A., Yuan, Y., Jones, B. F., Fischer, D., & Krishnamurthi, A. 2000, The Astronomical Journal, 119, 1303

Tokovinin, A. A. 1997, Astronomy and Astrophysics Supplement Series, 124, 75

Tonry, J. L., Stubbs, C. W., Lykke, K. R., Doherty, P., Shivvers, I. S., Burgett, W. S., Chambers, K. C., Hodapp, K. W., Kaiser, N., Kudritzki, R.-P., Magnier, E. A., Morgan, J. S., Price, P. A., & Wainscoat, R. J. 2012, The Astrophysical Journal, 750, 99

van Bueren, H. G. 1952, Bulletin of the Astronomical Institutes of the Netherlands, 11, 385

Van Cleve, J. E., Howell, S. B., Smith, J. C., Clarke, B. D., Thompson, S. E., Bryson, S. T., Lund, M. N., Handberg, R., & Chaplin, W. J. 2016, Publications of the Astronomical Society of the Pacific, 128, 075002

van Leeuwen, F. 2009, Astronomy & Astrophysics, 497, 209

van Leeuwen, F. & Alphenaar, P. 1982, The Messenger, 28, 15

van Rhijn, P. J. 1916, Publications of the Kapteyn Astronomical Laboratory Groningen, 26, 1

van Saders, J. L., Ceillier, T., Metcalfe, T. S., Aguirre, V. S., Pinsonneault, M. H., García, R. A., Mathur, S., & Davies, G. R. 2016, Nature, 529, 181

Vanderburg, A. & Johnson, J. A. 2014, Publications of the Astronomical Society of the Pacific, 126, 948

Vanderlinden, H.-L. 1934, Ciel et Terre, 50, 304

Vaughan, A. H., Preston, G. W., Baliunas, S. L., Hartmann, L. W., Noyes, R. W., Middelkoop, F., & Mihalas, D. 1981, The Astrophysical Journal, 250, 276

Vernazza, J. E., Avrett, E. H., & Loeser, R. 1981, The Astrophysical Journal Supplement Series, 45, 635

Vidotto, A. A., Gregory, S. G., Jardine, M., Donati, J. F., Petit, P., Morin, J., Folsom, C. P., Bouvier, J., Cameron, A. C., Hussain, G., Marsden, S., Waite, I. A., Fares, R., Jeffers, S., & do Nascimento, J. D. 2014a, Monthly Notices of the Royal Astronomical Society, 441, 2361

Vidotto, A. A., Jardine, M., Morin, J., Donati, J. F., Opher, M., & Gombosi, T. I. 2014b, Monthly Notices of the Royal Astronomical Society, 438, 1162

Vidotto, A. A., Jardine, M., Opher, M., Donati, J. F., & Gombosi, T. I. 2011, Monthly Notices of the Royal Astronomical Society, 412, 351

Vidotto, A. A., Opher, M., Jatenco-Pereira, V., & Gombosi, T. I. 2010, The Astrophysical Journal, 720, 1262

Vilhu, O. 1984, Astronomy and Astrophysics, 133, 117

Villadsen, J., Hallinan, G., Bourke, S., Güdel, M., & Rupen, M. 2014, The Astrophysical Journal, 788, 112

Vogt, S. S. 1975, The Astrophysical Journal, 199, 418

Walkowicz, L. M., Basri, G., & Valenti, J. A. 2013, The Astrophysical Journal Supplement Series, 205, 17

Walkowicz, L. M. & Hawley, S. L. 2009, The Astronomical Journal, 137, 3297

Walkowicz, L. M., Hawley, S. L., & West, A. A. 2004, Publications of the Astronomical Society of the Pacific, 116, 1105

Walter, F. M. 1982, The Astrophysical Journal, 253, 745

Weber, E. J. & Davis, Jr., L. 1967, The Astrophysical Journal, 148, 217

West, A. A. & Hawley, S. L. 2008, Publications of the Astronomical Society of the Pacific, 120, 1161

West, A. A., Hawley, S. L., Bochanski, J. J., Covey, K. R., Reid, I. N., Dhital, S., Hilton, E. J., & Masuda, M. 2008, The Astronomical Journal, 135, 785

West, A. A., Morgan, D. P., Bochanski, J. J., Andersen, J. M., Bell, K. J., Kowalski, A. F., Davenport, J. R. A., Hawley, S. L., Schmidt, S. J., Bernat, D., Hilton, E. J., Muirhead, P., Covey, K. R., Rojas-Ayala, B., Schlawin, E., Gooding, M., Schluns, K., Dhital, S., Pineda, J. S., & Jones, D. O. 2011, The Astronomical Journal, 141, 97

White, O. R. & Livingston, W. C. 1981, The Astrophysical Journal, 249, 798

Wielen, R. & Fuchs, B. 1988, in The Outer Galaxy: Proceedings of a Symposium Held in Honor of Frank J. Kerr, Vol. 306, 100–106

Wilson, O. C. 1963, The Astrophysical Journal, 138, 832

—. 1968, The Astrophysical Journal, 153, 221

—. 1970, The Astrophysical Journal, 160, 225

—. 1978, The Astrophysical Journal, 226, 379

Withbroe, G. L., Feldman, W. C., & Ahluwalia, H. S. 1991, in The Solar Interior and Atmosphere, ed. A. Cox, W. C. Livingston, & M. Matthews (Tucson: The University of Arizona Press), 1087–1106

Withbroe, G. L. & Noyes, R. W. 1977, Annual Review of Astronomy and Astrophysics, 15, 363

Wolter, U., Schmitt, J. H. M. M., & van Wyk, F. 2005, Astronomy and Astrophysics, 435, 261

Wood, B. E., Müller, H.-R., Zank, G. P., & Linsky, J. L. 2002, The Astrophysical Journal, 574, 412

Wood, B. E., Müller, H.-R., Zank, G. P., Linsky, J. L., & Redfield, S. 2005, The Astrophysical Journal Letters, 628, L143

Wright, E. L., Eisenhardt, P. R. M., Mainzer, A. K., Ressler, M. E., Cutri, R. M., Jarrett, T., Kirkpatrick, J. D., Padgett, D., McMillan, R. S., Skrutskie, M., Stanford, S. A., Cohen, M., Walker, R. G., Mather, J. C., Leisawitz, D., Gautier, III, T. N., McLean, I., Benford, D., Lonsdale, C. J., Blain, A., Mendez, B., Irace, W. R., Duval, V., Liu, F., Royer, D., Heinrichsen, I., Howard, J., Shannon, M., Kendall, M., Walsh, A. L., Larsen, M., Cardon, J. G., Schick, S., Schwalm, M., Abid, M., Fabinsky, B., Naes, L., & Tsai, C.-W. 2010, The Astronomical Journal, 140, 1868

Wright, N. J., Drake, J. J., Mamajek, E. E., & Henry, G. W. 2011, The Astrophysical Journal, 743, 48

Yadav, R. K., Christensen, U. R., Morin, J., Gastine, T., Reiners, A., Poppenhaeger, K., & Wolk, S. J. 2015a, The Astrophysical Journal Letters, 813, L31

Yadav, R. K., Gastine, T., Christensen, U. R., & Reiners, A. 2015b, Astronomy and Astrophysics, 573, A68

Zacharias, N., Finch, C. T., Girard, T. M., Henden, A., Bartlett, J. L., Monet, D. G., & Zacharias, M. I. 2012, VizieR Online Data Catalog, 1322, 0

Zahn, J.-P. 2008, in EAS Publications Series, Vol. 29, Tidal Effects in Stars, Planets, and Disks, 67–90, eprint: arXiv:0807.4870

Zuckerman, B. & Song, I. 2004, Annual Review of Astronomy and Astrophysics, 42, 685

Appendix A

Recalculating the χ Factor

Walkowicz et al. (2004), hereafter WHW04, describe the difficulty of computing $L_{H\alpha}/L_{bol}$: it requires flux-calibrated spectra and measurements of each star's distance. WHW04 therefore derive a distance-independent method for calculating $L_{H\alpha}/L_{bol}$ using the factor $\chi = f_0/f_{bol}$, where f_0 is the continuum flux level for the $H\alpha$ line and f_{bol} is the apparent bolometric flux. When the $H\alpha$ line EqW, $W_{H\alpha}$, is known, one may find

$$\frac{L_{H\alpha}}{L_{bol}} = -W_{H\alpha}\chi.$$

Calculating χ for a star requires photometry and a well-calibrated spectrum, which provide the means for calculating f_0 and f_{bol}. We define f_0 to be the mean flux in two windows: 6550−6560 and 6570−6580 Å (West & Hawley 2008). We determine f_{bol} by finding the bolometric correction and calculating the apparent bolometric magnitude, m_{bol}, then converting m_{bol} to f_{bol} using solar values. The absolute solar bolometric flux, $F_{\odot,bol}$, is

$$F_{\odot,bol} = \frac{L_\odot}{4\pi(10\text{ pc})^2},$$

where $L_\odot = 3.842 \times 10^{33}$ erg s^{-1} cm^{-2} is the luminosity of the Sun (Mamajek 2015). Given

[0]This chapter is a reproduction of the appendix to a paper that has been published by The Astrophysical Journal. It can be found at `http://iopscience.iop.org/article/10.1088/0004-637X/795/2/161/meta`. The article has been reformatted for Chapter 2 and this section.

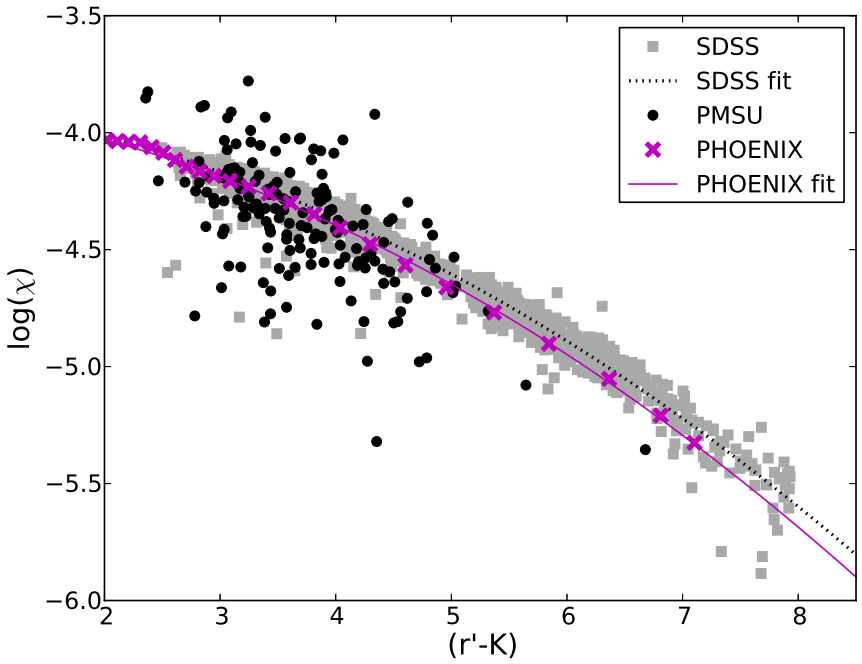

Figure A.1 χ calculated for SDSS and PMSU data and for PHOENIX model spectra. The PMSU data show significant scatter in χ and no obvious dependence of χ on color, while the SDSS data show less scatter and a smooth trend with color. The dotted line shows quadratic fit to the SDSS data. The solid line shows a quadratic fit to the PHOENIX model values, which are similar to, though slightly lower than, the typical SDSS values.

the absolute bolometric magnitude of the Sun, $M_{\odot,bol} = 4.74$ (Mamajek 2015), we can then calculate

$$f_{bol} = F_{\odot,bol} 10^{-0.4(m_{bol} - M_{\odot,bol})}$$

for each star.

WHW04 calculated χ for early-mid M dwarfs using stars from the 8 pc sample that have spectra in the PMSU spectroscopic survey (Reid et al. 1995). WHW04 used the Leggett et al. (1996) *K*-band bolometric corrections to determine f_{bol}. To calculate f_0, they used the region 6555−6560 Å. West & Hawley (2008) use the WHW04 χ values, but define the continuum windows as 6550−6560 and 6570−6580 Å. Additionally, WHW04 state that the spectra have been spectrophotometrically calibrated in the region around $H\alpha$, but Reid et al. (1995) state that the PMSU spectra are only calibrated to a relative, not an absolute, flux scale.

We computed χ for PMSU stars using photometry compiled by I. N. Reid[1] and fol-

[1] `http://www.stsci.edu/~inr/pmsu.html`

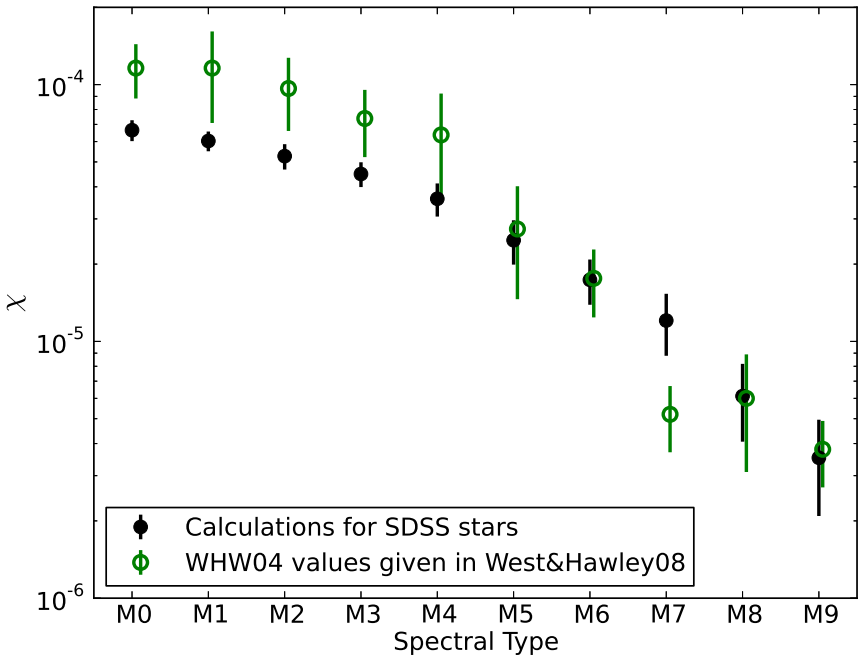

Figure A.2 A comparison of our χ values for SDSS M dwarfs and those listed in West & Hawley (2008). The West & Hawley (2008) values are shifted slightly to the right for clarity. For M0-M3 and M7 dwarfs, our values are inconsistent with those calculated by WHWO4 and West & Hawley (2008).

lowing the same procedure as WHW04, and we found two problems. First, our χ values for early M dwarfs do not match those calculated by WHW04: our values were systematically lower by ≈1/3 dex. After ruling out input photometry, bolometric corrections, and the continuum window for calculating f_0 as potential sources of the offset, we traced the discrepancy to a difference in calculating f_{bol}. Our values for $log(f_{bol})$ were consistently ≈0.5 dex lower than those given by WHW04's equation 8, which gives f_{bol} as a function of apparent K.[2] We compared our f_{bol} values to a number of model-derived and empirical values (Baraffe et al. 1998; Kraus & Hillenbrand 2007; Dotter et al. 2008; Casagrande et al. 2008; Boyajian et al. 2012, in addition to PHOENIX- and SDSS-based values; see discussion below) and in all cases our calculations matched the literature values, while the WHW04 results were consistently too low.

Second, the PMSU stars show a large scatter in χ, and therefore the WHW04 χ values do not have a well-defined dependence on color. This, along with the fact that we did not

[2]WHW04 give equations to calculate a star's bolometric flux as a function of its apparent magnitude and as a function of its color. These equations are not self-consistent, as apparent flux is distance-dependent, just like apparent magnitude, but color and absolute flux are distance-independent.

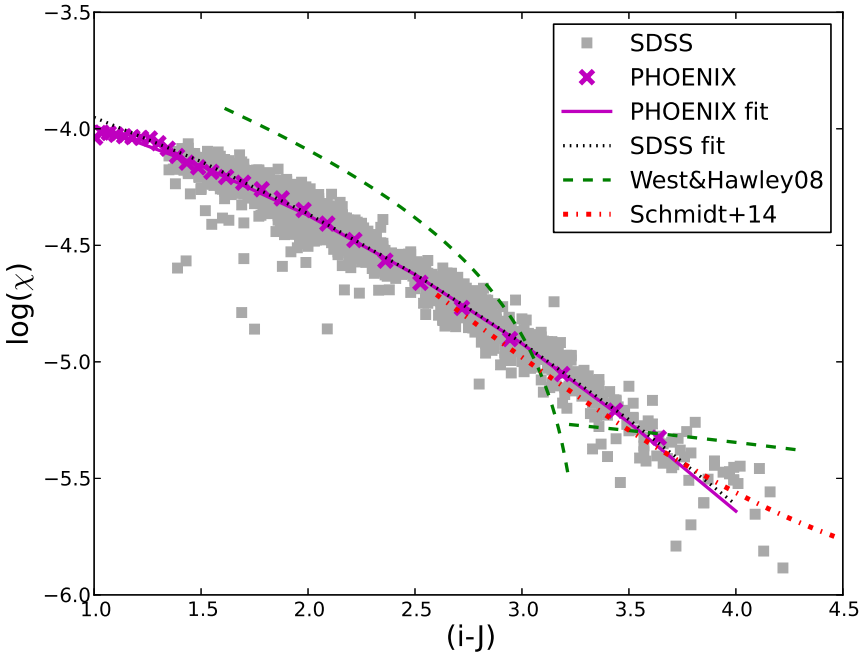

Figure A.3 χ calculated for SDSS M dwarfs and for PHOENIX model spectra. Also shown are the functions for χ vs. $(i-J)$ given by West & Hawley (2008) and Schmidt et al. (2014), and quadratic fits to the SDSS data and the PHOENIX model values. The PHOENIX values match the SDSS values very well, but the function from West & Hawley (2008) shows a very different trend of χ with color.

have a well-calibrated set of spectra to calculate χ for K dwarfs, motivated our calculation of χ from the PHOENIX models. To check the model values against empirical data, we also calculated χ for M dwarfs in SDSS. After matching the spectroscopic West et al. (2011) SDSS M dwarf catalog with the "high quality" SDSS/2MASS photometry of Covey et al. (2007), we calculated χ for nearly 2800 stars. (We use BC_r, calculated as a function of $(r-K)$ from the SED table in Kraus & Hillenbrand (2007), to obtain f_{bol}.) The results from both the PMSU and SDSS samples are shown in Figure A.1, where χ has been calculated by our procedure for all stars in that figure. The χ data for the SDSS stars show much less scatter than for the PMSU sample, and also a clearer color-dependence.

We also calculated the average χ for SDSS stars of each M subtype (using the SpTs listed in West et al. 2011) and compared these χ values with those presented in WHW04 and West & Hawley (2008). The average and standard deviation of χ for each SpT is given in Table A.1, and plotted with the WHW04 and West & Hawley (2008) values in Figure A.2. For M0-M3 and M7 dwarfs, our values are inconsistent with those calculated by these authors.

Table A.1. χ values for M stars, calculated from SDSS data

SpT	χ ($\times 10^{-5}$)
M0	6.6453 ± 0.6207
M1	6.0334 ± 0.5326
M2	5.2658 ± 0.5963
M3	4.4872 ± 0.4967
M4	3.5926 ± 0.5297
M5	2.4768 ± 0.4860
M6	1.7363 ± 0.3475
M7	1.2057 ± 0.3267
M8	0.6122 ± 0.2053
M9	0.3522 ± 0.1432

Note. — The χ values are the average of the SDSS distribution, and uncertainties are the standard deviation of that distribution.

To obtain χ for the full range of K and M dwarfs in our sample, we calculated χ from the PHOENIX ACES model spectra (Husser et al. 2013). We used spectra with $2500 \leq T_{eff} \leq 4800$ K, $log(g) = 5.0$, and solar metallicity. The continuum flux is measured between 6550−6560 and 6570−6580 Å, as above. We computed synthetic photometry by convolving these model spectra with the SDSS and 2MASS filter curves. The resulting optical and near-infrared colors and the corresponding χ values are given in Table A.2.

We fit a quadratic function to χ versus $(r' - K)$ and χ versus $(i - J)$, assuming 10% errors in χ and using typical photometric errors for SDSS and 2MASS magnitudes (2% and 5%, respectively; Abazajian et al. 2009; Skrutskie et al. 2006). The resulting values and fit are shown in Figures A.1 and A.3. The corresponding equations are:

$$\begin{aligned} log_{10}(\chi) &= (-0.0232 \pm 0.0022) \times (r' - K)^2 \\ &- (0.0334 \pm 0.0442) \times (r' - K) - (3.8477 \pm 0.0292) \\ log_{10}(\chi) &= (-0.0841 \pm 0.0091) \times (i - J)^2 \\ &- (0.1301 \pm 0.0377) \times (i - J) - (3.7746 \pm 0.0343) \end{aligned}$$

Table A.2. Colors and χ values from PHOENIX model spectra

T_{eff} (K)	SpT	$(g-r)$	$(r-i)$	$(i-z)$	$(z-J)$	$(J-H)$	$(H-K)$	$(r'-J)$	$(r'-K)$	χ ($\times 10^{-5}$)
5200	K0.3	0.660	0.192	0.069	0.935	0.491	0.025	1.183	1.699	9.170
5100	K0.9	0.704	0.207	0.082	0.954	0.513	0.029	1.229	1.771	9.633
5000	K1.4	0.751	0.223	0.094	0.974	0.536	0.033	1.277	1.847	9.592
4900	K2.0	0.800	0.241	0.108	0.995	0.562	0.038	1.328	1.928	9.421
4800	K2.6	0.852	0.260	0.122	1.018	0.591	0.043	1.384	2.018	9.292
4700	K3.3	0.911	0.281	0.137	1.042	0.619	0.050	1.443	2.112	9.209
4600	K3.9	0.974	0.305	0.154	1.065	0.645	0.057	1.507	2.210	9.142
4500	K4.4	1.037	0.333	0.174	1.086	0.668	0.066	1.575	2.309	9.087
4400	K4.8	1.096	0.366	0.196	1.104	0.684	0.077	1.647	2.408	8.673
4300	K5.3	1.153	0.403	0.222	1.122	0.695	0.089	1.726	2.510	8.211
4200	K6.0	1.205	0.442	0.250	1.138	0.698	0.105	1.807	2.610	7.645
4100	K6.7	1.249	0.484	0.278	1.155	0.696	0.122	1.894	2.711	7.156
4000	K7.9	1.287	0.533	0.312	1.174	0.689	0.140	1.994	2.823	6.836
3900	K9.3	1.318	0.589	0.351	1.197	0.682	0.156	2.110	2.948	6.533
3800	M0.3	1.343	0.654	0.393	1.224	0.677	0.170	2.241	3.088	6.211
3700	M0.9	1.361	0.732	0.442	1.255	0.672	0.180	2.397	3.248	5.867
3600	M1.5	1.376	0.820	0.494	1.290	0.667	0.187	2.568	3.422	5.502
3500	M2.1	1.391	0.916	0.548	1.329	0.662	0.194	2.754	3.610	5.026
3400	M2.7	1.408	1.021	0.604	1.375	0.657	0.200	2.957	3.814	4.483
3300	M3.3	1.430	1.134	0.663	1.427	0.653	0.208	3.177	4.039	3.918
3200	M3.9	1.453	1.264	0.727	1.489	0.651	0.218	3.430	4.298	3.331
3100	M4.5	1.474	1.419	0.799	1.562	0.652	0.227	3.724	4.603	2.716

We also fit quadratics to the SDSS M dwarf data for both colors, which yielded

$$\begin{aligned} log_{10}(\chi) &= (-0.0226 \pm 0.0007) \times (r'-K)^2 \\ &- (0.0374 \pm 0.0066) \times (r'-K) - (-3.8524 \pm 0.0148) \\ log_{10}(\chi) &= (-0.0703 \pm 0.0033) \times (i-J)^2 \\ &- (0.2025 \pm 0.0156) \times (i-J) - (3.6783 \pm 0.0175) \end{aligned}$$

Although the PHOENIX values are slightly below the SDSS values, the difference is $\lesssim$0.05 dex.

Schmidt et al. (2014) also calculate χ for $(i-J) > 2.6$ (SpTs later than M7). The χ values calculated here from SDSS and synthetic spectra are consistent with those from Schmidt et al. (2014) in the overlapping range.

Table A.2—Continued

T_{eff} (K)	SpT	$(g-r)$	$(r-i)$	$(i-z)$	$(z-J)$	$(J-H)$	$(H-K)$	$(r'-J)$	$(r'-K)$	χ ($\times 10^{-5}$)
3000	M5.1	1.485	1.603	0.882	1.643	0.656	0.235	4.065	4.957	2.183
2900	M5.6	1.494	1.817	0.974	1.746	0.659	0.243	4.466	5.368	1.703
2800	M6.3	1.489	2.068	1.078	1.866	0.663	0.248	4.933	5.844	1.252
2700	M7.2	1.480	2.346	1.189	1.999	0.668	0.252	5.445	6.365	0.886
2600	M8.0	1.566	2.539	1.294	2.142	0.675	0.257	5.879	6.811	0.618
2500	M8.5	1.757	2.623	1.371	2.269	0.682	0.257	6.164	7.103	0.472

*Spectral types are determined by interpolating the Teff-Spectral Type relationship assembled in table 5 of Kraus & Hillenbrand (2007).

Note. — Although we have given the colors as pairs of neighboring bands, better leverage on stellar properties is generally found with a wider spread in wavelength, e.g., $(i-J)$. We computed synthetic photometry by convolving model spectra with the SDSS and 2MASS filter curves.

Appendix B

Candidate Transiting and Eclipsing Systems in Praesepe

In our by-eye inspection/validation of the *K2* light curves and P_{rot} measurements, we identify six candidate eclipsing systems. We briefly discuss each them here, but with one exception, we make no attempt to confirm them at this time. The membership probabilities and spectral types noted below are all from Kraus & Hillenbrand (2007). We present the light curves for these seven objects in Figure B.1.

• *EPIC 211919680* (2MASS J08440390+1901129, HSHJ474, $M_* = 0.18\ M_\odot$, M5, $P_{mem} =$ 96%) shows sinusoidal modulation with $P_{rot} = 0.31$ d and eclipses every 4.77 d. There is no other star visible nearby in the SDSS *r*-band image. This star has not been previously identified as a binary system.

• *EPIC 211946007* (2MASS J08423944+1924520, HSHJ430, $M_* = 0.20\ M_\odot$, M4, $P_{mem} =$ 99%) shows sinusoidal modulation with $P_{rot} = 2.25$ d, consistent with the $P_{rot} = 2.24$ d measured by Scholz et al. (2011), and eclipses every 1.98 d. Three additional stars are visible in the SDSS *r*-band image: two faint companions near the target star that are blended on the *K2* chip, and an additional star just off the edge of the *K2* pixel stamp. This star had not been identified as a binary system.

[0]This chapter is a reproduction of the appendix to a paper that has been accepted by The Astrophysical Journal. The preprint can currently be found at `https://arxiv.org/abs/1704.04507`. The article has been reformatted for Chapter 4 and this section.

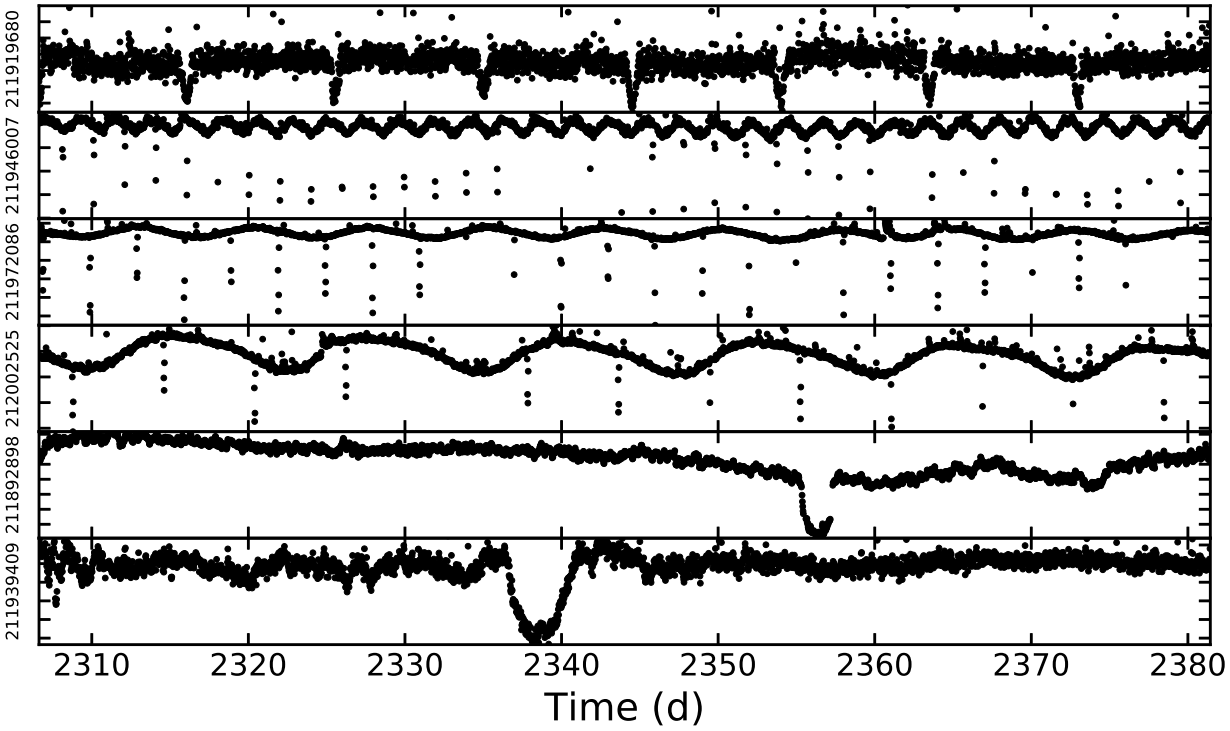

Figure B.1 Light curves for six candidate eclipsing systems identified by eye from Campaign 5 data; EPIC IDs are given on the left axis. The top four systems show signatures of rotation as well as multiple eclipses, and the bottom three show only one eclipse during Campaign 5. EPIC 211972086 (third panel) was preciously detected in PTF data, and has been confirmed with RVs (Kraus et al. in prep.)

• *EPIC 211972086* (2MASS J08504984+1948365, $M_* = 0.31\ M_\odot$, M3, $P_{mem} = 98\%$) was previously identified as a binary from PTF data and has been confirmed via radial velocity (RV) observations; analysis of this system is forthcoming in Kraus et al. (in prep). The *K2* light curve shows sinusoidal modulation with $P_{rot} = 7.49$ d, consistent with the PTF $P_{rot} = 7.43$ d, as well as eclipses. There is no other star visible nearby in the SDSS *r*-band image. The eclipsing binary (EB) period (≈6 d) is not detected in the periodogram.

• *EPIC 212002525* (2MASS J08394203+2017450, M4, $P_{mem} = 100\%$) shows sinusoidal modulation with $P_{rot} = 12.63$ d; the eclipse period looks slightly shorter than that but is not detected in the periodogram. There is one star visible in the corner of the *K2* pixel stamp. This star had not been identified as a binary system.

In addition to the above systems, EPIC 211929081 and EPIC 211939409 show no sinusoidal modulations but do have a possible single eclipse during Campaign 5. These single-eclipse candidates are admittedly more suspect than the four above, as a single

drop in flux could be due to any number of instrumental or astrophysical issues. The eclipse durations are longer than expected for two main sequence stars eclipsing each other; if these are real astrophysical eclipses, then the eclipse may come from a faint background giant contaminating the light curve, or from a gas giant planet with a large ring system. RV data are needed to confirm the cluster membership of these stars and check for companions.

• *EPIC 211892898* (2MASS J08433463+1837199, $M_* = 1.06\ M_\odot$, K4, $P_{mem} = 99\%$) has two nearby companions, at least one of which is blended into the *K2* PSF of the target. There is also a correlated increase in the white-noise component of the light curve during the eclipse ingress and egress. This star has not been previously identified as a binary system.

• *EPIC 211939409* (2MASS J08512585+1918564, $M_* = 0.36$ Msun, M3, $P_{mem} = 96\%$) has a neighboring object in the corner of the *K2* pixel stamp. This star has not been previously identified as a binary system.

Only Barros et al. (2016) have published EB candidates from Campaign 5, but due to their survey limits these authors did not detect any of the above candidates. Barros et al. (2016) restricted their analysis to stars with $K_p < 15$, which removes the four obvious EB candidates as they all have $K_p > 16.5$. Barros et al. (2016) also required more than one eclipse or transit for detection, which explains why these authors do not list the two single-eclipse events that we identified by eye. Barros et al. (2016) do not identify any other EB candidates in Praesepe, although as mentioned in Section 4.4 these authors do find one candidate planet in the cluster.

Three other studies have found candidate transiting planets in Praesepe (Pope et al. 2016; Libralato et al. 2016; Obermeier et al. 2016). These transits are mostly small and were missed when we inspected the light curves.

Appendix C

Acknowledgement of assistance, funding, software, facilities, and data

This work was supported by the NSF through grants AST-1255419 and AST-1517367. I thank my coauthors on the papers that form Chapters 2-4: Marcel Agüeros, Kevin Covey, Phill Cargile, Adam Kraus, Tom Barclay, Emily Bowsher, John Bochanski, Ann Marie Cody, Steve Howell, Taisiya Kopytova, Nick Law, Jenna Lemonias, Hector Arce, David Fierroz, and Alisha Kundert. I also gratefully acknowledge the hospitality of the *Kepler*/*K2* Science Team at NASA Ames Research Center, particularly the advice and support of Geert Barentsen, Knicole Colon, Mike Haas, Mark Messersmith, Fergal Mullally, and Susan E. Thompson, without whom Chapter 3 would not have been written.

I thank Stella Kafka and John Stauffer for sharing their spectra, which forms part of the analysis in Chapter 2. I also thank Tim Brown, Sean Matt, Subu Mohanty, and Ansgar Reiners for discussing and sharing their models with Marcel and I. I am grateful to Ruth Angus, Dan Foreman-Mackey, Rob Jeffries, Sean Matt, Marc Pinsonneault, Sarah Schmidt, Keivan Stassun, Lucianne Walkowicz, Andrew West, and Nicholas Wright for useful discussions and comments.

My work has greatly benefited from Python scientific libraries, including NumPy, SciPy (Jones et al. 2001), and Matplotlib (Hunter 2007), along with the IPython environment (Perez & Granger 2007). I have also made use of the *Astropy* package (Astropy

Collaboration et al. 2013), especially the affiliated *photutils* package.[1] I have used the *supersmoother* and *gatspy* packages developed by J. Vanderplas,[2] the *pywcsgrid2* package developed by J. Lee[3] and the *K2fov* package created by F. Mullally, T. Barclay, and G. Barentsen for NASA's Kepler/K2 Guest Observer Office (Mullally et al. 2016).

This dissertation includes data gathered with the 6.5 meter Magellan Telescopes located at Las Campanas Observatory, Chile. The WIYN Observatory is a joint facility of the University of Wisconsin-Madison, Indiana University, the National Optical Astronomy Observatory and the University of Missouri. This work is based on observations obtained at the MDM Observatory, operated by Dartmouth College, Columbia University, Ohio State University, Ohio University, and the University of Michigan. I thank John Thorstensen, Eric Galayda, and Jules Halpern for their help with the MDM observations, and the WIYN observing specialists for their assistance.

This research has made use of NASA's Astrophysics Data System Bibliographic Services, the SIMBAD database, operated at CDS, Strasbourg, France, the NASA/IPAC Extragalactic Database, operated by the Jet Propulsion Laboratory, California Institute of Technology, under contract with the National Aeronautics and Space Administration, and the VizieR database of astronomical catalogs (Ochsenbein et al. 2000).

This dissertation includes data collected by the *K2* mission. Funding for the *K2* mission is provided by the NASA Science Mission directorate. Some of the data presented in this paper were obtained from the Mikulski Archive for Space Telescopes (MAST). STScI is operated by the Association of Universities for Research in Astronomy, Inc., under NASA contract NAS5-26555. Support for MAST for non-*HST* data is provided by the NASA Office of Space Science via grant NNX09AF08G and by other grants and contracts.

This research has made use of the NASA/ IPAC Infrared Science Archive, which is operated by the Jet Propulsion Laboratory, California Institute of Technology, under contract with the National Aeronautics and Space Administration. The Two Micron All Sky Survey was a joint project of the University of Massachusetts and IPAC.

The Digitized Sky Survey was produced at the Space Telescope Science Institute under U.S. Government grant NAG W-2166. The images of these surveys are based on photographic data obtained using the Oschin Schmidt Telescope on Palomar Mountain and the UK Schmidt Telescope. The plates were processed into the present compressed digital form with the permission of these institutions.

[1] `http://photutils.readthedocs.org/en/latest/`

[2] `https://github.com/jakevdp/supersmoother`, `https://github.com/astroML/gatspy`

[3] `https://github.com/leejjoon/pywcsgrid2`

The Two Micron All Sky Survey was a joint project of the University of Massachusetts and the Infrared Processing and Analysis Center (California Institute of Technology). The University of Massachusetts was responsible for the overall management of the project, the observing facilities and the data acquisition. The Infrared Processing and Analysis Center was responsible for data processing, data distribution and data archiving.

Funding for SDSS-III has been provided by the Alfred P. Sloan Foundation, the Participating Institutions, the National Science Foundation, and the U.S. Department of Energy Office of Science. The SDSS-III web site is http://www.sdss3.org/.

SDSS-III is managed by the Astrophysical Research Consortium for the Participating Institutions of the SDSS-III Collaboration including the University of Arizona, the Brazilian Participation Group, Brookhaven National Laboratory, University of Cambridge, Carnegie Mellon University, University of Florida, the French Participation Group, the German Participation Group, Harvard University, the Instituto de Astrofisica de Canarias, the Michigan State/Notre Dame/JINA Participation Group, Johns Hopkins University, Lawrence Berkeley National Laboratory, Max Planck Institute for Astrophysics, Max Planck Institute for Extraterrestrial Physics, New Mexico State University, New York University, Ohio State University, Pennsylvania State University, University of Portsmouth, Princeton University, the Spanish Participation Group, University of Tokyo, University of Utah, Vanderbilt University, University of Virginia, University of Washington, and Yale University.